FACULTY
OF MATHEMATICS
AND PHYSICS
Charles University

DOCTORAL THESIS

Michael Greben

Advanced spectroscopic characterization of quantum dot ensembles

Department of Chemical Physics and Optics

Supervisor of the doctoral thesis: Prof. Jan Valenta, Ph.D.

Study programme: Physics

Specialization: Physics of Nanostructures

Prague 2018

I declare that I carried out this doctoral thesis independently, and only with the cited sources, literature and other professional sources.

I understand that my work relates to the rights and obligations under the Act No. 121/2000 Coll., the Copyright Act, as amended, in particular the fact that the Charles University has the right to conclude a license agreement on the use of this work as a school work pursuant to Section 60 paragraph 1 of the Copyright Act.

In Prague, January 2nd, 2018 Author signature:

Title: Advanced spectroscopic characterization of quantum dot ensembles

Author: Michael Greben

Department: Department of Chemical Physics and Optics

Supervisor of the doctoral thesis: Prof. Jan Valenta, Ph.D.

Abstract:

Semiconductor quantum dots (QDs) are small crystallites whose sizes (of the order of nm) cause spatial confinement of carriers in all 3 dimensions. As result, QDs often reveal very different physical properties in comparison with their bulk counterparts. From the optical point of view, the broadening of bandgap with QD-size shrinking is particularly interesting. It is a purely quantum mechanical effect that results from quantum confinement (QC), i.e. dimensional limitations of excitons. A strong spatial confinement leads to a relaxation of momentum (Heisenberg uncertainty principle), consequently, larger overlap of the wave-functions of carriers results in significant increase of probability of radiative recombination. Therefore ensembles of QDs are promising candidates for new generations of photonic and photovoltaic devices.

This PhD thesis is primary focused on detailed spectroscopic characterization of ensembles of direct (PbS) and indirect (Si) semiconductor QDs in both colloidal (toluene) and matrix-embedded (oxide or oxinitrides multilayers) forms. The oleic-acid capped PbS QDs were purchased commercially. Si QDs with dodecyl-functionalization were synthesized by non-thermal plasma method and the solid samples with Si QDs were fabricated by annealing multilayers of altering Si-rich and stoichiometric oxides deposited by the PECVD method (both types of Si QDs were fabricated and provided by our foreign collaborators).

The main aim of this work was to gain an insight on some fundamental problems in ensembles of QDs with an ambition to improve their optical characteristics, namely absorption and emission efficiencies. The optical properties of samples were characterized by time-integrated and time-resolved (TR) photoluminescence (PL) spectroscopies. The analysis of PL spectra and the position of their peak changing with size and material of QDs proved the QC-related origin of PL. Using the set-up with an integrating sphere we experimentally studied absolute quantum yield (QY) in dependence on various parameters (QD concentration etc.). To assess the absorption strength of Si QDs, namely absorption cross-section, we theoretically and experimentally developed PL modulation technique that is based on TR onset and decay transients. We paid special attention to careful investigation and setting of the optimum experimental parameters for TR PL experiments. By variation of the temperature and inter-QD distance in multilayer samples with Si QDs we proved the dependence of both absorption and emission properties on those parameters and determined the optimum oxide barrier thickness to maximize PL brightness. In addition, we developed a novel procedure to derive size-selected decays from spectrally resolved ones and retrieved 100% efficient size fraction of Si QDs in colloidal suspension of nearly fully-radiative QDs. These results were used for estimation of internal quantum efficiency (IQE) in solid samples. Finally, comparing results of IQE with PL QY we demonstrated and estimated the fraction of dark QDs in ensembles of QDs. Further investigation should be focused on understanding the physical properties of dark QDs to minimize their number and maximize the emission efficiency of ensembles of QDs.

Keywords: quantum dots, lifetime, quantum yield, internal quantum efficiency, absorption cross-section

Název práce: Pokročilá spektroskopická charakterizace souborů kvantových teček

Autor: Michael Greben

Školící pracoviště: Katedra chemické fyziky a optiky

Školitel: Prof. RNDr. Jan Valenta, Ph.D.

Abstrakt:

Polovodičové kvantové tečky (KT) jsou několik nanometrů velké krystality, v nichž je pohyb vybuzených elektronů a děr omezen ve všech třech rozměrech, což vede ke kvantování jejich energie – tzv. kvantový rozměrový jev (KRJ). V důsledku toho, KT často jeví velmi odlišné fyzikální vlastnosti ve srovnání s jejich objemovými protějšky. Z optického hlediska je zvláště zajímavé rozšiřování zakázaného pásu s klesající velikostí KT. Velká lokalizace částice v prostoru také vede k "rozmazání" hybnosti (Heisenbergův princip neurčitosti) a způsobí větší překrytí vlnových funkcí nosičů, a tedy významné zvýšení pravděpodobnosti zářivé rekombinace (v případě polovodičů s nepřímým zakázaným pásem). To dělá z povodičových KT slibné kandidáty pro nové generace fotonických a fotovoltaických součástek.

Tato disertační práce je primárně zaměřena na podrobnou spektroskopickou charakterizaci souborů přímých (PbS) a nepřímých (Si) polovodičových KT, a to jak v koloidní formě (toluen), tak zabudované v matrici (vícevrstvé oxidy a oxinitridy). PbS KT pasivované kyselinou olejovou byly získány od komerčních dodavatelů, Si KT pasivované dodecylovými řetězci byly syntetizovány metodou netermální plazmy a vícevrstvé pevné vzorky se Si KT byly vyrobeny žíháním multivrstev substechiometrického SiO_x ($x < 2$) a stechiometrického SiO_2, které byly deponovány metodou PECVD (obojí typ Si KT byl dodán zahraničními spolupracovníky).

Hlavním cílem práce bylo prozkoumat některé základní problémy v souborech KT za účelem zlepšení jejich optických vlastností, jmenovitě absorpční a emisní účinnosti. Optické vlastnosti vzorků byly charakterizovany časově integrovanou a časově rozlišenou (ČR) fotoluminiscenční (FL) spektroskopií. Pokud jde o emisní vlastnosti, analyzovali jsme FL spektra a pozici maxima v závislosti na velikosti a materiálu KT; výsledky jasně ukazují významný vliv KRJ efektu na FL. Použitím speciální aparatury s integrační koulí jsme experimentálně studovali absolutní kvantovy výtěžek (KV) FL v závislosti na různých parametrech (velikost a koncentrace KT a pod.). Za účelem posouzení absorpční schopnosti Si KT, vyjádřené absorpčním průřezem, jsme teoreticky a experimentálně vyvinuli FL modulační techniku, která je založena na porovnání kinetiky nástupu a vyhasínání FL při různých intenzitách excitace. Proto bylo důležité najít optimální experimentální parametry pro ČR FL experimenty. Změnou teploty a tloušťky bariér mezi KT ve vícevrstvých vzorcích se Si KT jsme prokázali závislost absorpčních a emisních vlastností na těchto parametrech a stanovili jsme optimální konfiguraci vzorku k maximalizování jasu FL. Navíc jsme vyvinuli novou výpočetní proceduru, která umožňuje zjistit FL kinetiku jednotlivých velikostních frakcí Si KT ze spektrálně rozlišených kinetik. Tak jsme mohli ukázat, že existují frakce Si KT v koloidní suspenzi, které mají 100% účinnost zářivé rekombinace. Tyto výsledky byly použity pro odhad vnitřní kvantové účinnosti (VKU) v pevných vzorcích. Konečně, porovnáním výsledků VKU s FL KV jsme prokázali a odhadli populaci temných KT. Další výzkum by měl být zaměřen na pochopení příčiny existence temných KT (původ nezářivé rekombinace), aby se případně mohla najít metoda, jak zabránit jejich vzniku a maximalizovat účinnost FL souborů Si KT.

Klíčová slova: kvantové tečky, doba doznívání, kvantový výtěžek, vnitřní kvantová účinnost, absorpční průřez.

"*Natural science does not simply describe and explain nature;*
it is part of the interplay between nature and ourselves;
it describes nature as exposed to our method of questioning."

Werner Heisenberg

Acknowledgments

I would like to express my sincere gratitude to all people who contributed to this thesis, to those who were motivating and inspiring me, giving me theoretical and experimental support, discussing difficult issues and collaborating on different stages of this research.

First and foremost, I wish to give my deepest gratitude to my great supervisor, Professor Jan Valenta, whose kind guidance was neither distracting nor ignoring over the years of the research. I am grateful to Jan for giving me the opportunity to be part of a set of fascinating projects and gently forwarding the work in the right direction. Without his patience, extensive and profound knowledge in the research topic, this work would not have been completed in the present form. Thanks to Jan I have made a huge leap in my professional development and got new perspectives about science.

I want to express my appreciation to Prof. Ivan Pelant, for our discussions as well as for giving a birth of the most educating and inspiring physical book "Luminescence Spectroscopy of Semiconductors" that was written in a coauthorship with my supervisor Jan.

My sincere thanks and deep appreciation go to Dr. Petro Khoroshyy who shared with me his expertise knowledge in programming on Python and thoroughly assisted me in tons of practical matters. Long and fruitful discussions with Petro gave me a tremendous progress in scientific thinking.

I wish to acknowledge the contributions and appreciate discussions of my collaborators that made this work possible:

- Daniel Hiller, Sebastian Gutsch and Margit Zacharias (IMTEK, Freiburg University, Germany) for fabricating ML samples;
- Xiaodong Pi and Xiangkai Liu (Zhejiang University, China) for providing colloidal suspension with Si QDs;
- Sergey Dyakov (Skolkovo Institute of Science and Technology, Russia) for theoretical discussions;
- Ilya Sychugov (Royal Institute of Technology, Stockholm, Sweden) for fruitful collaboration on TR decay analysis.

Furthermore, I would like to acknowledge all members from the Optical Spectroscopy group (KCHFO, Charles University in Prague), especially Prof. Jan Hala, the head of the group, for making creative and friendly atmosphere in the lab. Our weekly seminars, namely seminars of high resolution optical spectroscopy (Tuesdays) and seminar of chemical physics and optics (Thursdays), have been great educative platforms as well as a nice opportunities to present research to colleagues. I am grateful to Dr. Anna Fučíková for the assistance with chemical experiments and giving me the idea to attend summer schools. I owe my thanks to Doc. Roman Dědic and Dr. Jan Alster for helping me with some math calculations and for fruitful

discussions. Further, I cannot forget to thank Dr. Antonin Svoboda for interesting conversations and Doc. Jakub Pšenčík for discussions and soccer playing.

Other thanks belong to Martina Alsterová for taking efforts over so important team-building: managing “pondelni pivo” and jogging sessions. A special thank goes to Kateřina Ridzoňová, my companion on jogging and climbing wall. I would like to thank Marek Scholz, David Paleček, Jakub Dostál, Petra Šimáková and Lucie Augustovičová for the company during our walking trips.

My sincere thanks belong to Prof. Václav Holý for organizing Nanoseminar at our faculty for many years.

I wish to acknowledge my colleagues from other Departments of MFF UK:

– Kristupas Tikuišis, Michael Paukov and Daria Drozdenko for enjoyable and helpful discussions;

– Marek Vlk (Department of Theoretical Computer Science) for soccer games and not only;

– Matyáš Řehák (Astronomical Institute of MFF UK) for managing PhD student meetings;

This work would be hardly possible to accomplish without the coordinator of PhD study programs, Dagmar Zádrapová, as well as our former, Jana Heroutová, and present, Markéta Křížová, KCHFO department secretaries, who provided kind and endless support in matters.

I would like to express my gratitude to my friends: Ivan Pavelka, Igor Popov, Martin Kresta and Michala Krestová, Jaroslav Daněk, Pavel Tvrdík and others for deep friendship and longtime support over the years. In addition, I wish to thanks many other people who contributed to this work but have been forgotten to be mentioned here.

Last, but certainly far from least, I want to give my lovely special thanks to my precious family for their constant and selfless support as well as for stimulating my interest in natural sciences.

Michael Greben
Prague, December 2017

List of abbreviations

ACS	Absorption cross-section
CB	Conduction band
DOS	Density of states
EQE	External quantum efficiency
F-band	Fast (blue) PL band in Si QDs
FCA	Free carrier absorption
FWHM	Full width at half maximum
HLB	Homogeneous linewidth broadening
IQE	Internal quantum efficiency
IS	Integrating sphere
KV rule	Kasha-Vavilov rule
LED	Light emitting diode
ME	Mono-exponential
ML	Multilayer
MSE	Mono- and stretched exponential
NIR	Near-infrared
OA	Oleic acid
PDS	Photo-thermal deflection spectroscopy
PECVD	Plasma-enhanced chemical vapor deposition
PF	Purcell factor
PL	Photoluminescence
QC	Quantum confinement
QD	Quantum dot
QY	Quantum yield
RT	Room temperature
S-band	Slow (red) PL band in Si QDs
SE	Stretched exponent (exponential)
SI	Supporting information
SL	Single layer
SRON	Si-rich oxinitrides
TEM	Transmission electron microscopy
UV	Ultraviolet
VB	Valence band
VIS	Visible

Contents

Chapter 1

Introduction

In modern semiconductor optoelectronic and photonic industries the fabricated structures are rapidly shrinking towards nanoscale. Therefore, fundamental understanding of optical properties of nanometer-size crystallites is of primary practical importance.

Research of (quasi)zero-dimensional (0D) structures, also known as quantum dots (QDs), began in the early 1980s and from that time it is rapidly growing. Russian solid-state physicist A. I. Ekimov with colleagues discovered[1] the presence of semiconductor QDs (CdS, CdSe, CuCl and CuBr) in doped glasses. In collaboration with theoretician A. L. Efros it was proved[2] that the size of QDs determines its optical properties – quantum confinement (QC) effect. Around the same time, L. Brus and collaborators from AT&T Bell Labs were able[3] to synthesize colloidal CdS QDs with sizes around 4.5 nm. The name "quantum dots" was introduced[4] by M. Reed et al. (Texas Instruments) in 1987.

A lot of physical properties can be scaled with dimensions of QDs (e.g., electronic bandgaps, extinction coefficients, melting points etc.). Though at the atomic level the ideal QD core is structurally the same as bulk crystal, atomic-like optical behavior (bulk bands become quantized) arises solely due to finite dimensions of QDs (QC effect). The QC effect in QDs makes them almost ideal candidates for endless number of applications[5] including renewable energy technologies, nanophotonics, telecommunications and nanomedicine. After its discovery, there has been an enormous effort to improve the "classical" Cd-based QDs (CdS, CdSe, CdTe etc.) which resulted in fabrication methods producing very efficiently fluorescent QDs[6]. Besides them, a large number of QDs from other materials can be synthesized, including semiconductors from III–V (e.g., InAs and InP), IV–VI (e.g., PbS and PbSe), II–VI groups (e.g., HgTe) and many others.

In this work we shall focus on direct (mainly, PbS) and indirect (Si) semiconductor QDs because of the number of reasons:

1) PbS bulk is direct bandgap and naturally occurring mineral (e.g., galena, see Sec. 2.4.1).
2) Lead-based QDs have the highest photoluminescence (PL) efficiency (up to 70%, see Sec. 5.1.2.3) among all infrared-emitting QDs[7].
3) A large dielectric constant (consequently, small exciton binding energy) of PbS allows exciton dissociation even at room temperature (RT). In addition with tunable absorption onset across infrared region (it covers even the longest-wavelength junction that is required in multi-junction cells[8], see Fig. 1.1) and high carrier mobility[9], this have led to successful applications of PbS QDs

(which reveal sufficiently long carrier lifetime for efficient charge collection) in high-performance QD solar cells[10]. Up to now, the most intensive research for QD-based solar cells have been concentrated on this material[6].

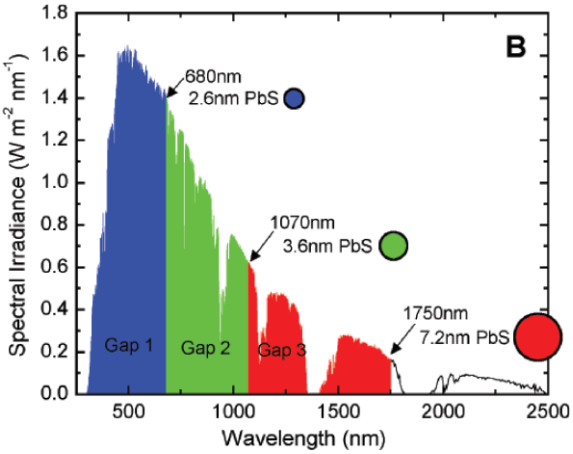

Figure 1.1. Illustration (after Ref. [8]) of the concept of a triple-junction tandem solar cell based on colloidal PbS QDs of three different sizes.

4) PbS is a narrow energy bandgap semiconductor that allows large tunability of optical properties with size variation (see Sec. 2.2). This makes PbS material particularly interesting for applications beyond the bandgap of silicon, e.g. for emission at the key infrared wavelengths (1.3 and 1.55 μm, the bands with the lowest losses in glass fibers) for telecommunication industry.
5) Though some of II-VI and III-V semiconductors have large exciton Bohr radius, most of them have heavy holes resulting in small hole Bohr radius. For instance[11], exciton Bohr radius of InAs and InSb are 29 nm and 61 nm, respectively, while the Bohr radius of its holes is only 2 nm. Therefore, strong QC regime can be archived only for very small QDs [for In(As,Sb) it is < 2nm]. Cd-based compounds (CdS, CdSe, CdTe) have[11] even smaller hole Bohr radius (≤ 1 nm). In contrast, in bulk PbS, relatively small hole mass is almost equal to the electron mass (see Sec. 2.4.1) that results in 10 nm Bohr radius for both carriers. Such large Bohr radius provides strong confinement even for quite large QDs (~10 nm), where the influence of surface effects is less pronounced. Therefore, PbS QDs look like an ideal platform to study excitons in strong QC regime[12].

Thanks to the above mentioned advantages, PbS QDs were already applied in LEDs[11,13,14], lasing[11,15], solar cells[16,17,18], photodetectors[11,19,20,21], luminescent solar concentrators[22,23] and biolabeling[24,25].

Although PbS QDs can be synthesized with cheap and relatively safe synthetic precursors[26], the presence of Pb may face environmental concerns. Therefore, it is necessarily to explore an alternative non-toxic semiconductor materials for application in environmentally friendly green photonics and photovoltaics. Silicon, being

biocompatible and biodegradable[27] as well as highly abundant (second most abundant element after oxygen in the Earth's crust), eliminates many deficiencies commonly found in the direct bandgap semiconductors. Moreover, silicon is absolutely dominant material in current microelectronic and photovoltaic technologies and represents cheap and well-studied semiconductor. However, it has one major drawback – as a consequence of the indirect bandgap, there is a mismatch between electron and hole wave functions in k-space. This requires participation of phonons in optical transitions that dramatically decreases the probability of radiative recombination (rate). This fundamental limitation is partially overcome thanks to the QC effect in nanocrystalline form of Si, which was recognized shortly after the discovery[28] of luminescent porous Si in 1990. This attracted increasing scientific interest to silicon as a promising alternative to the commonly used heavy-metal-containing QDs in different fields such as optoelectronics and photonics. Indeed, Si QDs can efficiently luminescent in near-infrared (NIR) region, as well as PbS QDs (Fig. 1.2).

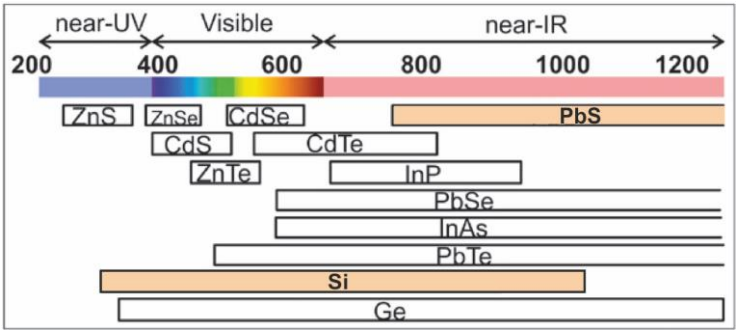

Figure 1.2. Spectral tunability of PbS and Si QDs emission in regards of other materials. Modified from Ref. [29,30].

Despite this potential, there is a number of serious problems that can make Si QDs less attractive in comparison with lead chalcogenides PbX (X = S, Se, Te) counterparts. In terms of PL quantum efficiency, Si QDs are still behind[31] the direct band-gap semiconductor QDs. Another issue is related to strong thermal broadening of the PL band (homogeneous broadening, see Sec. 5.1.1) in Si QDs as a direct consequence of the indirect bandgap nature of silicon. In addition, most of ensembles of Si QDs studied to date have relatively broad size polydispersity which complicates its application in biomedical tagging where partial-size PL emission must be discriminated to allow color identification across multiple detection channels. Moreover, the study of size-dependent properties requires monodispersion of an ensemble as polydispersion leads to averaging over QD size distribution. To become a competitive alternative to lead chalcogenides, Si QDs need to achieve better level of size uniformity as well as PL efficiency and stability.

Rich technological potential of Si QDs has just started to develop. Recently a number of relevant methods of size purification have been tested[32,33] and almost monodisperse Si QD ensembles were synthesized[34]. An increasing interest of scientific

community to nanocrystalline silicon is reflected in a large number of reviews with accent on synthesis[30,35,36,37,38], optical properties[29,39,40,41,42,43,44,45] and applications[46,47]. In photovoltaics nanocrystalline Si is a promising material for the top cell of all-Si tandem cells that can theoretically reach efficiencies much above the Shockley–Queisser limit of 31% for a single-junction Si solar cells[48,49]. Injection electroluminescence (EL) of Si QDs can be utilized in Si-based light emitting diodes (LEDs) or displays[29,45,50]. Just recently Meinardi et al. reported in Nature Photonics[51] on fabrication of highly efficient luminescent solar concentrators (LSC) based on Si QDs. Also, alkyl-terminated Si QDs were encapsulated into a solid matrix of the OSTE polymer where the resulting hybrids revealed enhanced PL quantum yield (QY) (~65%) in relation to the original toluene suspensions! Besides all, long-lived PL from Si QDs was utilized in bioimaging[29,45].

Though an extraordinary level of control over structural and optical properties of QD ensembles was archived, there is still number of important questions to be answered that are addressed in this work:

1) How to calculate properly the absorption cross-section (ACS) of an ensemble of QDs without *a priori* knowledge of QD concentration? How does ACS depend on QD size?
2) How does the PL QY depend on excitation and emission (QD size) wavelengths, QD concentration and condition of storage (aging, photostability etc.)?
3) How do both ACS and QY depend on inter-QD distance and temperature of the sample?
4) How broad homogeneous linewidth can obscure spectrally resolved PL measurements?
5) What are the PL kinetics of an ensemble of QDs? How does the decay lifetime depend on different parameters, e.g. QD concentration, excitation intensity, sample temperature, mean size of QDs and inter-QD distance.
6) Can an ensemble or its fraction reveal fully radiative relaxation? How does internal quantum efficiency (IQE) depend on QD size and sample temperature?
7) What is the fraction of dark QDs in an ensemble that makes external quantum efficiency (EQE) lower than internal quantum efficiency (IQE)?

Elaboration of the issues listed above, that will be considered throughout this work, should be a significant progressive step in fundamental understanding of the nature of optical properties of QD ensembles.

Chapter 2

Background and theory

2.1 Quantum confinement effect in 0D semiconductors

In quantum mechanics a state of a particle is described by a wave function Ψ which square describes the probability to find the particle in a certain volume dξ of space:

$$P(t) = \left|\Psi(\xi,t)\right|^2 d\xi = \Psi^*(\xi,t)\Psi(\xi,t)d\xi \tag{1}$$

where the wave function is normalized as $\int \left|\Psi(\xi,t)\right|^2 d\xi = 1$, and $\mathrm{d}\xi = \mathrm{d}x\mathrm{d}y\mathrm{d}z$.

Considering the classical "particle in the box" problem where a charge carrier (electron or hole) is confined in a potential box with width *a* [see Fig. 2.1(a)]

$$U(x,y,z) = \begin{cases} 0, \text{ for } 0 \le x \le a, 0 \le y \le a, 0 \le z \le a, \\ \infty, \text{for } x > a. \end{cases} \tag{2}$$

we wish to solve the steady-state Schrödinger equation:

$$-\frac{\hbar^2}{2m}\Delta\psi(x,y,z) + U(x,y,z)\psi(x,y,z) = E\psi(x,y,z) \tag{3}$$

where $\psi(x,y,z) = \Psi(x,y,z,t)/\varphi(t)$ represents the time-independent part of wave function, *m* is the effective mass of the charge carrier.

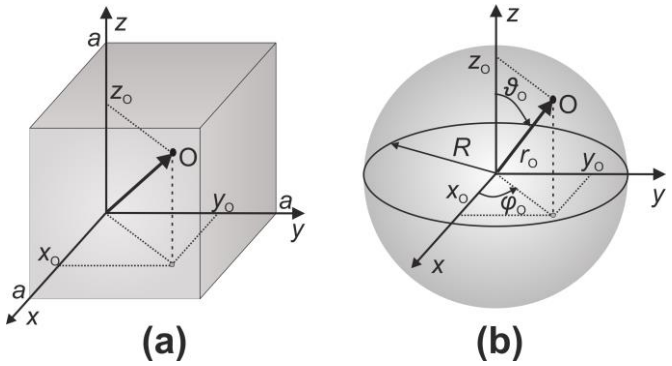

Figure 2.1. Illustration of rectangular (a) and spherical (b) potential wells with infinite walls.

The energy spectrum of the charge carrier in such system is a set of discrete levels[52]:

$$E_n = \frac{\hbar^2}{2m}\left(\frac{\pi n}{a}\right)^2 \tag{4}$$

For better approximation of zero-dimensional QD we use a sphere [see Fig. 2.1(b)] with radius R (radius of a QD) where a charge carrier is confined in a spherically symmetric potential wall:

$$U(r) = \begin{cases} 0, \text{ for } r \le R, \\ \infty, \text{for } r \le R. \end{cases} \tag{5}$$

The solution[52,53] of the corresponding Schrödinger equation in spherical coordinates has a similar form to Eq. (4):

$$E_{n,l} = \frac{\hbar^2}{2m}\left(\frac{\chi_{n,l}}{R}\right)^2 \tag{6}$$

where $\chi_{n,l}$ represents the nth root of the lth-order spherical Bessel function.

From Eq. (4) and Eq. (6) it is clear that unlike in bulk material, where the density of energy states is almost continuous, the energy spectrum of charge carriers in a QD is discrete.

To estimate the strength of QC, the dimension of a QD has to be compared (Fig. 2.2) with the exciton Bohr radius a_{X} of the respective material:

$$a_{e(h)(\mathrm{X})} = \frac{\varepsilon \hbar^2}{m_{e(h)(\mathrm{X})} e^2} \tag{7}$$

where ε represents dielectric constant of the QD material, $m_{e(h)(\mathrm{X})}$ stands for effective masses of electron, hole or exciton [$m_{\mathrm{X}} = 1/(1/m_e + 1/m_h)$], respectively, and $a_{\mathrm{X}} = a_e + a_h$.

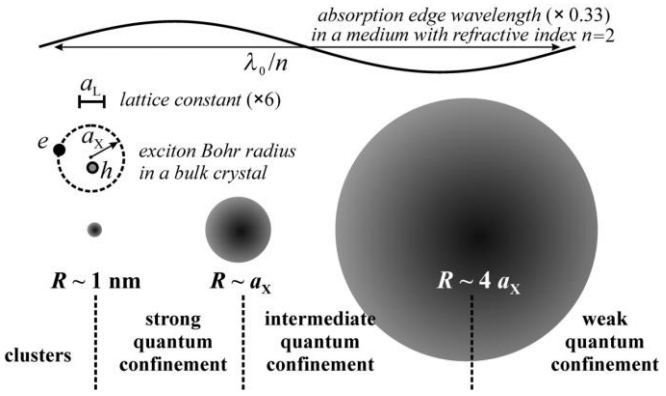

Figure 2.2. Illustration (after Ref. [53]) of strong, moderate (intermediate) and weak quantum confinement regimes in dependence on the relation between the quantum dot radius R and excitation Bohr radius a_{X}.

Interesting to note that normally the wider is the bandgap of a semiconductor, the smaller[54] is the corresponding exciton Bohr radius a_X. Above all, the radius of the QD must be much larger than crystalline lattice constant a_L to make valid the assumption of the periodicity of the crystal.

Three regimes of QC can be distinguished[11,55] (Fig. 2.2):

a) Strong confinement: the QD radius is smaller than the corresponding Bohr radius of both electron and hole ($a_L \ll R \ll a_e, a_h$). Both electron and whole experience strong QC and the electron-hole overlap is monotonically growing with size decrease in this regime[56].

b) Moderate confinement: the radius of a QD is much smaller than a_e, but larger than a_h ($a_h < R \ll a_e$). Therefore, only electrons experience strong confinement. Most of semiconductors belong to this regime[55].

c) Weak confinement: the radius of QD is much larger than both a_e and a_h, but still is smaller than a_X ($a_e \ll R < a_X$). The confinement is relatively small (electron-hole overlap is already size-independent[56]) though exciton wave function still feels QD boundaries. This means that exciton center-of-mass kinetic energy is quantized while the relative motion of the pair do not interfere with QC effect[57]. The energy term [see Eq. (8)] is dominated by the Coulomb interaction and this regime can be theoretically treated as a small perturbation of the bulk limit[57].

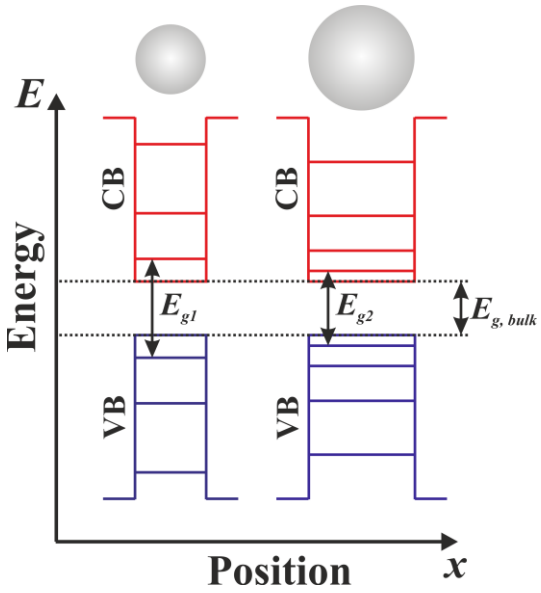

Figure 2.3. Illustration of the electronic structure and optical bandgap as functions of quantum dot size.

As a result of the spatial localization of the exciton in a small volume of a QD there is an increased overlap between electron and hole wave functions. This interaction is the Coulomb interaction ($\sim e^2 / 2\varepsilon r$) that cannot be completely neglected

even in strong QC regime. Keeping this into account, a rough approximation of the absorption spectrum can be estimated from the Eq. (6) as a set of discrete peaks at energies:

$$E_{n,l} = E_g + \frac{\hbar^2}{2m_X}\left(\frac{\chi_{n,l}}{R}\right)^2 - 1.786\frac{e^2}{2\varepsilon R} \tag{8}$$

From Eq. (8) it is clear that with size increase of the QD the distance between the energy levels is decreasing and in its limit approaches the bulk values (Fig. 2.3). This leads to a set of consequences that will be considered in the next section.

2.2 Excitation and emission in QDs

Next, instead of treating electron and hole as being independent we will consider the quasi-particle consisting of a correlated electron-hole pair (a boson) bound by the Coulomb forces (because of the overlap of wave functions) that is called exciton. Though there was a lot of discussions on whether an excited *e-h* pair really form an exciton in past, now it is commonly accepted that the excitonic luminescence dominates in semiconductors[53]. Under recombination of an exciton in a semiconductor material we will mean the process of falling the electron into the empty state associated with the hole by which both carriers (electron and hole) annihilate each other (electron losses its energy and the hole eventually disappears). Normally QDs are excited with non-resonant light, i.e. the incident photon has much higher energy than the QD bandgap. If this high-energy photon is absorbed by a QD, the electron is excited higher into the band [see Fig. 2.4(a)]. Then the "hot" electron relaxes rapidly through a cascade of interactions with phonons [see Fig. 2.4(a)-(b)] and eventually ends up at the bottom of the conduction band (CB). Finally, either a radiative recombination with the hole in valence band (VB) can take place resulting in emission of a photon [see Fig. 2.4(a)] or an energy transfer to phonons or defects in QD core or surface might occur. The total recombination rate of the transition to ground state is simply the sum of radiative and non-radiative contributions:

$$\frac{1}{\tau_{PL}} = \frac{1}{\tau_r} + \frac{1}{\tau_{nr}} \tag{9}$$

where τ_{PL}, τ_r and τ_{nr} are PL decay, radiative and non-radiative lifetimes, respectively.

One may argue that $E(\mathbf{k})$ band structure representation in Fig. 2.4(b) is not valid for QDs. Indeed, with shrinking the size of QD the quasi-continuous band structure $E(\mathbf{k})$ splits into a number of allowed energy states. Moreover, the band structure gets more "fuzzy" with QD size d decrease because of the enhanced uncertainty Δk

according to Heisenberg inequality ($\Delta p_x d \geq \frac{\hbar}{2}$). From computer simulations made by Kusova et al.[58] [see Fig. 2.4(c)] it is clear that we still can describe electronic energy states using **k**-vector concept up to a certain minimal size of a QD.

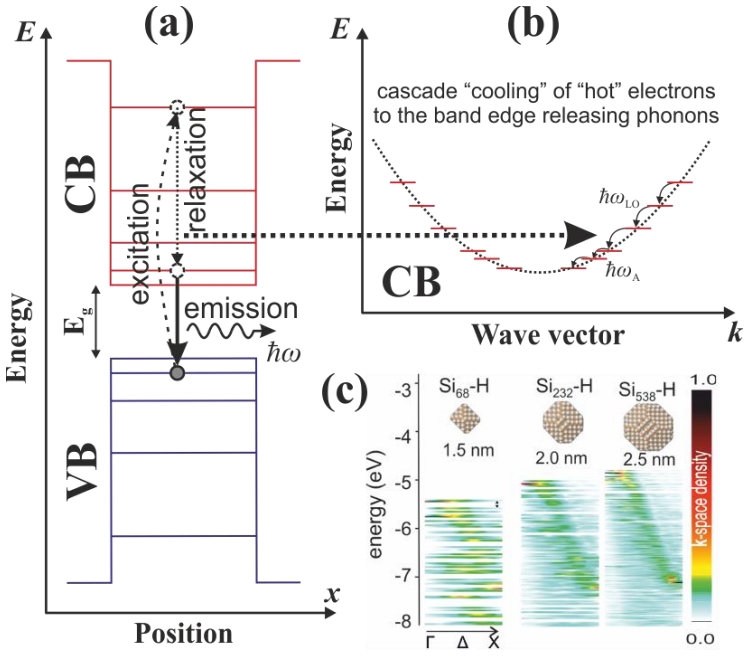

Figure 2.4. a) Representation of excitation, relaxation and emission processes in a QD. b) Relaxation of an excited electron via emission of phonons in a QD. c) 1D cross sections of the projected **k**-space density in H-passivated Si QDs of three different sizes obtained by theoretical calculations[58]. The band structure becomes gradually "fuzzy" and minigaps appear with decreasing QD size.

Theoretically speaking, for small enough QD the energy separation between the discrete allowed levels can become even bigger than the largest energy of a phonon $\hbar\omega_{\mathrm{LO}}$ (for Si $\hbar\omega_{\mathrm{LO}} = 0.064\,\mathrm{eV}$). Then a dramatic reduction of relaxation rate can be expected as the relaxation can take place only by interaction with multiple phonons in a sequence. This effect is commonly named as the phonon bottleneck[59]. In reality, however, it seems that relaxation mechanism "knows" how to break or counterbalance the phonon bottleneck restriction and different aspects of this phenomena still needs to be clarified[53]. Nevertheless, a reduction of electron-phonon coupling in QDs is expected to slow down the relaxation process of "hot" carriers.

To summarize, the edge emission in QDs is significantly enhanced in comparison with the bandgap emission of their bulk counterparts. However, emission spectrum of an ensemble of QDs is often inhomogeneously broadened because of size and shape distribution of QDs. Moreover, PL linewidth could be quite broad (far above thermal broadening) even in the case of a single QD (Sec. 5.1.1) made from indirect-band gap semiconductor material and the nature of it remains unclear (probably, the surface or matrix interface can play a role)[60].

As it was shown in Eq. (8), the direct consequence of size reduction of a semiconductor material is QC effect that results in bandgap opening [see Fig. 2.5(a)]. Therefore both emission and absorption spectra of small enough QDs are expected to exhibit a blue-shit in respect to its bulk counterpart and shift further towards higher energies with size shrinking of the QD [see Fig. 2.5(b)].

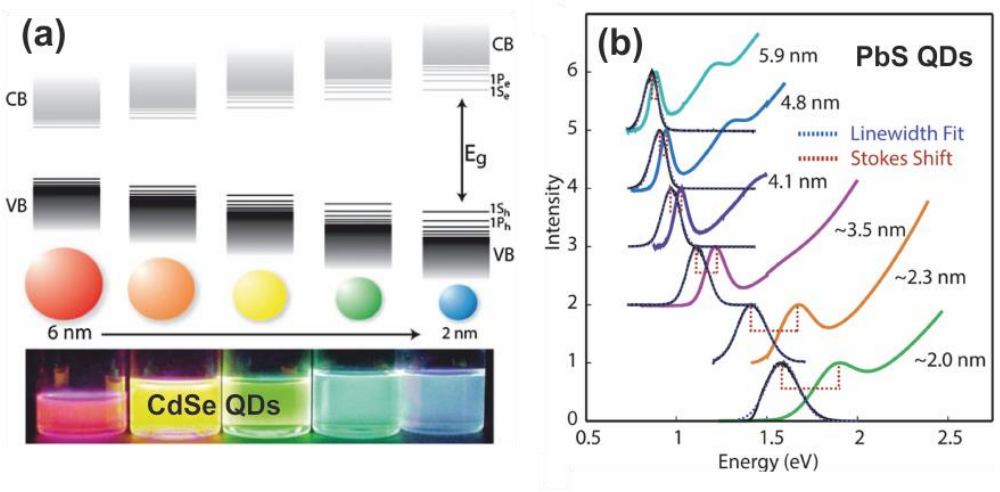

Figure 2.5. Schematic illustration of the quantum confinement effect in QDs: the bandgap of the semiconductor material opens (expands) with decreasing size of QDs (a) that results in blue shift of both emission (a, b) and absorption (b) of QDs. Taken from Ref. [61] (a) and Ref. [62] (b).

2.3 Effects in strongly excited/dense ensembles of QDs

2.3.1 Auger recombination process in QDs

The luminescence behavior of QDs fundamentally depend on the mean number of excitons created in a given QD during the excitation process. When the excitation intensity is strong enough to create in average $\langle N \rangle \geq 2$ excitons per QD, a special type of interaction between excitons leads to non-radiative recombination of one of two excitons in the given QD. This interaction is called Auger recombination and is significantly more pronounced in confined systems (in comparison with bulk materials) as a direct consequence of spatial localization of excitons in the QD. The excitons are confined in the volume of the QD and cannot escape (in case of high-enough barrier and well-passivated QD surface). A schematic representation of the Auger process is presented in Fig. 2.6. Within the stage 1 there are two *e-h* pairs created in the same QD thanks to absorbed energy of two exciting photons. During the stage 2 both “hot” electrons are “cooled” down to the bottom of CB and eventually two excitons are confined within the volume of the QD at the same time. However, in the stage 3, instead of radiatively recombining with subsequent

emission of two photons, one of the excitons recombines non-radiatively and transfers its energy to the electron (or hole) of the second exciton. As an example, an electron is selected as the energy acceptor in Fig. 2.6. Finally, the excited electron relaxes again to the bottom of CB with subsequent radiative (or non-radiative) recombination with the respective hole in VB [Fig. 2.6(b)].

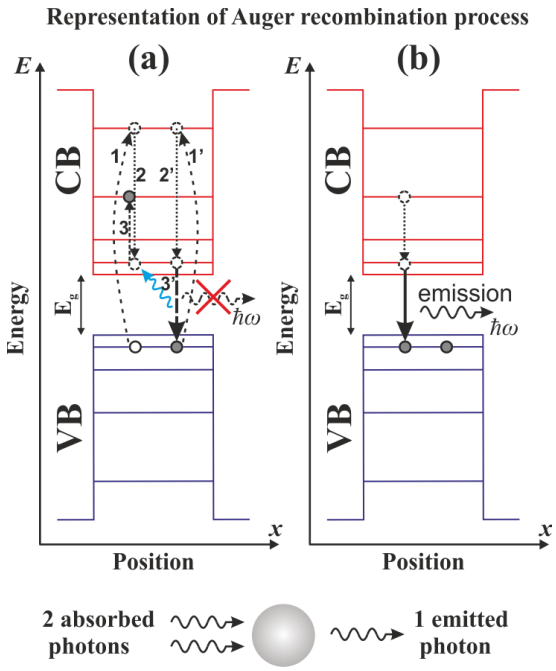

Figure 2.6. Schematic representation of the Auger process: a) a single QD is excited with two absorbed photons and as result, two e–h pairs are created. The recombination energy of one pair is transferred to the other one (blue arrow) resulting in a "hot" electron. b) The electron subsequently cools down and eventually recombines with a hole accompanied by an emission of a photon.

Depending on the material and the size of QDs, the Auger recombination in QDs is relatively fast with typical times in the order of ps or shorter[63] and hampers the multi-excitonic processes in QDs (e.g. the carrier multiplication). To make the carrier multiplication possible[64], it is necessarily to separate multiexcitonic states by, e.g. rapid extraction of individual excitons from the excited QD.

2.3.2 "Free" carrier absorption and reabsorption in ensembles of QDs

Besides Auger recombination, there are couple of other processes that limit the emission photon yield from an ensemble of QDs at high excitation powers. Firstly we will describe the effect of the so called "free" carrier absorption (FCA) where "free" is taken in quotes because the carriers in QDs are not free but confined and the term is inherited here from bulk semiconductor effects. The scheme of the FCA process is represented in Fig. 2.7(a)–(b). Within the stage 1 an incident

photon creates *e*-*h* pair and then "hot" electron is "cooling" down to the bottom of CB during the stage 2. During the stage 3, however, instead of radiatively recombining with the hole in VB, the electron can absorb another incident photon [Fig. 2.7(a)–(b)] and by this it gets back into high energy levels in CB. Then, again after fast relaxation (stage 4), only one photon is emitted (stage 5) while two photons were absorbed. Though this affects PL in a similar way as the Auger recombination considered above, there is a principal point that has to be mentioned. As a photon has very low momentum, to bring the excited electron into higher excited states, a second particle (phonon) has to participate in the process. From the point of view of perturbation theory, thus, FCA process is of the second order that makes its influence less pronounced in comparison with, e.g. Auger process. Although FCA process must be enhanced[65] in QDs in comparison with corresponding bulk semiconductors.

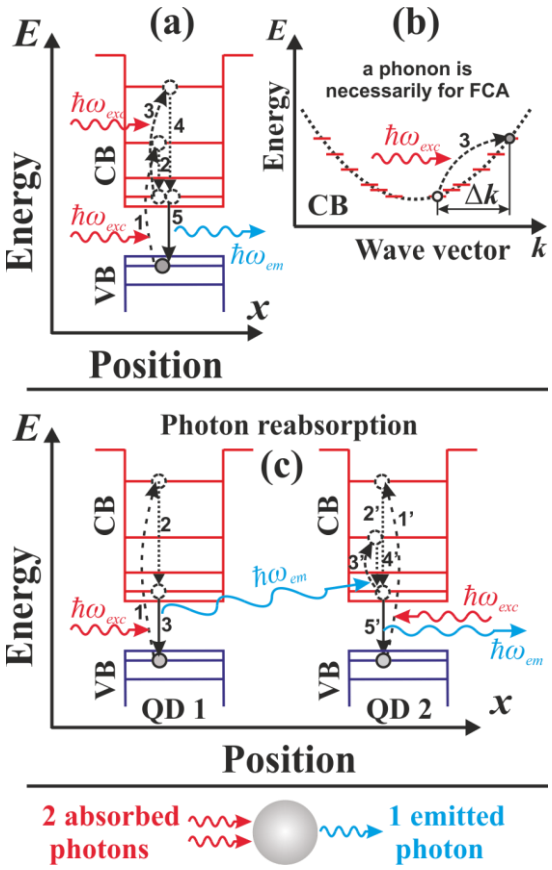

Figure 2.7. Schematic representation of the FCA process in real (a) and **k**-space (b) as well as photon reabsorption process in two QDs (c). In FCA process absorption of a second photon in a single QD results in interband transition of already excited carrier by the first photon. Unlike in FCA, where the second photon is coming from an excitation source, in photon reabsorption process the second photon is produced in emission by another QD in an ensemble.

The Auger and FCA processes become important only at high excitation powers (above the saturation limit, see Sec. 5.2.2). However, even at low excitation powers the photon reabsorption effect (see Sec. 5.1.2.1) takes place in highly dense ensembles

of QDs. The schematic representation is depicted in Fig. 2.7(c). As result of absorption of two incident photons each of two QDs confines two excitons in its ground state (1–2 stages). Then within the stage 3 the emitted photon by one QD can be absorbed by the second QD instead of reaching the detector. And again, only one emitted photon can be detected (stages 4–5) as result of absorption of two incident photons. The probability of reabsorption process depends on the absorption cross-section (ACS) of QDs (see Sec. 5.2.4) and QD concentration.

2.4 Lead sulfide and silicon semiconductors

2.4.1 Direct (PbS) and indirect (Si) bulk materials

a) Galena (lead glance) – natural mineral form of lead sulfide – is presented in Fig. 2.8(a).

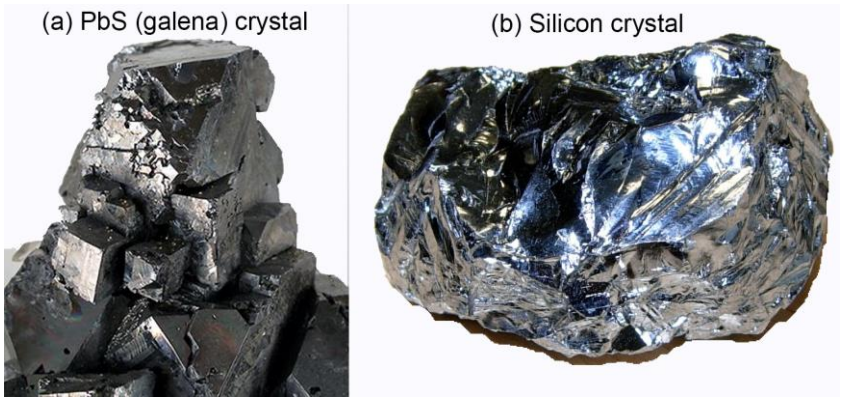

Figure 2.8. An aesthetic floater cluster of stacked, modified cubes of galena (after the Ref. [66]) and a piece of purified silicon polycrystal (after the Ref. [67]).

Lead sulfide is one of the lead chalcogenides semiconductors (PbX, where X = S, Se, Te) with narrow bandgap (0.42 eV at RT). Bulk PbS compound has a rock salt crystalline structure with a lattice constant of 0.594 nm and large dielectric constant $\varepsilon_{\mathrm{PbS}} = 17.2$. The effective masses of electron and hole are comparable and quite small, i.e. $m_e^{\mathrm{PbS}} = m_h^{\mathrm{PbS}} \approx 0.08 m_0$, where m_0 is the rest electron mass in a vacuum. Relatively small effective electron and hole masses lead [see Eq. (7)] to a large Bohr exciton radius ($a_e^{\mathrm{PbS}} = a_h^{\mathrm{PbS}} = 10\,\mathrm{nm}$, $a_{\mathrm{X}}^{\mathrm{PbS}} = 18\,\mathrm{nm}$, see paper V). The CB minimum and VB maximum both lying at the L-point (four equivalent L-points in the Brullouin zone) of the reciprocal space [Fig. 2.9(a)] which allows direct radiative transitions of excitons in PbS semiconductor.

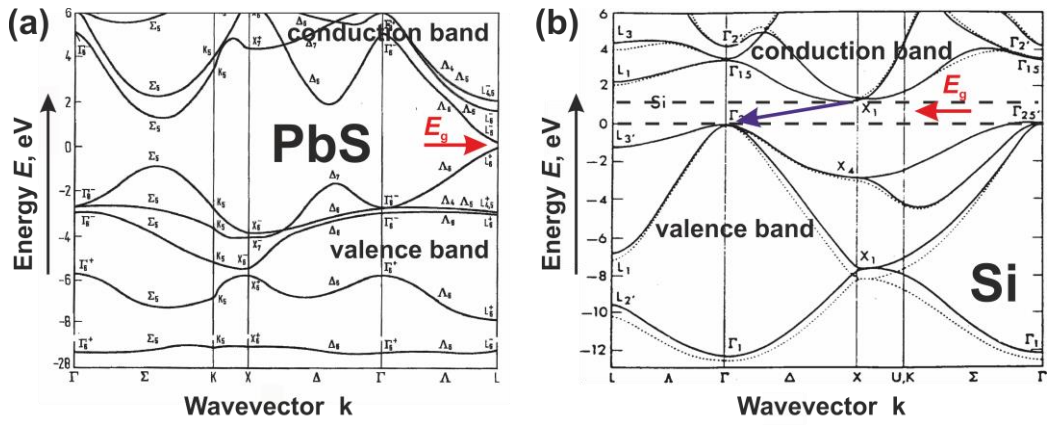

Figure 2.9. Theoretically calculated band structure of PbS (adopted from Ref. [68]) and Si (adopted from Ref. [69]). The red arrow indicates the bandgap.

b) The Earth's crust contains more than 90% of silicate minerals that makes Si [see Fig. 2.8(b)] the second most abundant element in the Earth's crust by mass (after oxygen). Silicon is a semiconductor with the diamond crystal structure having a lattice constant of 0.543 nm and dielectric constant $\varepsilon_{\mathrm{Si}} = 11.7-12$. The effective mass of hole is about 1.5 times heavier than the mass of electron in Si [$m_e^{\mathrm{Si}} = 0.26m_0$; $m_h^{\mathrm{Si}} = 0.36m_0 (0.39m_0)$]. The exciton Bohr radius is reported[44,70] in the range $a_{\mathrm{X}}^{\mathrm{Si}} = 4.3-5$ nm. Expectedly [see Eq. (7)], the corresponding Bohr radius of electrons and holes in Si will be even smaller. A direct transitions in Si are referred to the Γ-point of the reciprocal space [Fig. 2.9(b)]. However, this point does not correspond to the lowest energy states and "hot" electrons relax to the bottom of the CB that is located close to the X-point. A momentum mismatch between Γ- and X-points inhibits a direct recombination of photons and photon coupling with a phonon is necessarily to conserve the momentum. This band structure makes Si indirect semiconductor that results in dramatic decrease of probability of radiative recombination of excitons in comparison with direct semiconductors.

2.4.2 **Lead sulfide and silicon QDs**

Though above mentioned QC effect tune the electronic state energy levels of QDs, the fundamental band structure of the corresponding semiconductor bulk material yet plays a crucial role in PL even at nanoscale. Thus, Si remains indirect semiconductor even for the smallest sizes of QDs (≤ 2 nm). In this work under QDs we mean tiny crystals of semiconductors that consist of hundreds to a few thousand atoms each. Their sizes are in the range of few nm and are below the corresponding exciton Bohr radius where the QC effect plays a dominant role. The structural models of colloidal PbS and Si QDs are presented in Figure 2.10.

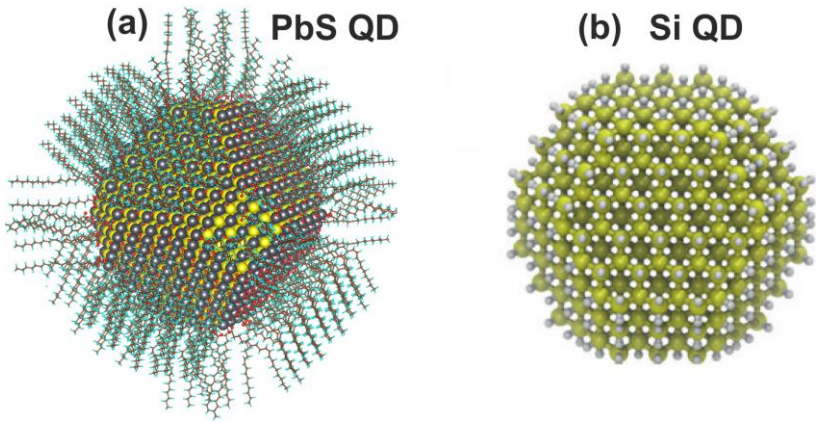

Figure 2.10. Calculated atomic structure of a) PbS QDs (5 nm diameter) terminated by oleic acid [PbS(100) surfaces] as well as by oleate and hydroxide [PbS(111) surfaces] ions (after Ref. [71]) and b) Si QDs (538 Si atoms) terminated by hydrogen (after Ref. [58]).

Beyond any doubts, one of the most outstanding features of PbS and Si QDs are their optical properties. Despite of the tremendous efforts of scientists to uncover the nature of optical processes at nanoscale, there are still a number of questions to be answered.

2.4.2.1 Photoluminescence of PbS QDs

PbS QDs absorb and emit light [see e.g., Fig. 2.5(b)] in the near infrared (NIR, 700–1000 nm) and short wavelenth infrared (SWIR, 1000–1800 nm) regions[62,72].

The surface passivation of PbS QDs that leads to the highest PL QY is based on organic ligands such as oleic-acid (OA). This capping provides passivation of surface dangling bonds and colloidal stability in nonpolar organic solvents (e.g. toluene). Colloidal PbS QDs reveal some interesting properties, mainly:

a) Large, size-dependent Stokes shift[73,74,75];
b) Small, NIR emitting (700–900 nm) PbS QDs have a broad PL linewidth (160–240 meV)[62], while larger QDs (1200–1600 nm) reveal a narrower PL band (< 100 meV) [62,72].
c) Extraordinarily long PL lifetime[76] (from hundreds of ns to μs) if to keep into account its direct semiconductor nature. The origin of this size-dependent PL kinetics is still a matter of great scientific debates.

2.4.2.2 Photoluminescence of Si QDs

Three fundamentally different optical emission bands in Si QDs were reported so far in literature [see Fig. 2.11(d)]:

a) Slow ‘red’ emission band (often called S-band) that is linked with the indirect excitonic radiative recombination in the QD core. As being related to fundamental bandgap transitions, the spectral position of the peak of this emission band blueshifts with size reduction of QDs that is in agreement with the QC model (see Sec. 2.1–2.2). The lifetimes of the S-band are typically in the μs range.
b) Fast ‘blue’ emission band (often called F-band) which origin is unclear yet. It is usually ascribed either to defect sites at the interface between QD and matrix, or to the matrix defects itself. This defect-related PL band is independent on QD size and reveal fast PL dynamics in the range of nanoseconds.
c) Ultrafast ‘green’ emission band recently discovered by de Boer and colleagues[77] which origin is still under debate[78]. Unlike S-band, this emission band reveal a redshift for smaller QDs and has a characteristic lifetime in the range of picoseconds.

Besides QC effect, the surface plays a crucial role[29] in determining PL optical properties of QDs. Indeed, as going to nanoscale, the surface-to-volume ratio is dramatically increasing as well as the fraction of surface atoms that might contain dangling bonds or other types of defects that contribute to the electronic structure. Therefore, PL becomes sensitive to surface reconstruction and passivation. There are mainly three different types of surface passivation [Fig. 2.11(a)–(c)]:

a) H-termination [Fig. 2.11(a)].

Theoretical calculations suggest that hydrogen-capping has a negligible influence on the optical properties of Si QDs and is often considered as a reference capping material. The unperturbed exciton recombination is occurring directly in the core of QDs (S-band) and PL peak can be tuned from ultraviolet (UV) to the NIR region by changing the mean size of QDs. Unfortunately, hydrogen and other short organic ligands exhibit low photochemical stability and is highly prone to oxidation upon exposure to air.

b) Functionalization by carbon-linked organic ligands [Fig. 2.11(b)].

The surface passivation with sp^3 hybridized carbon based ligands forms robust capping of photochemically stable bonds that prevents an oxidation of QD surface. Though, it affects the energy of optical transitions and PL becomes less tunable. For small enough QD sizes the fast F-band appears and S-band disappears. Pushing the PL peak to lower wavelengths besides 590 nm becomes hardly possible[32] (no further blue-shift) that indicates deviation from the QC model.

c) Oxide-based termination [Fig. 2.11(c)].

It provides superior photochemical stability and includes both Si QDs in oxide matrix and in colloidal solution. Oxide-capped Si QDs are the most thoroughly investigated though effect of oxygen on the PL properties is far more debated and less understood in comparison with previously addressed surface cappings. Upon exposure to air, PL emission of H-terminated Si QDs is redshifting due to oxidation. Thus, oxide-capped Si QDs reveal the poorest PL spectral

tunability compared to the previously considered type of surface functionalization. Depending on the mean size of QDs, all three types of above-presented PL emission bands can be observed in an ensemble of oxide-capped Si QDs.

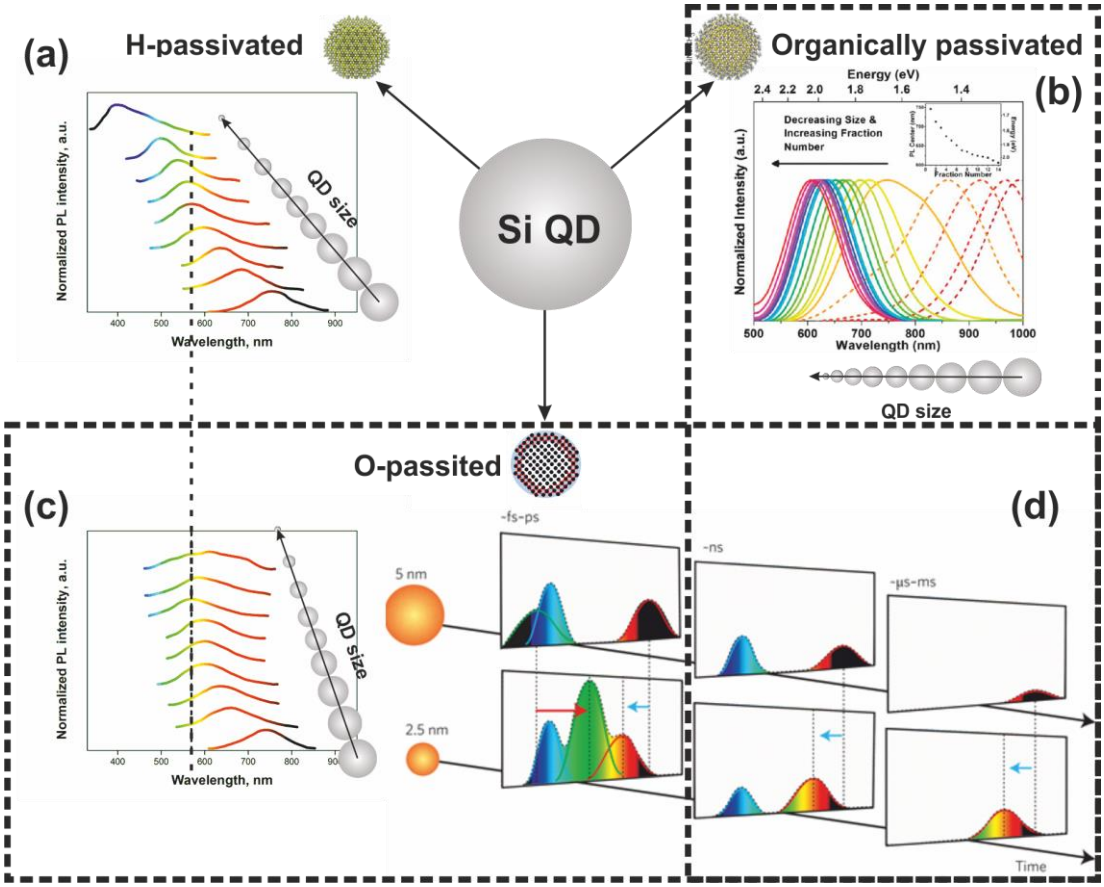

Figure 2.11. Size-dependent S-band PL spectra from Si QDs in dependence on surface capping: (a) H-passivated, (b) organically passivated and (c) oxide-passivated surfaces. Illustration of the three known bands in Si QDs: slow S-band in µs-range (capping: a, b or c), fast F-band in ns-range (capping: b or c), ultrafast green band in fs-ps range (capping: c). Parts (a and c) are adopted from Ref. [79], b – from Ref. [32] and d – from Ref. [80]. Models of QDs with different passivation are taken from Ref. [58] (a, b) and Ref. [41] (c).

In this thesis we are focusing only on the slow (µs decay) PL S-band in organically (dodecyl) capped and oxide-capped (matrix-embedded) Si QDs.

Chapter 3

Experimental methods

3.1 Fabrication of samples

3.1.1 Colloidal $A^{II,IV}B^{VI}$ QDs in toluene (hexane)

3.1.1.1 Oleic acid-capped PbS QDs in toluene

There are currently two well-developed methods to synthesize PbS QDs. The first route is based on the injection of bis(trimethylsilyl)sulfide (TMS) in octadecene to a hot solution of lead oleate (Hines and Scholes synthesis) which offers monodisperse QDs over a broad size range (2.5 – 8.8 nm)[26]. Recent modifications[73,81,82] of the method allow for synthesis of ultrasmall PbS QDs with sizes between 1 –2 nm. The second route includes lead chloride ($PbCl_2$) and elemental sulfur (S) as precursors and oleylamine used as a solvent (Cademartiri et al. synthesis[83]). Recently Cademartiri method was modified by adding tri-n-octylphosphine (TOP) to solution[84] which offers available size tunability between 3 and 10 nm.

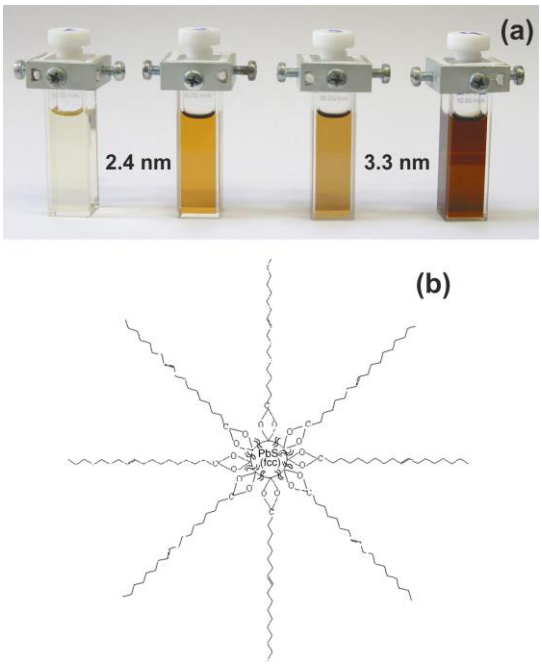

Figure 3.1. (a) Photograph of suspensions of OA-capped PbS QDs in toluene with different mean diameters and concentrations (for details, see paper V); (b) Representative model of OA-capped PbS QDs (after Ref. [85]).

In this study oleic-acid (OA) capped PbS QDs were purchased from MK Nano (mean diameter d = 2.4 nm and 3.3 nm) and STREM Chemicals (brand CANdots®) (d = 3 nm) and dispersed in toluene (Uvasol, Merck) at different concentrations [see Fig. 3.1(a)]. A schematic model of PbS QDs with long molecules of OA on the surface is shown in Fig. 3.1(b). The stock suspension nominal concentrations were 60, 50 and 93 μM/L for 2.4, 3 and 3.3 nm QD's sizes, respectively. The absorption (emission) peaks of 2.4 nm and 3.3 nm PbS QDs from MK Nano are reported to be at 763 nm (882 nm with FWHM = 118 nm) and 1021 nm (1136 nm with FWHM = 144 nm), respectively. The emission of PbS QDs (CANdots®) was reported at 1000 nm ±25 nm with FWHM < 180 nm. The claimed shelf life of PbS QDs (CANdots®) is twelve months.

Transmission electron microscopy (TEM) images (Fig. 3.2) presented by Basma[86] in her PhD thesis illustrate PbS QDs of two different sizes from MK Nano. These images confirm the nominal sizes of QDs and show no agglomerates.

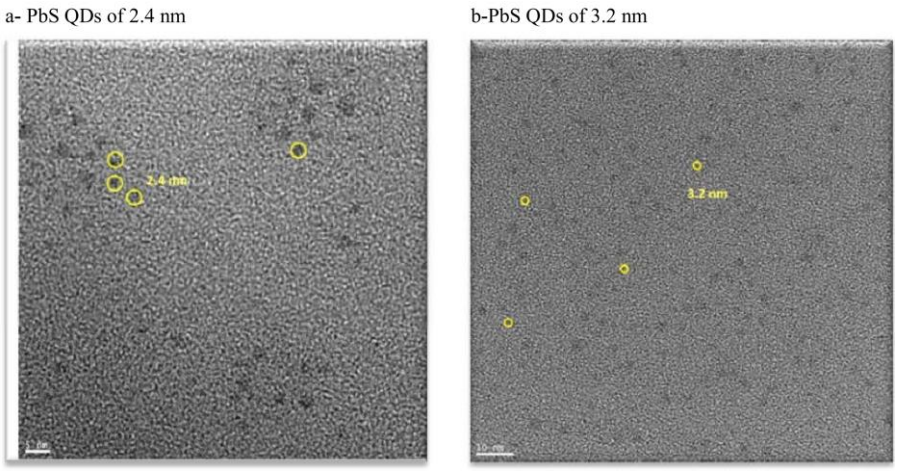

Figure 3.2. TEM images (after Ref. [86]) depict PbS QDs from MK Nano with nominal core sizes: a – 2.4 nm and b – 3.2 nm.

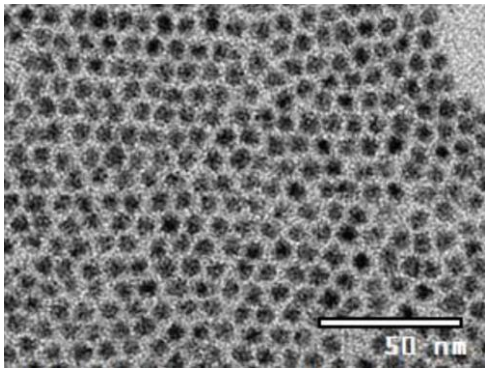

Figure 3.3. TEM image of PbS QDs from Strem Chemicals with nominal core size 3 nm. The image is presented from STREM (www.strem.com) CANdots® catalog.

TEM images (Fig. 3.3) presented in CANdots® catalog (catalog number: 82–1081) illustrate agglomerates-free PbS QDs from STREM Chemicals.

3.1.1.2 Oleylamine-capped CdSe QDs in hexane

The oleylamine capped CdSe QDs (mean diameter $d = 5.3$ nm ± 10%) were purchased from STREM Chemicals (brand CANdots®) and dispersed in hexane at different concentrations. The stock suspension nominal concentration was 50 μM/L. Emission peak is at 625 nm. TEM images (Fig. 3.4) of single CdSe QD and the ensemble of QDs were provided in CANdots® catalog. It confirms a perfect dispersion of crystalline CdSe QDs in hexane without agglomeration. The claimed shelf life is six months.

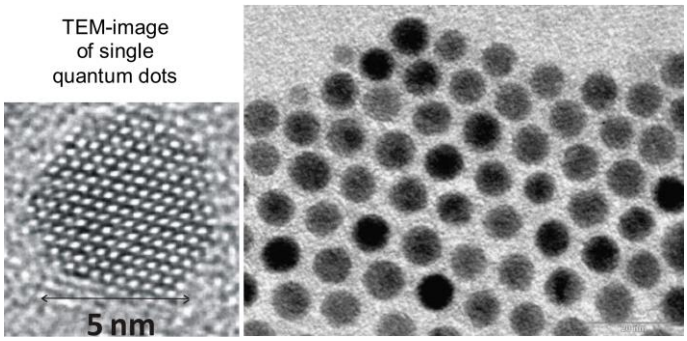

Figure 3.4. TEM images of single QD (left panel) as well as ensemble (right panel) of CdSe QDs from STREM Chemicals with nominal core size of 5.3 nm. The image is presented from STREM (www.strem.com) CANdots® catalog.

3.1.2 **Silicon QDs**

There are various ways to synthesize Si QDs in both colloidal solution and embedded in a matrix (Fig. 3.5). In this thesis we will focus on two fabrication approaches:

- Non-thermal plasma synthesis of Si QDs in colloidal suspension;
- Plasma-enhanced chemical vapor deposition (PECVD) with subsequent thermal annealing to synthesise multilayer (ML) structures;

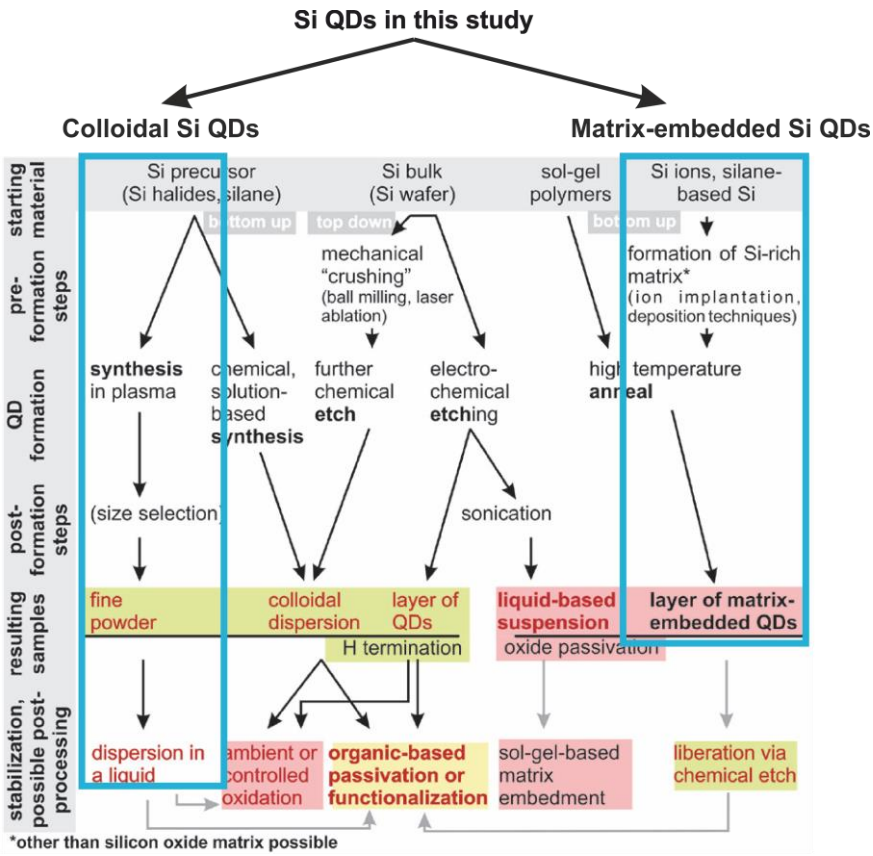

Figure 3.5. A general overview (modified from Ref. [29]) of the most common schemes of synthesis of Si QDs. Fabrication approaches considered in this study are fighlighted by blue rectangles.

3.1.2.1 Dodecyl-passivated Si QDs in toluene

Non-thermal plasma synthesis provides good control over the formation of high-quality QDs with strongly reduced agglomeration[38,87]. Plasma-synthesized Si QDs of 3.3 nm core size passivated by dodecene and dispersed in toluene were provided by Prof. Xiaodong Pi (Zhejiang University, China). Basic description of the procedure is the following. Firstly, H-passivated Si QDs were synthesized using non-thermal plasma from the mixture of SiH_4/Ar (10%/90% in volume) under pressure of the plasma between 3 and 20 mbar. Then Si QDs were hydrosilylated by the mixture of 1-dodecene ($C_{12}H_{24}$) and mesitylene (1:1 in volume) at 165 °C in the inert atmosphere of Ar. The remaining products (1-dodecene and mesitylene) were removed by rotatory evaporation. The extracted hydrosilylated Si QDs were dispersed in toluene. Further precipitation was obtained by adding a few drops of methanol to the solution. A subsequent density-gradient ultracentrifugation was carried out for the size selection. A basic scheme of the procedure is presented in Fig. 3.6 (for details see SI in Ref. [88]).

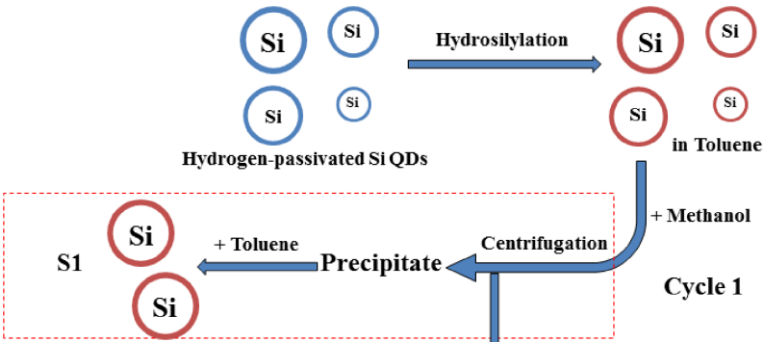

Figure 3.6. A sketch of fabrication of dodecyl-passivated Si QDs based on the non-thermal plasma synthesis of hydrogen-passivated Si QDs with subsequent size selection by the density-gradient ultracentrifugation. Taken from SI of Ref. [88].

TEM image [Fig. 3.7(a)] of drop-casted toluene suspension of Si QDs reveals excellent dispersion of QDs with no agglomerates. Selected area electron diffraction [insert in Fig. 3.7(a)] confirms the overall crystallinity of Si QDs. The sample (2.8 nm mean size) similar to materials investigated in this work reveals lognormal (close to Gaussian) distribution of sizes [Fig. 3.7(b)] that is in agreement with plasma-synthesized dodecene-capped Si QDs reported by Mangolini et al.[87].

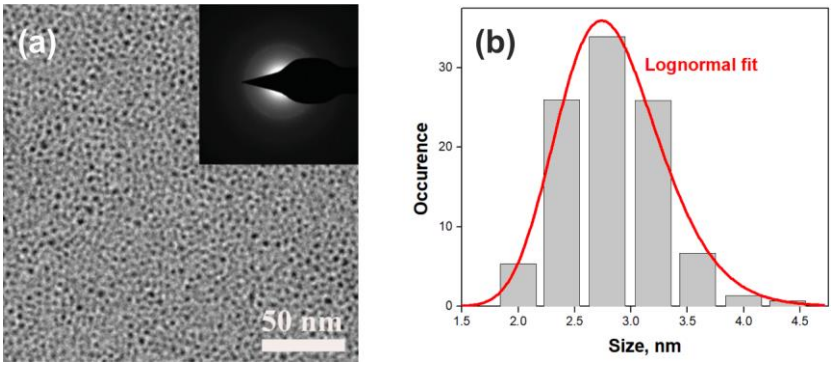

Figure 3.7. (a) Low-resolution TEM image of drop-casted toluene solution of Si QDs with the inset showing the selected area electron diffraction (that evidences overall crystallinity of QDs); (b) Size-distribution of ensemble of Si QDs with mean size 2.8 nm (similar to 3.3 nm that is studied in this work) together with its lognormal fit. The panel (a) is reproduced and the panel (b) is modified from Ref. [88].

3.1.2.2 Si QDs in SRON samples

All ML structures studied in this work are prepared by the superlattice approach in combination[89] with the phase separation by subsequent thermal annealing where the QD spacing in all three dimensions can be controlled. The samples were provided by our collaborators from the IMTEK group of Prof. Zacharias (Freiburg University, Germany).

The synthesis method is based on deposition of alternating layers of sub-stoichiometric oxinitrides and stoichiometric silicon dioxide (SiO_2) on fused silica

substrates using the Oxford Instruments "Plasmalab 100" PECVD system with the 13.56 MHz driven parallel plate reactor. The quartz substrate is chosen to avoid parasitic absorption from the substrate. The mixture of SiH_4/Ar (5%/90% in volume) and N_2O gases were used as precursor. The stoichiometry of the thin layers was controlled by tuning the flow ratio $\Gamma = [N_2O]/[SiH_4]$.

In Si-rich oxynitride (SRON) SiO_xN_y layers the stoichiometry parameter $y = 0.22–0.23$ was almost constant in all samples while the x-value was varied as 0.64, 0.85, 0.93 and 1 (see the table in attached paper VI). The deposited layer thickness was controlled by varying the deposition time and was chosen in the range 1.5–5 nm for sub-stoichiometric films and 1–2.8 nm for stoichiometric SiO_2 barriers. The number of periods is 40 bilayers for all ML samples. On top and below the ML stack, 10 nm of SiO_2 were deposited as a capping and a buffer layer, respectively. After superlattice was formed, subsequent thermal annealing was applied to samples in a quartz tube furnace at 1150 °C for 1 h in high purity N_2 gas in order to achieve phase separation of Si and SiO_2, i.e., to form Si QDs. Part of the samples was additionally passivated by annealing in H_2 at 450–500 °C. The H-bonds effectively passivate surface defects and increase the PL yield. The model of final ML structure is presented in Fig. 3.8. Superlattice approach enables effective control of the mean diameter of grown Si QDs by varying the thickness of the Si-rich layers and works well for sizes between 1 and 5 nm (see Sec. 5.2.1). Further details on the sample preparation are given in recent papers[90,91].

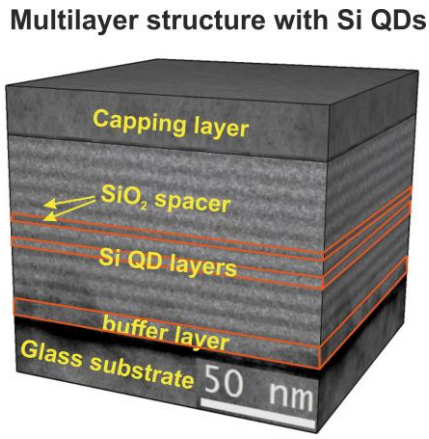

Figure 3.8. 3D sketch of a multilayer stack sample composition: SRON layers with embedded Si QDs are alternated by SiO_2 spacer layers. TEM image for the model is taken from Ref. [90].

Besides ML stack samples, thick single layer (SL) samples were prepared (i.e. a SRON monolayer without SiO_2 barriers). The thickness of Si-rich layers is 200 nm for all SL samples. The stoichiometry $y = 0.23$ was fixed and x-value was varied as 0.64, 0.93, 1.05, 1.1 and 1.15. All SL samples were additionally passivated by annealing in H_2.

Figure 3.9 demonstrates the plan-view TEM image with excellent contrast of the SRON sample. The size distribution is very narrow and can be well-fitted by a lognormal distribution.

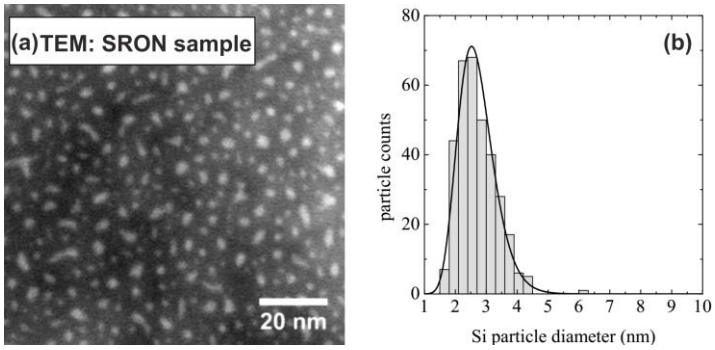

Figure 3.9. Energy-filtered TEM image (a) and corresponding size distribution with lognormal fit (b) of Si QDs for single 3.5 nm SRON layer with 2 nm buffer and capping SiO_2. Taken from Ref. [91].

3.2 Experimental characterization of samples

3.2.1 Time-integrated PL set-up

PL QY experiments were performed using a special home-built set-up (Fig. 3.10) based on an inverted microscope (Olympus IX-71) with the NIR-optimized objective lens (LMPlan IR 50×/0.55, working distance of 6 mm, focal length f = 3.6 mm).

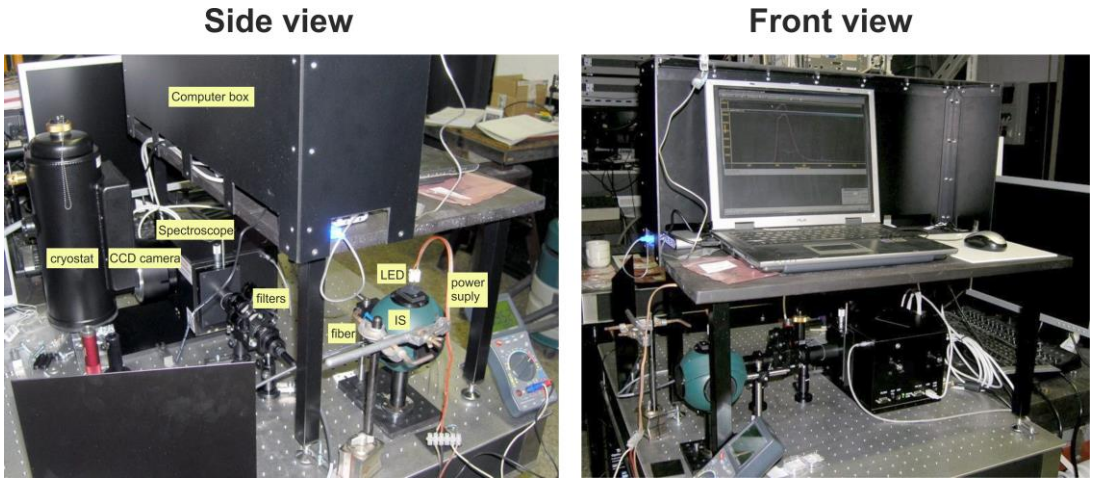

Figure 3.10. Photographs of home-build set-up with an IS for PL QY measurements.

The central component is an integrating sphere (IS) with diameter of 10 cm (SphereOptics GmbH). The inner surface of the IS is covered by the Spectraflex

coating. Samples are introduced in the IS in the position opposite to the excitation port (Fig. 3.11). The solid samples are placed into IS on one removable port that is introduced from the bottom of IS. The measured cuvettes were introduced from the top through a square port.

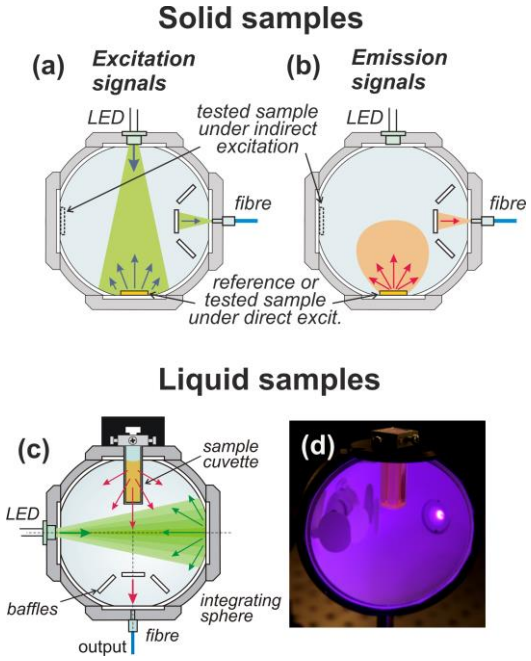

Figure 3.11. Schematical representation of experimental configuration of the IS for the PL QY determination of solid (a, b) and liquid (c, d) samples. Illustration of excitation/absorption (a, c) and emission (b) PL signals acquisition. (d) Photograph of IS cross-section (semi-sphere) with liquid sample and bright spot from excitation LED. The parts (a, b) are reproduced after Ref. [92] and (c) is taken from the paper V.

A set of various light-emitting diodes (LEDs) emitting in the range from UV to NIR region with the full-width at half-maximum (FWHM) being usually between 20–40 nm was used for PL excitation [Fig. 3.12(a)]. The power emitted by the respective LEDs is typically less than 1 mW and is not focused on the sample (Fig. 3.11). That means that we are several orders of magnitude below the saturating power density, which is, e.g. for Si QDs in the SiO_2 matrix, about 1 W/cm^2 (the average population is about one exciton per QD at this excitation power and PL saturation is observed for stronger pumping, see paper I). Alternatively, a laser-driven light source (LDLS, EQ-99X, Energetiq) coupled to the 15-cm monochromator (Acton SpectraPro SP-2150i) was used for the tunable excitation of PL QY.

The principal scheme of the PL QY set-up is shown in Fig. 3.13. The light from IS is collected by a fiber bundle placed in the direction perpendicular to the excitation axis. The baffles shield the collected signal against the direct visibility of both the excitation source and the sample.

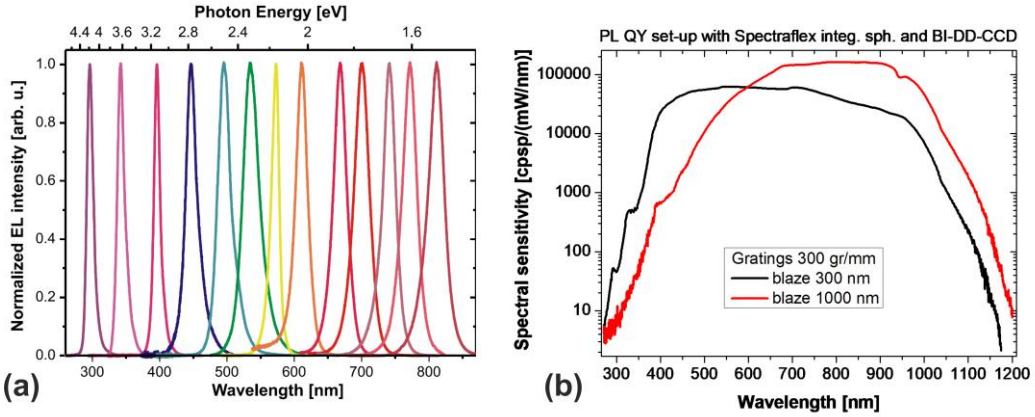

Figure 3.12. (a) Demonstration of normalized electroluminescence spectra of 13 selected LEDs from the whole set (of about 40 LEDs) available for the present study; (b) Apparatus sensitivity spectra of two different gratings (blazed at 300 and 1000 nm) obtained using 45 W tungsten halogen ($\lambda > 350$ nm) and deuterium ($\lambda < 400$ nm) standard lamps. The figures are taken/adopted from Ref. [92].

The coupling of the fiber output into a spectrometer is done with a double lens coupler specially adapted for the numerical apertures of both the fiber waveguide and the spectrometer. The output signal was imaged to an imaging spectrometer (Acton SpectraPro SP2150i, focal length $f = 15$ cm) with a deep-depletion back-illuminated charge-coupled device (CCD) camera (Spec-10:400B, Princeton Instruments).

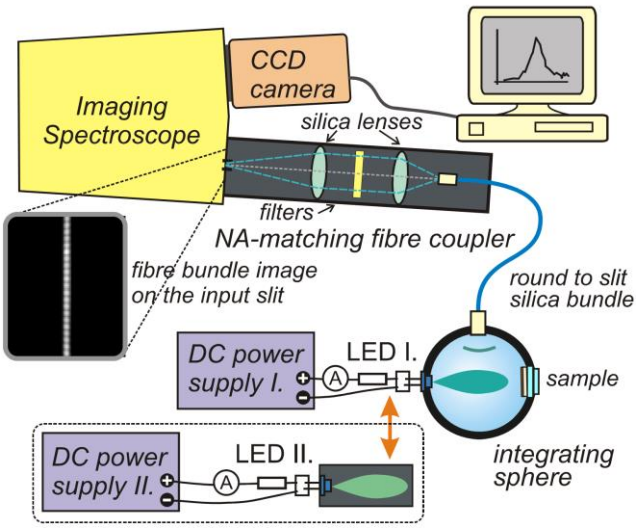

Figure 3.13. The general scheme (after Ref. [92]) of the experimental apparatus employed in measurements of absolute PL QY using an IS that was coupled to LEDs (excitation sources).

Two different gratings (blazed at 300 and 1000 nm) were used [see Fig. 3.12(b)] in the spectrometer in order to optimize the response in UV and NIR regions, respectively. The apparatus response was radiometrically calibrated in the range from 300 to 1100 nm (for details see appended paper VIII) using two radiation standards

(Newport Oriel): a 45-W tungsten halogen lamp (above 400 nm) and a deuterium lamp (below 400 nm). Special attention is paid to avoid stray-light effects in the spectrometer.

3.2.2 **Time-resolved PL set-up**

PL experiments were performed under excitation by a 405-nm diode laser whose continuous wave emission was modulated using a quartz acousto-optic cell [Fig. 3.14(b)]. The samples were typically excited by square-shaped pulses that have the duty cycle of 40%, the repetition rate of 900 Hz, and the edge switching time of about 100 ns. The laser is coupled in a home-made micro-spectroscopy set-up (Fig. 3.14) with an inverted microscope in the epifluorescence configuration with two detection branches for visible (VIS) and near-infrared (NIR) spectral regions, each one composed of an imaging spectrometer (Acton SpectraPro SP-2358i and SP-2558i, respectively) and a photomultiplier (PMT) for time-resolved PL detection (Hamamatsu H11526-20-NF and H10330A-45, respectively, for VIS and NIR). Pulses from PMTs are detected by two multichannel counting cards (Becker-Hickl, MSA-300). The details on the set-up can be found in the attached paper X. Advantage of the micro-PL set-up is a good control of the excitation spot size and the selected detection area which enables quite precise determination of excitation photon flux.

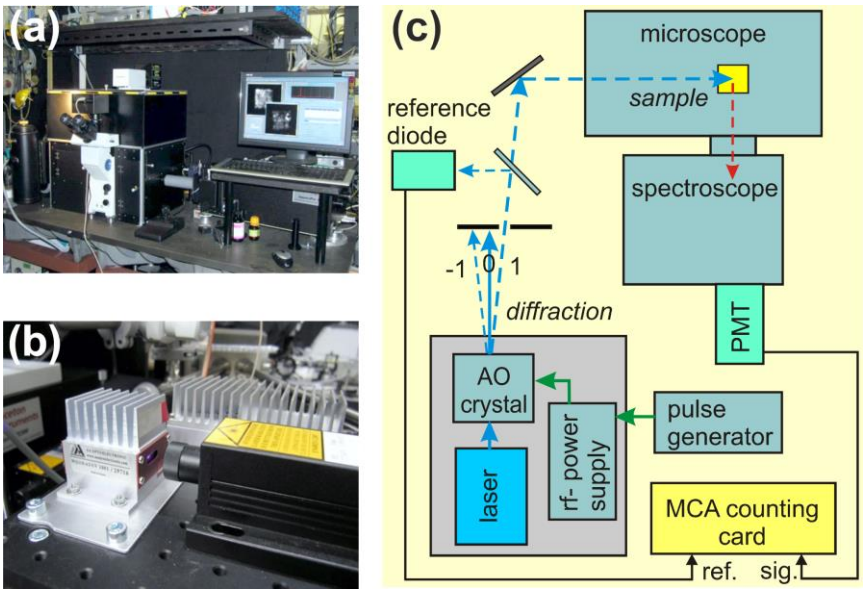

Figure 3.14. Photograph (a) of the home-made micro-PL set-up with two parallel detection branches (VIS and NIR). (b) Photograph of excitation diode laser (405 nm) with acousto-optical modulator (edge ~ 100 ns). (c) Principal scheme of the laser-modulation micro-PL set-up.

For the low-temperature experiments the samples were placed in a cryostat (Janis ST-500) that is shown in Fig. 3.15.

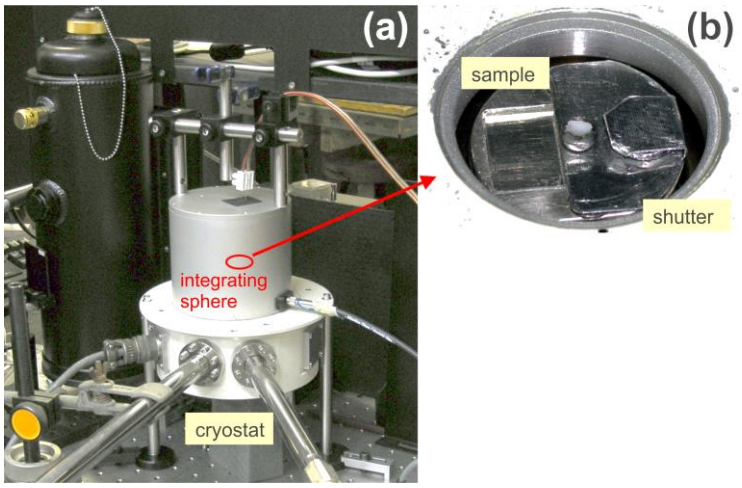

Figure 3.15. Photographs of the cryostat coupled to an IS (a) and samples in the holder (b).

A schematic representation together with a photograph of low-temperature experiments is shown in Fig. 3.16. The cryostat coupled to the above described set-up was used in experiments at cryogenic temperatures.

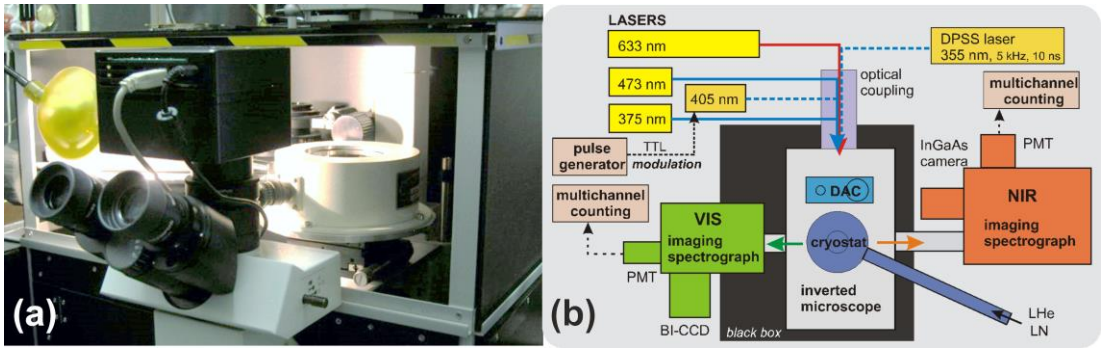

Figure 3.16. Photograph (a) and general scheme (b) of micro-PL set-up equipped with cryostat for low-temperature measurements.

3.2.3 Optical absorption spectra measurements

The absorption spectra were taken using the double-beam spectrophotometer (Specord 250, Analytik Jena) where the light is splitted into two beams: one directed to the tested sample and the second is guided to the port with a reference sample. The photo of the set-up is presented in Fig.3.17. The light is generated by the halogen and deuterium lamps that is monochromatized in the spectrometer system in the wavelength range 190–1100 nm. Two photodiodes are used as radiation detectors, which are Peltier temperature-controlled.

Figure 3.17. Photograph of the spectrophotometer (Specord 250) used for measurements of absorption spectra.

Chapter 4

Treatment of experimental data

4.1 PL quantum yield determination

PL QY is one of fundamental quantities for advanced characterization and application of luminescent materials (light-converting phosphors, fluorescence labels, etc.). Moreover, it is of particular importance for standardization of novel nanomaterials such as semiconductor QDs.

The PL QY value reveals the number of radiative transitions in the absorbing sample induced by an incoming photon flux. However, PL QY studies are related not only to characteristic depopulation exciton dynamics in QDs, but also to the sample quality, since the presence of non-radiative centers such as surface P_b-type defects would lead to QY quenching. By definition[92], PL QY η can be calculated as the ratio of the number of emitted photons [the difference between the investigated and the reference sample signals in the region of PL, Fig. 4.1(c)] and the number of absorbed photons [integrated decrease of the excitation source signal in the sample compared to the reference, Fig. 4.1(d)]:

$$\eta = \frac{\sum_{em.band} \left[\frac{I_{TS}^{em}(E_{em}) - I_{ref}^{em}(E_{em})}{C(E_{em}) \times T_{emF}(E_{em}) \times E_{em}}\right]}{\sum_{ex.band} \left[\frac{I_{ref}^{ex}(E_{ex}) - I_{TS}^{ex}(E_{ex})}{C(E_{ex}) \times T_{exF}(E_{ex}) \times E_{ex}}\right]} \tag{10}$$

where I^{em} and I^{ex} are the measured emission and excitation intensities for the tested and reference samples (marked by subscripts '*TS*' and '*ref*'). C is the sensitivity spectrum of the apparatus. The functions T_{exF} and T_{emF} represent transmittance spectra of filters used during acquisition of excitation and emission signal, and E_{ex} and E_{em} are the emission and excitation photon energies, respectively (note that the integration is replaced by summing as the spectra consist of discrete number of points – camera pixels).

The excitation and emission bands are detected separately (see Fig. 4.1) by choosing one or several (for a broad emission band) preselected detection windows and proper filters in the detection path. The color glass long-pass filters (with transmittance T_{emF}) were used to cut off the signal from higher diffraction orders of excitation photons which appears in a grating spectrometer in the region of the PL signal. The neutral density (ND) filters (with transmittance T_{exF}) were employed to

attenuate the detected (non-absorbed) excitation signal during excitation window acquisition and avoid saturation of the detector range.

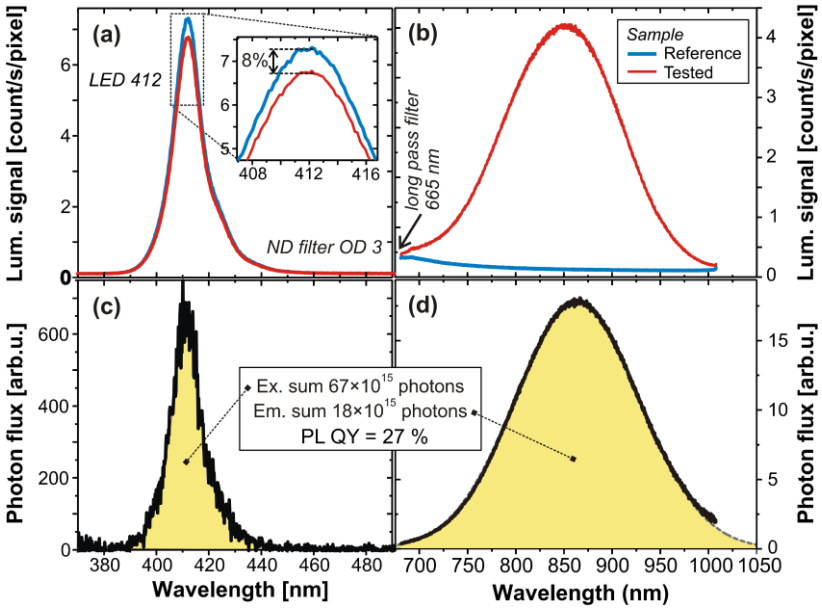

Figure 4.1. Representation (after Ref. [92]) of PL QY determination as the ratio of integrated emission (d) and excitation (c) signals obtained as the difference between reference and tested samples in excitation (a) and emission regions (b).

All colloidal ensembles of QDs studied in this work were dispersed in toluene that reveal absorption bands near 875 nm and 915 nm (Fig. 4.2).

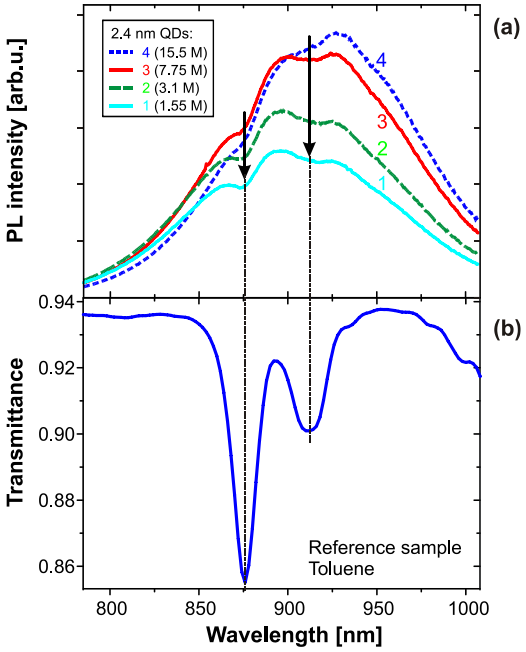

Figure 4.2. Demonstration of two dips in PL spectra of PbS QDs suspensions with different concentrations (a) as result of toluene absorption in the region that is clearly presented in transmittance spectrum of toluene (b). Taken from SI of the paper V.

Here we have to note that the solvent absorption effect becomes more pronounced in the IS setup as multiple reflections increase the light path through a cuvette. Thus, for precise QY measurements of toluene QDs suspensions emitting in the NIR range between 850 and 1000 nm, the appropriate correction must be applied in order to reveal undistorted PL spectra. Obviously, the calculation of PL QY using Eq. (10) cannot remove the solvent effect on PL. The PL loss was corrected by fitting the PL band shape using data at wavelengths outside the solvent absorption bands.

4.2 The fundamentals of time-resolved spectroscopy

4.2.1 Optimum TR PL experimental parameters

There are three basic points to be considered prior setting up an experimental apparatus for detection of a slow PL decay:

a) PL saturation: Long excited state lifetime leads to PL saturation and/or other non-linear effects already at quite low excitation power. In case of QDs, there is an enhanced probability of creating second exciton during the lifetime of the first one. Consequently, a fast non-radiative decay, e.g., Auger recombination, takes place and removes one or both excitons.

b) Incomplete decay – truncation: To observe the complete decay down to the background signal level, a long detection window has to be used after the excitation pulse. The decay window must be usually as long as at least 4 or 5 times the average lifetime[93]. Otherwise only a truncated signal is obtained, which increases the uncertainty of the background level and compromises the precision of fits.

c) Signal quality—noise: The signal quality, namely, the signal to noise (S/N) ratio determines the precision of the fitting parameters. In order to get a correct decay shape it was traditionally[94] required that the signal decay follows over three decades or more to get a correct decay shape which requires a very high S/N ratio.

The above given points imply the following three requirements for experiments: low excitation power, low pulse repetition rate, and long excitation pulses. All together these requirements make experiments very challenging to optimize, especially for QDs with a low PL QY. Therefore, it is necessary to determine carefully the optimum experimental conditions for obtaining the highest signal for a given decay parameters. Here a simple derivation for a mono-exponential decay with a characteristic decay time τ_{PL} (the multi-exponential or other forms of decays can be treated in a similar way) is presented. The PL signal increases up to $I_{PL}^{\max} = I_{PL}^{cw}(1-\exp(-T_1/\tau_{PL}))$ during the excitation pulse duration T_1. PL decay is then observed for the time T_2, long enough to allow observation of the major part of the decay shape ($\geq 4\tau_{PL}$), see Fig. 4.3(b). The

integral PL decay signal obtained during the interval T_2 is $I_{PL}^{\max}\tau_{PL}(1-\exp(-T_2/\tau_{PL}))$. One experimental cycle (T_1 + T_2) can be repeated with a repetition rate of $1/(T_1 + T_2)$. Altogether, the integral PL decay signal $I_{PL}^{\text{int.}dec.}$ (normalized to $I_{PL}^{\text{cw}}=1$) is presented in the following equation:

$$I_{PL}^{\text{int.}dec.}=\frac{(1-e^{-T_1/\tau_{PL}})(1-e^{-T_2/\tau_{PL}})\tau_{PL}}{T_1+T_2} \tag{11}$$

This relation is plotted in Fig. 4.3(a) as a function of T_1 for different T_2 equal to 3, 4, 5, or 6-times τ_{PL} ($\tau_{PL}=0.2$ ms). For a giving T_1 the optimum signal is obtained for around twice of τ_{PL}. To visualize, in Fig. 4.3(b) we simulated the PL signal for the lifetime of $\tau_{PL}=0.2$ ms and $T_2=4\tau_{PL}$. The optimum pulse length is calculated to be 386 μs.

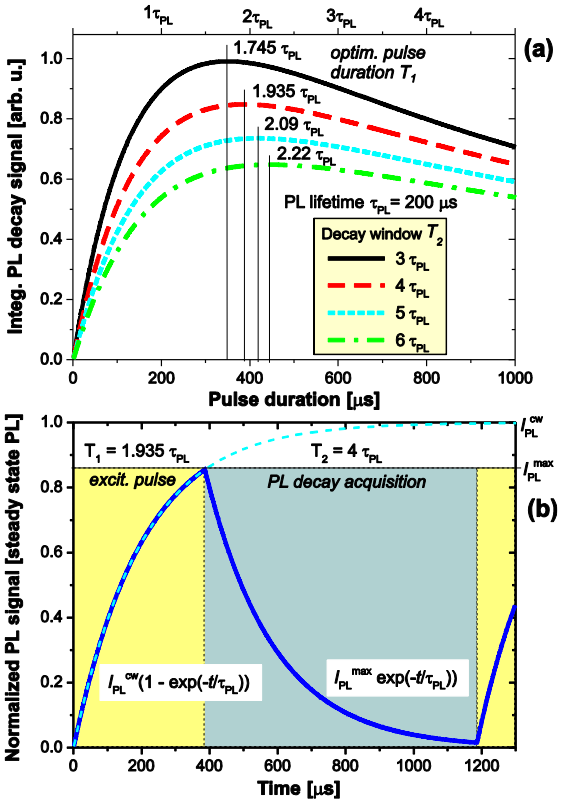

Figure 4.3. (a) Determination of the optimum pulse duration for a given average lifetime τ_{PL} (in this example 0.2 ms) and different observation time window (here equal to 3, 4, 5, and 6 times τ_{PL}); (b) PL kinetics simulated under the optimal conditions derived in (a) for $\tau_{PL}=0.2$ ms and the decay time window $4\tau_{PL}$. Taken from the paper IV.

For details on setting up the TR PL experiment see appended publications IV and X.

4.2.2 **Determination of average decay lifetimes**

PL transients of ensembles of QDs are often well fitted by stretched exponential (SE) function[53]:

$$I(t) = I(0)e^{-(\frac{t}{\tau_0})^{\beta}} + background \qquad (12)$$

where τ_0 is the PL characteristic lifetime parameter and β is the dispersion factor (varies from 0 to 1), *background* represents a "constant" background level of a detector (e.g. photomultiplier).

This decay law is relatively simple and describes quite well the PL transients of colloidal suspensions considered in Sec. 5.1.3. Unfortunately, the decay kinetics of matrix-embedded Si QDs considered in Sec. 5.2.3 do not reveal SE behavior [see Fig. 4.4(a)–(b)]. The SE fit is not perfect and one might notice a characteristic S-shape of fit residuals. An exact procedure to analyze such complex decays has not been developed yet (see appended paper X). The most straight-forward approach[95] is to use the multi-exponential (ME) fit [see Fig. 4.4(c)–(d)]:

$$I(t) = \sum_{i=1}^{N} A_i e^{-(\frac{t}{\tau_i})} + background \qquad (13)$$

where A_i and τ_i are partial amplitudes and lifetime parameters, accordingly, and N is the number of exponential components.

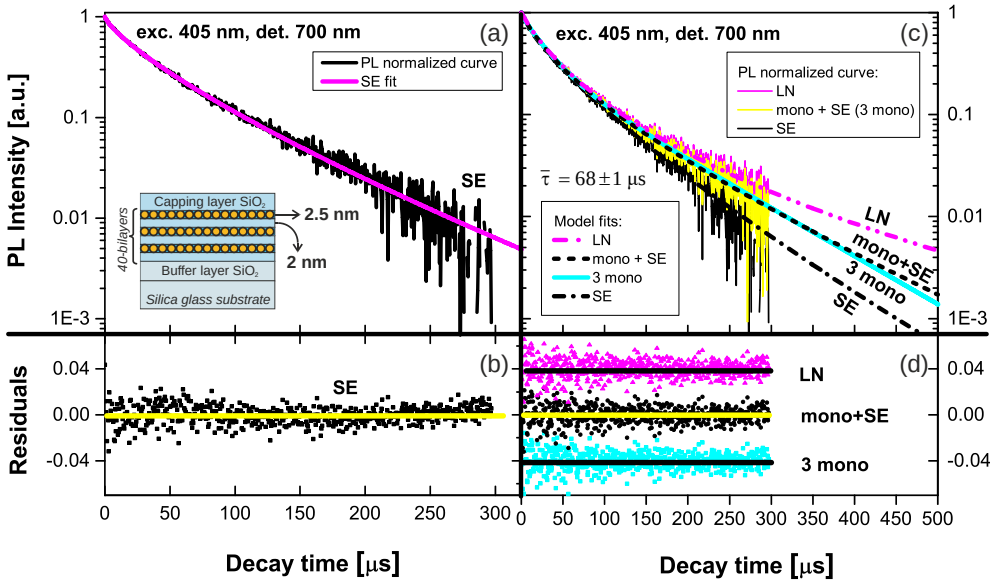

Figure 4.4. Upper panels (a, c) represent decay normalized curve and its stretched exponential (SE) fit (a) or fits by different other models (c): combination of 3 mono-exponentials (3 ME), combination of mono and stretched exponentials (MSE), lognormal (LN) distribution of rates. Lower panels (b, d) demonstrate residuals to corresponding fits. The insert in panel (a) illustrates studied ML sample structure. Taken from the paper III.

Alternatively, a combination of mono- and SE (MSE) fits can be employed[96]:

$$I(t) = A_1 e^{-(\frac{t}{\tau_1})} + A_2 e^{-(\frac{t}{\tau_2})^{\beta}} + background \tag{14}$$

Finally, the model proposed by van Driel et al.[97] can be used, which imply the lognormal (LN) distribution of decay rates:

$$I(t) = I(0)\int_0^{\infty} f(k)e^{-(kt)}dk + background \tag{15}$$

where $f(k)$ is LN distribution function of decay rates *k* and is given by:

$$f(k) = Ae^{-(\frac{\ln(k/k_m)}{\sinh^{-1}(k_d/2k_m)})^2} \tag{16}$$

where k_m and k_d represent the most frequent total decay rate and the width of rate distribution, respectively; *A* is an amplitude.

The average recombination time of emitted photons could be generally calculated[53] as:

$$\bar{\tau} = \frac{\int_0^{\infty} tI(t)dt}{\int_0^{\infty} I(t)dt} \tag{17}$$

Taking the SE [Eq. (12)], ME [Eq. (13)] and MSE [Eq. (14)] decay signals and introducing them into Eq. (17) we obtain:

$$\bar{\tau}_{SE} = \Gamma(\frac{2}{\beta}) / \Gamma(\frac{1}{\beta})\tau_0 \tag{18}$$

$$\bar{\tau}_{ME} = \sum_{i=0}^{N} A_i\tau_i^2 / \sum_{i=0}^{N} A_i\tau_i \tag{19}$$

$$\bar{\tau}_{MSE} = (A_1\tau_1^2 + A_2\frac{\tau_2^2}{\beta}\Gamma(\frac{2}{\beta})) / (A_1\tau_1 + A_2\frac{\tau_2}{\beta}\Gamma(\frac{1}{\beta})) \tag{20}$$

where Γ corresponds to gamma-function.

Eq. (20) was uniquely derived during this work and to my best knowledge was never published in literature. To calculate the average decay lifetime $\bar{\tau}_{LN}$ of LN decay model we had to compute numerically the Eq. (17) as it seems that there is no simple analytical representation.

Important to note that average lifetime does not depend on the fitting model [see Eq. (17)] and should be approximately the same (paper III) for all lifetime distributions which corresponding decay functions describe well experimental kinetics.

4.3 PL modulation technique for the ACS determination

Although ACS is a very important quantity for practice it is difficult to access and quantify it experimentally. One of the possible way on how to approach this problem is the PL modulation technique. It is based on the kinetic depopulation model originally presented by Chepic, Efros, Ekimov et al.[98] and subsequently modified by Kovalev et al.[99,100] and in our recent papers I and VII. At low excitation powers ($I_{ex}\sigma \ll 1/\tau_{PL}$) the solution of differential equations of the depopulation model looks as:

$$I_{PL}(t) = N_b I_{ex}\sigma \frac{\tau_{PL}(I_{ex})}{\tau_r} \times [1 - e^{-(\frac{1}{1/\tau_{PL}(I_{ex})} + I_{ex}\sigma)t}] = I_{PL}^{cw}[1 - e^{-(t/\tau_{ON}(I_{ex}))}] \qquad (21)$$

where σ describes the cross-section for absorption of photons, N_b is the total population of luminescing (bright) QDs; $\tau_{ON}(I_{ex})$, $\tau_{PL}(I_{ex})$ and τ_r stand for the onset, PL decay, and radiative lifetime, respectively.

From Eq. (21) it follows that a measure of the PL onset (rise) time as a function of I_{ex} will give direct information on ACS:

$$\frac{1}{\tau_{ON}(I_{ex})} = I_{ex}\sigma + \frac{1}{\tau_{PL}(I_{ex})} \qquad (22)$$

As it follows from Eq. (22), the inverse onset lifetime (onset rate) $1/\tau_{ON}(I_{ex})$ is a linear function of photon flux I_{ex} with an offset given by the inverse decay PL lifetime (PL rate) $1/\tau_{PL}$. Therefore, the ACS is often erroneously determined directly as a slope of $1/\tau_{ON}(I_{ex})$ function. However, according to our experiments (paper VII) the PL lifetime is also a function of excitation power $\tau_{PL}(I_{ex})$ (see Sec. 5.2.3). Considering the radiative relaxation τ_r as being power independent, this can be understood as saturation of non-radiative recombination decay paths resulting in an increase of non-radiative lifetime τ_{nr}. By analogy with Eq. (22), the dependence $1/\tau_{PL}(I_{ex})$ can be also approximated with a linear function (Fig. 4.5):

$$\frac{1}{\tau_{PL}(I_{ex})} = \gamma_{PL} I_{ex} + \frac{1}{\tau_0} \qquad (23)$$

where the low-excitation lifetime is $\tau_0 = \tau_{ON}(0) = \tau_{PL}(0)$ and γ_{PL} is a slope of the $1/\tau_{PL}(I_{ex})$ power dependence.

By substituting Eq. (23) into Eq. (22) we finally obtain:

$$\frac{1}{\tau_{ON}(I_{ex})} = (\sigma + \gamma_{PL})I_{ex} + \frac{1}{\tau_0} = \gamma_{ON} I_{ex} + \frac{1}{\tau_0} \qquad (24)$$

where γ_{ON} is a slope of the $1/\tau_{ON}(I_{ex})$ function.

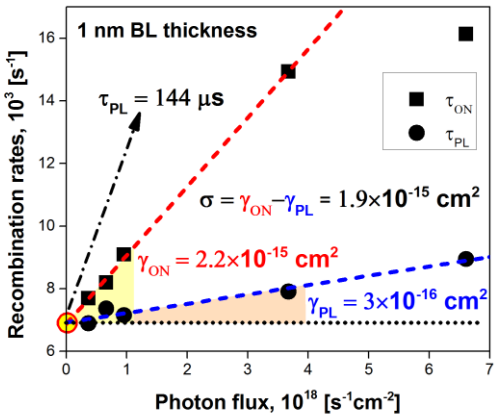

Figure 4.5. Representation of ACS determination procedure as a difference between onset and decay rate slopes ($\sigma = \gamma_{ON} - \gamma_{PL}$). Taken from the paper I.

From Eq. (24) it follows that the correct ACS value must be calculated as the difference between ON and PL rate slopes $\sigma = \gamma_{ON} - \gamma_{PL}$ (Fig. 4.5) where both slopes are determined within the linear dependence pumping range. This correct assessment that keeps into account intensity-dependent PL decay lifetime was developed within this work and was never introduced in literature, to the best of our knowledge.

4.4 Internal quantum efficiency

PL QY considered in Sec. 4.1 is defined as spectrally integrated value and have to be distinguished from internal quantum efficiency (IQE). We use the term "quantum efficiency" (both external and internal) for the spectrally dispersed (not integrated) values. Then, PL QY can be defined as the integrated value of EQE. The definition of IQE is more challenging since it has different meanings in literature. Thus, in papers[101,102] that employ theoretical approach, the radiative and non-radiative contributions to the PL decay was decoupled thanks to the fabrication of special wedged samples [that allows the variation of radiative decay rate by the modification of local density of states (DOS)], IQE is defined as the ratio of the radiative $k_r^{vac}(E)$ to the total $k_{PL}^{vac}(E)$ decay rates in a vacuum:

$$\eta_I(E) = \frac{k_r^{vac}(E)}{k_{PL}^{vac}(E)} \tag{25}$$

In "pure" experimental papers[29,103,104], IQE is defined as simply the ratio of radiative $k_r^e(E)$ and total $k_{PL}^e(E)$ decay rates in an environment:

$$\eta_I^*(E) = \frac{k_r^e(E)}{k_{PL}^e(E)} \tag{26}$$

Important to note that above mentioned "theoretical" [Eq. (25)] and "experimental" [Eq. (26)] definitions of IQE are not identical because of the following. The intensity signal of PL decay curve could be considered as a probability density of spontaneous emission. One cannot say when the spontaneous emission act of an emitter will occur; rather an ensemble of emitters has to be considered to predict the probability of decay. Then the spontaneous emission event may look to be a fundamental intrinsic property of the emitter itself and for a long time was believed to be independent on the surrounding up to the middle of XX century. However, after the pioneering work of Purcell and his co-workers[105] it became clear that the probability of spontaneous transitions with emission of radiation is not an absolute number, but could be modified by the surrounding environment. In other words, the system of interacting emitter with the surrounding electromagnetic field should be considered for proper calculation of the spontaneous decay rate of an excited emitter. To keep into account the effect of the environment, one has to consider Purcell factor (PF) that is simply the ratio of probabilities of radiative recombination in an environment and in vacuum:

$$F^P(E) = \frac{k_r^e(E)}{k_r^{vac}(E)} \tag{27}$$

Generally speaking, PF is a product of the photonic DOS $\sqrt{\varepsilon_e(E)}$ and the local field factor $f(\varepsilon_e)$ in the environment[106]:

$$F^P = \sqrt{\varepsilon_e(E)}\left(\frac{3\varepsilon_e(E)}{\varepsilon_{QD}(E) + 2\varepsilon_e(E)}\right)^2 \tag{28}$$

where $\varepsilon_{QD}(E)$ and $\varepsilon_e(E)$ are dielectric permittivities of QD material and QD environment, respectively.

Eq. (28) represents an estimation of PF for a single QD. As in practice one often deals with relatively dense ensembles of QDs, the effective dielectric permittivity must be considered instead of pure environment $\varepsilon_e(E)$ and can be estimated using, e.g. the Maxwell-Garnett approximation[106,107].

Considering, that non-radiative rate is the same in the environment and in vacuum [$k_{nr}^e(E) = k_{nr}^{vac}(E) = k_{nr}(E)$] and using the Eq. (9), (25) and (26), we obtain:

$$\frac{1}{\eta_I(E)} = \frac{k_{PL}^{vac}(E)}{k_r^{vac}(E)} = 1 + \frac{k_{nr}(E)}{k_r^{vac}(E)} = 1 + \frac{F^P(E)k_{nr}(E)}{k_r^e(E)} = \frac{k_r^e(E) + F^P(E)k_{nr}(E)}{k_r^e(E)} \tag{29}$$

After simplification, the Eq. (29) looks like:

$$\eta_I(E) = \frac{k_r^e(E)}{k_r^e(E) + F^P(E) k_{nr}(E)} = \frac{1}{1 + F^P(E)\dfrac{k_{nr}(E)}{k_r^e(E)}} = \frac{1}{1 + F^P(E)[\dfrac{k_{PL}^e(E)}{k_r^e(E)} - 1]} \quad (30)$$

Finally, the interconnection between $\eta_I^*(E)$ and $\eta_I(E)$ can be written as:

$$\eta_I(E) = \frac{1}{1 + F^P(E)[\dfrac{1}{\eta_I^*(E)} - 1]} \quad (31)$$

$$\eta_I^*(E) = \frac{1}{1 + \dfrac{1}{F^P(E)}[\dfrac{1}{\eta_I(E)} - 1]} \quad (32)$$

Important to note, that for the first time we introduce a clear distinction of two definitions of IQE (η_I and η_I^*) and derive the Eq. (31) and Eq. (32) within this work.

From Eq. (32) it follows that $\eta_I^*(E) \approx \eta_I(E)$ in two cases only:

- $F^P \to 1$ or in other words, the medium is close to a vacuum (an air, for instance);
- $k_{nr}(E) \to 0$, then $\eta_I^*(E) \approx \eta_I(E) \approx 1$.

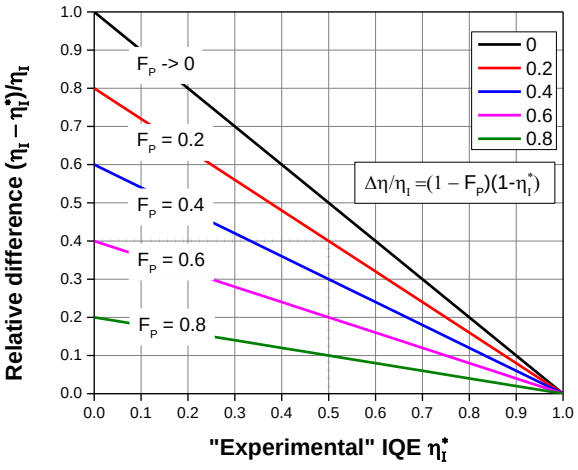

Figure 4.6. Relative difference [given by Eq. (33)] between "theoretical" [given by Eq. (31)] and "experimental" [given by Eq. (32)] IQE [$\Delta\eta_I(E)/\eta_I(E)$] as a function of "experimental" IQE for different PFs (0, 0.2, 0.4, 0.6 and 0.8).

We can estimate how large is the error that one introduces assuming generally (that is the case in many papers) $\eta_I^*(E) \approx \eta_I(E)$:

$$\frac{\Delta\eta_I(E)}{\eta_I(E)} = \frac{\eta_I(E) - \eta_I^*(E)}{\eta_I(E)} = 1 - \eta_I^*(E)[1 + F^P(E)(\frac{1}{\eta_I^*(E)} - 1)] = \\ = [1 - F^P(E)][1 - \eta_I^*(E)] \quad (33)$$

If to assume that PF is wavelength-independent, the relative difference [Eq. (33)] can be represented as in Fig. 4.6. The smaller is "experimental" IQE $[\eta_I^*(E) = k_r^e(E)/k_{PL}^e(E)]$ and PF $F^P(E)$, the larger is the relative difference between the η_I^* and η_I values of IQE (Fig. 4.6). For instance, if to consider $F^P = 0.2$ and $\eta_I^* = 0.5$, then the relative difference is 40%.

Important to note, that Eq. (31) and Eq. (32) contain one parameter that, in fact, is extremely difficult to assess, namely, PF $F^P(E)$ (see discussion in Sec. 5.2.6).

4.5 The fraction of dark/bright QDs in an ensemble

In real samples, one generally observe (compare results in Sec. 5.2.5 and Sec. 5.2.6):

$$\eta_I^*(E) = \frac{k_r^e(E)}{k_{PL}^e(E)} \geq \frac{p_{em}(E)}{p_{abs}(E)} = \eta_E(E) \quad (34)$$

where $\eta_E(E)$ stands for EQE[108], i.e., the ratio of numbers of absorbed $p_{abs}(E)$ and emitted $p_{em}(E)$ photons with energies between E and $E + \Delta E$, accordingly. IQE $\eta_I^*(E)$ is obtained by Eq. (26).

The difference between IQE and EQE in Eq. (34) can be explained by considering the presence of dark QDs, i.e., QDs that absorb but do not emit photons (see Fig. 4.7). One may assume that besides dark QDs, there might be anything (including matrix defects, substrate, QD reabsorption) apart from any QDs that absorb but do not emit light. Although it might be the case (and we assume it is) we focus on the presence of dark QDs as they nominally should reveal much higher ACS than other sources of losses (like matrix defects) which are neglected in this model.

Assuming that a QD absorbs at most one photon during one excitation pulse in low excitation power regime[100] (before the saturation limit) and that all monodisperse QDs have the same emission rate, the numbers of absorpbed and emitted photons can be converted into the corresponding numbers of absorbing $n_{abs}(E)$ and emitting (bright) $n_b(E)$ QDs at energy E:

$$p_{abs}(E) = n_{abs}(E); \quad p_{em}(E) = n_b(E)\frac{k_r^e(E)}{k_{PL}^e(E)} \tag{35}$$

where $n_{abs}(E)$ and $n_b(E)$ are the numbers of absorbing and emitting (bright) QDs at energy E.

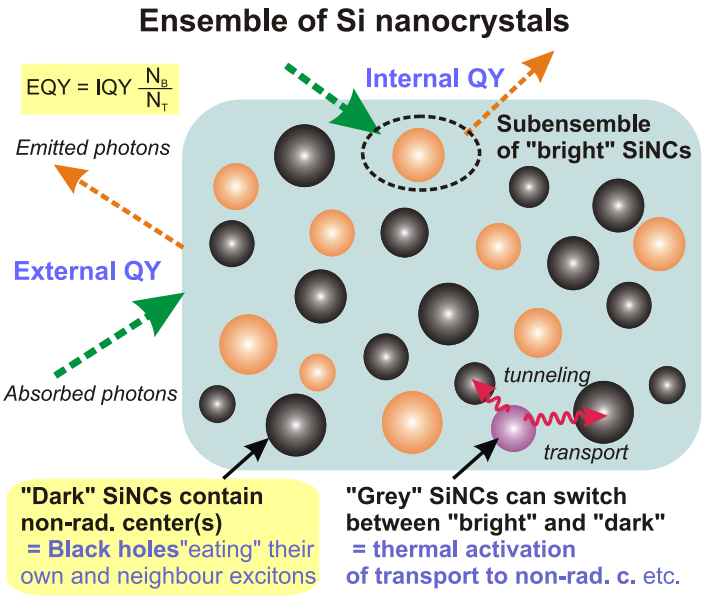

Figure 4.7. Schematic illustration of an ensemble with bright, dark and possibly grey (can switch between dark and bright states) QDs. While IQE parameter probes only bright QDs, EQE is related to the whole ensemble of QDs [including dark and in dark states (here and after – dark) QDs].

The average (spectrally integrated) value of EQE η_E can be determined[103] by considering all possible emission energies E (spectral integration):

$$\begin{aligned}
\eta_E &= \frac{P_{em}}{P_{abs}} = \frac{\int_{E_i=0}^{\infty} p_{em}(E_i)dE_i}{\int_{E_j=0}^{\infty} p_{abs}(E_j)dE_j} = \frac{1}{N_{abs}}\int_0^{\infty} n_b(E)\frac{k_r^e(E)}{k_{PL}^e(E)}dE = \\
&= \frac{1}{N_{abs}}\int_0^{\infty} n_b(E)\eta^*(E)dE = \frac{N_b}{N_{abs}}\int_0^{\infty}\frac{n_b(E)}{N_b}\eta^*(E)dE = \\
&= \frac{N_b}{N_{abs}}\int_0^{\infty}\rho(E)\eta^*(E)dE = \frac{N_b}{N_{abs}}\langle\eta^*\rangle
\end{aligned} \tag{36}$$

where averaged IQE $\langle\eta^*\rangle = \int_0^{\infty}\rho(E)\eta^*(E)dE$ is obtained by scaling the IQE normalized by weight factors ρ over the entire spectral region, and weight factors are given as $\rho(E) = n_b(E)/N_b$. P_{abs} and P_{em} are total numbers of absorbed and emitted photons, respectively; N_{abs} and N_b are total numbers of absorbing and emitting QDs, respectively.

Consequently, the fraction of bright QDs in an ensemble is given as:

$$\frac{N_b}{N_{abs}} = \frac{\eta_E}{\langle \eta^* \rangle} \tag{37}$$

If IQE $\eta^*(E)$ can be approximated with a value η^*, i.e. $\eta^*(E)$ does not vary significantly with energy *E*, the evarage IQE $\langle \eta^* \rangle$ is simplified as:

$$\langle \eta^* \rangle = \int_0^\infty \rho(E)\eta^*(E)dE = \frac{\int_0^\infty n_b(E)dE}{N_{em}}\eta^* = \eta^* \tag{38}$$

Chapter 5

Optical characterization of ensembles of QDs

5.1 Optical study of colloidal ensembles

5.1.1 PL emission spectra of colloidal QDs

In this subsection we will illustrate and compare optical properties of direct (PbS) and indirect (Si) semiconductor QDs. Though for both nano-size materials QC model is valid, there are some fundamental differences in their absorption and emission mechanisms.

Our calculations showed (paper V) that the spectral position of the first absorption peak of PbS QDs that were bought from MK Nano depends on QD size (diameter) according to the equation derived by Moreels et al.[109]:

$$E_{g,PbS}^{abs}(d[\mathrm{nm}]) = E_{b,PbS} + \frac{1}{0.0252\ \frac{d^2}{\mathrm{eV}\times\mathrm{nm}^2} + 0.283\ \frac{d}{\mathrm{eV}\times\mathrm{nm}}} \tag{39}$$

where $E_{b,PbS} = 0.41\,\mathrm{eV}$ is the bulk bandgap of lead sulfide.

There are no exciton peaks (paper VII) in the absorbance spectra of Si QDs as Si is an indirect bandgap semiconductor[110]. PL emission spectra of ensembles of colloidal PbS and Si QDs with mean size 3.3 nm each that were diluted in toluene are depicted in Fig. 5.1(a). The emission clearly depends on the material of QD that is intuitive according to the QC model (see Sec. 2.1). Thus, the optical emission bandgap of PbS QDs from MK Nano were shown[82] to depend on QD size as:

$$E_{g,PbS}^{em}(d[\mathrm{nm}]) = E_{b,PbS} + \frac{1}{0.0097\ \frac{d^2}{\mathrm{eV}\times\mathrm{nm}^2} + 0.350\ \frac{d}{\mathrm{eV}\times\mathrm{nm}} + 0.125\,\frac{1}{\mathrm{eV}}} \tag{40}$$

In its turn the corresponding dependence for Si QDs was proposed by Belyakov et al.[40] as a function:

$$E_{g,Si}^{em}(d[\mathrm{nm}]) = \sqrt{E_{b,Si}^2 + \frac{19.2\ \mathrm{eV}^2\times\mathrm{nm}^2}{d^2}} \tag{41}$$

where $E_{b,Si} = 1.12\,\mathrm{eV}$ is the bulk bandgap of silicon.

Considering the size of our QDs as 3.3 nm and using the Eq. (40)–(41) we obtain $E_{g,PbS}^{em}(3.3\,\mathrm{nm}) = 1.13\,\mathrm{eV}$ and $E_{g,Si}^{em}(3.3\,\mathrm{nm}) = 1.73\,\mathrm{eV}$ that is in perfect agreement with our experimental observation presented in Fig. 5.1.

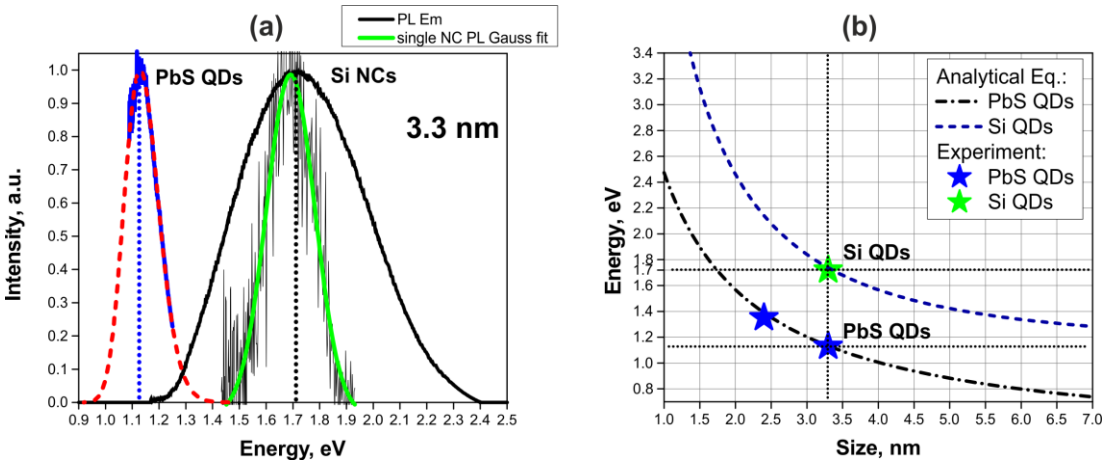

Figure 5.1. (a) PL emission spectra of ensembles of PbS (blue) and Si (black) QDs in toluene (presented in the paper II) with the same mean size 3.3 nm each and an example of PL spectrum of single Si QD with the Gauss fit (green line). Dashed red line represents lognormal fit of the PbS QD spectrum; (b) Analytical dependences of the optical bandgap of PbS [dash-dotted line, Eq. (40)] and Si [dashed line, Eq. (41)] QDs together with experimentally obtained values for PbS (blue stars) and Si (green star) QDs.

The PL linewidth of an ensemble of QDs is a product of both intrinsic (homogeneous broadening) and ensemble (inhomogeneous broadening) contributions. The homogeneous linewidth broadening (HLB) is a characteristics of each single QD and it is ultimately limited by the finite excited state lifetime through the uncertainty principle. This linewidth can be result of emission from one or multiple states and each of them can be coupled to the local surrounding (for instance, exciton-phonon interaction). The exciton fast trapping at surface defect states can also lead to a large HLB. For CdSe QDs the typical RT homogeneous linewidth was reported[111] to be $\Gamma_{\text{hom}}^{CdSe} \sim 50-60$ meV. In contrast, the homogeneous linewidth of PbS QDs was confirmed to be significantly broader from $\Gamma_{\text{hom}}^{PbS} < 100$ meV (Ref. [112]) to $\Gamma_{\text{hom}}^{PbS} \sim 170$ meV (Ref. [113]). For colloidal Si QDs the homogeneous linewidth at RT was shown[60] (paper II) to be even broader $\Gamma_{\text{hom}}^{Si} \sim 200-220$ meV [Fig. 5.1(a)] that can be related to the indirect nature of silicon.

The heterogeneous size polydispersity of QDs in an ensemble results in inhomogeneous linewidth broadening which is the convolution of multiple single QD homogeneous linewidths. This effect dominantly influences the overall emission spectrum[114] and could be much suppressed by preparation of NCs of nearly uniform size[34]. Unlike CdSe QDs, PbS QDs manifest PL ensemble linewidth that is highly size-dependent. Thus, for bigger PbS QDs (~4–6 nm) the linewidth is expected to be <100 meV whereas for smaller ones (~2 nm) the ensemble linewidth is usually broader (160–240 meV)[62]. The FWHM of ensemble PL of our 3.3 nm PbS QDs is estimated ~150 meV [Fig. 5.1(a), dashed red line] that is still narrower than single Si

QD emission [Fig. 5.1(a), green line]. The PL linewidth from the ensemble of colloidal Si QDs is very broad (FWHM >570 meV) that is comparable with the inhomogeneous PL broadening of porous Si (up to 500 meV)[49].

5.1.2 PL quantum yield of colloidal QDs

5.1.2.1 PL QY vs concentration

Generally speaking, the PL QY is the quantity that should not be dependent on concentration of emitters by definition (see Sec. 4.1). Therefore, very often QY values are measured (and reported in literature) for only one particular concentration of QDs in a solution. The primary aim of this section is to point out the importance of measuring PL QY over the range of concentrations.

Indeed, for large size PbS (3.3 nm) and CdSe (5.3 nm) QDs the PL QY is concentration-independent in a certain range of solution concentrations [Fig. 5.2(a)].

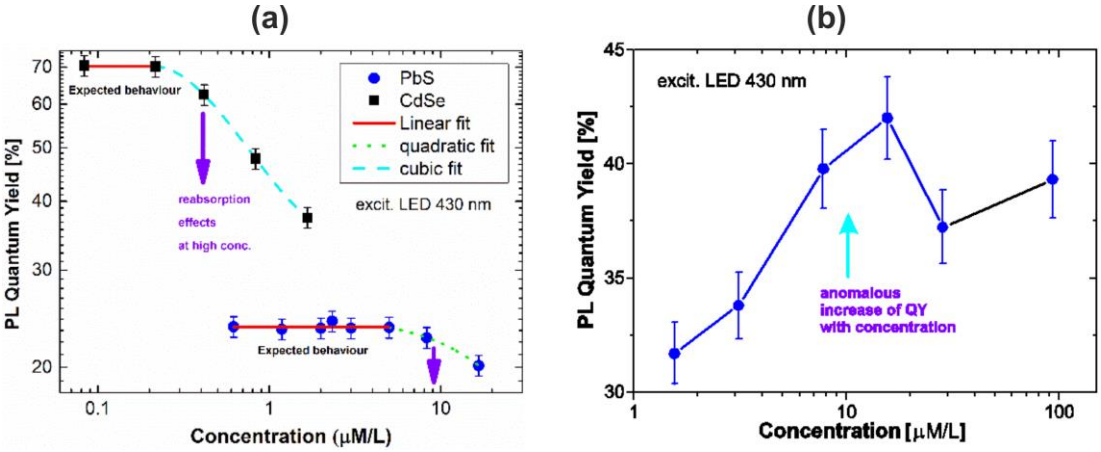

Figure 5.2. Dependences of PL QY on concentration for (a) 3 nm PbS (●) and 5.3 nm CdSe (■) as well as for (b) 2.4 nm PbS QD solutions in toluene (PbS) and hexane (CdSe). The right panel is taken from the paper V.

However, after some concentration threshold QY is a decreasing function of increasing concentration. This is due to the well-known effect of reabsorption – emitted light can be reabsorbed by QDs in the region of the spectral overlap between absorption and emission (see Sec. 2.3.2). The reabsorption effect is particularly pronounced for IS setups as random and multiple light reflections on the inner wall lead to the increased effective optical light pass through a sample. Therefore, suspensions of QDs should be diluted enough before measurements or a reabsorption correction should be applied.

For small size PbS (2.4 nm) QDs PL QY occurred to be concentration-dependent even at small concentrations [Fig. 5.2(b)]. A similar QY dependence was previously reported for QDs of CdTe[115] and CdSe/ZnSe/ZnS[116] and was attributed to the ligand

surface desorption. Recent results[117] of our colleagues from Amsterdam University as well as our simple simulations indicate that such anomalous dependence can be an artefact of IS measurements of highly diluted emitters that is related to insufficient sample absorption. This is in agreement with the idea that small QDs might have lower ACS than large QDs (see Sec. 5.2.4) and therefore the effect can be observed at higher concentrations. Important to note, however, that after we added 10 μL of OA in toluene, we observed no decrease of QY with decreasing concentration (Fig. 5.3), so indicating that the ligand desorption from surfaces of QDs can be the origin of the abnormal QY concentration dependence in our case.

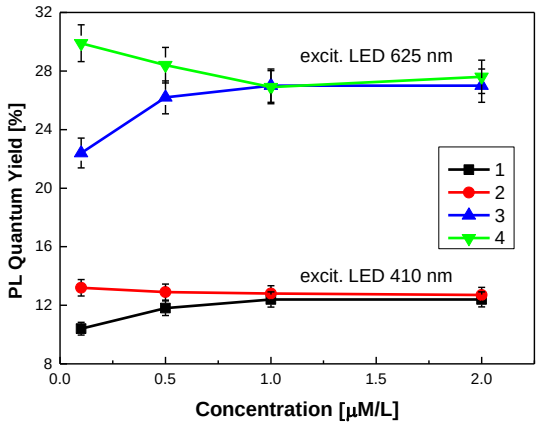

Figure 5.3. The effect of OA concentration in solution on QY concentration dependence for low concentrated suspensions of 3.3 nm PbS QDs. The samples without (1, 3) and with (2, 4) additional 10 μL volume of OA solution (1:4 OA in toluene) were excited by LEDs emitting at 410 nm (1, 2) and 625 nm (3, 4). This experiment was done upon the request of JAP referees with a delay of about 7 month after measurements presented in Fig. 5.2. During this time the QD stock solution continued to degrade (although claimed shelf life of these PbS QDs was twelve months), the absolute value of QY is decreased, but the stabilizing effect of OA is clearly observed. Taken from SI of the paper V.

Conclusively, the QY should be measured for a set of different solution concentrations to reveal concentration-independent interval that is related to artefact-free true value of QY for a sample.

5.1.2.2 PL QY vs excitation photon energy

Many PL QY set-ups have limited number of available excitation wavelengths (laser lines or lamps with band-pass filters). But this limitation is commonly considered to be acceptable as the Kasha-Vavilov (KV) rule, which states the independence (especially for organic fluorescent materials) of both the luminescent spectral shape and its QY on the excitation photon energy, is believed to be fulfilled.

However, QDs with its complex size and surface-dependent optical properties often violate the KV rule and measuring of PL QY over extend excitation range is necessary.

The general trend in QY excitation spectra is the same independently on QD material: PL QY is decreasing for excitation addressing higher states above the bandgap (Fig. 5.4). That is somehow intuitive as more non-radiative pathways related to surface and other trap states[118] can be opened for hotter carriers relaxation. This QY behavior points out that for a given value of QY there should be reported an excitation energy used.

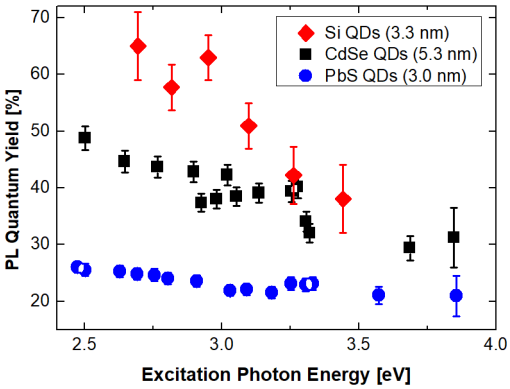

Figure 5.4. PL QY dependence on the excitation photon energy for 3 nm PbS (●), 3.3 nm Si (♦) and 5.3 nm CdSe (■) QD solutions in toluene (PbS, Si) and hexane (CdSe). The concentration of PbS and CdSe QD solutions was 2 μM/L each.

5.1.2.3 PL QY vs emission photon energy

The dependence of PL QY on emission photon energy (QD size) is expected due to a couple of reasons. Firstly, the probability of exciton radiative recombination defined by QC model is size-dependent (paper II). Secondly, the surface chemistry might depend on the QD size including ligand adsorption-desorption equilibria. As it was demonstrated above, the absolute values of QY can vary in a broad range depending on several parameters (mainly on excitation light energy and solution concentration) which complicated the comparison of literature data.

In this section the idea of size-dependent QY is illustrated in Fig. 5.5 on example of PbS QDs capped by oleic acid and suspended in toluene or hexane (the data are taken from different papers for comparison). In spite of the fact that presented QY values were obtained for different QY measurement techniques, excitation photon energies, QD synthesis methods, QD sizes and concentrations, solvents etc., most of PL QY values in Fig. 5.5 are quite systematic. That is quite evident that QY is generally decreasing for bigger PbS QDs that is in agreement with recent works[7,119]. In conclusion, for the purpose to maximize PL QY one should better work with diluted

enough solutions of rather small PbS QDs while near-resonant energy excitation should be employed (until multiple exciton generation is not expected).

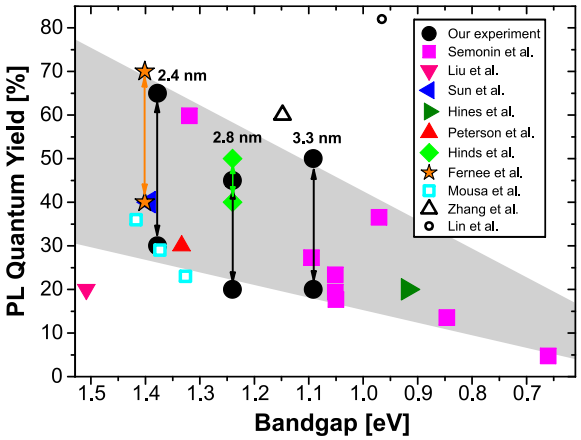

Figure 5.5. Relation between PL QY and optical bandgap based on results of present study (black circles) and different literature data for PbS/OA QDs in toluene or hexane. The arrows define the limits where the PL QY of corresponding QD size (emission energy) could vary depending on the excitation photon energy or solution concentration. Taken from the paper V.

5.1.2.4 PL QY decrease due to aging and UV light illumination

Once the PL QY is maximized, we are faced with another problem, i.e. aging degradation of QD surface due to oxidation. The concentration dependence of air-stability of PbS/OA QDs stored in a darkness is presented in Fig. 5.6(a). After 13 days of storage the 2.4 nm QDs ($\lambda_{em} = 900$ nm) reveal absorption peak blue shift of 12 nm for 7.75 μM/L (0.25 mL/3 mL) while for the 3.3 nm QDs ($\lambda_{em} = 1136$ nm) it is only 4 nm for almost the same molar concentration 8 μM/L (0.4 mL/3 mL). Faster aging [Fig. 5.6(a)] of PbS/OA QDs suspended in toluene was reported by Liu et al.[120] for highly diluted solution (0.03 mL/3 mL) of even smaller QDs ($\lambda_{em} = 822$ nm). Therefore, we can state that our PbS/OA QDs reveal better air-stability for larger QD sizes. The same size-dependent stability trend was reported also for PbS/OA[121] and CdTe[122] QDs.

One can see in Fig. 5.6(a) that stability of suspensions is improving with an increase of QD concentration comparing PbS QD suspensions diluted in different concentrations but having the same size of QDs. This is in agreement with the hypothesis of the ligand adsorption-desorption equilibria mentioned in Sec. 5.1.2.1: the ligand is less stable in more diluted solutions and therefore the higher QD surface area is oxidized. In addition, the stability of smaller QDs is clearly more dependent on concentration which can be explained by their higher ligand desorption probability and consequently, more prone to oxidation surface.

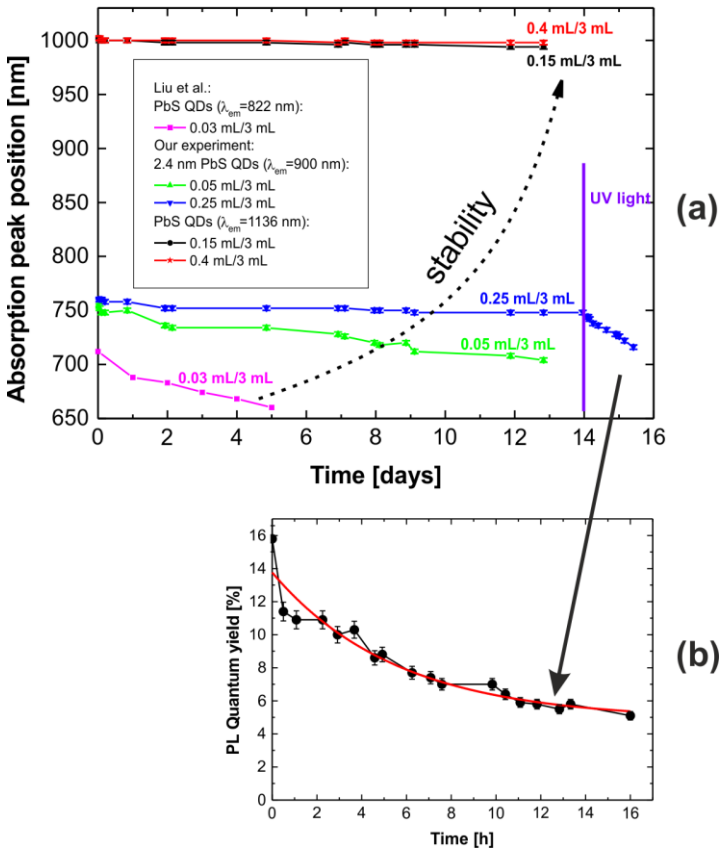

Figure 5.6. (a) The shift of absorption peak of OA-capped PbS QDs in toluene with different sizes and at different concentrations stored in darkness. The UV light marked region is related to the storage regime under continuous UV light illumination which accelerates degradation of PbS QDs. (b) The panel (taken from SI of the paper V) represents an exponential decrease of PL QY with duration of the UV illumination.

The aging process, i.e. QD surface oxidation and ligand degradation can be stimulated by UV light illumination. Figure 5.6(b) reveals accelerated blue shifting of absorption maximum of PbS QDs upon exposure to UV light (380 nm LED). The absorbed dose during one irradiation step was 9.8×10^{15} photons. This means the average absorption of 0.7 photon per single QD for a sample which contains 1.4×10^{16} QDs. Adsorbed oxygen molecules modify the surface and create new non-radiative trapping centers that reduces the PL QY. Therefore, one may see exponential dropping of PL QY upon UV illumination time [Fig. 5.6(b)].

In conclusion, larger QDs in higher concentrated suspensions proved better stability though one has to keep in mind the reabsorption effect for too concentrated samples. Also samples should be better stored in dark conditions to avoid stimulated surface aging of QDs.

5.1.3 PL transients of colloidal QDs

5.1.3.1 Spectrally resolved PL kinetics

Colloidal lead chalcogenide QDs possess extraordinary long (keeping into account the direct semiconductor nature) decay lifetimes from hundreds of nanoseconds to microseconds that is a few orders of magnitude longer as compared to *e.g.*, CdSe QDs. Such slow PL kinetics were reported previously for lead selenide[123,124] and lead sulfide[24,73,125,126] QDs. PL decays of PbS QDs are often mono-exponential[73,76,125]. PL decay lifetimes of Si QDs are significantly longer (because of indirect nature of silicon) of the order of tens to hundreds of microseconds[88] (paper II). PL kinetics of Si QDs are usually fitted by the SE function[88,127].

PL decay transients of PbS and Si QDs in toluene are presented in Fig. 5.7. Independently on the QD material, the curves can be fitted by the biexponential function [see Eq. (13)].

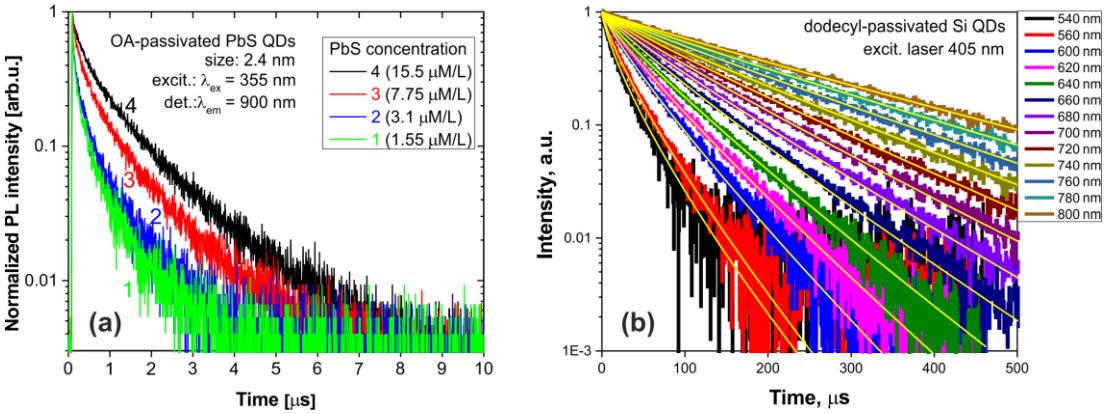

Figure 5.7. Time-resolved PL decay curves of 2.4 nm PbS (a) and 3.3 nm Si (b) QD suspensions at different concentrations (a) and emission energies (b). Left and right panels are taken from papers V and II, respectively.

In case of PbS QDs, the partial lifetimes τ_1 and τ_2 are in the range of 40 – 215 ns and 415 – 1240 ns, respectively. The biexponential decay with short and long components is quite typical for colloidal QDs[128] and was previously reported also for PbS QDs[24,129]. The shorter lifetime is generally attributed to the intrinsic radiative recombination of initially excited carriers in a QD core and the longer lifetime is believed to be related to involved surface-localized states. The fast lifetime component (~ 100 ns) was theoretically estimated for 3 nm diameter of PbS QDs in tetrachloromethane[76] and experimentally observed for PbS QDs in TCE and water[24]. This is in good agreement with our fast lifetime component and we believe it comes from the QD core (paper V). The long lifetime component is usually of the order of microseconds[24,129] and could be attributed to the recombination of spatially separated carriers in surface-localized states and core states[74]. Due to the poor overlap of

wavefunctions of these separated carriers the radiative lifetime is getting much longer[76]. Indeed, as it was shown recently the radiative surface sites could serve as efficient luminescent centers for strongly quantum confined PbS[74] or CdSe[130] QDs and do not necessarily cause PL quenching. The observation of broader homogeneous linewidth of PL spectra of single PbS QDs (discussed in the Sec. 5.1.1) can indicate the exciton trapping in surface states or defect sites[112].

The PL lifetime is getting shorter as the solution becomes more diluted as can be seen in Fig. 5.7(a). This is fully consistent with our previous observation of surface changes with concentration considered in Sec. 5.1.2.1. The enhanced oxidation of less concentrated samples partially eliminates luminescent surface states as result of concomitant surface passivation that suppresses the fraction of surface-related emission related to long PL lifetime component. In addition, the surface quality degrades because of newly introduced non-radiative quenching defects that also leads to the decay lifetime shortening.

The interpretation of partial components of decays from Si QDs is not straight forward because of the HLB effect (paper II) that will be considered in the next Sec. 5.1.3.2. This effect was neglected, when PbS QDs were considered, because the corresponding homogeneous linewidth is much narrower (even the ensemble linewidth is narrower than the homoheneous linewidth of Si QDs: $\Gamma_{ens}^{PbS} \sim 150\,\text{meV}$ against $\Gamma_{\text{hom}}^{Si} \geq 200\,\text{meV}$). As it will be shown in Sec. 5.1.3.2 the appearance of the fast component in addition to the main slow one at certain emission energies (primary sizes) of Si QDs can be due to a contribution of neighbor decays from QDs with close to primary sizes and thus, this additional mono-exponent does not have any further physical significance (paper II).

Besides biexponential fitting, PL transients presented in Fig. 5.7 of both PbS and Si QDs can be fitted also by the conventional SE function [see Eq. (12)]. In relation to this, it is important to note, that partial components in PL transients of PbS QDs do not necessarily both correspond to separate recombination channels as well. The appearance of the second component can be the result of a PL lifetime distribution in an ensemble of QDs. Dispersion parameter β is gradually decreasing as the solution becomes more diluted (0.62 – for 15.5 μM/L and 0.47 – for 1.55 μM/L). Again, this can be explained by the QD surface oxidation (less concentrated QDs are more prone to oxidation) that introduces new non-radiative channels and thus, increases the distribution of lifetimes (decreases the dispersion parameter). As result, the average decay lifetime is shorter for less concentrated QD solutions (1.3 μs – for 15.5 μM/L and 0.5 μs – for 1.55 μM/L).

Interestingly, PL lifetimes of PbS and Si QDs depend on QD size in a contrary way. Thus, the lifetime is shortening for smaller Si QDs [Fig. 5.7(b), Fig. 5.9(a)] while it is getting longer for PbS QDs[76,131] (not shown here) as the size is decreasing.

5.1.3.2 Size-selected PL kinetics

Here it is important to distinguish spectrally resolved and size-selected decays. Under the spectrally resolved decay [see Fig. 5.7(b)] we mean a decay measured at a certain photon energy (wavelength), whereas the size-selected decay is related to TR dynamics of QDs having a certain size. Figure 5.8 illustrates the difference between spectrally resolved and size-selected PL. When a spectrally resolved PL intensity is probed (slit selection in Figure 5.8), it is in fact a convolution of some distribution of size-selected PL.

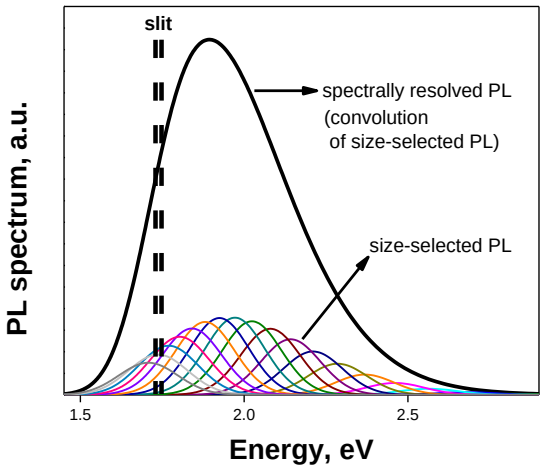

Figure 5.8. Simulated partial size-selected PL spectra (color curves) convolute in the PL emission spectrum of the whole ensemble of QDs (black curve). Thus, spectrally resolved PL experimental measurements (presented by a slit of certain bandwidth) probe many partial sizes of QDs simultaneously.

It is extraordinary complex problem to retrieve size-selected decays from spectrally resolved ones as the unique physical information about individual contributions is lost in ensemble transients. Indeed, even in the (hypothetic) case that spectrally resolved PL decay is measured using a spectrometer with an infinitely narrow slit at a detection energy E_{det}, there is a contribution from QDs of different sizes to the measured signal (because of the broad emission line of even a single QD).

One may try to approach this problem mathematically under a certain set of assumptions. Thus, Sangghaleh et al.[132] proposed a fitting-free procedure where it was a priori assumed that individual decays are mono-exponential and therefore 100% efficient. Later we introduced a novel procedure (paper II) to resolve size-selected decays without this assumption. Though we supposed that dependences of both spectrally resolved and size-selected SE fitting parameters on energy are described by the same functions that was supported by the quality of simulated decay curve fits. A set of spectrally resolved PL decay data of colloidal Si QDs measured at different

emission energies E_{det} is shown in Fig. 5.7(b). The values of average PL lifetimes $\tau_{PL}(E_{\text{det}})$ and dispersion factors $\beta_e(E_{\text{det}})$ at different E_{det} were obtained from the corresponding SE fits [see Eq. (12)] and are presented in Fig. 5.9. Both of them are increasing exponentially with increasing size of QDs until $E_{\text{det}} = 1.5$ eV. Then a steep decrease (below $E_{\text{det}} = 1.4$ eV) of $\beta_e(E_{\text{det}})$ is observed for bigger QD sizes.

The corresponding size-selected decays were deconvoluted mathematically and the corresponding intrinsic average PL lifetimes $\tau_{PL}(E)$ and $\beta(E)$ are presented in Fig. 5.9. More details on the procedure of deconvolution can be found in the paper II appended to this thesis.

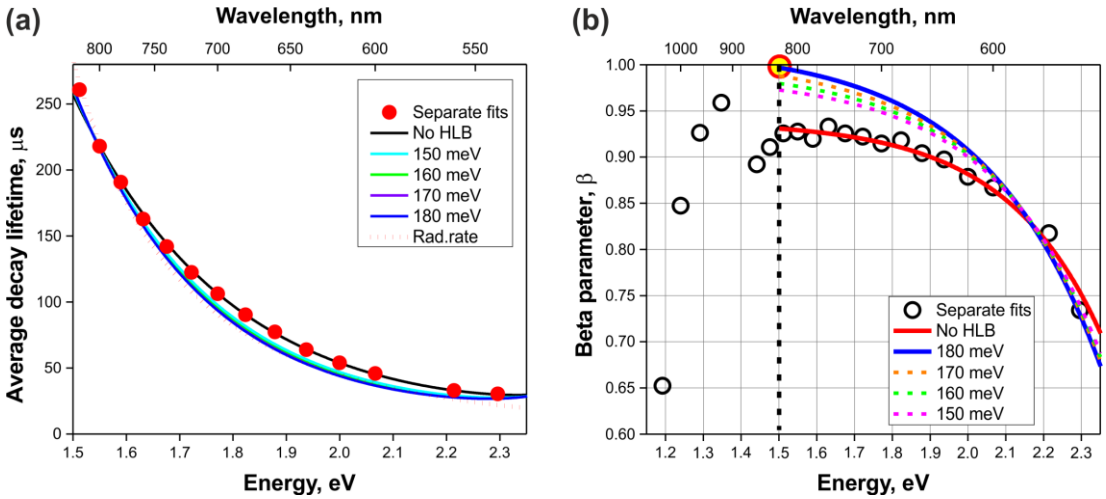

Figure 5.9. Spectral distribution of average PL decay lifetimes (a) and dispersion factors (b) obtained from separate SE fits (red dots) compared to the values retrieved for different values of standard deviations ω_{hom} in Gauss fit of single QD (solid lines). Taken from the paper II.

Dispersion factors of size-selected decays are gradually increasing with size increase [Fig. 5.9(b)] and reach the value near unity at $\varepsilon = 1.5$ eV. The fact that size-selected $\beta(E)$ are higher than spectrally resolved $\beta_e(E_{\text{det}})$ is expected as the partial overlap of different individual decays introduces more lifetime dispersion and eventually decrease of the dispersion factor $\beta_e(E_{\text{det}})$. Considering the standard deviation of Gaussian fit [see Fig. 5.1(a)] of single QD $\omega_{\text{hom}} = 180$ meV we proved that $\beta(1.5\,\text{eV}) \approx 1$ which means that size-selected decay at this energy is mono-exponential. This indicates the lack of dispersion in lifetimes for the corresponding size of QDs. The most straight forward explanation of this fact is the absence of any competitive non-radiative channels and, therefore, Si QDs of the corresponding size [4 nm $\leq d <$ 4.5 nm, see Fig. 5.1(b) and Fig. 5.9(b)] should be considered as fully radiative (i.e. 100% efficient) with monodisperse decay lifetime. To conclude,

properly synthesized monodisperse Si QDs of that size could find practical applications in extremely efficient new generation of nanophotonic devices.

5.2 Optical study of SRON Si QDs

5.2.1 PL emission spectra of Si QDs

In this section we will illustrate and compare optical properties of Si QDs embedded in SiO_xN_y (SRON) multilayers (ML) and in colloidal suspension (described above in Sec. 5.1).

In contrast to colloidal Si QDs, the inhomogeneous PL linewidth from an ensemble of SRON Si QDs is relatively narrow[49] (FWHM ~ 250 meV) and is a little broader than the homogeneous PL linewidth (FWHM ~ 210 meV) from a single Si QD in a colloidal suspension (Fig. 5.10). The PL spectrum of SRON Si QDs is well fitted by the lognormal function. This is somehow expected (see appended paper X) if to keep into account the lognormal distribution of QD sizes[91]. Besides that, PL emission of SRON Si QDs is significantly redshifted in comparison with colloidal ones (see Fig. 5.10).

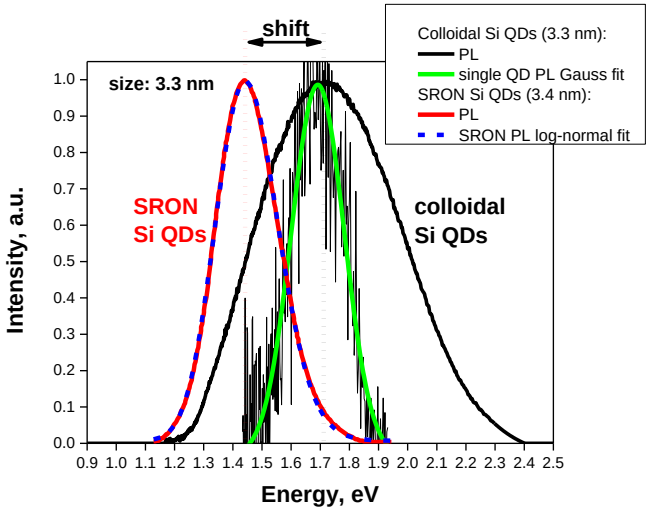

Figure 5.10. Illustration of the significant spectral shift between PL emission spectra of colloidal Si QDs (black and green lines) and Si QDs in SRON sample with similar mean size 3.3–3.4 nm.

The dependence of PL peak position on QD size [Fig. 5.11(b)] was retrieved from known[133] dependences of the optical bandgap and QD size on SiO_xN_y layer thickness [Fig. 5.11(a)]. The dependence of a PL peak position on QD size can be well described by Eq. (41) shifted by 2.1 nm along the *x*-axis:

$$E_{g,Si}^{em}(d[\mathrm{nm}]) = \sqrt{E_{b,Si}^2 + \frac{19.2\ \mathrm{eV}^2\times\mathrm{nm}^2}{(d+2.1\ \mathrm{nm})^2}} \tag{42}$$

The PL shift in matrix-embedded QDs was suggested[134] to arise from compressive strains that are exerted on QDs by SiO_2 matrix. Again, the Eq. (42) confirms the QC effect in SRON Si QDs.

SRON samples provide higher density of Si QDs and extreme stability (no aging for years) in comparison with colloidal ones. The position of PL peak of our dodecyl-passivated Si QDs in dependence on QD size is practically identical with H- and alkyl-capped Si QDs [see Fig. 5.11(b)].

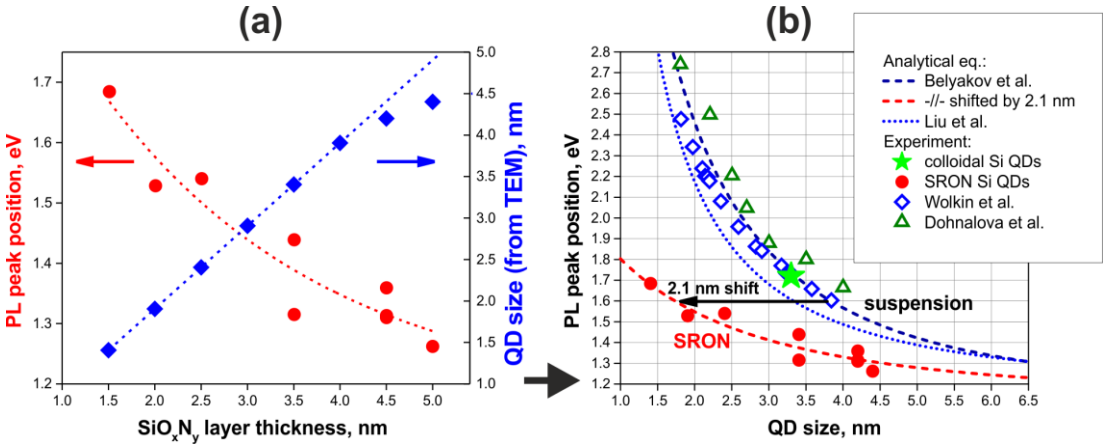

Figure 5.11. (a) PL peak position and QD size as a function of SRON layer thickness (data are taken from Ref. [133]) Dashed blue (linear fit) and red (exponential fit) lines are used to calculate results presented in (b) – red data. (b) Dependence of PL peak position on QD size for colloidal (non-oxidized) samples, namely H-capped (Wolkin et al.[79]), alkyl-capped (Dohnalova et al.[135]) and dodecyl-capped (present study) Si QDs as well as solid (oxidized) SRON (red circles) samples [obtained from results in (a)]. Dashed blue and red lines are according to Eq. (41) and Eq. (42), respectively, dotted blue line is defined in Ref. [88].

To summarize, a comparison of matrix-embedded and colloidal Si QDs reveal that its optical properties cannot be described by focusing on the intrinsic QC properties of QDs only. Clearly the matrix (surrounding)[58] and surface passivation[29,60] play an important role in luminescence.

5.2.2 PL intensity versus excitation power in ML samples

According to kinetic depopulation model (mentioned in Sec. 4.3) the PL amplitude I_{PL}^0 depends (paper I) on excitation power I_{ex} as:

$$I_{PL}^0(I_{ex}) = \frac{N_b I_{ex}\sigma/\tau_r}{1/\tau_{PL}(I_{ex}) + I_{ex}\sigma + I_{ex}^2\sigma^2\tau_A} \tag{43}$$

where σ describes the cross-section for absorption of photons, $\tau_{PL}(I_{ex})$, τ_r and τ_A stand for PL decay, radiative and Auger lifetime, respectively.

At low excitation powers ($I_{ex}\sigma \ll 1/\tau_{PL} \ll 1/\tau_A$) the Eq. (43) represents linear dependence of steady state PL intensity on excitation power that corresponds to zone 1 in Figure 5.12 (blue region):

$$I_{PL}^{0}(I_{ex}) = N_b I_{ex}\sigma\tau_{PL}(I_{ex})/\tau_r(I_{ex}) \tag{44}$$

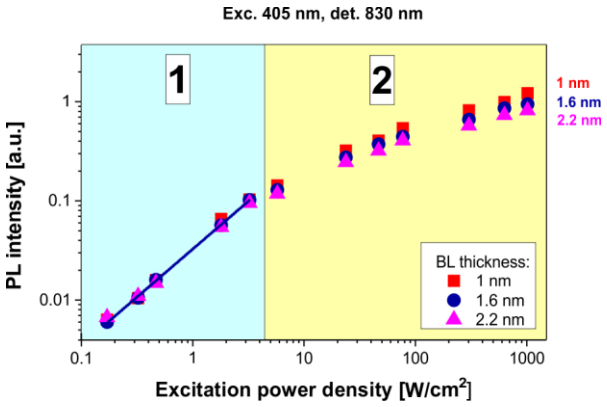

Figure 5.12. PL intensity amplitude under continuous-wave excitation as a function of the excitation photon flux for SRON samples with 1 nm (squares), 1.6 nm (circles) and 2.2 nm (triangles) oxide barrier thickness. Taken from the paper I.

The function in Eq. (43) should tend to saturate at moderate excitation powers ($I_{ex}\sigma \ll 1/\tau_A$):

$$I_{PL}^{0}(I_{ex}) = \frac{N_b I_{ex}\sigma/\tau_r(I_{ex})}{1/\tau_{PL}(I_{ex}) + I_{ex}\sigma} \tag{45}$$

In high power regime ($I_{ex}\sigma \gg 1/\tau_{PL}$) the Auger part ($I_{ex}^2\sigma^2\tau_A$) in Eq. (43) that cannot be neglected any more should lead to slight decrease of PL amplitudes under strong excitation:

$$I_{PL}^{0}(I_{ex}) = \frac{N_b/\tau_r(I_{ex})}{1 + I_{ex}\sigma\tau_A} \tag{46}$$

Indeed, this behavior was observed in ML samples studied under pulsed excitation[136]. However, under continuous wave excitation the complete saturation is never achieved (Fig. 5.12–5.13). De Jong et al. attributed[136] the increase of PL above the expected saturation point to the laser-induced heating of Si QDs embedded in oxide matrix. Another model to explain this phenomena is based on the assumption that allows radiative recombination from biexcitons[137] (two e-h pairs in a QD). For now the solution of this problem is still opened and further investigations in this direction are needed to reveal the truth. It must be noted that Eq. (43) and Eq. (46) are uniquely derived within this work and to the best of our knowledge have never been published in literature.

Figure 5.13 represents normalized PL intensities of both SL and ML samples in dependence on excitation power while the sample temperature is varied. As the excitation power increases, the difference between curves clearly become more pronounced.

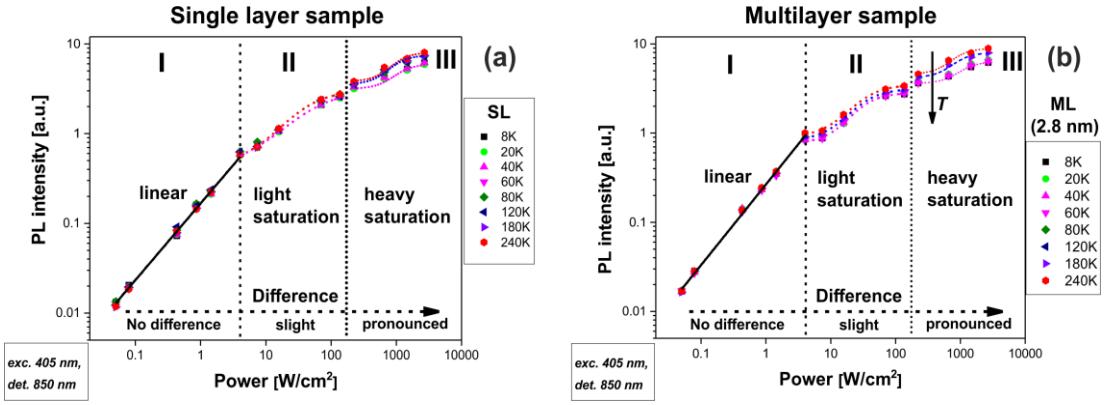

Figure 5.13. Normalized PL intensity versus excitation power density for single- (200 nm of $SiO_{1.1}N_{0.22}$) and multilayer SRON samples (4.5 nm of $SiO_{0.93}N_{0.23}$ and 2.8 nm of SiO_2 spacer) for a set of different temperatures. Region I represents linear regime (below saturation), while regions II and III are in power regime above the saturation point. Dashed and dotted lines serve as an eye guide and are obtained by logistic fittings.

5.2.3 PL transients of ML samples

PL decay kinetics of SRON samples under excitation below the saturation power density (which is about 1 W/cm^2 for Si QDs in the SiO_2 matrix) generally can be described by three-exponential decay fits [see Eq. (13)]. When excitation power increases above the saturation point, four-exponential decay fits or a combination of mono- and stretched exponential decay (MSE) fits must be applied (see Fig. 5.14).

In Figure 5.15(a) a typical spectral lifetime dispersion of Si QDs in ML samples is presented. One may notice a certain maximum around $E^* \approx 1.2$ eV that corresponds to the slowest spectrally resolved decay in the ensemble. For the energies above E^* the lifetime is shortening with photon energy increase in agreement with the QC model. For energies lower than E^* the lifetime is shortening with energy decrease up to the corresponding bulk energy bandgap. Below this bandgap the lifetime reaches approximately a constant value.

An increase of excitation power results in exponential decrease of both onset (ON) and decay (PL) lifetimes [Fig. 5.15(b)]. However, there is a change of the lifetime decrease slope near the PL saturation level [blue/yellow border in Fig. 5.15(b)] that indicates the appearance of an additional mode (Auger recombination) in the decay process for pumping above the saturation threshold (yellow zone).

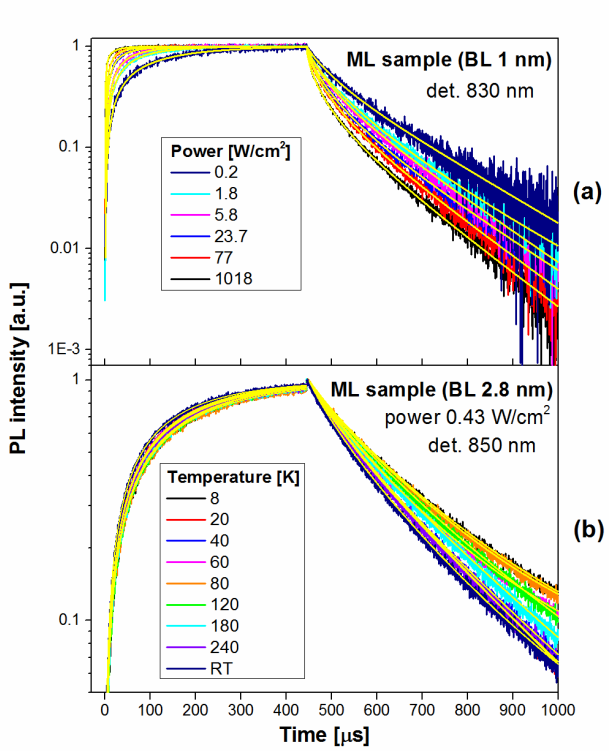

Figure 5.14. PL transients with corresponding fits [Eq. (13–14)] of multilayer SRON samples with 1 nm (a) and 2.8 nm (b) barrier thicknesses detected at 830 nm (a) and 850 nm (b) and excited by square pulses as a function of a) power density at RT and b) temperature at constant power below saturation. Taken from the paper I.

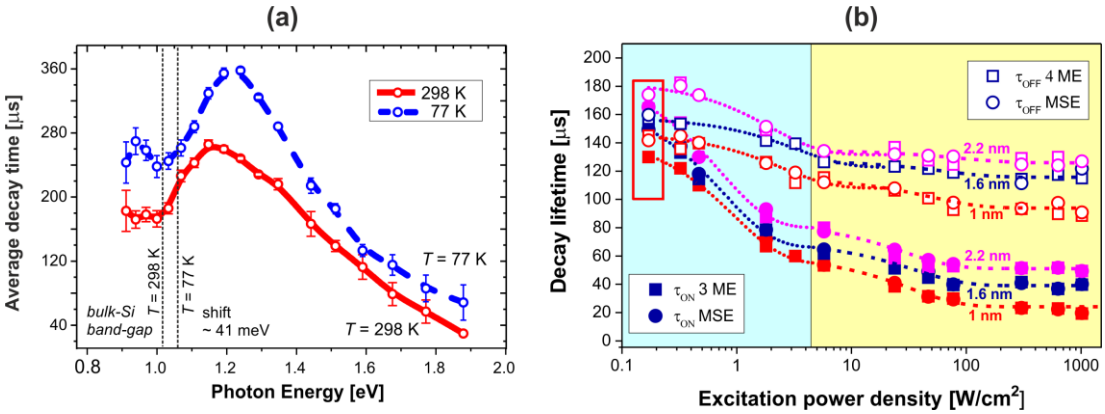

Figure 5.15. Dependence of spectrally resolved average decay times of SRON samples on (a) emission photon energy (after the paper VI) at 77 (red circles) and 294 K (blue circles) and on (b) excitation power density (after the paper I) for ML samples with different spacer thicknesses. Dashed lines in (a) indicate the bulk Si band-gap for corresponding two temperatures and dashed/dotted lines in (b) represent exponential fits in linear (dotted lines, blue area) and above saturation (dashed lines, yellow area) regions. The lifetimes are obtained by 2 ME (a) and 3–4 ME (b) or MSE (b) fitting models using Eq. (13–14).

Beside the τ_r-dominant interval[138] of temperatures (T < 70 K), a shortening of decay lifetimes with an increase of the temperature is observed [Fig. 5.14(b)] that is due to thermally activated τ_{nr} non-radiative processes.

There is also a dependence of lifetimes on the QD separation distance (paper I). Thus, the lifetime is increasing as the barrier thickness increases (Fig. 5.16).

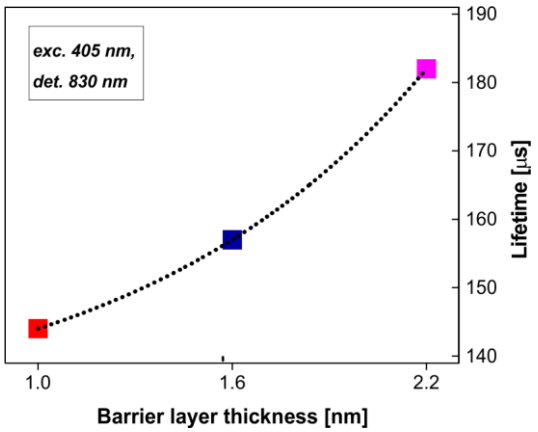

Figure 5.16. The dependence of extracted PL lifetime (see Sec. 4.2.2–4.3) on spacer thickness x in SRON samples. The dotted line is an eye guide from exponential fit. Taken from the paper I.

The following hypotheses can be considered to explain the phenomena:

a) The variation in the effective medium (matrix with other QDs)[106] can result in longer lifetimes for better separated QDs due to a change of PF[52].
b) A possible laser-induced heating[136] of QDs embedded in SiO_2 can result in shortening of radiative lifetime. Therefore, as the barrier thickness decreases, the effective temperature of QDs is increasing, because more energy is accumulated and dissipated in a smaller volume of the sample. Consequently, that leads to shorter decay lifetimes and lower values of PL QY [Fig. 5.20(b)].

However, those points themselves cannot explain the variation of both ACS and PL QY in dependence on barrier thickness. Therefore, in Sec. 5.2.7 we introduce two more points that can also explain the variation of lifetime in Fig. 5.16.

5.2.4 **Optical absorption cross-section of ML samples**

ACS directly reflects the probability of optical transitions and is defined as the ratio[106] of photon absorption rate for single QD and photon flux which in fact provides a relationship[139] between the QD concentration and the sample optical density. Therefore, if the absolute value of ACS is determined, the concentration of QDs in a studied sample can be directly probed by measuring the optical absorption coefficient[107]. Besides this, ACS is related to the transition oscillator

strength and therefore, is a very useful parameter for a variety of theoretical calculations as it defines an upper limit of the exciton radiative lifetime of a QD[139].

The ACS of nanostructured materials deviates from the respective bulk materials near the band edge when QC effect plays a role. In its turn, the ACS values of indirect bandgap semiconductor QDs[100] are much lower[45] than that reported for the direct bandgap ones[139] at the same absorption energy.

The filled symbols in Fig. 5.17(a) represents the ACS that was calculated according to the PL modulation technique described in Sec. 4.3 and in the appended publications I and VII. By definition ACS is related only to the absorption wavelength and in principle, should not be dependent on emission wavelength of a QD. The apparent emission-wavelength dependence of ACS [Fig. 5.17(a)] is a result of a size distribution (inhomogeneous broadening) in an ensemble of QDs that leads to ACS dispersion. Therefore, the ACS $\sigma(\lambda_{exc}, \lambda_{em})$ should be considered as a function of both excitation λ_{exc} and emission λ_{em} wavelengths[100], where λ_{em} corresponds to a size-selected fraction of QDs in the ensemble.

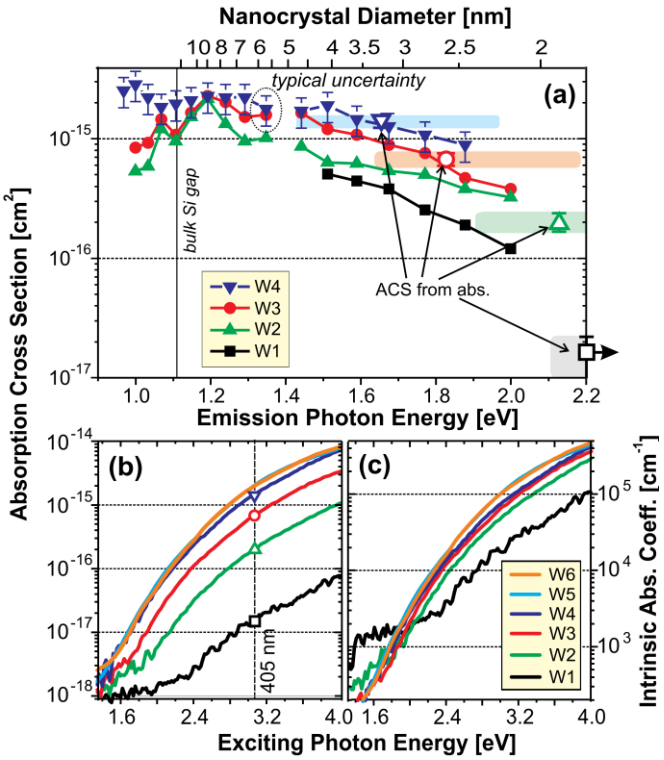

Figure 5.17. (a) ACS (determined via PL-modulation technique) plotted as function of emission photon energy for SRON samples with different thickness of Si-rich layers (nominally, W1 – 1.5 nm, W2 – 2.5 nm, W3 – 3.5 nm, W4 – 4.5 nm) and 2 nm SiO_2 spacer. Open symbols show ACS values obtained via absorption at 405 nm and plotted here at corresponding position of the mean QD size with indicated halfwidth of the size distribution (light rectangles). Non-normalized (b) and normalized to the mean QD volume (c) ACS spectra calculated from absorbance and morphology data. Taken from the paper VII.

The decrease of QD size results in momentum relaxation of carriers that should lead to an increase of the absorption probability of an excitation photon (enhancement of the oscillator strength). At the same time, a size reduction is the reason of a decrease of DOS according to QC model (see Fig. 2.3) that should lower the ACS. Therefore, the ACS is a product of two competitive effects and in case of QDs is not trivial. In that logic the modulation of DOS with QD size seems to affect ACS stronger than the oscillator strength because the ACS is decreasing with an increase of emission energy [Fig. 5.17(a)].

As it was mentioned in Sec. 5.2.2, the saturation model cannot describe well our experimental data and thus, only linear PL regimes are exploited in ACS determination by PL modulation technique. Logically the question might arise whether the kinetic depopulation model is correct for the linear PL regime. To verify this we determined the ACS by another completely independent technique [Fig. 5.17(b)–(c)] that is based on measuring of absorbance by the photothermal deflection spectroscopy (PDS) combined with morphology information obtained by the high-resolution TEM (for details see appended paper VII). PDS experiment was done at Institute of Physics, Academy of Science. Thus, absorbance A that is logarithm[107] of the ratio of incident to transmitted light power corrected for reflection and scattering losses (here the natural logarithm labeled as A_e is used):

$$A_e = \alpha d = \sigma c_V d = \sigma c_A \tag{47}$$

where α is the absorption coefficient, c_V and c_A are the molar concentration and area density of absorbing QDs, respectively.

Figure 5.17(b) demonstrates the ACS values obtained from the absorbance and the morphology data [using Eq. (47)]. There is a monotonous increase of ACS values $\sigma(\lambda_{exc})$ with increasing absorbed photon energy[100] and the ACS decrease $\sigma(\lambda_{em})$ for QDs with larger mean sizes. This can be due to decreasing volume of absorbing Si QDs. After dividing the ACS by the QD volume (this quantity is called intrinsic absorption coefficient μ_i) it becomes clear [see Fig. 5.17(c)] that for Si QDs with diameter larger than about 3 nm, all μ_i spectra are almost equal. For smaller QDs, μ_i values are reduced in agreement with Fig. 5.17(a).

In Figure 5.17(a) we compare results of the PL-modulation technique with ACS values obtained by absorption measurements. The PL emission wavelength is converted into QD diameter using calculation by Luo, Stradins, and Zunger[140]. Finally, absorption-derived ACS values are plotted (open symbols) at the position of the corresponding size-distribution peaks. We obtained perfect agreement of ACS from both methods for samples (W3 and W4) for which the real size distributions[91] are taken.

In principle, the two methods may reveal different values of ACS because one approach is related to extinction and the other to PL-excitation. Though, the direct comparison of ACS values obtained by two independent methods confirms that PL modulation technique is reliable and can be trustfully used for the ACS determination.

5.2.5 **PL QY of ML samples**

An example of PL QY excitation spectrum (all samples give very similar results) is presented in Fig. 5.18(a). For a semiconductor, one generally tends to expect a decrease in PL QY for excitation addressing higher states above the band gap as more non-radiative paths can be opened for relaxation of hotter carriers (see Sec. 5.1.2.2). We found only very weak variation of QY with excitation wavelengths for the studied samples, i.e., the KV rule is well fulfilled.

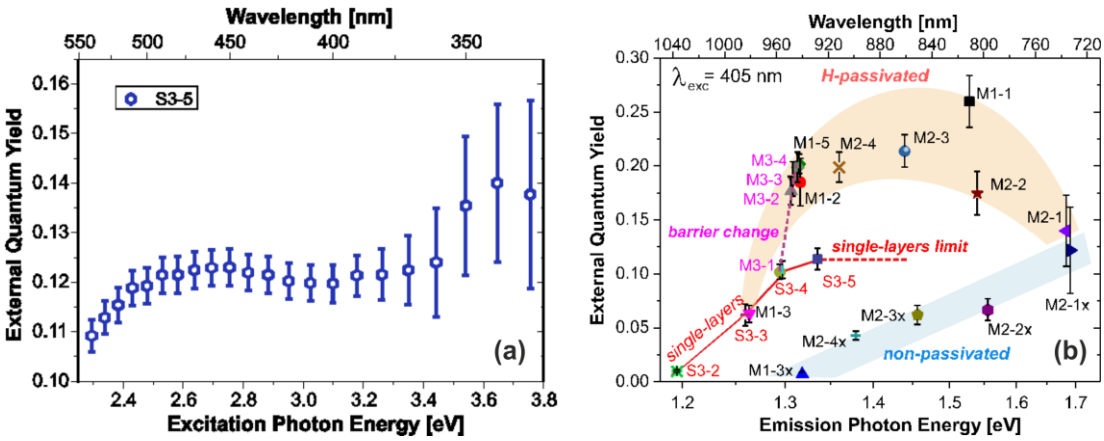

Figure 5.18. (a) PL QY excitation spectrum of single layer SRON sample measured under the tunable laser excitation at RT. (b) Summary of PL QY values (405 nm excitation) plotted versus PL peak photon energy for SRON samples. Taken from the paper VI.

The following characteristic features can be highlighted:

a) Over the green-blue-violet spectral region, the PL QY values are very uniform around 12%. The commonly observed rapid decrease toward lower photon energies (below 2.4 eV) is proposed to be due to preferred absorption into defect states. When approaching the band gap, the intrinsic absorption of Si QDs rapidly drops (paper VII), and the defect absorption becomes important. The presence of an exponential absorption tail in similar H-passivated samples was proved recently by PDS and associated with nonparamagnetic structural defects like Si-O-Si bridging bonds or distorted Si-Si bonds at the Si QD interface[141]. Similar decrease of QY at the long-wavelength edge was also observed in porous Si[142].

b) The increase of PL QY at high photon energies above 3.5 eV is within the experimental error. In this ultraviolet spectral region, the sensitivity of the CCD detector drops rapidly, which makes the overall sensitivity calibration extremely difficult and increase the experimental uncertainty. Otherwise, such an increase of EQY may be related to any effects of carrier multiplication, like the so called space-separated quantum cutting (SSQC) – i.e., generation of two excitons after absorption of a single photon using Auger mechanism of energy

transfer between excitons[118]. However, the precision of our experiment in the UV region does not allow to prove that SSQC effect (that is still under debate) takes place in our samples.

Figure 5.18(b) represents PL QY as a function of PL emission energy for many SRON samples under the study. The sample description can be found in the appended paper VI. It seems that there is a limit of about 12% for SL samples. The observed QY maximum from ML samples is around 27%.

From Figure 5.18(b) we extract the following main parameters to maximize the PL QY:

- ✓ the optimum size of QDs is about 3.5–4 nm (which gives PL peak around 810-850 nm, see Sec. 5.4);
- ✓ the oxide barrier thickness must be at least 2 nm (see Sec. 5.2.7);
- ✓ the stoichiometry of the deposited SRON layer must be around $x \approx 1$;
- ✓ the best possible defect passivation by H_2 post-annealing has crucial importance.

The absolute values of PL QY of SRON Si QDs are still at least two times lower than typical QY values (50–70%) of dodecyl-capped Si QDs[87,88,132].

5.2.6 IQE of Si QDs in ML samples

From Eq. (25) and Eq. (26) it follows that one has to separate radiative and non-radiative contributions to the PL decay in order to get information on IQE. Here we propose an approach to estimate IQE via comparison of decay kinetics of ML samples with dodecyl-passivated Si QDs suspension in toluene described in Sec. 5.1.3. The later reveal IQE close to unity (see Sec. 5.1.3.2). Further we will treat SRON layers as SiO_2 layers, where we assume that the presence of nitrogen does not change too much the dielectric permittivity of the oxide. In assumption[132] that all kinds of Si QDs have the same spectrally-selected radiative rate in a vacuum, and approximating size-selected decays by spectrally resolved ones, we have:

$$\frac{k_r^{tol}(E)}{F_{tol}^{P}(E)} = \frac{k_r^{SiO_2}(E)}{F_{SiO_2}^{P}(E)} \tag{48}$$

where $k_r^{tol}(E)$, $F_{tol}^{P}(E)$ and $k_r^{SiO_2}(E)$, $F_{SiO_2}^{P}(E)$ are radiative rates and PFs in toluene and in silica, respectively.

Figure 5.19(b) represents PL spectra and decay lifetimes of Si QDs in ML samples and in toluene. We proved (for details see appended paper II) that EFA theoretical calculations of radiative lifetime approximate well the average decay time of colloidal Si QDs down to about 1.5 eV [Fig. 5.19(b)]. Therefore, assuming the colloidal sample as fully radiative, i.e. $k_r^{tol}(E) = k_{PL}^{tol}(E)$, we can rewrite the Eq. (25) using the Eq. (48):

$$\eta_I(E) = \frac{1}{1 - F^P_{SiO_2}(E) + F^P_{tol}(E) \times \dfrac{k^{SiO_2}_{PL}(E)}{k^{tol}_{PL}(E)}} \tag{49}$$

where $k^{tol}_{PL}(E)$ and $k^{SiO_2}_{PL}(E)$ are total decay rates in toluene and in silica, respectively.

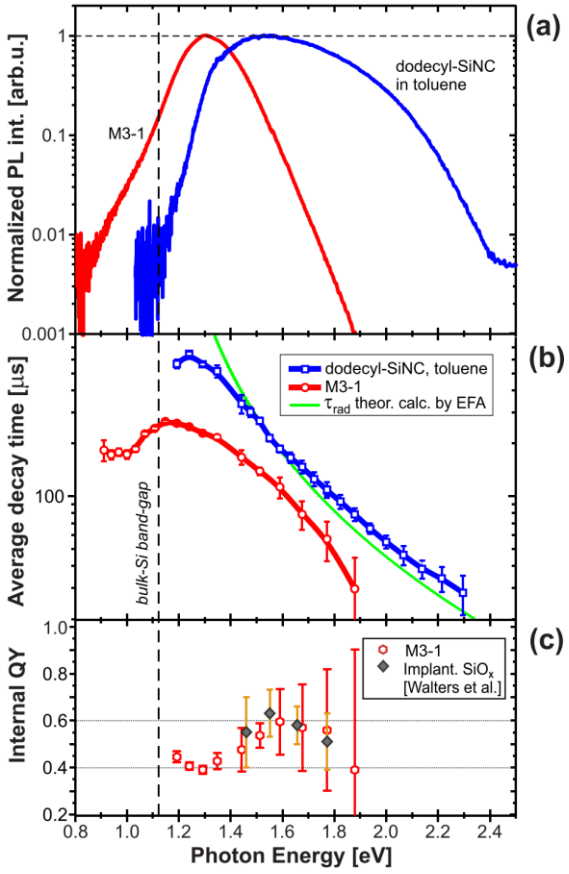

Figure 5.19. (a) Normalized PL spectra of SRON ML sample (red line) and dodecyl-passivated Si QD suspension (see Sec. 5.1.1) in toluene (blue line) at room-temperature. (b) Spectrally selected average decay times for the two samples compared with theoretical calculation of the radiative lifetime by the envelop function approximation (EFA) (green line, paper II). (c) Estimation of IQE for the SRON sample obtained as the ratio of red and blue data from panel (b). Data from Ref. [101] are given by gray rectangles. Taken from the paper VI.

By keeping into account that dielectric constant of nonpolar liquids is independent of frequency[143] ($\varepsilon^{toluene} = 2.38$) and using the high frequency dielectric constants 12 and 2.1 for Si and SiO_2, respectively, we obtain from Eq. (28) that $F^P_{tol} = 0.28$ and $F^P_{SiO_2} = 0.22$. Here, dielectric permittivities were considered as frequency-independent. The effective medium in the solid sample has higher dielectric constant due[106] to the close proximity of Si QDs. Using morphology data obtained by Gutsch et al.[91] we estimated the volume filling factor of Si to be 0.1 and according to the approach of Poddubny[106] the corresponding effective permittivity of SiO_2 increases

to about 2.4. That means that both media screen the field with approximately equal values of the PF.

Therefore, we estimated the "experimental" IQE $\eta_I^*(E)$ [see Fig. 5.19(c)] by Eq. (26) as $\eta_I^*(E) = k_r^{SiO_2}(E)/k_{PL}^{SiO_2}(E) = k_{PL}^{tol}(E)/k_{PL}^{SiO_2}(E)$. The maximum of IQE around 1.5–1.6 eV roughly corresponds to the PL QY maximum presented above in Fig. 5.18(b).

In its turn, "theoretical" IQE $\eta_I(E)$ can be obtained from $\eta_I^*(E)$ using Eq. (31) or Eq. (49) and keeping into account $F_{tol}^P \approx F_{SiO_2}^P \approx 0.28$. Taking the value in the peak of IQE $\eta_I^*(1.6\text{ eV}) = 60\%$, we get $\eta_I(1.6\text{ eV}) = 0.84$. This means that in a vacuum the peak of IQE of M3–1 sample is around $\eta_I(1.6\text{ eV}) = 84\%$ unlike 60% in the matter.

Important to note that above-presented calculations of PF in ML sample are very rough and do not keep into account the sample configuration[144,145,146,147]. Therefore the absolute values of $\eta_I^*(E)$ in Fig. 5.19(c) might serve only as a very rough estimation.

Surprisingly, our results of $\eta_I^*(E)$ agree well with calculations of $\eta_I(E)$ presented by Walters et al.[101] [gray squares in Fig. 5.19(c)]. We note that this coincidence must be considered as accidental as those two parameters are fundamentally different and cannot be directly compared.

5.2.7 The dependence of ACS and PL QY on T and inter-QD distance

Figure 5.20 represents the variation of ACS and QY in dependence on the barrier thickness and temperature of SRON samples. Besides τ_r-dominated temperature interval (T < 70 K), an increase in separation of inter-QD layers as well as decrease of sample temperature lead to an exponential decrease (increase) of ACS (QY).

By adjusting the stoichiometry parameter *x*, a thick SL sample has been prepared, which has almost the same shape of PL spectrum as the ML sample with 1 nm barrier [see insert in Fig. 5.20(b)]. This means that the size distribution of Si QDs in those samples are very similar and the only difference is the presence or absence of a SiO_2 spacer with variable thickness. It occurs that SL and ML (1 nm barrier) samples have almost the same value of PL QY (~10%).

Therefore, we can state that:

(i) The transition from a thick layer with Si QDs (containing random distributed QDs) to the well separated (> 2 nm) stack of confined layers increases the PL QY to approximately double value [Fig. 5.20(b)] and decreases (paper I) the ACS by factor 1.6;

(ii) The barrier of 1 nm or thinner becomes ineffective and the PL QY of ML structures is equal to those of the equivalent SL sample [Fig. 5.20(b)].

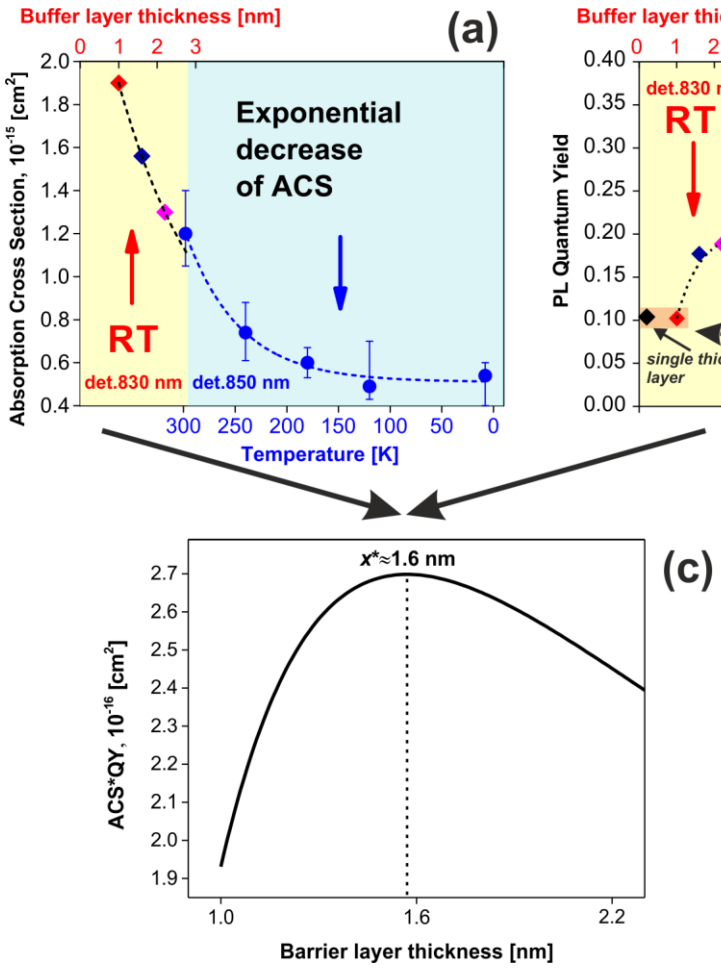

Figure 5.20. Dependences of ACS (a) and PL QY (b) of SRON samples on inter-QD distance and temperature. The insert in (b) represent PL spectra of SL and one of ML samples that are almost identical (and thus, PL QY for the samples is the same). (c) Illustration of determination of optimum inter-QD distance to maximize PL sample brightness as a peak of the product $\sigma(x)\cdot\eta^{*}(x)$ in its dependence on buffer layer thickness x [see Eq. (51)]. Part (c) is taken from the paper I.

The variation of ACS and PL QY on inter-QD distance can be explained by two hypotheses (that also address the variation of lifetimes considered in Sec. 5.2.3):

a) A lower number of defects for better separated QDs (which can be substantiated by higher QY [Fig. 5.20(b)] can result in longer lifetimes (see Sec. 5.2.3), lower DOS and thus lower ACS [Fig. 5.20(a)].

b) In presence of exciton migration (carrier hopping), a QD can be excited either directly through photon absorption or indirectly through an energy transfer from a nearby QD. Therefore, as QD separation decreases, the hopping lifetime, τ_{hop}, becomes shorter and, consequently, the decay lifetime decreases as well (see Fig. 5.16). Moreover, a system of interacting QDs works as antenna, because a QD can be excited either directly through photon absorption or indirectly through an exciton hopping from a nearby QD. Therefore, an ACS enhancement is expected in samples with thinner barriers where the interaction

is taking place. At the same time, an energy transfer from smaller to bigger QDs can result in a decrease of PL QY because of different emission efficiencies of those QDs as well as Auger recombination in double excited QDs (optically and by exciton transfer).

Figure 5.20(a)–(b) show almost two-times decrease (increase) of ACS (QY) when the temperature is varied from RT to 120 K. This variation of ACS and PL QY with temperature ($T \leq 120$ K) can be approximated by an exponential function:

$$z(T) = z_0 + Ce^{-(T-T_0)/\Delta T} \tag{50}$$

where z_0, T_0, C and Δx are vertical offset and horizontal shift, amplitude and characteristic temperature, respectively.

The variation of ACS with T is due to two reasons:

(i) The occupation number of phonons that participate in photon-assisted transitions is a function of temperature;

(ii) The band gap of a QD shifts in dependence on temperature that leads to changes of DOS at a certain energy.

Important to note that for $T > 120$ K the ACS of the SL sample in comparison with the ML (2.8 nm barrier thickness) sample is about. 1.6-times larger. For $T < 120$ K the ACS values for both SL and ML samples are almost the same. A similar tendency is observed for PL QY that is approximately the same for both SL and ML samples at $T < 100$ K (see paper IX). At $T = 120$ K the PL QY reaches its maximum of about 32% [Fig. 5.20(b)].

Above 120 K the decrease of PL QY with increasing T is more pronounced for the SL sample. This observation suggests that the difference in PL QY between SL and ML (> 1 nm barrier) samples at RT is thermally activated.

In assumption that both IQE ($\eta_I^* = \tau_{PL}/\tau_r$) and PL QY ($\eta = N_{em}/N_{abs}$) scale with the barrier thickness x in the same way, i.e. the fraction of bright QDs N_{em} does not depend on x, the Eq. (44) can be modified at the low-excitation limit as:

$$I_{PL}(x) \sim N_T I_{ex} \sigma(x) \eta_I^*(x) \tag{51}$$

By using $\sigma(x)$ and $\eta(x)$ dependences presented in Fig. 5.20(a)–(b), we can approximate the ACS and QY by an exponential function:

$$y(x) = y_0 + Ae^{-(x-1\,\mathrm{nm})/\Delta x} \tag{52}$$

where y_0 is an offset, A is an amplitude and Δx is a characteristic distance.

For applications we usually wish to maximize the PL brightness of a sample at certain I_{ex}. As the inter-QD distance becomes larger, the PL intensity $I_{PL}(x)$ is a product of a competitive decrease of ACS and increase of QY. Therefore, there is an optimum barrier thickness that maximize the function presented in Eq. (51) and for our ML structures it is approximately $x^* \approx 1.6$ nm [see Fig. 5.20(c)].

5.3 The fraction of dark/bright Si QDs

The fraction of dark/bright QDs in an ensemble is a value that is extremely difficult to assess experimentally because there is no procedure yet that allows to probe this number directly. Here is an attempt to summarize an estimated fraction of bright QDs and IQE values of Si QDs in solid and liquid samples at different temperatures:

a) Both SL and ML SRON samples mentioned in Sec. 5.2.7 have maximum of PL QY of ~35% at T = 120 K [Fig. 5.20(b)]. As there is no difference between SL and ML samples at this T (see paper IX) one may assume that the observed EQY is limited by non-radiative losses of excitation in dark QDs while IQE of bright QDs $\langle \eta^* \rangle = \eta_I^*$ is equal[102] to 100%. Important to note that in that case $\eta_I^* = \eta_I = 100\%$ (see Sec. 4.4). Then the average fraction of bright QDs at T = 120 K can be estimated by using the Eq. (37) as $N_b / N_{abs} = 35\%$.

b) The ML sample considered in Sec. 5.2.6 reveals the PL QY $\eta_E \approx 10\%$ [see Fig. 5.18(b)], while the IQE $\eta_I^*(E)$ is varied between 40–60% [see Fig. 5.19(c)] and the average IQE can be estimated about $\eta_I^* \approx 50\%$. Therefore, the average fraction of bright QDs at RT in the ensemble is $N_b / N_{abs} = 0.1/0.5 = 20\%$.

In a) we assumed that $\eta_I^*(120\ \mathrm{K}) = 100\%$. Indeed, modifying the Eq. (44), we obtain:

$$I_{PL}^0(T) = N_b(T) I_{ex} \sigma(T) \eta_I^*(T) \ \Rightarrow \ \eta_I^*(T) = \frac{I_{PL}^0(T)}{N_b(T)\sigma(T)} \tag{53}$$

In Sec. 5.2.7 we demonstrated that the ratio $I_{PL}^0(T)/\sigma(T)$ increases approximately twofold when the sample is cooled from RT down to ~120 K. Assuming that the fraction of bright QDs N_b is T-independent and keeping into account that $\eta_I^*(300\ \mathrm{K}) \approx 50\%$ we obtain doubling of the IQE value up to $\eta_I^*(120\ \mathrm{K}) = \eta_I(120\ \mathrm{K}) = 100\%$ with the decrease of temperature.

c) As was shown above in Sec. 5.1.3.2, IQE of colloidal sample approaches unity on the broad interval of emission energies. In its turn we obtained the value of PL QY to be near 60% that is in agreement with some samples presented in the work by Sangghaleh *et al.*[132]. Consequently, the lower limit of the fraction of bright QDs is approximately estimated as $N_b / N_{abs} = 60\%$. That is 2–3 times larger than in solid (a and b points) samples.

5.4 The optimum size of Si QDs

One of the central points of this work is the conclusion that the maximum at 1.45 – 1.55 eV in PL efficiency of Si QDs presented in Fig 5.18(b) is universal for all ensembles of Si QDs including colloidal[32,87,88,148] and matrix-embedded[149] Si QDs as well as B and P doped[150] Si QDs. A similar magic size was observed also in CdSe QDs[151].

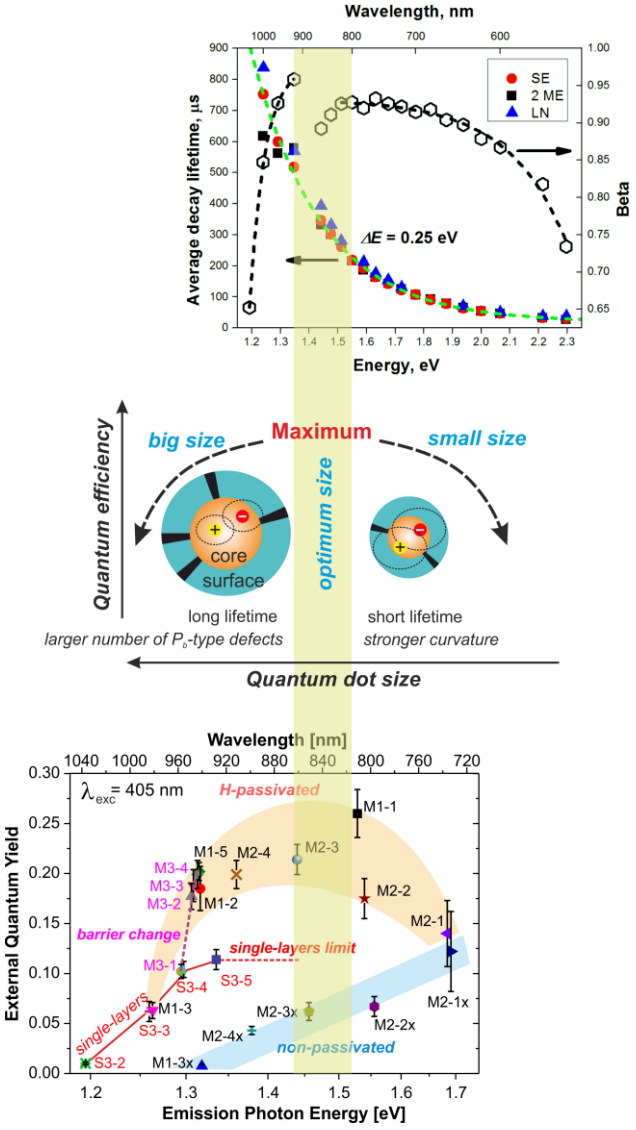

Figure 5.21. Schematic representation of a decrease of quantum efficiency (both external and internal – here is illustrated by dispersion parameter) for both larger and smaller sizes than the optimum size of Si QDs. The upper panel is taken from the paper II and lower panel is a duplicate of figure 5.18.

We showed in Sec. 5.1.3.2 that the peak spectral position of the dispersion parameter β is located [see Fig. 5.9(b) and Fig. 5.21] near the values of energies

(~ 1.5 eV), i.e. QDs with the corresponding sizes reveal the lowest dispersion in lifetime distribution.

One of the possible reason of this phenomena is explained in Fig. 5.21. Our experiments show (paper VI) that the number of PL-quenching P_b-type defects is increasing as the QD size becomes larger. That can explain the PL efficiency quenching for larger QDs (emitting below 1.4 eV).

It is somehow more challenging to interpret a decrease of PL efficiency for smaller QDs (emitting above 1.5 eV). This behavior is observed for both IQE[103] and PL QY and therefore, cannot be attributed to a varying fraction of dark QDs. Thus, Miura et al.[102] reported IQE growth with increasing size of Si QDs that ultimately reaches 100% for QDs emitting in a limited energy range (1.45–1.5 eV). A new type of interface defects can be the result of stronger curvature for smaller QDs and consequently, more poor passivation leading to higher probability of surface trapping of the exciton and subsequent PL quenching (see Fig. 5.21).

To summarize, the real origin of the existence of optimum size in an ensemble of QDs is still not proven and further experiments must be done to uncover the nature of the discussed phenomena.

Chapter 6

Conclusions and outlook

6.1 Conclusions

This PhD thesis presents a comprehensive study and advanced optical characterization of ensembles of direct (PbS) and indirect (Si) QDs. The primary aim of this work was to gain an insight on some fundamental problems (listed in Introduction) in QD ensembles as well as quantify important optical parameters that are difficult to assess experimentally. Almost all spectroscopic experiments (except PDS data) were performed at Charles University in Prague.

In this work we made a proper comparison of optical properties of certain size (3.3 nm) colloidal suspensions of Si QDs with both colloidal solutions of PbS QDs and matrix-embedded Si QDs of corresponding equal sizes.

PL spectra of QD (both PbS and Si) suspensions in toluene unexpectedly revealed 3 peaks (Fig. 4.2) that was not easy to explain. On the early stages of the research we thought it is originated from QD agglomerates, but then it became clear that there are two dips (instead of peaks) related to the absorption of toluene (Sec. 4.1). We demonstrated (Sec. 5.1.1) a spectral shift of PL peak position in dependence on QD size and material (PbS or Si) that supports QC effect (Sec. 2.1). Another strong argument that PL is originated from QC excitons is size-dependent variation of lifetimes for all investigated QDs. TR studies of QD ensembles in toluene reveal (Fig. 5.7) either strongly non-exponential PL decays of PbS QDs in ns-range or near-exponential (Fig. 6.1(a)) decays of Si QDs in μs-range.

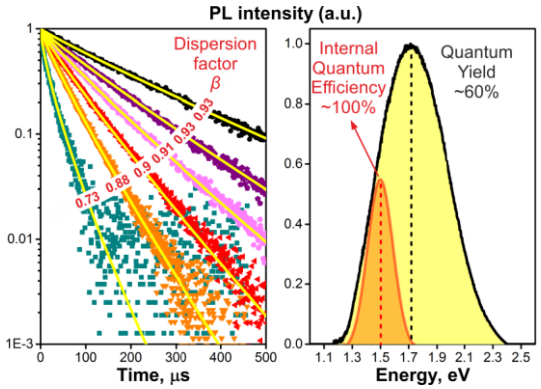

Figure 6.1. Left panel: Spectrally resolved PL decays of colloidal Si QDs detected at different energies. Right panel: PL spectrum of the ensemble of colloidal Si QDs with PL QY about 60% and schematic partial PL spectrum of single size QDs in the ensemble with IQE about 100%.

6.1.1 **Ensembles of PbS QDs**

We have studied absolute PL QY of OA-capped PbS colloidal QDs in toluene in dependence on excitation and emission (QD size) wavelengths, QD concentration and conditions of storage. To maximize PL QY we recommend to deal with diluted enough solutions of rather small PbS QDs while near-resonant energy excitation should be preferably chosen.

As it was mentioned in Introduction, the stability of QD colloidal solution is a crucial parameter for a device fabrication. Our investigations clearly point out the important role of surface states for relaxation processes. We demonstrate that larger QDs in higher concentrated suspensions (revealing rather low PL QY) are less prone to surface oxidation and hence, proved better stability in comparison with smaller QDs and less concentrated suspensions. Thus, we observed anomalous decrease of QY with decreasing concentration for highly diluted suspensions. The ligand desorption and QD-oxidation are shown to be responsible for this phenomenon. Excess of oleic acid in suspensions makes the QY values concentration-independent over the entire reabsorption-free range. Moreover, UV light illumination leads to enhanced photo-oxidation processes in OA-capped surface of PbS QDs and exponential decrease of PL QY with UV exposure time. To summarize, PL QY and stability of PbS QD solutions are competitive in their dependence on QD size and concentration. Therefore, there must be an optimum concentration of a certain (optimum) size of PbS QDs when both QY and stability are maximized.

TR studies (Sec. 5.1.3.1) of PbS QDs revealed PL decays that can be fitted by biexponential or SE functions. This suggests either two separate decay processes (recombination in the QD core or through involved surface-localized states) or a lifetime distribution in an ensemble of PbS QDs. We showed that the lifetime distribution is broadening as QD solution becomes more diluted. This can be explained by the QD surface oxidation (less concentrated QDs are more prone to oxidation) that introduces new non-radiative channels. As result, the average decay lifetime becomes shorter for less concentrated QD solutions (Fig. 5.7).

These results definitely give better understanding of the optical properties of PbS/OA QDs and can be used for fabrication of the brightest and most stable QDs.

6.1.2 **Ensembles of Si QDs**

6.1.2.1 Properly developed theoretical and experimental background

To provide advanced optical characterization of samples it was necessary to develop both theoretical and experimental backgrounds for this work:

✓ **Fundamentals of TR PL analysis (papers IV and X)**

In the framework of this study we developed a proper TR PL analysis that resulted in writing of the paper IV and the Review (appended paper X).

In paper IV:

a) Optimum TR PL experimental parameters were derived to find a compromise between signal saturation, truncation, and quality (Sec. 4.2.1).

b) We showed up that unlike common erroneous believe, the measured decay lifetime distribution is, in general, dependent on the excitation pulse length as a direct consequence of different onset dynamics! Moreover, we derived the short- and long-pulse limits as 0.1 times the shortest lifetime in the distribution and 3 times the longest time, respectively. Outside these limits the decay lifetime distribution is independent on the pulse duration (but different!). In this work we study lifetimes in the long-pulse limit.

In paper X:

a) We theoretically analyze the most common cases of mono-exponential PL decays (homogeneous ensemble of non-interacting QDs and isolated individual QDs) and demonstrate why inhomogeneous ensemble of QDs is non-exponential. Using probability density function in the form of both continuous and discrete distribution of rates (lifetimes) and Laplace transform we provide treatment of mono-, stretch- (SE) and multi-exponential (ME) as well as lognormal (LN) PL decay models and some complex cases. This brings better understanding of physics of decay processes.

b) Under certain assumptions we derive SE PL signal from SE population relaxation kinetics. We underline that the first derivative of SE function, which is often used in literature for PL decay fitting describes the total intensity decay rather than experimentally probed PL decay.

c) We explicitly show the difference between intensity average (average decay) $\bar{\tau}$ and amplitude-average $\langle\tau\rangle$ lifetimes. There is accumulating number of publications where these terms are misused and therefore, the understanding of the fundamental difference between $\bar{\tau}$ and $\langle\tau\rangle$ is of great practical importance to its proper use in diverse conditions. In this work only intensity average lifetimes $\bar{\tau}$ were calculated.

d) We derive expressions to calculate precisely or approximately the average decay lifetimes for some common decays (Sec. 4.2.2). Eq. (20) was uniquely derived within this work. These expressions were practically used for data treatment throughout this PhD thesis.

✓ **PL modulation technique (papers I and VII)**

Within this work we uniquely derived the general solution [Eq. (43)] of the kinetic depopulation model (Sec. 4.3 and Sec. 5.2.2) as well as an analytical limit for the high power regime [Eq. (46)]. We demonstrated that the model fails to describe

the PL intensity dependence of ML structures on excitation power at strong pumping above the expected saturation limit (see Sec. 5.2.2). Though we proved that this model, which is commonly applied for ACS determination, is correct on the linear regime of excitation powers which was not shown in former reports (see Sec. 5.2.4). Moreover, from detailed time-resolved studies we show up the dependence of decay lifetime on excitation power (see Sec. 5.2.3) that must be kept into account (see Sec. 4.3) for the correct determination of ACS by PL modulation approach. Thereby, the proper use of the technique which is commonly incorrectly applied is finally presented.

- ✓ **Procedure to deconvolute size-selected decays from spectrally resolved ones (paper II)**

  Within this work (Sec. 5.1.3.2) we developed the unique mathematical procedure to resolve size-selected decays from experimentally measured spectrally resolved decays. Thanks to this it became possible to retrieve 100% efficient size fraction of Si QDs in colloidal ensemble of nearly fully-radiative QDs at RT [see Fig. 6.1(b)]. The obtained results were supported by EFA theoretical calculations and subsequently used in calculations of IQE of ML samples.

- ✓ **"Experimental" and "theoretical" IQE**

  For the first time we propose (see Sec. 4.4) to distinguish two principally different IQE definitions, namely **"theoretical"** η_I (related to lifetimes in a vacuum) and **"experimental"** η_I^* (related to lifetimes in an environment). Intermixing those values in literature causes a lot of misunderstanding and wrong conclusions. We derived the analytical interconnection between η_I and η_I^*, calculated the relative difference in dependence on different parameters and considered the limits when these two values are equal. These results are completely unique and have never been published yet.

- ✓ **The fraction of bright QDs in an ensemble**

  We derive the general equation [Eq. (37)] that allows to estimate the fraction of bright QDs in an ensemble and interconnects spectrally integrated external (quantum yield) and internal quantum efficiencies. This derivation is done within this work and has never been published in literature.

6.1.2.2 Highlights of main results related to Si QDs

Above developed powerful fundamental knowledge was applied to study ensembles of Si QDs in solid and liquid samples. The main results are summarized:

- ✓ **Si QDs in solid vs liquid environment**

  The comparison of PL peak position of Si QDs in ML samples and in toluene reveals a pronounced PL shift that underlines the role of matrix and the QD surface in PL emission process (see Sec. 5.2.1). Though we clearly register dependences of PL peak position and decay lifetime on QD size, the QC model itself obviously cannot fully explain optical properties of QDs. Down to very small sizes (~2 nm) silicon remains an indirect semiconductor that leads to relatively slow PL transients of the S-band: from tens to hundreds of μs. In contrast to dodecyl-passivated Si QDs, the kinetics of Si QDs in ML structures are strongly non-exponential and this property becomes more pronounced with an increase of excitation power (see Sec. 5.2.3).

- ✓ **ACS and PL QY vs excitation & emission wavelengths in ML samples (papers VI, VII and IX)**

  Based on the above-developed PL modulation technique and the PDS experiment we analyzed (Sec. 5.2.4) the ACS $\sigma(\lambda_{exc}, \lambda_{em})$ as a function of both excitation λ_{exc} and emission λ_{em} (certain size) wavelengths. The typical value of calculated ACS of ML samples is around 10^{-15} cm^2 for Si QDs with mean diameters between 3 and 5 nm. For smaller QDs, the ACS values are lower. The ACS is decreasing as excitation wavelength λ_{exc} becomes longer.

  The typical value of measured PL QY for ML samples at RT was about 10–20%. We propose optimum configuration parameters and experimental conditions to maximize the PL QY (see Sec. 5.2.5). The PL QY is sensitive mostly to the thickness of PL active layer [layer with QDs and oxide barrier layer] and to the passivation procedures (annealing in H_2 dramatically improves the QY). We found the maximum of PL QY of about 27% in well-passivated ML samples with a Si QD size of about 4 nm and a SiO_2 barrier thickness of 2 nm or larger. PL QY of SL samples is upper-limited near 12%. We found only slight variations of PL QY in dependence on excitation wavelength [Fig. 5.18(a)].

- ✓ **ACS and PL QY vs inter-QD distance & temperature in ML samples (papers I and IX)**

  Our results indicate that unlike common believe, the ACS depends on inter-QD distance and sample temperature (see Sec. 5.2.7). This observation is far from being trivial and was never reported in literature up to now. In its turn, PL QY varies in dependence on mentioned parameters in an opposite way as compared to ACS. Thus, roughly doubling the barrier thickness (from ~1 to 2.2 nm) decreases the ACS by factor 1.6 and increases the PL QY to approximately double value (from 10 to 19%). Therefore, we point out and estimate an optimum separation distance in ML structures (~1.6 nm for our samples) to maximize PL brightness that can be helpful for the construction of efficient luminescent devices. In

addition, decay lifetime is shortening (Fig. 5.16) with a decrease of inter-QD spacing. The large variation of ACS, PL QY and lifetime values with barrier thickness is attributed to a modulation of either defect population states or of the efficiency of energy transfer between confined QD layers.
With temperature decrease (from RT down to 120 K) we observe an exponential decrease of the ACS that can be explained by smaller occupation number of phonons and expansion of the bandgap of Si QDs at low temperatures. In contrast, PL QY reaches its maximum (T = 120 K) of about 32%. Comparing SL and ML samples at different temperatures we uncovered thermally-activated processes in Si QDs that lead to PL QY reduction at RT.

- ✓ **IQE vs temperature (papers VI and IX)**

  IQE is a parameter that is extremely difficult to assess experimentally. By employing the above-mentioned deconvolution procedure (Sec. 5.1.3.2) we proved that some fraction of Si QDs in colloidal ensemble emitting near 1.5 eV is fully radiative (IQE is 100%) even at RT. These results were used for calculations of IQE in solid samples. Thus, average IQE η_I^* of SRON sample at RT was estimated to be about 50%. At sufficiently low temperature (T ≈ 120 K) we show that IQE is likely reaching unity (for all ML samples).

- ✓ **Bright and dark QDs in an ensemble (papers II, VI and IX)**

  In spite of extremely high IQE (near unity), the PL QY of Si QDs in the solution does not exceed 60%. This pronounced difference between PL QY and IQE can be explained (Sec. 5.3) by the presence of dark QDs in the colloidal ensemble $(n_d < 40\%)$ that is about two-times less than the corresponding fraction of dark Si QDs in ML structures ($n_d \approx 70-80\%$).

- ✓ **Magic size of Si QDs in an ensemble (papers II and VI)**

  We point out (Sec. 5.4) that independently on the form of nanocrystalline silicon, there exist an optimum size of QDs (emitting near 1.45 – 1.55 eV) where both IQE and PL QY are maximized.

We believe that presented detailed study brings a deeper insight into the origin of PL of Si QDs in both solid and liquid samples and builds a strong solid background for further applied scientific research to implement the results in photonic and/or photovoltaic devices.

6.2 Outlook

Clearly, the stability of studied colloidal PbS QDs particularly when being exposed to UV light is not yet enough for real applications. Therefore, further studies should be focused on investigating the role of surface and experimenting with different types of passivating ligands (e.g. inorganic core/shell passivation[119,152]), doping[150] or incorporation of QDs in a polymer[153].

Though matrix-embedded Si QDs reveal superior stability, there is still a number of issues to be addressed in future studies:

a) What is the nature of spectral shift in PL maxima of Si QDs in solid and liquid samples? A combination of theoretical calculations with an experiment can be helpful.
b) What is the origin of broad homogeneous linewidth in colloidal ensembles of Si QDs? Rapidly developing single-dot techniques[44] are a promising way to find the answer.
c) Though experimentally measured PL decays of Si QDs resemble the shape of many mathematical models (SE, lognormal, etc.), the physical kinetic model is still unclear and is a matter of further investigations.
d) What is the mechanism generating additional photons above an expected value of saturation in intensity dependence on power? This problem was recently addressed in the paper by de Jong et al.[136] and was ascribed to sample heating during cw-excitation based on theoretical calculations. Additional experimental confirmation should be obtained to clarify this.
e) It might be interesting to try to fabricate[34] monodisperse fraction of Si QDs emitting near $1.45 - 1.55$ eV that corresponds to an optimum size in an ensemble (see Sec. 5.4). This should maximize IQE of an ensemble of Si QDs. The origin of this "magic" optimum size must be also investigated further.
f) It seems that in ensembles of matrix-embedded Si QDs the fraction of dark QDs dominates. Therefore, to increase PL from a sample, further efforts can be focused on understanding this phenomena and maximizing the fraction of bright QDs.
g) It is still a matter of debates whether there is or not any form of interaction (energy transfer) between Si QDs in solid samples. A proper experiment must be done to figure it out.

Bibliography

[1] Ekimov, A. I.; Onushchenko, A. A. Quantum Size Effect in the Optical-Spectra of Semiconductor Micro-Crystals. *Sov. Phys. Semicond.* **1982**, *16*, 775–778.

[2] Ekimov, A. I.; Efros, A. L.; Onushchenko, A. A. Quantum Size Effect in Semiconductor Microcrystals. *Solid State Commun.* **1985**, *56*, 921–924.

[3] Rossetti, R.; Nakahara, S.; Brus, L. E. Quantum Size Effects in the Redox Potentials, Resonance Raman Spectra, and Electronic Spectra of CdS Crystallites in Aqueous Solution. *J. Chem. Phys.* **1983**, *79*, 1086–1088.

[4] Reed, M.; Randall, J.; Aggarwal, R.; Matyi, R.; Moore, T.; Wetsel, A. Observation of Discrete Electronic States in a Zero-Dimensional Semiconductor Nanostructure. *Phys. Rev. Lett.* **1988**, *60*, 535–537.

[5] Klimov, V. *Nanocrystal Quantum Dots*; CRC Press, 2010.

[6] Kovalenko, M. V.; Manna, L.; Cabot, A.; Hens, Z.; Talapin, D. V.; Kagan, C. R.; Klimov, V. I.; Rogach, A. L.; Reiss, P.; Milliron, D. J.; *et al.* Prospects of Nanoscience with Nanocrystals. *ACS Nano* **2015**, *9*, 1012–1057.

[7] Pichaandi, J.; van Veggel, F. C. J. M. Near-Infrared Emitting Quantum Dots: Recent Progress on Their Synthesis and Characterization. *Coord. Chem. Rev.* **2014**, *263–264*, 138–150.

[8] Tang, J.; Sargent, E. H. Infrared Colloidal Quantum Dots for Photovoltaics: Fundamentals and Recent Progress. *Adv. Mater.* **2011**, *23*, 12–29.

[9] Akhtar, J.; Azad Malik, M.; O'Brien, P.; Wijayantha, K. G. U.; Dharmadasa, R.; Hardman, S. J. O.; Graham, D. M.; Spencer, B. F.; Stubbs, S. K.; Flavell, W. R.; *et al.* A Greener Route to Photoelectrochemically Active PbS Nanoparticles. *J. Mater. Chem.* **2010**, *20*, 2336.

[10] Zhao, T.; Goodwin, E. D.; Guo, J.; Wang, H.; Diroll, B. T.; Murray, C. B.; Kagan, C. R. Advanced Architecture for Colloidal PbS Quantum Dot Solar Cells Exploiting a CdSe Quantum Dot Buffer Layer. *ACS Nano* **2016**, *10*, 9267–9273.

[11] Sargent, E. H.; Konstantatos, G. *Colloidal Quantum Dot Optoelectronics and Photovoltaics*; Konstantatos, G.; Sargent, E. H., Eds.; Cambridge University Press: Cambridge, 2013.

[12] Rogach, A. L.; Eychmüller, A.; Hickey, S. G.; Kershaw, S. V. Infrared-Emitting Colloidal Nanocrystals: Synthesis, Assembly, Spectroscopy, and Applications. *Small* **2007**, *3*, 536–557.

[13] Sun, L.; Choi, J. J.; Stachnik, D.; Bartnik, A. C.; Hyun, B.; Malliaras, G. G.; Hanrath, T.; Wise, F. W. Bright Infrared Quantum-Dot Light-Emitting Diodes through Inter-Dot Spacing Control. *Nat. Nanotechnol.* **2012**, *7*, 369–373.

[14] Sanchez, R. S.; Binetti, E.; Torre, J. A.; Garcia-Belmonte, G.; Striccoli, M.; Mora-Sero, I. All Solution Processed Low Turn-on Voltage near Infrared LEDs Based on Core–shell PbS–CdS Quantum Dots with Inverted Device Structure. *Nanoscale* **2014**, *6*, 8551–8555.

[15] Hoogland, S.; Sukhovatkin, V.; Howard, I.; Cauchi, S.; Levina, L.; Sargent, E. H.

A Solution-Processed 1.53 Mm Quantum Dot Laser with Temperature-Invariant Emission Wavelength. *Opt. Express* **2006**, *14*, 3273.

[16] Wu, J.; Wang, Z. M. *Quantum Dot Solar Cells*; Wu, J.; Wang, Z. M., Eds.; Lecture Notes in Nanoscale Science and Technology; Springer New York: New York, 2014; Vol. 15.

[17] Luther, J. M.; Law, M.; Beard, M. C.; Song, Q.; Reese, M. O.; Ellingson, R. J.; Nozik, A. J. Schottky Solar Cells Based on Colloidal Nanocrystal Films. *Nano Lett.* **2008**, *8*, 3488–3492.

[18] Kim, G.-H.; Walker, B.; Kim, H.-B.; Kim, J. Y.; Sargent, E. H.; Park, J.; Kim, J. Y. Inverted Colloidal Quantum Dot Solar Cells. *Adv. Mater.* **2014**, *26*, 3321–3327.

[19] McDonald, S. A.; Konstantatos, G.; Zhang, S.; Cyr, P. W.; Klem, E. J. D.; Levina, L.; Sargent, E. H. Solution-Processed PbS Quantum Dot Infrared Photodetectors and Photovoltaics. *Nat. Mater.* **2005**, *4*, 138–142.

[20] Konstantatos, G.; Sargent, E. H. Solution-Processed Quantum Dot Photodetectors. *Proc. IEEE* **2009**, *97*, 1666–1683.

[21] Im, S. H.; Kim, H.; Seok, S. Il. Near-Infrared Responsive PbS-Sensitized Photovoltaic Photodetectors Fabricated by the Spin-Assisted Successive Ionic Layer Adsorption and Reaction Method. *Nanotechnology* **2011**, *22*, 395502.

[22] Shcherbatyuk, G. V; Inman, R. H.; Wang, C.; Winston, R.; Ghosh, S. Viability of Using near Infrared PbS Quantum Dots as Active Materials in Luminescent Solar Concentrators. *Appl. Phys. Lett.* **2010**, *96*, 191901.

[23] Aeberhard, U.; Vaxenburg, R.; Lifshitz, E.; Tomić, S. Fluorescence of Colloidal PbSe/PbS QDs in NIR Luminescent Solar Concentrators. *Phys. Chem. Chem. Phys.* **2012**, *14*, 16223.

[24] Hyun, B.; Chen; Rey, D. A.; Wise, F. W.; Batt, C. A. Near-Infrared Fluorescence Imaging with Water-Soluble Lead Salt Quantum Dots. *J. Phys. Chem. B* **2007**, *111*, 5726–5730.

[25] Turyanska, L.; Moro, F.; Knott, A. N.; Fay, M. W.; Bradshaw, T. D.; Patanè, A. Paramagnetic, Near-Infrared Fluorescent Mn-Doped PbS Colloidal Nanocrystals. *Part. Part. Syst. Charact.* **2013**, *30*, 945–949.

[26] Hines, M. A.; Scholes, G. D. Colloidal PbS Nanocrystals with Size-Tunable Near-Infrared Emission: Observation of Post-Synthesis Self-Narrowing of the Particle Size Distribution. *Adv. Mater.* **2003**, *15*, 1844–1849.

[27] Fucikova, A.; Valenta, J.; Pelant, I.; Kalbacova, M. H.; Broz, A.; Rezek, B.; Kromka, A.; Bakaeva, Z. Silicon Nanocrystals and Nanodiamonds in Live Cells: Photoluminescence Characteristics, Cytotoxicity and Interaction with Cell Cytoskeleton. *RSC Adv.* **2014**, *4*, 10334–10342.

[28] Canham, L. T. Silicon Quantum Wire Array Fabrication by Electrochemical and Chemical Dissolution of Wafers. *Appl. Phys. Lett.* **1990**, *57*, 1046–1048.

[29] Dohnalová, K.; Gregorkiewicz, T.; Kůsová, K. Silicon Quantum Dots: Surface Matters. *J. Phys. Condens. Matter* **2014**, *26*, 173201.

[30] Shirahata, N. Colloidal Si Nanocrystals: A Controlled Organic-Inorganic Interface and Its Implications of Color-Tuning and Chemical Design toward

Sophisticated Architectures. *Phys. Chem. Chem. Phys.* **2011**, *13*, 7284–7294.

[31] Li, Q.; He, Y.; Chang, J.; Wang, L.; Chen, H.; Tan, Y. W.; Wang, H.; Shao, Z. Surface-Modified Silicon Nanoparticles with Ultrabright Photoluminescence and Single-Exponential Decay for Nanoscale Fluorescence Lifetime Imaging of Temperature. *J. Am. Chem. Soc.* **2013**, *135*, 14924–14927.

[32] Mastronardi, M. L.; Maier-Flaig, F.; Faulkner, D.; Henderson, E. J.; Kübel, C.; Lemmer, U.; Ozin, G. A. Size-Dependent Absolute Quantum Yields for Size-Separated Colloidally-Stable Silicon Nanocrystals. *Nano Lett.* **2012**, *12*, 337–342.

[33] Miller, J. B.; Van Sickle, A. R.; Anthony, R. J.; Kroll, D. M.; Kortshagen, U. R.; Hobbie, E. K. Ensemble Brightening and Enhanced Quantum Yield in Size-Purified Silicon Nanocrystals. *ACS Nano* **2012**, *6*, 7389–7396.

[34] Brown, S. L.; Miller, J. B.; Anthony, R. J.; Kortshagen, U. R.; Kryjevski, A.; Hobbie, E. K. Abrupt Size Partitioning of Multimodal Photoluminescence Relaxation in Monodisperse Silicon Nanocrystals. *ACS Nano* **2017**, *11*, 1597–1603.

[35] Cheng, X.; Lowe, S. B.; Reece, P. J.; Gooding, J. J. Colloidal Silicon Quantum Dots: From Preparation to the Modification of Self-Assembled Monolayers (SAMs) for Bio-Applications. *Chem. Soc. Rev.* **2014**, *43*, 2680.

[36] Ghosh, B.; Shirahata, N. Colloidal Silicon Quantum Dots: Synthesis and Luminescence Tuning from the near-UV to the near-IR Range. *Sci. Technol. Adv. Mater.* **2014**, *15*, 14207.

[37] Dasog, M.; Kehrle, J.; Rieger, B.; Veinot, J. G. C. Silicon Nanocrystals and Silicon-Polymer Hybrids: Synthesis, Surface Engineering, and Applications. *Angew. Chemie Int. Ed.* **2016**, *55*, 2322–2339.

[38] Kortshagen, U. R.; Sankaran, R. M.; Pereira, R. N.; Girshick, S. L.; Wu, J. J.; Aydil, E. S. Nonthermal Plasma Synthesis of Nanocrystals: Fundamental Principles, Materials, and Applications. *Chem. Rev.* **2016**, *116*, 11061–11127.

[39] Cullis, A. . G.; Canham, L. T.; Calcott, P. D. J. The Structural and Luminescence Properties of Porous Silicon. *J. Appl. Phys.* **1997**, *82*, 909–965.

[40] Belyakov, V. A.; Burdov, V. A.; Lockwood, R.; Meldrum, A. Silicon Nanocrystals: Fundamental Theory and Implications for Stimulated Emission. *Adv. Opt. Technol.* **2008**, *2008*, 1–32.

[41] Saar, A. Photoluminescence from Silicon Nanostructures: The Mutual Role of Quantum Confinement and Surface Chemistry. *J. Nanophotonics* **2009**, *3*, 32501.

[42] Gusev, O. B.; Poddubny, A. N.; Prokofiev, A. A.; Yassievich, I. N. Light Emission from Silicon Nanocrystals. *Semiconductors* **2013**, *47*, 183–202.

[43] Barbagiovanni, E. G.; Lockwood, D. J.; Simpson, P. J.; Goncharova, L. V. Quantum Confinement in Si and Ge Nanostructures: Theory and Experiment. *Appl. Phys. Rev.* **2014**, *1*, 11302.

[44] Sychugov, I.; Valenta, J.; Linnros, J. Probing Silicon Quantum Dots by Single-Dot Techniques. *Nanotechnology* **2017**, *28*, 72002.

[45] Mazzaro, R.; Romano, F.; Ceroni, P. Long-Lived Luminescence of Silicon Nanocrystals: From Principles to Applications. *Phys. Chem. Chem. Phys.* **2017**,

19, 26507–26526.

[46] Pavesi, L. Will Silicon Be the Photonic Material of the Third Millenium? *. *J. Phys. Condens. Matter* **2003**, *15*, R1169–R1196.

[47] Priolo, F.; Gregorkiewicz, T.; Galli, M.; Krauss, T. F. Silicon Nanostructures for Photonics and Photovoltaics. *Nat. Nanotechnol.* **2014**, *9*, 19–32.

[48] Yang, D. *Handbook of Photovoltaic Silicon*; Yang, D., Ed.; Springer Berlin Heidelberg: Berlin, Heidelberg, 2017.

[49] Valenta, J.; Mirabella, S. *Nanotechnology and Photovoltaic Devices*; Pan Stanford, 2015.

[50] Nanocrystals in Their Prime. *Nat. Nanotechnol.* **2014**, *9*, 325–325.

[51] Meinardi, F.; Ehrenberg, S.; Dhamo, L.; Carulli, F.; Mauri, M.; Bruni, F.; Simonutti, R.; Kortshagen, U.; Brovelli, S. Highly Efficient Luminescent Solar Concentrators Based on Earth-Abundant Indirect-Bandgap Silicon Quantum Dots. *Nat. Photonics* **2017**, *11*, 177–185.

[52] Gaponenko, S. *Introduction to Nanophotonics*; Cambridge University Press: New York, 2010.

[53] Pelant, I.; Valenta, J. *Luminescence Spectroscopy of Semiconductors*; Oxford University Press: New York, 2012.

[54] Koole, R.; Groeneveld, E.; Vanmaekelbergh, D.; Meijerink, A.; de Mello Donegá, C. Size Effects on Semiconductor Nanoparticles. In *Nanoparticles*; Springer Berlin Heidelberg: Berlin, Heidelberg, 2014; pp. 13–51.

[55] Barbagiovanni, E. G.; Lockwood, D. J.; Simpson, P. J.; Goncharova, L. V. Quantum Confinement in Si and Ge Nanostructures. *J. Appl. Phys.* **2012**, *111*, 34307.

[56] Gaponenko, S. V. *Optical Properties of Semiconductor Nanocrystals*; Cambridge University Press: Cambridge, 1998.

[57] Bányai, L.; Koch, S. W. *Semiconductor Quantum Dots*; World Scientific, 1993; Vol. 2.

[58] Kůsová, K.; Hapala, P.; Jelínek, P.; Pelant, I. Band Structure of Silicon Nanocrystals. In *Silicon Nanophotonics: Basic Principles, Present Status, and Perspectives*; Pan Stanford Publishing Pte. Ltd., 2016; pp. 109–144.

[59] Talapin, D. V; Lee, J.; Kovalenko, M. V; Shevchenko, E. V. Prospects of Colloidal Nanocrystals for Electronic and Optoelectronic Applications. *Chem. Rev.* **2010**, *110*, 389–458.

[60] Sychugov, I.; Fucikova, A.; Pevere, F.; Yang, Z.; Veinot, J. G. C.; Linnros, J. Ultranarrow Luminescence Linewidth of Silicon Nanocrystals and Influence of Matrix. *ACS Photonics* **2014**, *1*, 998–1005.

[61] Donegá, C. de M. Synthesis and Properties of Colloidal Heteronanocrystals. *Chem. Soc. Rev.* **2011**, *40*, 1512–1546.

[62] Caram, J. R.; Bertram, S. N.; Utzat, H.; Hess, W. R.; Carr, J. A.; Bischof, T. S.; Beyler, A. P.; Wilson, M. W. B.; Bawendi, M. G. PbS Nanocrystal Emission Is Governed by Multiple Emissive States. *Nano Lett.* **2016**, *16*, 6070–6077.

[63] Trinh, M. T.; Limpens, R.; Gregorkiewicz, T. Experimental Investigations and Modeling of Auger Recombination in Silicon Nanocrystals. *J. Phys. Chem. C* **2013**, *117*, 5963–5968.

[64] Bruhn, B.; Limpens, R.; Chung, N. X.; Schall, P.; Gregorkiewicz, T. Spectroscopy of Carrier Multiplication in Nanocrystals. *Sci. Rep.* **2016**, *6*, 20538.

[65] Mustafeez, W.; Majumdar, A.; Vučković, J.; Salleo, A. A Direct Measurement of the Electronic Structure of Si Nanocrystals and Its Effect on Optoelectronic Properties. *J. Appl. Phys.* **2014**, *115*, 0–6.

[66] https://commons.wikimedia.org/wiki/File:Calcite-Galena-elm56c.jpg.

[67] https://commons.wikimedia.org/wiki/File:SiliconCroda.jpg.

[68] Madelung, O. *Semiconductors: Data Handbook*; Springer Berlin Heidelberg: Berlin, Heidelberg, 2004.

[69] Chelikowsky, J. R.; Cohen, M. L. Nonlocal Pseudopotential Calculations for the Electronic Structure of Eleven Diamond and Zinc-Blende Semiconductors. *Phys. Rev. B* **1976**, *14*, 556–582.

[70] Delerue, C.; Allan, G.; Lannoo, M. Theoretical Aspects of the Luminescence of Porous Silicon. *Phys. Rev. B* **1993**, *48*, 11024–11036.

[71] Zherebetskyy, D.; Scheele, M.; Zhang, Y.; Bronstein, N.; Thompson, C.; Britt, D.; Salmeron, M.; Alivisatos, P.; Wang, L.-W. Hydroxylation of the Surface of PbS Nanocrystals Passivated with Oleic Acid. *Science (80-.).* **2014**, *344*, 1380–1384.

[72] Weidman, M. C.; Beck, M. E.; Hoffman, R. S.; Prins, F.; Tisdale, W. A. Monodisperse, Air-Stable PbS Nanocrystals via Precursor Stoichiometry Control. *ACS Nano* **2014**, *8*, 6363–6371.

[73] Warner, J. H.; Thomsen, E.; Watt, A. R.; Heckenberg, N. R.; Rubinsztein-Dunlop, H. Time-Resolved Photoluminescence Spectroscopy of Ligand-Capped PbS Nanocrystals. *Nanotechnology* **2005**, *16*, 175–179.

[74] Fernée, M. J.; Thomsen, E.; Jensen, P.; Rubinsztein-Dunlop, H. Highly Efficient Luminescence from a Hybrid State Found in Strongly Quantum Confined PbS Nanocrystals. *Nanotechnology* **2006**, *17*, 956–962.

[75] Lewis, J. E.; Wu, S.; Jiang, X. J. Unconventional Gap State of Trapped Exciton in Lead Sulfide Quantum Dots. *Nanotechnology* **2010**, *21*, 455402.

[76] Ushakova, E. V; Litvin, A. P.; Parfenov, P. S.; Fedorov, A. V; Artemyev, M.; Prudnikau, A. V; Rukhlenko, I. D.; Baranov, A. V. Anomalous Size-Dependent Decay of Low-Energy Luminescence from PbS Quantum Dots in Colloidal Solution. *ACS Nano* **2012**, *6*, 8913–8921.

[77] de Boer, W. D. A. M.; Timmerman, D.; Dohnalová, K.; Yassievich, I. N.; Zhang, H.; Buma, W. J.; Gregorkiewicz, T. Red Spectral Shift and Enhanced Quantum Efficiency in Phonon-Free Photoluminescence from Silicon Nanocrystals. *Nat. Nanotechnol.* **2010**, *5*, 878–884.

[78] Luo, J.; Li, S.; Sychugov, I.; Pevere, F.; Linnros, J.; Zunger, A. Absence of Redshift in the Direct Bandgap of Silicon Nanocrystals with Reduced Size. *Nat. Nanotechnol.* **2017**, *12*, 930–932.

[79] Wolkin, M. V.; Jorne, J.; Fauchet, P. M.; Allan, G.; Delerue, C. Electronic States and Luminescence in Porous Silicon Quantum Dots: The Role of Oxygen. *Phys. Rev. Lett.* **1999**, *82*, 197–200.

[80] Kovalev, D. Silicon Photonics: Moving into the Red. *Nat. Nanotechnol.* **2010**, *5*, 827–828.

[81] Choi, H.; Ko, J.; Kim, Y.; Jeong, S. Steric-Hindrance-Driven Shape Transition in PbS Quantum Dots: Understanding Size-Dependent Stability. *J. Am. Chem. Soc.* **2013**, *135*, 5278–5281.

[82] Reilly, N.; Wehrung, M.; O'Dell, R. A.; Sun, L. Ultrasmall Colloidal PbS Quantum Dots. *Mater. Chem. Phys.* **2014**, *147*, 1–4.

[83] Cademartiri, L.; Bertolotti, J.; Sapienza, R.; Wiersma, D. S.; von Freymann, G.; Ozin, G. A. Multigram Scale, Solventless, and Diffusion-Controlled Route to Highly Monodisperse PbS Nanocrystals. *J. Phys. Chem. B* **2006**, *110*, 671–673.

[84] Moreels, I.; Justo, Y.; De Geyter, B.; Haustraete, K.; Martins, J. C.; Hens, Z. Size-Tunable, Bright, and Stable PbS Quantum Dots: A Surface Chemistry Study. *ACS Nano* **2011**, *5*, 2004–2012.

[85] Chen, S.; Liu, W. Oleic Acid Capped PbS Nanoparticles: Synthesis, Characterization and Tribological Properties. *Mater. Chem. Phys.* **2006**, *98*, 183–189.

[86] Basma, Z. El. Growth and Characterization of ZnO Nanostructures for Photovoltaic Applications, Lille University, 2012.

[87] Mangolini, L.; Jurbergs, D.; Rogojina, E.; Kortshagen, U. Plasma Synthesis and Liquid-Phase Surface Passivation of Brightly Luminescent Si Nanocrystals. *J. Lumin.* **2006**, *121*, 327–334.

[88] Liu, X.; Zhang, Y.; Yu, T.; Qiao, X.; Gresback, R.; Pi, X.; Yang, D. Optimum Quantum Yield of the Light Emission from 2 to 10 Nm Hydrosilylated Silicon Quantum Dots. *Part. Part. Syst. Charact.* **2016**, *33*, 44–52.

[89] Zacharias, M.; Heitmann, J.; Scholz, R.; Kahler, U.; Schmidt, M.; Bläsing, J. Size-Controlled Highly Luminescent Silicon Nanocrystals: A SiO/SiO2 Superlattice Approach. *Appl. Phys. Lett.* **2002**, *80*, 661–663.

[90] Hartel, A. M.; Hiller, D.; Gutsch, S.; Löper, P.; Estradé, S.; Peiró, F.; Garrido, B.; Zacharias, M. Formation of Size-Controlled Silicon Nanocrystals in Plasma Enhanced Chemical Vapor Deposition Grown SiOxNy/SiO2 Superlattices. *Thin Solid Films* **2011**, *520*, 121–125.

[91] Gutsch, S.; Hiller, D.; Laube, J.; Zacharias, M.; Kübel, C. Observing the Morphology of Single-Layered Embedded Silicon Nanocrystals by Using Temperature-Stable TEM Membranes. *Beilstein J. Nanotechnol.* **2015**, *6*, 964–970.

[92] Valenta, J. Determination of Absolute Quantum Yields of Luminescing Nanomaterials over a Broad Spectral Range: From the Integrating Sphere Theory to the Correct Methodology. *Nanosci. Methods* **2014**, *3*, 11–27.

[93] Leung, R. W. K.; Yeh, S.-C. A.; Fang, Q. Effects of Incomplete Decay in Fluorescence Lifetime Estimation. *Biomed. Opt. Express* **2011**, *2*, 2517.

[94] Jonscher, A. K.; Polignac, A. de. The Time Dependence of Luminescence in

Solids. *J. Phys. C Solid State Phys.* **1984**, *17*, 6493–6519.

[95] Lakowicz, J. R. *Principles of Fluorescence Spectroscopy*; Lakowicz, J. R., Ed.; Springer US: Boston, MA, 2006.

[96] Linnros, J.; Lalic, N.; Galeckas, A.; Grivickas, V. Analysis of the Stretched Exponential Photoluminescence Decay from Nanometer-Sized Silicon Crystals in SiO2. *J. Appl. Phys.* **1999**, *86*, 6128–6134.

[97] Van Driel, A. F.; Nikolaev, I. S.; Vergeer, P.; Lodahl, P.; Vanmaekelbergh, D.; Vos, W. L. Statistical Analysis of Time-Resolved Emission from Ensembles of Semiconductor Quantum Dots: Interpretation of Exponential Decay Models. *Phys. Rev. B - Condens. Matter Mater. Phys.* **2007**, *75*, 1–8.

[98] Chepic, D. I.; Efros, A. L.; Ekimov, A. I.; Ivanov, M. G.; Kharchenko, V. A.; Kudriavtsev, I. A.; Yazeva, T. V. Auger Ionization of Semiconductor Quantum Drops in a Glass Matrix. *J. Lumin.* **1990**, *47*, 113–127.

[99] Kovalev, D.; Heckler, H.; Polisski, G.; Koch, F. Optical Properties of Si Nanocrystals. *Phys. Status Solidi* **1999**, *215*, 871–932.

[100] Kovalev, D.; Diener, J.; Heckler, H.; Polisski, G.; Künzner, N.; Koch, F. Optical Absorption Cross Sections of Si Nanocrystals. *Phys. Rev. B* **2000**, *61*, 4485–4487.

[101] Walters, R. J.; Kalkman, J.; Polman, A.; Atwater, H. A.; de Dood, M. J. A. Photoluminescence Quantum Efficiency of Dense Silicon Nanocrystal Ensembles in SiO2. *Phys. Rev. B* **2006**, *73*, 132302.

[102] Miura, S.; Nakamura, T.; Fujii, M.; Inui, M.; Hayashi, S. Size Dependence of Photoluminescence Quantum Efficiency of Si Nanocrystals. *Phys. Rev. B* **2006**, *73*, 245333.

[103] Limpens, R.; Gregorkiewicz, T. Spectroscopic Investigations of Dark Si Nanocrystals in SiO2 and Their Role in External Quantum Efficiency Quenching. *J. Appl. Phys.* **2013**, *114*, 74304.

[104] Seo, J.; Fudala, R.; Kim, W.-J.; Rich, R.; Tabibi, B.; Cho, H.; Gryczynski, Z.; Gryczynski, I.; Yu, W. Hybrid Optical Materials of Plasmon-Coupled CdSe/ZnS Coreshells for Photonic Applications. *Opt. Mater. Express* **2012**, *2*, 1026–1039.

[105] Purcell, E. M. Spontaneous Emission Probabilities at Radio Frequencies. *Phys. Rev.* **1946**, *69*, 674.

[106] Poddubny, A. N. Local Field Corrections to the Spontaneous Emission in Arrays of Si Nanocrystals. *J. Opt.* **2015**, *17*, 35102.

[107] Hens, Z.; Moreels, I. Light Absorption by Colloidal Semiconductor Quantum Dots. *J. Mater. Chem.* **2012**, *22*, 10406–10415.

[108] Vial, J. C.; Bsiesy, A.; Gaspard, F.; Hérino, R.; Ligeon, M.; Muller, F.; Romestain, R.; Macfarlane, R. M. Mechanisms of Visible-Light Emission from Electro-Oxidized Porous Silicon. *Phys. Rev. B* **1992**, *45*, 14171–14176.

[109] Moreels, I.; Lambert, K.; Smeets, D.; De Muynck, D.; Nollet, T.; Martins, J. C.; Vanhaecke, F.; Vantomme, A.; Delerue, C.; Allan, G.; *et al.* Size-Dependent Optical Properties of Colloidal PbS Quantum Dots. *ACS Nano* **2009**, *3*, 3023–3030.

[110] Yu, Y.; Fan, G.; Fermi, A.; Mazzaro, R.; Morandi, V.; Ceroni, P.; Smilgies, D.-

M. .; Korgel, B. A. Size-Dependent Photoluminescence Efficiency of Silicon Nanocrystal Quantum Dots. *J. Phys. Chem. C* **2017**.

[111] Schlegel, G.; Bohnenberger, J.; Potapova, I.; Mews, A. Fluorescence Decay Time of Single Semiconductor Nanocrystals. *Phys. Rev. Lett.* **2002**, *88*, 137401.

[112] Peterson, J. J.; Krauss, T. D. Fluorescence Spectroscopy of Single Lead Sulfide Quantum Dots. *Nano Lett.* **2006**, *6*, 510–514.

[113] Fernée, M. J.; Jensen, P.; Rubinsztein-Dunlop, H. Origin of the Large Homogeneous Line Widths Obtained from Strongly Quantum Confined PbS Nanocrystals at Room Temperature. *J. Phys. Chem. C* **2007**, *111*, 4984–4989.

[114] Meier, C.; Gondorf, A.; Lüttjohann, S.; Lorke, A.; Wiggers, H. Silicon Nanoparticles: Absorption, Emission, and the Nature of the Electronic Bandgap. *J. Appl. Phys.* **2007**, *101*, 103112.

[115] Grabolle, M.; Spieles, M.; Lesnyak, V.; Gaponik, N.; Eychmüller, A.; Resch-Genger, U. Determination of the Fluorescence Quantum Yield of Quantum Dots: Suitable Procedures and Achievable Uncertainties. *Anal. Chem.* **2009**, *81*, 6285–6294.

[116] Laverdant, J.; Marcillac, W. D. De; Barthou, C.; Chinh, V. D.; Schwob, C.; Coolen, L.; Benalloul, P.; Nga, P. T.; Maître, A. Experimental Determination of the Fluorescence Quantum Yield of Semiconductor Nanocrystals. *Materials (Basel).* **2011**, *4*, 1182–1193.

[117] van Dam, B.; Bruhn, B.; Dohnalova, K. Limits of Emission Quantum Yield Determination. **2017**, 1–7.

[118] Timmerman, D.; Valenta, J.; Dohnalová, K.; de Boer, W. D. a. M.; Gregorkiewicz, T. Step-like Enhancement of Luminescence Quantum Yield of Silicon Nanocrystals. *Nat. Nanotechnol.* **2011**, *6*, 710–713.

[119] Justo, Y.; Geiregat, P.; van Hoecke, K.; Vanhaecke, F.; De Mello Donega, C.; Hens, Z. Optical Properties of PbS/CdS Core/Shell Quantum Dots. *J. Phys. Chem. C* **2013**, *117*, 20171–20177.

[120] Liu, T.; Li, M.; Ouyang, J.; Zaman, M. B.; Wang, R.; Wu, X.; Yeh, C.; Lin, Q.; Yang, B.; Yu, K. Non-Injection and Low-Temperature Approach to Colloidal Photoluminescent PbS Nanocrystals with Narrow Bandwidth. *J. Phys. Chem. C* **2009**, *113*, 2301–2308.

[121] Peterson, J. J.; Krauss, T. D. Photobrightening and Photodarkening in PbS Quantum Dots. *Phys. Chem. Chem. Phys.* **2006**, *8*, 3851.

[122] Poznyak, S. K.; Osipovich, N. P.; Shavel, A.; Talapin, D. V; Gao, M.; Eychmüller, A.; Gaponik, N. Size-Dependent Electrochemical Behavior of Thiol-Capped CdTe Nanocrystals in Aqueous Solution. *J. Phys. Chem. B* **2005**, *109*, 1094–1100.

[123] Du, H.; Chen, C.; Krishnan, R.; Krauss, T. D.; Harbold, J. M.; Wise, F. W.; Thomas, M. G.; Silcox, J. Optical Properties of Colloidal PbSe Nanocrystals. *Nano Lett.* **2002**, *2*, 1321–1324.

[124] Wehrenberg, B. L.; Wang, C.; Guyot-Sionnest, P. Interband and Intraband Optical Studies of PbSe Colloidal Quantum Dots. *J. Phys. Chem. B* **2002**, *106*, 10634–10640.

[125] Clark, S. W.; Harbold, J. M.; Wise, F. W. Resonant Energy Transfer in PbS Quantum Dots. *J. Phys. Chem. C* **2007**, *111*, 7302–7305.

[126] Hyun, B.; Bartnik, A. C.; Lee, J.; Imoto, H.; Sun, L.; Choi, J. J.; Chujo, Y.; Hanrath, T.; Ober, C. K.; Wise, F. W. Role of Solvent Dielectric Properties on Charge Transfer from PbS Nanocrystals to Molecules. *Nano Lett.* **2010**, *10*, 318–323.

[127] Brown, S. L.; Krishnan, R.; Elbaradei, A.; Sivaguru, J.; Sibi, M. P.; Hobbie, E. K. Origin of Stretched-Exponential Photoluminescence Relaxation in Size-Separated Silicon Nanocrystals. *AIP Adv.* **2017**, *7*, 55314.

[128] Chena, L.-Y.; Chou, H.; Chenc, C.-H.; Tseng, C. Surface Modification of CdSe and CdS Quantum Dots-Experimental and Density Function Theory Investigation. In *Nanocrystals - Synthesis, Characterization and Applications*; InTech, 2012.

[129] Cheng, C.; Li, J.; Cheng, X. Photoluminescence Lifetime and Absorption Spectrum of PbS Nanocrystal Quantum Dots. *J. Lumin.* **2017**, *188*, 252–257.

[130] Wang, X.; Qu, L.; Zhang, J.; Peng, X.; Xiao, M. Surface-Related Emission in Highly Luminescent CdSe Quantum Dots. *Nano Lett.* **2003**, *3*, 1103–1106.

[131] Litvin, A. P.; Parfenov, P. S.; Ushakova, E. V; Fedorov, A. V; Artemyev, M. V.; Prudnikau, A. V; Cherevkov, S. A.; Rukhlenko, I. D.; Baranov, A. V. Size-Dependent Room-Temperature Luminescence Decay from PbS Quantum Dots. In *Proc. of SPIE*; Zhou, Z.; Wada, K., Eds.; 2012; Vol. 8564, p. 85641Z.

[132] Sangghaleh, F.; Sychugov, I.; Yang, Z.; Veinot, J. G. C.; Linnros, J. Near-Unity Internal Quantum Efficiency of Luminescent Silicon Nanocrystals with Ligand Passivation. *ACS Nano* **2015**, *9*, 7097–7104.

[133] Hartel, A. M. Structural and Optical Properties of PECVD Grown Silicon Nanocrystals Embedded in SiOxNy Matrix, Albert-Ludwigs University, 2013.

[134] Kůsová, K.; Ondič, L.; Klimešová, E.; Herynková, K.; Pelant, I.; Daniš, S.; Valenta, J.; Gallart, M.; Ziegler, M.; Hönerlage, B.; *et al.* Luminescence of Free-Standing versus Matrix-Embedded Oxide-Passivated Silicon Nanocrystals: The Role of Matrix-Induced Strain. *Appl. Phys. Lett.* **2012**, *101*, 143101.

[135] Dohnalová, K.; Poddubny, A. N.; Prokofiev, A. a; de Boer, W. D.; Umesh, C. P.; Paulusse, J. M.; Zuilhof, H.; Gregorkiewicz, T. Surface Brightens up Si Quantum Dots: Direct Bandgap-like Size-Tunable Emission. *Light Sci. Appl.* **2013**, *2*, e47.

[136] de Jong, E. M. L. D.; Rutjes, H.; Valenta, J.; Trinh, M. T.; Poddubny, A. N.; Yassievich, I.; Capretti, A.; Gregorkiewicz, T. Thermally Stimulated Exciton Emission in Si Nanocrystals. *Light Sci. Appl.* **2018**.

[137] Pevere, F.; Sychugov, I.; Sangghaleh, F.; Fucikova, A.; Linnros, J. Biexciton Emission as a Probe of Auger Recombination in Individual Silicon Nanocrystals. *J. Phys. Chem. C* **2015**, *119*, 7499–7505.

[138] Hartel, A. M.; Gutsch, S.; Hiller, D.; Zacharias, M. Intrinsic Nonradiative Recombination in Ensembles of Silicon Nanocrystals. *Phys. Rev. B* **2013**, *87*, 35428.

[139] Yu, P.; Beard, M. C.; Ellingson, R. J.; Ferrere, S.; Curtis, C.; Drexler, J.; Luiszer, F.; Nozik, A. J. Absorption Cross-Section and Related Optical Properties of

Colloidal InAs Quantum Dots. *J. Phys. Chem. B* **2005**, *109*, 7084–7087.

[140] Luo, J.-W.; Stradins, P.; Zunger, A. Matrix-Embedded Silicon Quantum Dots for Photovoltaic Applications: A Theoretical Study of Critical Factors. *Energy Environ. Sci.* **2011**, *4*, 2546.

[141] Lee, B. G.; Hiller, D.; Luo, J. W.; Semonin, O. E.; Beard, M. C.; Zacharias, M.; Stradins, P. Strained Interface Defects in Silicon Nanocrystals. *Adv. Funct. Mater.* **2012**, *22*, 3223–3232.

[142] Pavesi, L. Influence of Dispersive Exciton Motion on the Recombination Dynamics in Porous Silicon. *J. Appl. Phys.* **1996**, *80*, 216–225.

[143] Morgan, S. O.; Yager, W. A. Dielectric Properties of Organic Compounds. *Ind. Eng. Chem.* **1940**, *32*, 1519–1528.

[144] Iacona, F.; Franzò, G.; Ceretta Moreira, E.; Priolo, F. Silicon Nanocrystals and Er3+ Ions in an Optical Microcavity. *J. Appl. Phys.* **2001**, *89*, 8354–8356.

[145] Dyakov, S. A.; Zhigunov, D. M.; Hartel, A.; Zacharias, M.; Perova, T. S.; Timoshenko, V. Y. Enhancement of Photoluminescence Signal from Ultrathin Layers with Silicon Nanocrystals. *Appl. Phys. Lett.* **2012**, *100*.

[146] Ferre, R.; Garrido, B.; Pellegrino, P.; Perálvarez, M.; García, C.; Moreno, J. A.; Carreras, J.; Morante, J. R. Optical-Geometrical Effects on the Photoluminescence Spectra of Si Nanocrystals Embedded in SiO2. *J. Appl. Phys.* **2005**, *98*, 84319.

[147] Hiller, D.; Zelenina, A.; Gutsch, S.; Dyakov, S. A.; López-Conesa, L.; López-Vidrier, J.; Estradé, S.; Peiró, F.; Garrido, B.; Valenta, J.; *et al.* Absence of Quantum Confinement Effects in the Photoluminescence of Si3N4–embedded Si Nanocrystals. *J. Appl. Phys.* **2014**, *115*, 204301.

[148] Rinck, J.; Schray, D.; Kübel, C.; Powell, A. K.; Ozin, G. A. Size-Dependent Oxidation of Monodisperse Silicon Nanocrystals with Allylphenylsulfide Surfaces. *Small* **2015**, *11*, 335–340.

[149] Limpens, R.; Lesage, A.; Fujii, M.; Gregorkiewicz, T. Size Confinement of Si Nanocrystals in Multinanolayer Structures. *Sci. Rep.* **2015**, *5*, 17289.

[150] Fujii, M. All-Inorganic Colloidal Silicon Nanocrystals. In *Silicon Nanophotonics: Basic Principles, Present Status, and Perspectives, 2nd Ed*; Pan Stanford Publishing Pte. Ltd., 2016; pp. 191–220.

[151] Qu, L.; Peng, X. Control of Photoluminescence Properties of CdSe Nanocrystals in Growth. *J. Am. Chem. Soc.* **2002**, *124*, 2049–2055.

[152] Stouwdam, J. W.; Shan, J.; van Veggel, F. C. J. M.; Pattantyus-Abraham, A. G.; Young, J. F.; Raudsepp, M. Photostability of Colloidal PbSe and PbSe/PbS Core/Shell Nanocrystals in Solution and in the Solid State. *J. Phys. Chem. C* **2007**, *111*, 1086–1092.

[153] Marinins, A.; Zandi Shafagh, R.; van der Wijngaart, W.; Haraldsson, T.; Linnros, J.; Veinot, J. G. C.; Popov, S.; Sychugov, I. Light-Converting Polymer/Si Nanocrystal Composites with Stable 60–70% Quantum Efficiency and Their Glass Laminates. *ACS Appl. Mater. Interfaces* **2017**, *9*, 30267–30272.

List of appended publications

I. **Greben, M**.; Khoroshyy, P.; Gutsch, S.; Hiller, D.; Zacharias, M.; Valenta, J. Changes of the Absorption Cross Section of Si Nanocrystals with Temperature and Distance. *Beilstein J. Nanotechnol.* 2017, *8*, 2315–2323. DOI: 10.3762/bjnano.8.231

II. **Greben, M.**; Khoroshyy, P.; Liu, X.; Pi, X.; Valenta, J. Fully Radiative Relaxation of Silicon Nanocrystals in Colloidal Ensemble Revealed by Advanced Treatment of Decay Kinetics. *J. Appl. Phys.* 2017, *122*, 34304. DOI: 10.1063/1.4993584

III. **Greben, M.**; Valenta, J.; Khoroshyy, P. The Advanced Analysis of Slow Non-Stretched Exponential Decay Kinetics from Si Nanocrystals. In *Physics, Chemistry and Application of Nanostructures*; 2017; pp. 110–113. DOI: 10.1142/9789813224537_0026

IV. **Greben, M.**; Valenta, J. Note: On the Choice of the Appropriate Excitation-Pulse-Length for Assessment of Slow Luminescence Decays. *Rev. Sci. Instrum.* 2016, *87*, 126101. DOI: 10.1063/1.4971368

V. **Greben, M.**; Fucikova, A.; Valenta, J. Photoluminescence Quantum Yield of PbS Nanocrystals in Colloidal Suspensions. *J. Appl. Phys.* 2015, *117*, 144306. DOI: 10.1063/1.4917388

VI. Valenta, J.; **Greben, M.**; Gutsch, S.; Hiller, D.; Zacharias, M. Photoluminescence Performance Limits of Si Nanocrystals in Silicon Oxynitride Matrices. *J. Appl. Phys.* 2017, *122*, 144303. DOI: 10.1063/1.4999023

VII. Valenta, J.; **Greben, M.**; Remeš, Z.; Gutsch, S.; Hiller, D.; Zacharias, M. Determination of Absorption Cross-Section of Si Nanocrystals by Two Independent Methods Based on Either Absorption or Luminescence. *Appl. Phys. Lett.* 2016, *108*, 23102. DOI: 10.1063/1.4939699

VIII. Valenta, J.; **Greben, M.** Radiometric Calibration of Optical Microscopy and Microspectroscopy Apparata over a Broad Spectral Range Using a Special Thin-Film Luminescence Standard. *AIP Adv.* 2015, *5*, 47131. DOI: 10.1063/1.4918970

IX. Valenta, J.; **Greben, M.**; Gutsch, S.; Hiller, D.; Zacharias, M. Effects of Inter-Nanocrystal Distance on Luminescence Quantum Yield in Ensembles of Si Nanocrystals. *Appl. Phys. Lett.* 2014, *105*, 243107. DOI: 10.1063/1.4904472

X. **Greben, M**.; Khoroshyy, P.; Sychugov, I.; Valenta, J. Non-exponential decay kinetics: Correct assessment and description illustrated by slow luminescence of Si nanostructures. Submitted to *Appl. Phys. Rev.* 2017.

List of other publications/presentations

Conferences

A. Valenta, J.; **Greben, M.**; Fucikova, A. Enhancement of Absorption Cross-Section and Luminescence Yield of Semiconductor Quantum Dots and up-Converting Particles. In *Physics, Chemistry and Application of Nanostructures*; 2017; pp. 78–80.
DOI: 10.1142/9789813224537_0018

B. **Greben, M.**; Valenta, J. Quantum Yield vs Photon Energy Dependence of Colloidal PbS Quantum Dots. In *Book of abstracts of the Fifth international school and conference on photonics "Photonica 2015";* 2015; pp. 56–57.

C. **Greben, M.** Advanced optical spectroscopy of semiconductor nanostructures. In *Bulletin spektroskopické společnosti Jana Marka Marci* č. 174*;* 2016; pp. 19–20.

D. **Greben, M.**; Valenta, J. Can Colloidal Silicon Nanocrystal Reveal Fully Radiative Relaxation? Poster T.1.3 at E-MRS Fall Meeting, Warsaw, Poland, September 18 – 21, 2017.

E. **Greben, M.**; Valenta, J. Description of the non-trivial kinetics of luminescence from Si nanostructures: what is the most representative lifetime? Oral talk O.10.2 at E-MRS Spring Meeting, Lille, France, May 2 – 6, 2016.

F. **Greben, M.**; Raichlova, A.; Valenta, J. Spectral Dependence of Photoluminescence Quantum Yield in Semiconductor Nanocrystals: Violation of the Kasha-Vavilov Rule. Poster W34 at *8th International Conference on Quantum Dots*; Pisa, Italy, May 11–16, 2014.

G. Valenta, J.; **Greben, M.**; Kůsová, K.; Ondič, L.; Hapala, P.; Jelínek, P.; Cibulka, O.; Pelant, I. Effects of Tensile/compressive Strain on Optical Properties of Silicon Nanocrystals: Toward Direct Bandgap Silicon. Poster W147 at *8th International Conference on Quantum Dots*; Pisa, Italy, May 11–16, 2014.

Summer schools (presentation: posters)

a. International WE-Heraeus-Physics School on "Exciting nanostructures: Probing and tuning the electronic properties of confined systems", Physikzentrum Bad Honnef, Germany, July 17-21, 2017.

b. "3^{d} EPS-SIF International School on Energy" 69th course on "Materials for Energy and Sustainability-V", Erice, Sicily, Italy, July 13–19, 2016.

c. International WE-Heraeus-Physics School on "Physical properties of nanoparticles: Characterization and applications", Physikzentrum Bad Honnef, Germany, July 26-31, 2015.

d. International school of atomic and molecular spectroscopy on "Nano-optics: principles enabling basic research and applications", Erice, Sicily, Italy, July 04–19, 2015.

Publications beyond the scope of this thesis

1. Komarov, F.; Vlasukova, L.; Milchanin, O.; **Greben, M.**; Parkhomenko, I.; Mudryi, A.; Wendler, E.; Zukowski, P. Light Emitting Single-Crystalline Silicon Wafers Implanted with V and III Group Ions. *Acta Phys. Pol. A* 2014, *125*, 1288–1291.
   DOI: 10.12693/APhysPolA.125.1288

2. Komarov, F.; Vlasukova, L.; **Greben, M.**; Milchanin, O.; Zuk, J.; Wesch, W.; Wendler, E.; Togambaeva, A. Structural and Optical Properties of Silicon Layers with InSb and InAs Nanocrystals Formed by Ion-Beam Synthesis. *Nucl. Instruments Methods Phys. Res. Sect. B Beam Interact. with Mater. Atoms* 2013, *307*, 102–106.
   DOI: 10.1016/j.nimb.2013.01.023

3. Komarov, F.; Vlasukova, L.; Milchanin, O.; **Greben, M.**; Komarov, A.; Mudryi, A.; Wesch, W.; Wendler, E.; Zuk, J.; Kulik, M.; *et al.* Ion Beam Synthesis of InAs Nanocrystals in Si: Influence of Thin Surface Oxide Layers. *Acta Phys. Pol. A* 2013, *123*, 809–812.
   DOI: 10.12693/APhysPolA.123.809

4. Komarov, F.; Vlasukova, L.; **Greben, M.**; Milchanin, O.; Zuk, J.; Wesch, W.; Wendler, E.; Togambaeva, A. Optical Properties of Silicon Layers with InSb and InAs Nanocrystals Formed by Ion-Beam Synthesis. In *Physics, Chemistry and Applications of Nanostructures*; 2013; pp. 86–89.
   DOI: 10.1142/9789814460187_0020

5. **Greben, M. V.**; Komarov, F. F.; Vlasukova, L. A.; Milchanin, O. V.; Mudryi, A. V.; Parkhomenko, I. N. The Comparative Investigations of Structural and Optical Properties of GaSb Nanocrystals/Si Layers. In *Proceedings of the International Conference "Nanomaterials: Applications and Properties"*; 2013; Vol. 2, p. 02PCN16.

6. Komarov, F. F.; Vlasukova, L. A.; Milchanin, O. V.; **Greben, M. V.**; Komarov, A. F.; Mudryi, A. V.; Wesch, W.; Wendler, E.; Togambaeva, A. K. The Effect of Thin Surface Oxide Layers on Ion Beam Synthesis of InAs Nanocrystals in Si. In *Proceedings of VII International Conference "Plasma Physics and Plasma Technology"*; 2012; pp. 491–494.

7. Komarov, F. F.; Vlasukova, L. A.; Milchanin, O. V.; **Greben, M. V**.; Mudryi, A. V.; Wesch, W. Effects of Annealing Regims on the Structural and Optical Properties of InAs and GaSb Nanocrystals Created by Ion-Beam Synthesis in Si Matrix. In *Proceedings of the International Conference "Nanomaterials: Applications and Properties"*; 2011; Vol. 1, pp. 409–415.

8. Vlasukova, L. A.; **Greben, M. V.**; Milchanin, O. V.; Mudryi, A. V.; Vujtik, V. Influence of Annealing Regimes on Structural and Optical Properties of InAs Nanocrystals into Ion Implanted Silicon. In *Proceedings of 9 International conference "Interaction of radiation with solids"*; 2011; pp. 20–22.

List of awards

- E-MRS Young Scientist Award of Symposium O (Group IV semiconductors at the nanoscale – towards applications in photonics, electronics and life sciences), E-MRS Spring Meeting, Lille, France, May 2 – 6, 2016.

- Award of the best published work of young scientists in the field of Spectroscopy 2016 (Spectroscopic society of Ioannes Marcus Marci), Brno, Czech Republic, December 2, 2016.

List of grant projects

- EU 7th framework programme, Small and medium collaborative project – Nanotech-call: ***Silicon Nanodots for Solar Cell Tandem*** – NASCEnT, 2010–2013 (leader: S. Janz, Fraunhofer ISE Freiburg, Czech part: J. Valenta).

- Czech-Japan bilateral project, programme Kontakt II. from Ministry of Education, Youth and Sports (MEYS) Czech R., LH14246, ***Doped silicon nanocrystals – new nanomaterials for photonics and bio-applications***, 2014–2016, (leader of the Czech part: J. Valenta) with the group of Prof. Minoru Fujii, Kobe University.

- Visegrad group (V4) – Japan Joint Research Project on Advanced Materials: ***Nanophotonics with Metal – Group-IV-Semiconductor Nanocomposites*** (NaMSeN), 8F15001 (MEYS), 2015-2018, (main leader: J. Valenta), collaborating institutions: Kobe University, Warsaw University of Technology, Institute of Physics Slovak Academy of Sciences, Wigner Research Centre for Physics Hungarian Academy of Sciences.

- Deutche Forschungsgemeinschaft + Czech Science Foundation bilateral project, 16-09745J and ZA 191/36-1: ***Understanding the luminescence efficiency of silicon quantum dots***, 2016-2018 (leader of the czech part: P. Malý).

- Czech Science Foundation, standard project 16-22092S: ***Fluoride nanostructural thin films with outstanding optical and luminescence properties***, 2016-2018 (leaders: J. Lančok, *Institute of Physics, CAS* and J. Valenta).

- Charles University Center, UNCE/SCI/010, ***Center for nano- and bio-photonics***, 2018-2023, (leader: J. Valenta).

- Czech Science Foundation, standard project 18-12533S: ***Advanced fluorescent gold nanoclusters and their DNA-programmable assembly***, 2018-2020 (leaders: J. Valenta and P. Cigler, *Inst. Org. Chemistry & Biochemistry, CAS*).

Reprints of author’s publications

Paper I

BEILSTEIN JOURNAL OF NANOTECHNOLOGY

Changes of the absorption cross section of Si nanocrystals with temperature and distance

Michael Greben*[1], Petro Khoroshyy[2], Sebastian Gutsch[3], Daniel Hiller[3], Margit Zacharias[3] and Jan Valenta[1]

Full Research Paper

Open Access

Address:
[1]Department of Chemical Physics and Optics, Faculty of Mathematics and Physics, Charles University, Ke Karlovu 3, 121 16 Prague 2, Czech Republic, [2]Institute of Organic Chemistry and Biochemistry, Czech Academy of Sciences, Flemingovo namesti 2, 160 00 Prague 6, Czech Republic and [3]Faculty of Engineering, IMTEK, Albert-Ludwigs-University Freiburg, Georges-Köhler-Allee 103, 79110 Freiburg, Germany

Email:
Michael Greben* - leibnits@gmail.com

* Corresponding author

Keywords:
absorption cross section; average lifetime; nanocrystal distance; photoluminescence decay; silicon nanocrystals

Beilstein J. Nanotechnol. **2017,** *8,* 2315–2323.
doi:10.3762/bjnano.8.231

Received: 01 July 2017
Accepted: 29 September 2017
Published: 06 November 2017

Associate Editor: R. Jin

Abstract

The absorption cross section (ACS) of silicon nanocrystals (Si NCs) in single-layer and multilayer structures with variable thickness of oxide barriers is determined via a photoluminescence (PL) modulation technique that is based on the analysis of excitation intensity-dependent PL kinetics under modulated pumping. We clearly demonstrate that roughly doubling the barrier thickness (from ca. 1 to 2.2 nm) induces a decrease of the ACS by a factor of 1.5. An optimum separation barrier thickness of ca. 1.6 nm is calculated to maximize the PL intensity yield. This large variation of ACS values with barrier thickness is attributed to a modulation of either defect population states or of the efficiency of energy transfer between confined NC layers. An exponential decrease of the ACS with decreasing temperature down to 120 K can be explained by smaller occupation number of phonons and expansion of the band gap of Si NCs at low temperatures. This study clearly shows that the ACS of Si NCs cannot be considered as independent on experimental conditions and sample parameters.

Introduction

For decades, silicon – an abundant, nontoxic material with high attainable purity – has been a dominant material for microelectronics and photovoltaics. However, the constantly increasing energy consumption and environmental issues challenge researchers to develop fundamentally new concepts to overcome the limitations of current technologies. The nanocrystalline form of silicon, which reveals all advantages of the quantum confinement effect [1], is a promising candidate for the development of a new generation of Si photovoltaic and photonic devices [2]. SiO_2-embedded silicon nanocrystals (Si NCs) can be relatively easy integrated into current CMOS technology. In photovoltaics, nanocrystalline Si is a promising material for the

top cell of all-Si tandem cells that can theoretically reach efficiencies much above the Shockley–Queisser limit of 31% for single-junction solar cells [2]. Current injection into Si NCs can be utilized in Si-based light emitting diodes or displays [3]. A device fabrication process demands an effective control of size, shape and density of Si NCs. All those requirements can be met via the superlattice approach in combination [4] with the phase-separation of sub-stoichiometric oxides (SiO_x) where the NC spacing in all three dimensions can be controlled.

The emission properties such as quantum yield (QY) of such Si NC/SiO_2 multilayer (ML) structures were studied as a function of inter-nanocrystal distance, temperature, excitation and emission wavelength [5,6]. However, there is still little knowledge about one of the most crucial optical parameters for spectroscopic studies and the design of Si NC optoelectronic devices, which is related to the strength of light absorption: the absorption cross section (ACS), σ. The ACS directly reflects the probability of optical transitions and is defined as the ratio [7] between photon absorption rate for a single NC and the photon flux, which in fact provides a relationship [8] between the NC concentration and the optical density of the sample. Consequently, if the absolute value of the ACS is determined, the concentration of NCs in a studied sample can be directly calculated from measurements of the optical absorption coefficient [9]. The NC concentration is necessary for many scientific studies and practical applications such as biolabeling [3]. Besides this, the ACS is related to the transition oscillator strength and therefore, is a very useful parameter for a variety of theoretical calculations as it defines an upper limit of the exciton radiative lifetime of a NC [8]. Though the ACS is a very important quantity for practice it is not easily accessible experimentally, which explains a very limited number of reports in the literature. Recently we presented a comparative study of ACS determination by two completely independent methods including a photoluminescence (PL) modulation technique [10]. In this work, we employ this procedure to analyze the dependence of the ACS of ML structures on mainly two important parameters: inter-nanocrystal distance and temperature. It will be shown that, contrary to popular belief, the ACS depends on the temperature. Moreover, we combine our knowledge on QY and ACS to derive the optimum separation barrier thickness to maximize PL intensity yield at a given excitation intensity.

Experimental

The investigated ML samples were deposited as alternating layers of silicon-rich silicon oxynitride (SRON: SiO_xN_y) with 4.5 nm thickness and of stoichiometric SiO_2 (1, 1.6, 2.2 or 2.8 nm thick) on fused silica substrates by plasma-enhanced chemical vapor deposition (PECVD). On top and below the superlattice stack, 10 nm of SiO_2 were deposited as a buffer and capping layer, respectively. The samples were subsequently annealed in a quartz tube furnace at 1150 °C for 1 h in high-purity N_2 in order to form Si NCs and then passivated by annealing in H_2 at 500 °C for defect passivation. In addition to ML samples, one single layer (SL) sample with a thick SRON 200 nm monolayer without barriers was taken for comparison. The SRON stoichiometry parameter was almost constant $y = 0.23 \pm 0.002$ in all samples while the x value was chosen as 0.93 and 1.1 for ML and SL samples, respectively. For further details on the sample preparation as well as structural properties of the samples see our recent paper [11].

The PL experiments were performed under excitation with a 405 nm diode laser the beam of which was modulated using a quartz acousto-optic cell. The edge switching time is about 100 ns. The laser is coupled to a custom-made micro-spectroscopy set-up with an inverted microscope in the epifluorescence configuration with two detection branches for visible and near-infrared spectral regions, each one composed of an imaging spectrometer, and a camera for spectral and a photomultiplier for time-resolved PL detection. The output of the photomultipliers is coupled in a multichannel counting card (Becker-Hickl, MSA-300). The details on the set-up can be found in our recent paper [12]. Advantage of the micro-PL set-up is a good control of the excitation spot size and the selected detection area, which enable a quite precise determination of the excitation photon flux. For the low-temperature experiments the samples are placed in a cryostat (Janis ST-500).

Results and Discussion

ACS model

Let us consider the model originally presented by Kovalev et al. [13,14] and then slightly modified in our recent paper [10]. A Si NC is considered as a quasi-two-level system with only three possible NC occupation states: ground state, single (one e–h pair in a NC) and double (two e–h pairs in a NC) excited state. Assuming the corresponding occupations as N_0, N_1 and N_2 we can obtain the system of three differential equations describing optical dynamics of above mentioned model:

$$\frac{\mathrm{d}N_0}{\mathrm{d}t} = -N_0 I_{\mathrm{ex}} \sigma + \frac{N_1}{\tau_{\mathrm{PL}}\left(I_{\mathrm{ex}}\right)}, \tag{1}$$

$$\frac{\mathrm{d}N_1}{\mathrm{d}t} = N_0 I_{\mathrm{ex}} \sigma - N_1 I_{\mathrm{ex}} \sigma - \frac{N_1}{\tau_{\mathrm{PL}}\left(I_{\mathrm{ex}}\right)} + \frac{N_2}{\tau_{\mathrm{A}}}, \tag{2}$$

$$\frac{\mathrm{d}N_2}{\mathrm{d}t} = N_1 I_{\mathrm{ex}} \sigma - \frac{N_2}{\tau_{\mathrm{A}}}, \tag{3}$$

where σ describes the cross section for the absorption of photons, I_{ex} represents the excitation intensity expressed in areal photon flux (photons per second per square centimeter), $\tau_{PL}(I_{ex})$ and τ_A stand for PL decay and Auger lifetime, respectively. Here the PL lifetime $\tau_{PL}(I_{ex})$ is considered as a function of the excitation intensity (discussed below). The total population of luminescing nanocrystals is $N_T = N_0 + N_1 + N_2$. To complete the model we should summarize all of its assumptions: (1) The Auger lifetime is considered to be power-independent and much shorter (for Si NCs in the nanosecond-range or shorter [15]) than $\tau_{PL}(I_{ex})$. Therefore, all higher excited states are not taken into account supposing that Auger recombination efficiently quenches the population of double excited NCs. (2) The ground state and single-excited state roughly have the same ACS, σ, as we assume that the presence of one e–h pair does not influence the absorption of the second one (because of the relatively high [1] density of optical states (DOS) in Si NCs).

According to the first assumption, $\tau_A \ll \tau_{PL}(I_{ex})$ and therefore relaxation of biexcitons in Equation 3 for a given fraction of excitons N_1 (Equation 2) can be considered as instantaneous on the slow time-scale evolution of N_1. Consequently, from Equation 3 we assume the population $N_2 = N_1 I_{ex}\sigma\tau_A$ and Equation 2 can be rewritten as:

$$\frac{dN_1}{dt} = N_T I_{ex}\sigma - \left(I_{ex}\sigma + I_{ex}^2\sigma^2\tau_A + \frac{1}{\tau_{PL}\left(I_{ex}\right)} \right) N_1. \quad (4)$$

By taking into account [1] that the PL intensity is $I_{PL} = N_1/\tau_r$ we can write the solution of Equation 4 in the form:

$$\begin{aligned} I_{PL}(t) &= \frac{N_T I_{ex}\sigma/\tau_r\left(I_{ex}\right)}{1/\tau_{PL}\left(I_{ex}\right) + I_{ex}\sigma + I_{ex}^2\sigma^2\tau_A} \times \\ &\left[1 - e^{-\left(1/\tau_{PL}(I_{ex}) + I_{ex}\sigma + I_{ex}^2\sigma^2\tau_A\right)t}\right] \\ &= I_{PL}^{cw}\left[1 - e^{-\left(t/\tau_{ON}(I_{ex})\right)}\right], \end{aligned} \quad (5)$$

where τ_r stands for the radiative lifetime, which is believed to be independent on the excitation power, and τ_{ON} is the onset (ON) lifetime.

Equation 5 represents the most general solution of Equations 1–3. Consequently, from Equation 5 we derive:

$$\frac{1}{\tau_{PL}\left(I_{ex}\right)} + I_{ex}\sigma + I_{ex}^2\sigma^2\tau_A = \frac{1}{\tau_{ON}\left(I_{ex}\right)}. \quad (6)$$

The solution of Equation 6 defines the ACS as a function of $\tau_{ON}(I_{ex})$, $\tau_{PL}(I_{ex})$ and even τ_A:

$$\sigma = \frac{1}{I_{ex}}\left[\sqrt{\frac{1}{4\tau_A^2} + \frac{1}{\tau_A}\left(\frac{1}{\tau_{ON}\left(I_{ex}\right)} - \frac{1}{\tau_{PL}\left(I_{ex}\right)}\right)} - \frac{1}{2\tau_A}\right]. \quad (7)$$

However, the Auger decay time τ_A is not easily determined (literature reports values within a broad range from picoseconds [15] to nanoseconds [16]). Therefore, we have to avoid strong-pumping regimes where double-excitation of NCs takes place.

Assuming $N_2/N_1 \to 0$ we have $I_{ex}\sigma\tau_A \to 0$ (see Equation 3) and the Auger part $I_{ex}\sigma(I_{ex}\sigma\tau_A)$ is negligibly small in comparison with the term $I_{ex}\sigma$ in Equation 5 and can be neglected in regimes of low and moderate excitation powers:

$$\begin{aligned} I_{PL}(t) &= \frac{N_T I_{ex}\sigma/\tau_r}{1/\tau_{PL}\left(I_{ex}\right) + I_{ex}\sigma} \times \left[1 - e^{-\left(\frac{1}{1/\tau_{PL}(I_{ex})} + I_{ex}\sigma\right)t}\right] \\ &= I_{PL}^{cw}\left[1 - e^{-\left(t/\tau_{ON}(I_{ex})\right)}\right]. \end{aligned} \quad (8)$$

Thus, Equation 6 simplifies to the well-known equation [10,17,18] that will be used throughout for the ACS determination in this paper:

$$\sigma = \frac{1}{I_{ex}}\left[\frac{1}{\tau_{ON}\left(I_{ex}\right)} - \frac{1}{\tau_{PL}\left(I_{ex}\right)}\right]. \quad (9)$$

Average lifetime calculations

Though very often PL transients of Si NCs are well fitted by stretched exponential function [1], there is a number of reports where stretched exponential fit fails for both colloidal [19,20] and matrix-embedded NCs [21,22]. Instead, sometimes a log-normal rate distribution model [23] could be helpful to describe the de-excitation dynamics of the NC ensemble. Unfortunately, neither stretched exponential nor log-normal decay models can fit our experimentally measured PL curves (Figure 1).

Our goal is to extract the average ON and PL lifetimes as a function of different parameters. Thus, two fitting models were employed for this and the resulting lifetimes were compared. In the first approach, the sum of N mono-exponentials (ME) was utilized:

$$I_{PL}(t) = \sum_{i=1}^{N} A_i^{PL} e^{-\left(\frac{t}{\tau_i^{PL}}\right)} + \text{background}, \quad (10)$$

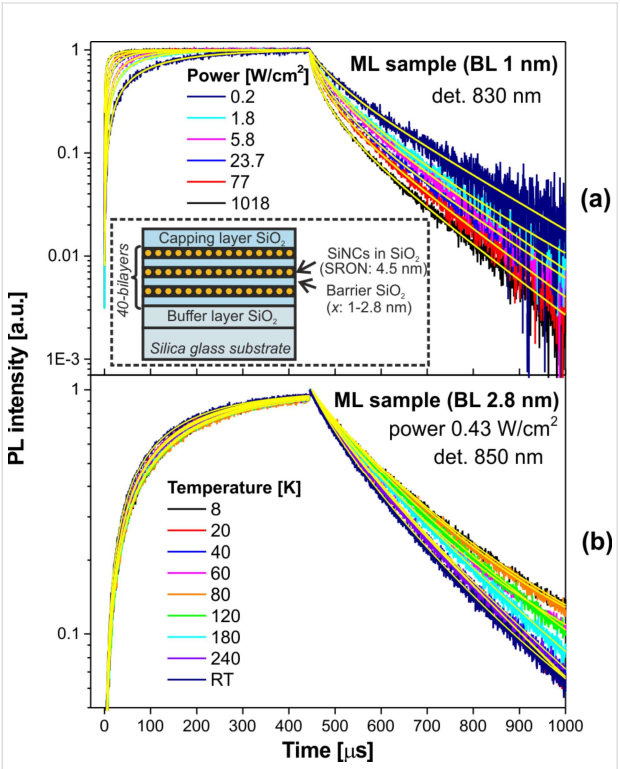

Figure 1: Time-resolved PL signals of multilayer samples (barrier layer (BL) is 1 nm (a) or 2.8 nm (b)) detected at 830 nm (a) and 850 nm (b) and excited by square pulses, as well as their corresponding fits by Equations 10–13 as a function of a) power density ranging from 0.2 to 1018 W/cm^2 at room temperature and b) temperature ranging from 8 K up to room temperature. The inset illustrates the multilayer sample structure.

where A_i and τ_i are the according amplitudes and lifetime parameters, respectively; the background is a "constant" signal background level of a detector.

In the second approach, a combination of one mono- and one stretched-exponential (MSE) was used:

$$I_{\mathrm{PL}}(t) = A_1^{\mathrm{PL}} e^{-\left(\frac{t}{\tau_1^{\mathrm{PL}}}\right)} + A_2^{\mathrm{PL}} e^{-\left(\frac{t}{\tau_2^{PL}}\right)^{\beta}} + \text{background}, \quad (11)$$

where β is the dispersion factor, which varies from 0 to 1.

Usually the onset (rise) PL dynamics is not analyzed in processing of time-resolved PL data. Recently we demonstrated that special attention needs to be paid to the excitation pulse length [24]. Here we show how to utilize the knowledge of the average ON lifetime. According to Equation 8 the PL onset kinetics for the two fitting models are described as:

$$I_{\mathrm{ON}}(t) = \sum_{i=1}^{N} A_i^{\mathrm{ON}} \left(1 - e^{-\left(\frac{t}{\tau_i^{\mathrm{ON}}}\right)}\right) + \text{background}, \quad (12)$$

$$I_{\mathrm{ON}}(t) = A_1^{\mathrm{ON}} \left(1 - e^{-\left(\frac{t}{\tau_1^{\mathrm{ON}}}\right)}\right) + A_2^{\mathrm{ON}} \left(1 - e^{-\left(\frac{t}{\tau_2^{\mathrm{ON}}}\right)^{\beta}}\right) + \text{background}. \quad (13)$$

The average PL decay time of photons can be generally calculated [1] according to the statistical formula

$$\overline{\tau} = \frac{\int_0^{\infty} tI(t)\,\mathrm{d}t}{\int_0^{\infty} I(t)\,\mathrm{d}t}. \quad (14)$$

Finally, both average ON and PL lifetimes can be calculated by introducing Equation 10 and Equation 11 into Equation 14:

$$\overline{\tau}_{\mathrm{ME}} = \frac{\sum_{i=0}^{N} A_i \tau_i^2}{\sum_{i=0}^{N} A_i \tau_i}, \quad (15)$$

$$\overline{\tau}_{\mathrm{MSE}} = \frac{A_1\tau_1^2 + A_2 \frac{\tau_2^2}{\beta} \Gamma\left(\frac{2}{\beta}\right)}{A_1\tau_1 + A_2 \frac{\tau_2}{\beta} \Gamma\left(\frac{1}{\beta}\right)}, \quad (16)$$

where Γ corresponds to the gamma function.

Although in this paper a precise data treatment was carried out we remind the reader about possible approximate calculations of average lifetimes for such complex decay kinetics [10,21].

PL modulation technique

Spectrally resolved PL traces were measured at different temperatures while the excitation power was varied over four orders of magnitude (Figure 1). The power dependence of PL amplitudes (detected at 830 nm) from samples with different thicknesses of the oxide barrier layers (BL) are depicted in Figure 2a. The steady-state PL intensity in the low-excitation region $I_{\mathrm{ex}} \ll 1/\sigma\tau_{\mathrm{PL}}(I_{\mathrm{ex}})$ follows from Equation 8 and reveals a linear dependence on the power (Figure 2a):

$$I_{\mathrm{PL}}(0) = N_{\mathrm{T}} I_{\mathrm{ex}} \sigma \frac{\tau_{PL}(I_{\mathrm{ex}})}{\tau_{\mathrm{r}}}. \qquad (17)$$

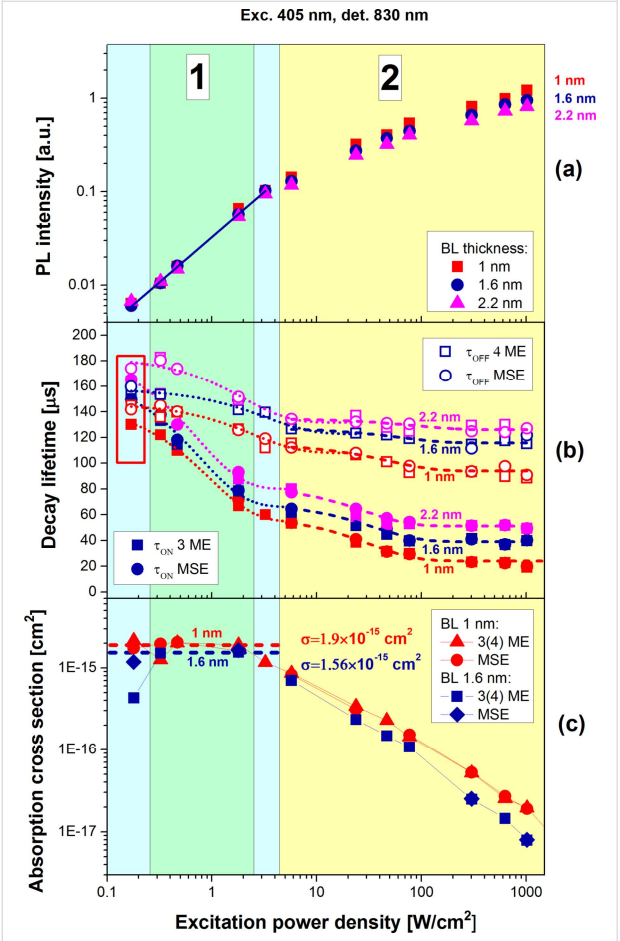

Figure 2: a) PL intensity under continuous-wave excitation as a function of the excitation photon flux for samples with 1 nm (squares), 1.6 nm (circles) and 2.2 nm (triangles) oxide barrier thickness. b) The ON (filled symbols) and PL (opened symbols) characteristic lifetimes extracted by fitting with either a combination of 3–4 mono-exponentials (ME) (squares) given by Equation 10 and Equation 12, or mono- and stretched exponentials (circles) (MSE) given by Equation 11 and Equation 13 and their corresponding exponential fits (dotted and dashed lines). c) The final ACS obtained from Equation 9 for samples with separation barriers of 1 and 1.6 nm. Throughout the figure the red, royal blue and pink colors represent samples with 1, 1.6 and 2.2 nm barrier thickness, respectively. The cyan and yellow areas stand for the linear regime and the saturation regime, respectively. The green area restricts the region of trusted ACS determination.

For moderate and high pump fluxes this intensity begins to saturate (Equation 8 and Equation 5, accordingly). Although the Auger-related PL saturation phenomena was utilized in several papers [14,25,26] for ACS determination, here we are forced to reject this approach as the saturation models cannot fit well our experimental data. Instead, we turn to the PL modulation technique that was described in detail recently [10] and exploit only the linear PL regimes.

The power dependence of both ON and PL lifetimes extracted by the ME and MSE methods is presented in Figure 2b. Both methods result in almost identical lifetime values. This indicates an independence of the average lifetime on fitting models, and each model describes the PL decay curves quite well. As expected [10], an increase of excitation power results in shortening of both ON and PL lifetimes (Figure 2b). Also the PL kinetics become more non-exponential, i.e., the distribution of lifetimes becomes broader [27] (Figure 1a). Thus, both characteristic lifetimes τ_{ON} and τ_{PL} are roughly equal at low excitation in agreement with Equation 9 while for higher pumping both lifetimes decrease exponentially with increasing pumping power. It is important to note a change of the slope of the lifetime decrease near the PL saturation level (which is usually ca. 1 W/cm^2 for Si NCs) after the power was increased by approximately two orders of magnitude (Figure 2b). This transition gives evidence for the appearance of an additional mode (Auger recombination) in the decay process for pumping above the saturation threshold. To the best of our knowledge this has not been reported before for lifetimes. Moreover, τ_{ON} expectedly decreases faster than τ_{PL} with increase of excitation pumping as it is predicted by Equation 9.

Finally, the ACS was calculated by using Equation 9 and its variation with power is presented in Figure 2c. Normally, the ACS is considered [14] as a product of both DOS and the transition oscillator strength, neither of which is expected to be power-dependent. However, from Figure 2c it follows that the ACS is gradually decreasing when pumping near and above the saturation. Firstly, we have to remind that Equation 9 is valid only under the assumption that the fraction of NCs with two e–h pairs is negligibly small ($N_2 \approx 0$). Otherwise, Equation 7 must be used instead. Above we restricted the validity of the described model to the linear power regime and therefore, excitation powers above saturation will not be considered. Secondly, both ON and PL lifetimes are almost equal at very low excitation and, therefore, the ACS is noisy. In between, there is a very narrow intermediate region of excitation powers where the described model is valid and the ACS can be reliably determined [10] as a constant value (Figure 2, green region).

As it follows from Equation 9, the inverse onset lifetime (onset rate), $1/\tau_{ON}$, is a linear function of the photon flux I_{ex} with an offset given by the inverse decay PL lifetime (PL rate), $1/\tau_{PL}$. Therefore, the ACS is usually determined directly as the slope of the function $1/\tau_{ON}(I_{ex})$. However, our experiments show that the PL lifetime, $\tau_{PL}(I_{ex})$, is also a function of the excitation power [28] (Figure 2b). Assuming the radiative relaxation, τ_r, to be independent on the power, this can be understood by the saturation of non-radiative recombination decay paths resulting in an increase of non-radiative lifetime τ_{nr}. Analogous to

$1/\tau_{ON}(I_{ex})$, the dependence $1/\tau_{PL}(I_{ex})$ can also be approximated with a linear function (Figure 3):

$$\frac{1}{\tau_{PL}\left(I_{ex}\right)} = \gamma_{PL} I_{ex} + \frac{1}{\tau_0}, \qquad (18)$$

where the low-excitation lifetime is $\tau_0 = \tau_{ON}(0) = \tau_{PL}(0)$, and γ_{PL} is the slope of the $1/\tau_{PL}(I_{ex})$ power dependence.

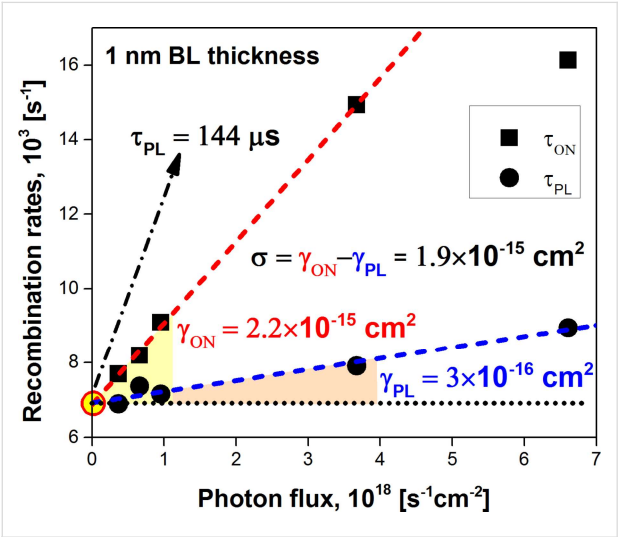

Figure 3: The extracted recombination rates $\gamma_{ON} = 1/\tau_{ON}$ and $\gamma_{PL} = 1/\tau_{PL}$ at λ_{det} = 830 nm of the ML sample with 1 nm BL thickness as functions of the excitation photon flux. The dashed lines are the corresponding linear function fits. The ACS is determined according to Equation 19.

Finally, after substituting Equation 18 into Equation 9 we obtain

$$\frac{1}{\tau_{ON}\left(I_{ex}\right)} = \left(\sigma + \gamma_{PL}\right) I_{ex} + \frac{1}{\tau_0} = \gamma_{ON} I_{ex} + \frac{1}{\tau_0}, \qquad (19)$$

where γ_{ON} is the slope of the function $1/\tau_{ON}(I_{ex})$.

According to Equation 19, the correct ACS value must be calculated as the difference between the slopes of ON and PL rate $\sigma = \gamma_{ON} - \gamma_{PL}$ (Figure 3) where both slopes are determined within the pumping range of linear dependence. Obviously, the variation of $\tau_{PL}(I_{ex})$ was automatically included in the calculations presented in Figure 2c.

In this way, we have calculated the ACS of ML samples in which the barrier thickness was varied (Figure 4a). As the separation increases, a transition from poorly separated NCs (1 nm or less) to a well-separated (above 2 nm) stack of confined layers is characterized [5] by an exponential increase of PL QY. In its turn, the ACS is decreasing with an increase of the NC separation barrier thickness (Figure 4a).

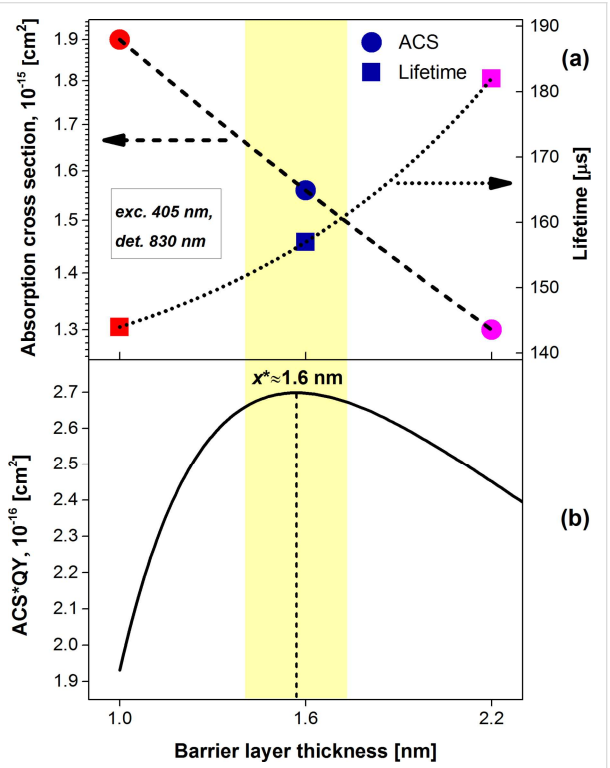

Figure 4: The dependence of (a) extracted PL lifetime $\tau(x)$ and calculated ACS $\sigma(x)$ and (b) the product $\sigma(x)\cdot\eta(x)$ as a function of BL thickness x. The dashed and dotted lines in (a) are exponential fits. The corresponding fit parameters of the ACS according to Equation 21 are: $y_0 = 4.55\cdot10^{-16}$ cm^2, $A = 1.445\cdot10^{-16}$ cm^2 and $\Delta x = 2.2366$ nm.

As presented in Figure 3, the PL modulation method directly gives us the true value of the lifetime τ_0 (the low-excitation limit) as the intersection of ON–PL rate slopes (at $I_{ex}\rightarrow0$). In contrast to the ACS, the lifetime increases with an increase of the barrier thickness (Figure 4a). These variations of ACS and lifetime can be caused either by changes in the population of defect states or by changes of possible interactions between NC layers. On one hand, a lower number of defects for better separated NCs (which can be substantiated by higher QY [5]) can result in longer lifetimes, lower DOS and thus lower ACS (Figure 4a). On the other hand, in presence of exciton migration some neighboring NCs can work as antenna, because a NC can be excited either directly through photon absorption or indirectly through an energy transfer from a nearby NC. Therefore, an ACS enhancement is expected for the system of interacting NCs with thinner barrier. Moreover, as NC separation decreases, the hopping lifetime, τ_{hop}, becomes shorter and, consequently, the PL lifetime decreases as well (Figure 4a). Separate experiments must be performed to figure out the real origin of the observed trend. Nevertheless, a similar (but much

stronger) enhancement of ACS was reported by Priolo et al. [17] for a sample in which a substantial energy transfer was expected.

An optimum inter-nanocrystal distance

Recently, we showed [5] that unlike ACS the PL QY is exponentially growing with increase of separation between confined NC layers. The quantum yield is a quantity that, in principle, must be independent on the number of absorbed photons [1]. In assumption that the internal quantum efficiency, $\eta_I = \tau_{PL}/\tau_r$, scales with the barrier thickness x in the same way as PL QY [5] ($\eta = N_{em}/N_{abs}$), i.e., the fraction of bright NCs N_{em} does not depend on x, the Equation 17 can be modified at the low-excitation limit as:

$$I_{PL}(x) \approx N_T I_{ex} \sigma(x) \eta(x). \quad (20)$$

By using the dependence of $\sigma(x)$ presented in Figure 4a and the previous results [5] we could approximate the ACS and the QY with exponential functions:

$$y(x) = y_0 + Ae^{-(x-1\,\mathrm{nm})/\Delta x}, \quad (21)$$

where y_0 is an offset, A is an amplitude and Δx is a characteristic distance.

For applications we usually aim to maximize the PL yield of photons at a certain I_{ex}. Thus, the PL intensity $I_{PL}(x)$ is a product of a decreasing ACS and an increasing QY as the inter-NC distance becomes larger. An optimum barrier thickness of $x^* \approx 1.6$ nm can be easily found as the value that maximizes the function presented in Equation 20 (Figure 4b) for our ML structures.

Temperature dependence of the ACS

Contrary to the common assumption, the ACS should be generally considered as temperature-dependent [5,29]. There are two mechanisms responsible for this dependence. First, for the phonon-assisted transitions the occupation number of phonons is an exponential function [1] of temperature containing the Bose–Einstein statistical factor:

$$N_{ph} = \left[\exp\left(\frac{\hbar\Omega_{ph}}{k_B T} \right) - 1 \right]^{-1}, \quad (22)$$

where Ω_{ph} is the typical (average) phonon energy and k_B is the Boltzmann constant.

Second, with varying temperatures the band gap of a NC is shifting. This changes the effective DOS at a certain energy. Following the phenomenological expression proposed by Cardona's group [30] we can write:

$$E_{gap}(T) = E_{gap,0} - B\left(2N_{ph} + 1\right), \quad (23)$$

where B is a temperature-independent constant related to the strength of the electron–phonon interaction, and $E_{gap,0}$ corresponds to the band gap at 0 K.

The ACS is equal [9,10] to the absorption coefficient α normalized by the volume concentration of NCs, c_V, ($\sigma = \alpha/c_V$). Finally, by substituting Equation 23 into the approximation presented by Kovalev et al. [29], the temperature dependence of the ACS at a fixed energy of absorbed photons, $\hbar\omega \gg E_g + \hbar\Omega_{ph}$, can be estimated as:

$$\sigma(T) \propto \left(2N_{ph} + 1\right)\left[\hbar\omega - E_{gap,0} + B\left(2N_{ph} + 1\right)\right]^2. \quad (24)$$

The first term on the right-hand side of Equation 24 is governed by the occupation number of phonons while the second term represents a function of the difference between photon energy and the band gap. It is also clear from Equation 24 that the higher the energy of a photon, $\hbar\omega$, the larger the expected ACS, which is in agreement with experimental observations [14,17,25]. This can be understood by considering an increase of DOS with energy.

One of the main advantages of the PL modulation technique is that it can be relatively easily carried out at low temperatures. We experimentally measured the onset and decay curves at various sample temperatures (Figure 1b) and calculated the ACS $\sigma(T)$ according to the procedure that was described in the previous section (Figure 5).

Besides a τ_r-dominated temperature interval ($T < 70$ K) [21], we observed a shortening of PL lifetimes (Figure 1b) as the temperature increases due to thermally activated non-radiative processes, τ_{nr}. We compared the SL sample and the ML sample with 2.8 nm barrier thickness. Recently [5], we showed by QY analysis that the SL sample consisting of a single thick layer of Si NCs (containing randomly distributed NCs) contains poorly separated NCs (comparable to the ML structure with barriers of 1 nm or thinner) in contrast to the ML sample with a thick barrier (2.8 nm). The routine was carried out with both samples at two emission wavelengths (800 and 850 nm) to obtain better statistics and avoid any experimental artefacts. Therefore, the

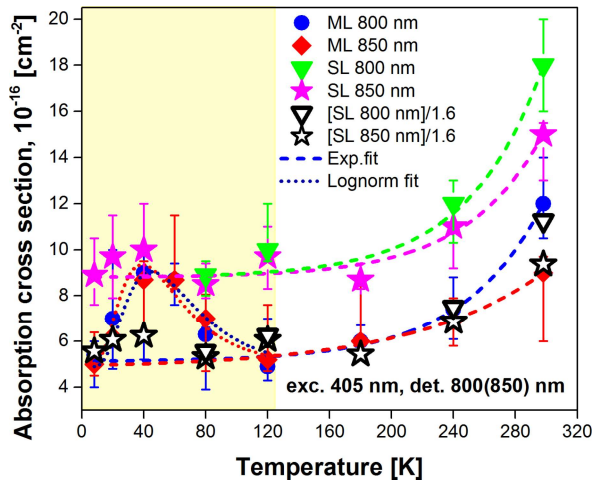

Figure 5: The variation of the ACS σ(T) of ML sample with 2.8 nm barrier thickness (circles and diamonds) and SL sample (filled triangles and stars) calculated at 800 nm (circles and upper triangles) and 850 nm (diamonds and stars). The open triangles and stars stand for the ACS of the SL sample normalized by a factor of 1.6. The dashed and dotted lines represent exponential and log-normal fits, respectively.

ACS of the SL sample is expected to be comparable with the values of ML samples with separation barriers of 1 and 1.6 nm.

In contrast to Equation 24, the temperature dependence of ACS of both samples occurred to be well described by a simple exponential function in a broad interval of temperatures (Figure 5):

$$\sigma = \sigma_0 + Ce^{(T-T_0)/\Delta T}, \qquad (25)$$

where σ_0, T_0, C and ΔT are vertical offset and horizontal shift, amplitude and characteristic temperature, respectively.

It is clear from Equation 25 and Figure 5 that the ACS σ(T) cannot be approximated with a constant value for all temperatures. Thus, there is decrease of the ACS to about one half when the temperature is decreased from room temperature to 120 K and the emission at 800 nm is measured. Independently of the inter-NC distance, we obtained a slight decrease of the ACS for longer emission wavelengths at room temperature (Figure 5). This result is qualitatively in agreement with the ACS trend reported by Garcia et al. and Garrido et al. [25,31] though an opposite behavior was presented in other papers [10,14] for the mentioned wavelengths. By definition, the ACS is an absorption characteristic of the excitation wavelength and should not be dependent on the emission wavelength of a NC. However, there is always a size distribution (inhomogeneous broadening) in an ensemble of NCs that results in ACS dispersion [2,10]. Assuming that NCs with a certain size emit photons at λ_{em}, the ACS $\sigma(\lambda_{exc}, \lambda_{em})$ should be considered as a function of both excitation and emission wavelengths [14]. Notably, when decreasing the temperature of samples below ca. 150–180 K, the ACS becomes independent (Figure 5) on the emission wavelength (i.e., the NC size). Interestingly, wavelength-independent ACS values were reported by Priolo et al. even for room-temperature measurements [17]. One may notice in Figure 5 a transition from an exponential (Equation 25) to a log-normal [32] dependence of σ(T) for the ML sample at low temperatures. This feature must be verified in future experiments. For temperatures $T \geq 120$ K, the ACS of the SL sample in comparison with the ML sample is ca. 1.6-times larger (Figure 5). Assuming that this difference is caused by energy transfer processes between NCs in the SL sample (while it is reduced in ML sample) we can conclude that this process should be temperature-independent at least for high temperatures ($T \geq 120$ K).

Conclusion

In summary, we presented a thorough study of ACS changes with inter-NC distance, σ(x), and temperature, σ(T), in Si NCs. The classical system of kinetic equations was strictly solved and the most general solution was obtained. It helped us to define the limits of the original model and correctly implement the PL modulation technique employed for ACS determination. We demonstrated that doubling the barrier thickness from about 1 to 2.2 nm results in decrease of the ACS by factor of ca. 1.5. An optimum barrier thickness of ca. 1.6 nm was calculated to obtain maximal PL brightness, which can be helpful for the construction of efficient luminescent devices. ACS changes with the barrier thickness can be due to modification of defect states and/or varying probabilities of energy transfer between NC layers. Cooling the sample below 150–180 K makes the ACS independent on the emission wavelength (800 and 850 nm). An exponential decrease of the ACS in both SL and ML samples was revealed after decreasing the temperature down to 120 K. A smaller occupation number of phonons and an expansion of the band gap of Si NCs at low temperatures were proposed to cause these phenomena.

Acknowledgments

This work was supported by the bilateral Czech–German DFG–GACR projects 16-09745J and ZA 191/36-1.

References

1. Pelant, I.; Valenta, J. *Luminescence Spectroscopy of Semiconductors;* Oxford University Press: Oxford, United Kingdom, 2012. doi:10.1093/acprof:oso/9780199588336.001.0001
2. Valenta, J.; Mirabella, S. *Nanotechnology and Photovoltaic Devices;* Pan Stanford Publishing: Stanford, CA, U.S.A., 2015. doi:10.1201/b18090

3. Dohnalová, K.; Gregorkiewicz, T.; Kůsová, K. *J. Phys.: Condens. Matter* **2014,** *26,* 173201. doi:10.1088/0953-8984/26/17/173201
4. Zacharias, M.; Heitmann, J.; Scholz, R.; Kahler, U.; Schmidt, M.; Bläsing, J. *Appl. Phys. Lett.* **2002,** *80,* 661–663. doi:10.1063/1.1433906
5. Valenta, J.; Greben, M.; Gutsch, S.; Hiller, D.; Zacharias, M. *Appl. Phys. Lett.* **2014,** *105,* 243107. doi:10.1063/1.4904472
6. Hartel, A. M. Structural and Optical Properties of PECVD Grown Silicon Nanocrystals Embedded in SiO_xN_y Matrix. Ph.D. Thesis, Albert-Ludwigs University, Freiburg, Germany, 2013.
7. Poddubny, A. N.; Prokofiev, A. A.; Yassievich, I. N. *Appl. Phys. Lett.* **2010,** *97,* 231116. doi:10.1063/1.3525375
8. Yu, P.; Beard, M. C.; Ellingson, R. J.; Ferrere, S.; Curtis, C.; Drexler, J.; Luiszer, F.; Nozik, A. J. *J. Phys. Chem. B* **2005,** *109,* 7084–7087. doi:10.1021/jp046127i
9. Hens, Z.; Moreels, I. *J. Mater. Chem.* **2012,** *22,* 10406–10415. doi:10.1039/c2jm30760j
10. Valenta, J.; Greben, M.; Remeš, Z.; Gutsch, S.; Hiller, D.; Zacharias, M. *Appl. Phys. Lett.* **2016,** *108,* 23102. doi:10.1063/1.4939699
11. Hartel, A. M.; Hiller, D.; Gutsch, S.; Löper, P.; Estradé, S.; Peiró, F.; Garrido, B.; Zacharias, M. *Thin Solid Films* **2011,** *520,* 121–125. doi:10.1016/j.tsf.2011.06.084
12. Valenta, J.; Greben, M. *AIP Adv.* **2015,** *5,* 47131. doi:10.1063/1.4918970
13. Kovalev, D.; Heckler, H.; Polisski, G.; Koch, F. *Phys. Status Solidi B* **1999,** *215,* 871–932. doi:10.1002/(SICI)1521-3951(199910)215:2<871::AID-PSSB871>3.0.CO;2-9
14. Kovalev, D.; Diener, J.; Heckler, H.; Polisski, G.; Künzner, N.; Koch, F. *Phys. Rev. B* **2000,** *61,* 4485–4487. doi:10.1103/PhysRevB.61.4485
15. Trinh, M. T.; Limpens, R.; Gregorkiewicz, T. *J. Phys. Chem. C* **2013,** *117,* 5963–5968. doi:10.1021/jp311124c
16. Mahdouani, M.; Bourguiga, R.; Jaziri, S.; Gardelis, S.; Nassiopoulou, A. G. *Physica E* **2009,** *42,* 57–62. doi:10.1016/j.physe.2009.08.020
17. Priolo, F.; Franzò, G.; Pacifici, D.; Vinciguerra, V.; Iacona, F.; Irrera, A. *J. Appl. Phys.* **2001,** *89,* 264–272. doi:10.1063/1.1331074
18. Pavesi, L.; Dal Negro, L.; Mazzoleni, C.; Franzò, G.; Priolo, F. *Nature* **2000,** *408,* 440–444. doi:10.1038/35044012
19. Nguyen, A.; Gonzalez, C. M.; Sinelnikov, R.; Newman, W.; Sun, S.; Lockwood, R.; Veinot, J. G. C.; Meldrum, A. *Nanotechnology* **2016,** *27,* 105501. doi:10.1088/0957-4484/27/10/105501
20. Brown, S. L.; Miller, J. B.; Anthony, R. J.; Kortshagen, U. R.; Kryjevski, A.; Hobbie, E. K. *ACS Nano* **2017,** *11,* 1597–1603. doi:10.1021/acsnano.6b07285
21. Hartel, A. M.; Gutsch, S.; Hiller, D.; Zacharias, M. *Phys. Rev. B* **2013,** *87,* 35428. doi:10.1103/PhysRevB.87.035428
22. Linnros, J.; Lalic, N.; Galeckas, A.; Grivickas, V. *J. Appl. Phys.* **1999,** *86,* 6128–6134. doi:10.1063/1.371663
23. Nikolaev, I. S.; Lodahl, P.; van Driel, A. F.; Koenderink, A. F.; Vos, W. L. *Phys. Rev. B* **2007,** *75,* 115302. doi:10.1103/PhysRevB.75.115302
24. Greben, M.; Valenta, J. *Rev. Sci. Instrum.* **2016,** *87,* 126101. doi:10.1063/1.4971368
25. Garcia, C.; Garrido, B.; Pellegrino, P.; Ferre, R.; Moreno, J. A.; Morante, J. R.; Pavesi, L.; Cazzanelli, M. *Appl. Phys. Lett.* **2003,** *82,* 1595–1597. doi:10.1063/1.1558894
26. Rinnert, H.; Jambois, O.; Vergnat, M. *J. Appl. Phys.* **2009,** *106,* 23501. doi:10.1063/1.3169513
27. Sangghaleh, F.; Bruhn, B.; Schmidt, T.; Linnros, J. *Nanotechnology* **2013,** *24,* 225204. doi:10.1088/0957-4484/24/22/225204
28. Pavesi, L. *J. Appl. Phys.* **1996,** *80,* 216–225. doi:10.1063/1.362807
29. Kovalev, D.; Polisski, G.; Ben-Chorin, M.; Diener, J.; Koch, F. *J. Appl. Phys.* **1996,** *80,* 5978–5983. doi:10.1063/1.363595
30. Lautenschlager, P.; Garriga, M.; Vina, L.; Cardona, M. *Phys. Rev. B* **1987,** *36,* 4821–4830. doi:10.1103/PhysRevB.36.4821
31. Garrido, B.; López, M.; Pérez-Rodriguez, A.; Garcia, C.; Pellegrino, P.; Ferré, R.; Moreno, J.; Morante, J.; Bonafos, C.; Carrada, M.; Claverie, A.; de la Torre, J.; Souifi, A. *Nucl. Instrum. Methods Phys. Res., Sect. B* **2004,** *216,* 213–221. doi:10.1016/j.nimb.2003.11.037
32. Bohm, G.; Zech, G. *Introduction to Statistics and Data Analysis for Physicists;* Verlag Deutsches Elektronen-Synchrotron: Hamburg, Germany, 2010.

License and Terms

Paper II

JOURNAL OF APPLIED PHYSICS **122**, 034304 (2017)

Fully radiative relaxation of silicon nanocrystals in colloidal ensemble revealed by advanced treatment of decay kinetics

Michael Greben,[1,a)] Petro Khoroshyy,[2] Xiangkai Liu,[3] Xiaodong Pi,[3] and Jan Valenta[1]
[1]*Department of Chemical Physics and Optics, Faculty of Mathematics and Physics, Charles University, Ke Karlovu 3, 121 16 Prague 2, Czechia*
[2]*Laboratory of Advanced Optical Microscopy, Institute of Organic Chemistry and Biochemistry, Czech Academy of Sciences, Flemingovo namesti 2, 160 00 Prague 6, Czechia*
[3]*State Key Laboratory of Silicon Materials and School of Materials Science and Engineering, Zhejiang University, Hangzhou, Zhejiang 310027, China*

(Received 17 May 2017; accepted 29 June 2017; published online 18 July 2017)

A comprehensive study of the spectrally resolved photoluminescence (PL) decay kinetics of dodecyl-passivated colloidal silicon nanocrystals (Si NCs) is presented. The correct treatment of average decay lifetime is demonstrated. We report on importance to distinguish the external quantum efficiency (QE) from the internal QE. The external QE of the ensemble of Si NCs is measured to be ~60%, while the internal QE of Si NCs emitting around ~1.5 eV is evaluated to be near unity. This difference between internal and external QE is attributed to a fraction of "dark" (absorbing but non-emitting) Si NCs in the ensemble. This conclusion is based on the analysis of deconvoluted size-selected decay curves retrieved by the presented mathematical procedure. The homogeneous line-broadening is estimated to be around 180 meV by experimentally challenging single-NC PL measurements. In addition, radiative lifetimes are calculated by the envelope function approximation and confirm the observed exponential increase of lifetime with decreasing emission photon energy. *Published by AIP Publishing.* [http://dx.doi.org/10.1063/1.4993584]

I. INTRODUCTION

Nanocrystalline silicon (Si) is a very promising material for a series of important applications such as photovoltaics,[1–4] optoelectronics,[5,6] and biolabelling.[7,8] In spite of the recent tremendous development of single-dot techniques,[9] the fundamental knowledge of deexcitation dynamics in Si nanocrystal (NC) ensembles is still poor. The decay of single Si NC was first theoretically described[10] and then experimentally confirmed recently[11] to be rather monoexponential at room temperature (RT) in the microsecond time-scale. Although nearly monoexponential slow decays of Si NCs embedded in SiO_2 were reported,[12,13] the non-exponential photoluminescence (PL) decay is generally a marker of an ensemble of Si NCs. The origin of this complex behavior is still under debate, while a set of different models were proposed: a distribution of NC radiative[10] and/or non-radiative[11] rates, interaction of matrix-embedded NCs,[14] NC blinking,[15] or even homogeneous line-broadening (HLB) effect.[16] The latter effect together with the inhomogeneous line-broadening (ILB) due to the NC size distribution complicates studies of fundamental PL properties of Si NC ensembles. Despite a recent dramatic breakthrough in the size-separation of monodisperse fractions of Si NCs,[17] there are still many challenges in the preparation of NCs of highly uniform sizes, shapes, surface passivation, etc. In the same time, a broad homogeneous linewidth of Si NCs influences both PL emission spectra and time-resolved (TR) kinetics of NC ensemble.

II. MATERIALS AND METHODS

Si NCs were synthesized by nonthermal plasma.[18,19] The powder of Si NCs was treated with HF acid to ensure hydrogen passivation at the NC surface after the transfer in air from the synthesis system. The mixture of 1-dodecene and mesitylene was then used to hydrosilylate Si NCs at 165 °C in the atmosphere of Ar. After hydrosilylation, rotatory evaporation was performed to remove the remaining 1-dodecene and mesitylene. The resulting dodecyl-passivated Si NCs were finally dispersed in toluene to form a colloid. The average size of NCs was estimated to be around 3.3 nm by transmission electron microscopy (TEM) characterization.

The PL external quantum yield (QY) was measured using an integrating sphere (IS) with 10-cm diameter, covered by Spectraflex (Sphere Optics). To excite the sample, we used the laser-driven light source (EQ-99X, Enegetiq) coupled to the 15-cm monochromator (Acton SpectraPro SP-2150i) and connected with IS via a silica fibre bundle (excitation peak FWHM is ~6 nm, typical power 3–8 μW) with an excitation wavelength of 405 nm. The detection system is the same as described below.

TR PL experiments were performed under excitation by a 405-nm diode laser whose beam was modulated using a quartz acousto-optic cell. The resulting square-shaped pulses have the edge switching time of about 100 ns. The laser is coupled to a homemade micro-spectroscopy set-up with an inverted microscope (Olympus IX-71) in the epi-fluorescence configuration. There are two detection branches for visible (VIS) and near-infrared (NIR) spectral regions, each one composed of an imaging spectrometer (Acton SpectraPro SP-2358i and SP-2558i, respectively) and a photomultiplier (PMT) for time-resolved PL detection (Hamamatsu H11526-20-NF and H10330A-45, respectively, for VIS and NIR). Pulses from PMTs are detected by two multichannel counting cards (Becker-Hickl, MSA-300).

[a)]leibnits@gmail.com

More details on the set-up can be found in our recent paper.[20]

PL spectra of single Si NCs were measured in a droplet of highly diluted suspension placed between two silica cover glasses. PL was excited by a continuous 405-nm diode laser through an objective lens and collected by the same lens (50×/0.6) in an inverted microscope (Olympus IX-71). PL spectra were dispersed and detected by an imaging spectrograph (Acton SpectraPro SP-2358i) coupled to a back-illuminated CCD (PI Acton Spec-10:400BR/LN).

III. RESULTS AND DISCUSSION

To overcome above mentioned issues, we employed a computer modelling in combination with theoretical calculations. We successfully deconvoluted size-selected PL lifetimes and dispersion factors of the stretched exponential (SE) decays. A transition from spectrally resolved non-exponential to size-selected monoexponential decay was revealed for NCs emitting around 1.5 eV, which indicates 100% internal quantum efficiency (IQE) for that size of NCs.[16] The obtained decay lifetimes occurred to be in a good agreement with theoretically calculated ones. There are only a few studies of IQE of Si NCs embedded in SiO_2 (Refs. 21–23), and to our best knowledge, only 1 report on IQE of colloidal Si NCs.[16] For embedded Si NCs, IQE was calculated by decoupling the radiative and non-radiative decay channels using a variation of the Purcell factor[24] by proximity of a reflecting interface in specially prepared structures. However, the IQE of colloidal Si NCs normally stays elusive because of a lack of a procedure to probe it directly. This work brings a new fundamental knowledge on IQE of an ensemble of free standing Si NCs.

A. Decay kinetics fitting models

The investigated material was a toluene suspension of plasma-synthesized SiNCs passivated by dodecyl. Figure 1(a) shows spectrally resolved PL transients measured at different emission energies of the sample. All PL decay curves reveal non-exponential decay dynamics and can be well fitted by using the classical stretched exponential (SE) function

$$I(t) = I(0)e^{-(t/\tau_0)^{\beta}} + background, \tag{1}$$

where τ_0 is the PL lifetime parameter (constant) and β is the dispersion factor (varies from 0 to 1), *background* represents a "constant" signal background level of a detector (e.g., photomultiplier).

The high quality of SE fits does not exclude other possible decay models. Thus, we applied a set of fitting models and compared the results. The most straight-forward approach is to try the multi-exponential (ME) fit

$$I(t) = \sum_{i=1}^{N} A_i e^{-(t/\tau_i)} + background, \tag{2}$$

where A_i and τ_i are amplitudes and lifetime parameters, accordingly, and N is the number of exponential components.

Another model was applied for Si NCs in a couple of papers,[25,26] which imply the lognormal (LN) distribution of decay rates. The decay signal could be modeled by taking the Laplace transform of the decay rate probability density function (PDF) $f(k)$

$$I(t) = I(0)\int_0^{\infty} f(k)e^{-(kt)}dk + background, \tag{3}$$

where $f(k)$ for LN distribution of decay rates k is given by

$$f(k) = Ae^{-\left(\frac{\ln(k/k_m)}{\sinh^{-1}(k_d/2k_m)}\right)^2}, \tag{4}$$

where k_m and k_d represent the most frequent total decay rate and the width of rate distribution, respectively; A is an amplitude.

The average recombination time of emitted photons could be generally calculated[27] as

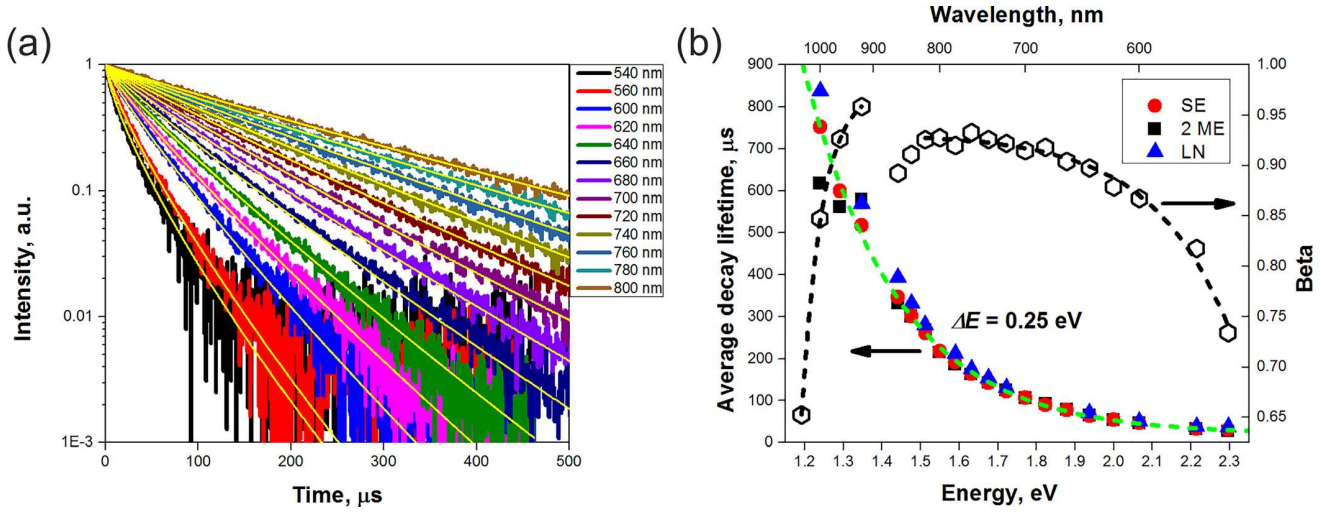

FIG. 1. (a) Experimental PL decay curves of Si NCs and their corresponding fits by Eq. (14) for different emission wavelengths. (b) PL average lifetimes obtained by fitting with different decay models as well as dispersion factor β of SE fits in dependence on emission photon energy. The dashed green line is an exponential fit of SE average lifetimes, while dashed black lines correspond to exponential fits of dispersion factors β.

$$\bar{\tau} = \frac{\int_0^\infty tI(t)dt}{\int_0^\infty I(t)dt}. \quad (5)$$

Taking the SE [Eq. (1)] and ME [Eq. (2)] decay signals and introducing them into Eq. (5), we obtain

$$\bar{\tau}_{SE} = \Gamma\left(\frac{2}{\beta}\right)/\Gamma\left(\frac{1}{\beta}\right)\tau_0, \quad (6)$$

$$\bar{\tau}_{ME} = \sum_{i=0}^{N} A_i\tau_i^2 \Big/ \sum_{i=0}^{N} A_i\tau_i, \quad (7)$$

where Γ corresponds to gamma-function.

To calculate the average decay lifetime $\bar{\tau}_{LN}$ of LN decay model, we had to compute numerically the Eq. (5) as there is no simple analytical representation.

B. Lifetime dispersion

In fact, all the above mentioned models fit the measured curves quite well, whereas the extracted distributions of lifetimes are expectedly different. Nevertheless, the calculated average lifetimes are almost the same within an experimental error for emission energies above 1.5 eV. For too long lifetimes ($E < 1.5$ eV), it becomes difficult to acquire high quality decay curves without truncation and overexcitation.[28] Consequently, some uncertainty appears in background extraction and the average lifetimes given by different models are not the same. The final extracted average lifetimes are presented in Fig. 1(b). The lifetime is increasing exponentially ($\Delta E = 0.25$ eV) with increasing size of NCs [Fig. 1(b)] that is in remarkable agreement with previous reports[29,30]

$$\bar{\tau} = Ae^{-\frac{E}{\Delta E}}. \quad (8)$$

This strong spectral dispersion of recombination lifetimes is well known for Si NCs and can be qualitatively explained by the quantum confinement (QC) model.

The radiative lifetime is related to the oscillator strength (OS) as[31,32]

$$\frac{1}{\tau_r} = \frac{n}{\tau_r^{vac}} = \frac{2ne^2}{\hbar^2 m_0 c^3} E_{mn}^2 f(E_{mn}), \quad (9)$$

where τ_r^{vac} is the radiative lifetime in vacuum, n is the refractive index of the medium, E_{mn} is the transition photon energy ($E_{mn} = E_m - E_n$) and $f(E_{mn})$ is its corresponding oscillator strength, e and m_0 are the free-electron charge and mass, respectively, $\hbar$ is the reduced Planck's constant, and c stands for the speed of light in vacuum.

The PL decay lifetime τ_{PL} is a product of both radiative τ_r and non-radiative τ_{nr} lifetimes

$$\frac{1}{\tau_{PL}} = \frac{1}{\tau_{nr}} + \frac{1}{\tau_r}. \quad (10)$$

With the decreasing size of NCs, the emission energy E_{mn} increases as a direct consequence of the quantum confinement (QC) effect and the oscillator strength enhances owing to the breakdown of the k-conservation rule as well as a better overlap of electron and hole wavefunctions. Since, in general, nonradiative lifetimes are much less dependent on the gap,[15] the shortening of PL decay lifetime is expected [see Eq. (9)] for smaller NCs (larger E_{mn}). Another interpretation[33] of exponential spectral lifetime dependence [Eq. (8)] implies an escape of excited carriers by tunneling through NC barriers into a surrounding medium. To generalize, the variation in size changes the PL lifetime from the ns-range ($d \sim 1$ nm, quasi-direct transitions) to the μs-range ($d \sim$ few nm) and even the ms-range (bulk Si).

Since the decay of single Si NC is expected to be monoexponential,[11] the dispersion factor $\beta \leq 1$ in the SE model should be considered as a characteristics of an ensemble of NCs. The larger is the dispersion of lifetimes (rates), the lower[11] is the parameter β. The dependence of $\beta(E)$ on emission energy is presented in Fig. 1(b). Two energy intervals could be clearly distinguished: exponential increase (above 1.5 eV) and then steep decrease (below 1.4 eV) of $\beta(E)$ with decreasing energy (increasing NC size). In the region around 1.5 eV, a discontinuity of $\beta(E)$ appears that could also be found in the paper by Sangghaleh *et al.*[16] Although we do not exclude possible physical origin of that there are two important arguments pointing that it could be nothing else but experimental artifact. First, the considered interval is staying on the edge of detection sensitivity limit[20] and the calculations could suffer from lower precision. Second, the solvent (toluene) has an absorption features around 1.4 eV (Ref. 34) that could obscure the results. Therefore, improved experiments with different detectors optimized for this spectral region have to be conducted to investigate this anomaly that is apart from the current study.

C. Homogeneous and inhomogeneous broadening

The PL linewidth of an ensemble of nanocrystals is a product of both homogeneous and inhomogeneous broadening. The HLB is a characteristic of each single NC that is mainly a consequence of exciton-phonon interactions. Reducing temperature or embedding NCs in a proper matrix can reduce HLB.[35] At RT, the emission of individual Si NCs is quite broad with FWHM up to $\Delta E \sim 150$ meV (Ref. 36) for matrix-embedded NCs and up to $\Delta E \sim 200$ meV for free-standing ones.[35] In comparison with direct-band-gap quantum dots such homogeneous linewidth is significantly broader and its origin remains unclear. In its turn, a size distribution in an ensemble of nanocrystals results in ILB that dominantly influences the overall emission spectrum.[31] This effect could be much suppressed by preparation of NCs of nearly uniform size.[17] The spectral influence of HLB on the emission spectrum of an ensemble of Si NCs was previously considered in a couple of papers.[31,37] Surprisingly, the impact of HLB on TR PL results was ignored and to our best knowledge was considered only recently.[16]

It is generally supposed[38] that the PL emission energy (wavelength) probes the decay lifetime of a specific size of NCs in an ensemble. Then, according to the QC model (see Sec. III B), the PL lifetime is expected to vary with energy independently on the size distribution of the nanocrystals.

However, there are two important aspects that have to be kept into account. First, the kinetics of single-size NCs is not necessarily monoexponential because of possible dispersion of decay rates for different reasons. This rate dispersion could be ensemble-dependent. Second, the idea that a spectrally resolved decay is a characteristic of a certain size of NCs in an ensemble strictly speaking is not correct. Even in case that spectrally resolved PL decay is measured using a spectrometer with an infinitely narrow slit at a detection energy E_{det}, there is a contribution from nanocrystals of different sizes to the measured signal [because of the broad emission line (HLB) of even a single NC]. Therefore, in this paper, we distinguish spectrally resolved and size-selected decays. Under spectrally resolved decay, we mean a decay measured at a certain photon energy (wavelength), whereas a size-selected decay is related to TR dynamics of NCs having a certain size. In other words, a spectrally resolved decay is a convolution of some distribution of size-selected decays.

The mathematical fitting-free procedure of extracting size-selected decays and corresponding intrinsic lifetimes from spectrally resolved decays was described recently by Sangghaleh *et al.*[16] It was *a priori* assumed that individual decays of size-selected NCs are monoexponential and therefore 100% efficient. In this paper, we introduce the unique procedure to resolve size-selected decays without this assumption.

D. Deconvolution of size-selected decays

First, we assume our NCs as non-interacting, i.e., any energy transfer between them is not permitted. This assumption is believed to be true as we deal with free-standing Si NCs in a suspension where NCs are far apart compared to a film. Second, strictly speaking, we should consider each NC size to act as an inhomogeneously broadened emitter having a Gaussian distribution of photon energies [see Fig. 2(c)] with a mean value ε and standard deviation ω_{hom} (this effect

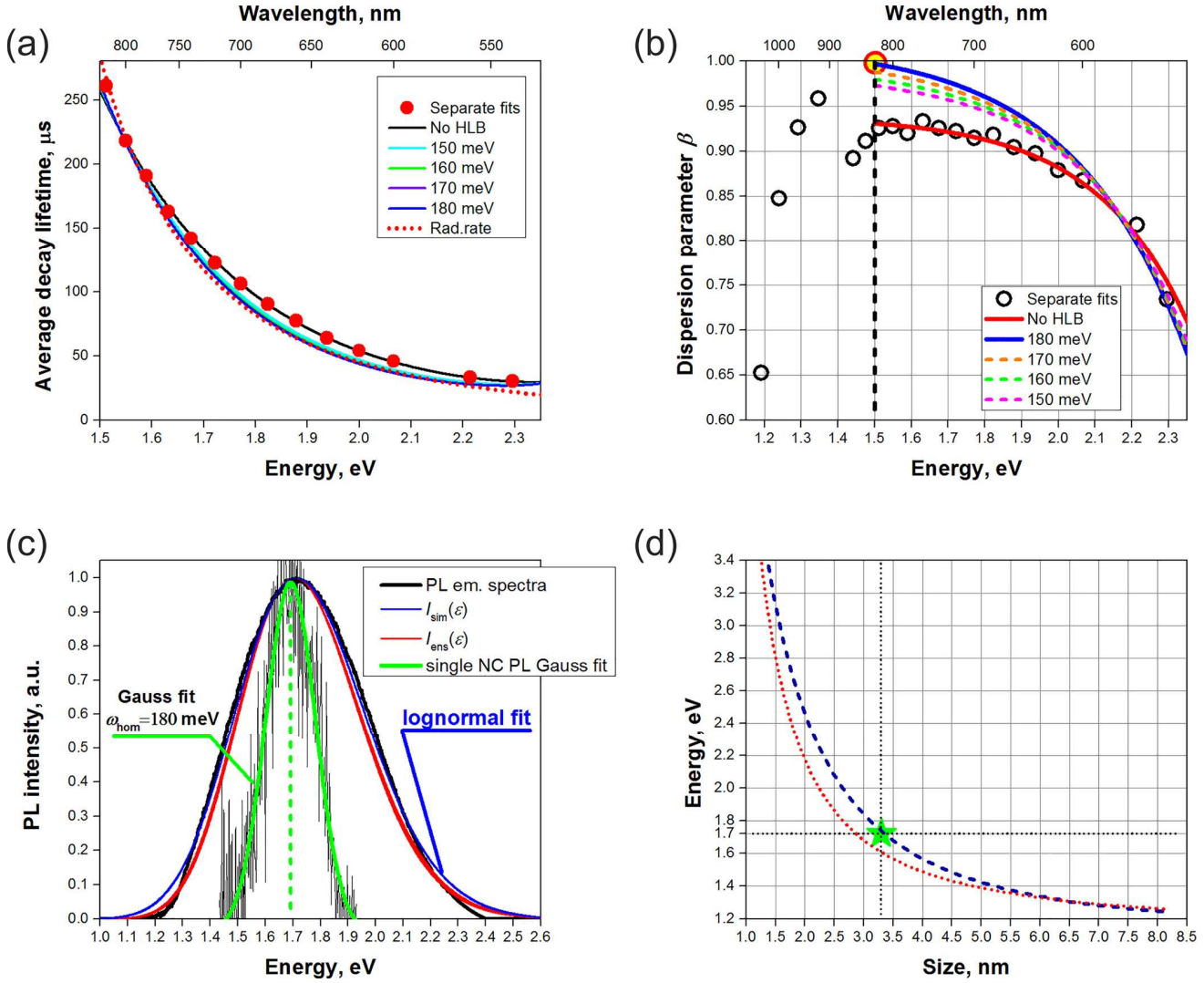

FIG. 2. Spectral distribution of average PL decay lifetimes (a) and dispersion factors (b) obtained from separate SE fits (red dots) [see Fig. 1(a)] compared to the values retrieved for different ω_{hom} (solid lines). The dotted line was theoretically calculated by EFA modelling. (c) PL emission spectra of single Si NC and ensemble of NCs (black lines). The fit $I_{sim}(\varepsilon)$ of PL spectrum by the lognormal distribution function (blue line) and accordingly retrieved size-selected PL amplitudes $I_{ens}(\varepsilon)$ (red line) of the ensemble of Si NCs. The Gauss fit of single Si NC PL spectrum (green line) gives homogeneous linewidth of 180 meV. (d) Dependence of the optical bandgap of Si NCs on the NC size modelled by Eq. (19) (dashed line) and Eq. (20) (dotted line) as well as experimentally measured (green star).

can take place due to variations of NC shapes, surface states, etc.). Although we do not expect a significant difference in homogeneous broadening of single NC and inhomogeneous broadening of monodisperse ensemble of the same size NCs, we will further distinguish "homogeneous" broadening of single size NCs and inhomogeneous broadening of the whole ensemble of Si NCs due to the size dispersion. Also, we assign the epsilon symbol ε that represents an energy to underline the size-selected nature of an energy-dependent quantity in contrast to symbol E used in Sec. III B. Consequently, the PL intensity of size-selected NCs with mean emission energy ε that contribute to the detected signal at energy E_{det} is given by

$$I_{\mathrm{det}}(\varepsilon) = I_{ens}(\varepsilon) e^{-2\frac{(E_{\mathrm{det}}-\varepsilon)^2}{\omega_{\mathrm{hom}}^2}}, \tag{11}$$

where $I_{ens}(\varepsilon)$ represents the amplitude of size-selected PL intensity at mean energy ε.

Now, it is evident that we have to retrieve the PL spectrum of size-selected PL amplitudes $I_{ens}(\varepsilon)$ in order to compute the individual decays $I_{\mathrm{det}}(\varepsilon)$. The experimental PL spectrum itself does not represent these amplitudes as it stands as a convolution of many individual homogeneously broadened PL spectra.

It is well known that Si NCs exhibit the lognormal size distribution in most cases,[37] and therefore, we could approximate

$$I_{ens}(\varepsilon) = e^{-\frac{\log(\varepsilon/E_0)^2}{2\omega_{ens}^2}}, \tag{12}$$

where E_0 corresponds to the mean size, and ω_{ens} is the width parameter for the shape profile.

Finally, the normalized PL emission spectrum is simulated as

$$I_{sim}(E_{\mathrm{det}}) = \int_{\varepsilon} I_{\mathrm{det}}(\varepsilon) d\varepsilon = \int_{\varepsilon} e^{-\frac{\log(\varepsilon/E_0)^2}{2\omega_{ens}^2}} e^{-2\frac{(E_{\mathrm{det}}-\varepsilon)^2}{\omega_{\mathrm{hom}}^2}} d\varepsilon. \tag{13}$$

Then, by minimizing the difference between experimentally measured and simulated spectra $(I_{\exp}(E_{\mathrm{det}}) - I_{sim}(E_{\mathrm{det}}))$ for all emission energies E_{det}, we could obtain fitting parameters E_0 and ω_{ens}. The overall simulated PL emission spectrum $I_{sim}(\varepsilon)$ and the retrieved size-selected PL amplitudes $I_{ens}(\varepsilon)$ are presented in Fig. 2(c) considering ω_{hom} between 150 and 180 meV. The obtained fit parameters (E_0 and ω_{ens}) are 1.739 eV, 136.4 meV and 1.735 eV, 126.1 meV, respectively. The latter ones were used to model size-selected amplitudes $I_{ens}(\varepsilon)$ in further simulations.

In the most general case, there is some lifetime distribution even for monodisperse NCs as it was shown recently.[17] Therefore, we consider here that size-selected decays have stretched exponential form $I_{\mathrm{det}}(\varepsilon) e^{-\left(\frac{t}{\tau_{0i}(\varepsilon)}\right)^{\beta_i(\varepsilon)}}$. Finally, a spectrally resolved decay curve for a given detection energy E_{det} can be numerically constructed as a combination of individual size-selected decays

$$\begin{aligned} I_{\mathrm{det}}^{sim}(t) &= \int I_{\mathrm{det}}(\varepsilon) e^{-\left(t/\tau_{0i}(\varepsilon)\right)^{\beta_i(\varepsilon)}} d\varepsilon \\ &= \int_{\varepsilon} e^{-\frac{\log(\varepsilon/E_0)^2}{2\omega_{ens}^2}} e^{-2\frac{(E_{\mathrm{det}}-\varepsilon)^2}{\omega_{\mathrm{hom}}^2}} e^{-\left(t/\tau_{0i}(\varepsilon)\right)^{\beta_i(\varepsilon)}} d\varepsilon. \end{aligned} \tag{14}$$

On the other hand, the fit of our normalized experimentally measured decay curve is presented in the form

$$I_{\mathrm{det}}^{\exp}(t) = e^{-\left(t/\tau_e(E_{\mathrm{det}})\right)^{\beta_e(E_{\mathrm{det}})}}. \tag{15}$$

After minimization of the difference $(I_{\mathrm{det}}^{\exp}(t) - I_{\mathrm{det}}^{sim}(t))$ sets of $\boldsymbol{\tau_{oi}}(E_{\mathrm{det}})$ and $\boldsymbol{\beta_i}(E_{\mathrm{det}})$ are obtained as fitting parameters. The issue is that $\boldsymbol{\tau_{oi}}(E_{\mathrm{det}})$ and $\boldsymbol{\beta_i}(E_{\mathrm{det}})$ are vectors, and while dealing with a huge number of fitting parameters, we have only 1 equation and only one pair of experimentally measured $\tau_e(E_{\mathrm{det}})$ and $\beta_e(E_{\mathrm{det}})$ for a given energy E_{det}.

Although it seems to be impossible to solve this inverse problem, there is a trick to do it. From Fig. 1(b), it is clear that both the lifetime and dispersion factor are functions of emission energy. In contrast to the exponential average lifetime dependence [Eq. (8)], we could approximate the spectral dispersion of lifetime parameter in the form of Boltzmann sigmoidal function

$$\tau_{oi}(\varepsilon) = A_1 + \frac{A_2 - A_1}{1 + e^{\frac{(\varepsilon - x_0)}{dx}}}, \tag{16}$$

where A_1, A_2, x_0, and dx are some parameters.

In its turn, the energy dependence of dispersion factor is clearly exponential for energies above 1.5 eV [see Fig. 1(b)]

$$\beta_i(\varepsilon) = B_1 + B_2 e^{\frac{\varepsilon - y_0}{dy}}, \tag{17}$$

where B_1, B_2, y_0, and dy is the second set of 4 parameters.

Thus, energy interval only above 1.5 eV was considered for modelling. It is noteworthy that energy $E = 1.5$ eV, where the exponential dependence of dispersion factor is interrupted, is related to the Si NC size $a_B = 4.5$ nm [see Fig. 2(d)] which roughly corresponds to the Bohr exciton radius of silicon.[1] In fact, using Eqs. (16) and (17), we replace a high number of unknown fitting parameters $\tau_{oi}(\varepsilon)$ and $\beta_i(\varepsilon)$ by only eight fitting parameters. If neglecting the HLB (taking $\omega_{\mathrm{hom}} \to 0$), we should get $I_{ens}(\varepsilon) = I_{sim}(\varepsilon)$ and $\tau_{oi}(E_{\mathrm{det}}) = \tau_e(E_{\mathrm{det}})$, $\beta_i(E_{\mathrm{det}}) = \beta_e(E_{\mathrm{det}})$ [see Figs. 2(a) and 2(b)]. This is an important step to check whether the modelled parameters describe well the ones obtained by separate fits. For a real broad linewidth ω_{hom}, the energy dependencies of size-selected lifetime parameters and the dispersion factor are generally unknown but we assume them to have the same forms as given in Eqs. (16) and (17). The validity of such an assumption could be assessed by controlling the quality of simulated decay curve fits. Indeed, the fits presented in Fig. 1(a) are good independently on the chosen linewidth ω_{hom}. Finally, we obtain eight fitting parameters in the Eq. (14) by fitting the measured decays for every E_{det}. The average decay lifetimes were constructed by putting Eqs. (16) and (17) into Eq. (6). The retrieved individual size-selected average decay lifetimes and dispersion factors for different ω_{hom} are presented in Figs. 2(a) and 2(b).

Dispersion factors of size-selected decays are gradually increasing with energy decrease (size increase) and they reach the value near unity at the edge of considered interval ($E = 1.5$ eV). This means that size selected decay at this energy is monoexponential which indicates the lack of

dispersion in lifetimes for corresponding size of NCs. The most straight forward explanation of this fact is the absence of any competitive non-radiative channels. Therefore, Si NCs of the corresponding size should have IQE of 100% (see Sec. III E).[16] Our results are in agreement with work of Miura *et al.*[21] where IQE was reported to reach 100% for large NCs emitting in a limited energy range (1.4–1.5 eV). To estimate the "homogeneous" broadening of size-selected decays, we have measured PL spectra of single NCs at the energy next to the PL emission peak [see Fig. 2(c)]. Indeed, we obtained $\omega_{\text{hom}} \sim 180\,\text{meV}$ that according to our modelling results in $\beta_i(1.5\,\text{eV}) \approx 1$ [see Fig. 2(b)]. The fact that size-selected $\beta_i(\varepsilon)$ are higher than spectrally resolved $\beta_e(\varepsilon)$ is expected as partial overlapping of different individual decays introduces more lifetime dispersion and eventually lowering the dispersion factor $\beta_e(\varepsilon)$.

E. Envelope function approximation (EFA) lifetime calculations

One may notice in Fig. 2(b) that the dispersion factor is close to 1 for photon energy around 1.5 eV that suggests the absence of (dispersive) non-radiative decay channels; it means $\tau_{PL} \approx \tau_r$. Let us compare the experimentally obtained decay times with theoretical calculation of $\tau_r(\varepsilon)$ employing the envelope function approximation (EFA) described in detail by Belyakov *et al.*[37] The general idea is that the probability of recombination per unit time (emission rate) for a given phonon-assisted transition (only TO and LO modes are taken into account as TA phonon contribution is negligible) could be computed using Fermi's golden rule and the second order perturbation theory

$$W = \frac{2\pi}{\hbar}|M_{12}|^2\delta\left(\varepsilon_g(R) - \hbar\omega \pm \hbar\omega_0\right), \tag{18}$$

where $\delta(E - E' - \hbar\omega \pm \hbar\omega_0)$ is the Dirac delta-function that reflects the energy conservation law for the electron transition and the sign $\pm$ corresponds to absorption or emission of a phonon with energy $\hbar\omega_0$, $\varepsilon_g(R)$ is the optical bandgap of the NC of radius R, $\hbar\omega$ stands for the photon energy, and M_{12} is the matrix element that envelops electron-photon and electron-phonon interaction operators.

One of the main challenges of Eq. (18) is the conversion $\varepsilon_g(R)$ of the NC size into the optical bandgap. In Ref. 37, the following conversion formula was presented:

$$\varepsilon_g(R[\text{nm}]) = \sqrt{\varepsilon_{\text{bulk}}^2 + \frac{4.8\text{eV}^2\times\text{nm}^2}{R^2}}, \tag{19}$$

where $\varepsilon_{\text{bulk}} = 1.12\,\text{eV}$ is the bulk bandgap of silicon, and R is the NC radius in nanometres.

Recently, another relationship between $\varepsilon_g(R)$ and NC radius R was introduced for dodecyl passivated Si NCs[18]

$$\varepsilon_g(R[\text{nm}]) = \varepsilon_{\text{bulk}} + \frac{0.83}{2R}\frac{\text{eV}}{\text{nm}} + \frac{2.56}{4R^2}\frac{\text{eV}}{\text{nm}^2}. \tag{20}$$

Although for sizes above exciton Bohr radius a_B, both the above mentioned lines are almost the same [see Fig. 2(d)], for smaller NCs, there is a significant difference. We have used the conversion presented in Eq. (19) for EFA calculations as it describes the mean size of our sample more accurately [see Fig. 2(d)].

As our NCs are not in a vacuum, but are immersed in a medium (toluene), it is important to keep into account the correction by Purcell factor F_P

$$\frac{1}{\tau_{PL}^T(\varepsilon)} = F_P\frac{1}{\tau_{PL}^{vac}(\varepsilon)}, \tag{21}$$

where $\tau_{PL}^T(\varepsilon)$ and $\tau_{PL}^{vac}(\varepsilon)$ are radiative lifetimes of NCs in toluene and in a vacuum, accordingly.

In its turn, the Purcell factor could be calculated[39] as

$$F_P = \sqrt{\varepsilon_T}f(\varepsilon_T), \tag{22}$$

where $\varepsilon_T = 2.38$ is the dielectric constant of toluene, and $f(\varepsilon_T)$ describes the local field factor

$$f(\varepsilon_T) = \left(\frac{3\varepsilon_T}{\varepsilon_{Si} + 2\varepsilon_T}\right)^2, \tag{23}$$

where $\varepsilon_{Si} = 12$ is the dielectric constant of silicon.

The correction of Eq. (22) is encompassed in Eq. (18). The close correspondence between the final calculated radiative lifetimes and retrieved size-selected lifetimes is presented in Fig. 2(a). This indicates that the possible reason for lifetime dispersion is the distribution of radiative lifetimes[10] and the absence of non-radiative recombination channels.

F. The fraction of bright and dark Si NCs in an ensemble

In general, we have to distinguish external (EQE) and internal (IQE) quantum efficiencies. The average EQE or quantum yield[40] is defined simply as the ratio of emitted N_{em} and absorbed N_{abs} photons for the whole ensemble of NCs (note that average EQE is defined as the spectrally integrated value)

$$\eta_E = \frac{N_{em}}{N_{abs}}. \tag{24}$$

The definition of IQE is more challenging since it has different meanings in literature. Thus, in Refs. 21 and 22 where radiative and non-radiative lifetimes are decoupled thanks to a variation of radiative decay rate by the modification of local density of optical states using a special sample, the IQE is defined as

$$\eta_I^*(\varepsilon) = \frac{k_r^{vac}(\varepsilon)}{k_{PL}^{vac}(\varepsilon)} = \frac{\tau_{PL}^{vac}(\varepsilon)}{\tau_r^{vac}(\varepsilon)} = \frac{F_P(\varepsilon)\tau_{PL}^T(\varepsilon)}{F_P^*(\varepsilon)\tau_r^T(\varepsilon)}, \tag{25}$$

where $F_P^*(\varepsilon)$ is the radiative part of the Purcell factor, i.e., $F_P^*(\varepsilon) = \frac{\tau_r^{vac}(\varepsilon)}{\tau_r^T(\varepsilon)}$.

When using the approximation $F_P(\varepsilon) = F_P^*(\varepsilon)$ in Eq. (25), we obtain the definition that is normally used in other types of papers (for instance, see Ref. 41)

$$\eta_I(\varepsilon) = \frac{\tau_{PL}^T(\varepsilon)}{\tau_r^T(\varepsilon)}. \quad (26)$$

Generally speaking, Eq. (25) and Eq. (26) are not identical and cannot be directly compared. Moreover, it seems to be meaningless to compare IQE defined by Eq. (26) for Si NCs in different media, because τ_r, and consequently, τ_{PL} are functions of the local environment. For colloidal NCs, it is difficult or even impossible to obtain $F_P^*(\varepsilon)$; therefore, we will continue with IQE definition given by Eq. (26) for further calculations.

In real samples, one generally observe

$$\eta_I(\varepsilon) = \frac{\tau_{PL}^T(\varepsilon)}{\tau_r^T(\varepsilon)} \geq \frac{N_{em}(\varepsilon)}{N_{abs}(\varepsilon)} = \eta_E(\varepsilon), \quad (27)$$

where $\eta_E(\varepsilon)$ corresponds to EQE,[33] i.e., number of absorbed $N_{abs}(\varepsilon)$ and emitted $N_{em}(\varepsilon)$ photons with energies between ε and $\varepsilon + \Delta\varepsilon$, accordingly.

The higher value of IQE compared to EQE can be explained by considering the presence of "dark" NCs, i.e., NCs that absorb but do not emit photons. In low excitation power regime, a NC normally absorbs at most one photon during one excitation pulse, so we get for an ensemble of monodisperse NCs that all have the same emission rate

$$\eta_E(\varepsilon) = \frac{N_{em}(\varepsilon)}{N_{abs}(\varepsilon)} = \frac{n_b(\varepsilon)k_r^T(\varepsilon)}{n_{abs}(\varepsilon)k_{PL}^T(\varepsilon)} = \frac{n_b(\varepsilon)}{n_{abs}(\varepsilon)}\eta_I(\varepsilon), \quad (28)$$

where $n_{abs}(\varepsilon)$ is the number of absorbing NCs and $n_b(\varepsilon)$ represents the number of emitting NCs (bright NCs) at energy ε.

The average value of EQE [see Eq. (24)] can be found[41] by scaling Eq. (28) over all possible emission energies ε

$$\eta_E = \sum_{\varepsilon} \frac{n_b(\varepsilon)}{n_{abs}(\varepsilon)}\eta_I(\varepsilon) = \frac{n_b}{n_{abs}}\eta_I, \quad (29)$$

where η_I, n_{abs}, and n_b represent average IQE, average number of absorbing, and emitting NCs, respectively.

As was shown earlier on the broad interval of emission energies (NC sizes), IQE approaches unity. In its turn, we have measured the absolute QY using the integrating sphere and obtained the value near 60% that is in agreement with some samples presented in the work by Sangghaleh *et al.*[16]

Therefore, from Eq. (29), the upper limit of the fraction of bright NCs is approximately estimated

$$\frac{n_b}{n_{abs}} = \frac{\eta_E}{\eta_I} = 0.6. \quad (30)$$

Hence, in our colloidal ensemble, we estimated the number of bright Si NCs to be roughly two times larger than in ensemble of Si NCs embedded in the SiO_2 matrix[41,42] which is most probably due to better surface passivation of Si NCs and large separation between NCs.

IV. CONCLUSIONS

Spectrally resolved PL measurements of near fully radiative colloidal Si NCs were studied in detail. A set of decay models was applied to extract PL decay parameters. The average PL decay lifetimes were confirmed to be independent of a fit model within a selected energy interval. The strong exponential dispersion of PL lifetimes confirms a quantum confinement model in the ensemble of 0-D emitters (quantum dots). Although the average lifetime dispersion is monotonous, we report on a sudden change of dispersion factor energy dependence at low photon energy emission tail. Thus, the dispersion factor of total PL lifetimes of NCs emitting above 1.5 eV were shown to be exponentially increasing with decreasing NC size. In contrast, large NCs emitting below 1.4 eV revealed dispersion factor β increasing with the increase of NC sizes. A numerical procedure was applied to extract size-selected decays from spectrally resolved decay measurements which is the key point of the paper. The NCs emitting around 1.5 eV were confirmed to be fully radiative demonstrating size-selected monoexponential decay behavior. The lifetimes of smaller NCs in a broad range of sizes were confirmed to be nearly fully radiative from comparison with theoretical lifetime calculations by the EFA method. We succeed to measure PL spectra of single Si NCs and estimated the homogeneous line-broadening to be around 180 meV. In the paper, we distinguished two definitions of IQE that could be found in the literature (one of them omitting a local medium effect). The average IQE of studied NCs was estimated to be near 100% on the broad energy interval. At the same time, the average EQE of the whole ensemble was determined around 60% that is still far away from 100%. One possible explanation is a presence of "dark" NCs in the ensemble and hence the further efforts should be concentrated on an attempt to reduce that fraction of NCs. In addition, the NCs emitting around 1.5 eV ($d \sim 4.5$ nm) are of special interest as synthesized monodisperse NCs of that size could find practical applications in extremely efficient new generation nanophotonic devices.

ACKNOWLEDGMENTS

This work was supported by the Visegrad Group (V4)-Japan Joint Research Program on Advanced Materials (project NaMSeN) 8F15001 financed by the Ministry of Education, Youth and Sports of the Czech Republic and by the International Visegrad Fund and also by the bilateral Czech-German DFG-GACR Project No. 16–09745J. Partial support from the National Basic Research Program of China under Grant No. 2013CB632101 is acknowledged. One of the authors (M.G.) would like to thank Professor A. Meldrum (University of Alberta, Canada) for discussions.

[1]J. Valenta and S. Mirabella, *Nanotechnology and Photovoltaic Devices* (Pan Stanford Publishing, 2015).
[2]S. Zhao, X. Pi, C. Mercier, Z. Yuan, B. Sun, and D. Yang, Nano Energy **26**, 305 (2016).
[3]C.-Y. Liu, Z. C. Holman, and U. R. Kortshagen, Adv. Funct. Mater. **20**, 2157 (2010).
[4]Y. Ding, R. Gresback, Q. Liu, S. Zhou, X. Pi, and T. Nozaki, Nano Energy **9**, 25 (2014).
[5]F. Maier-Flaig, J. Rinck, M. Stephan, T. Bocksrocker, M. Bruns, C. Kübel, A. K. Powell, G. A. Ozin, and U. Lemmer, Nano Lett. **13**, 475 (2013).
[6]T. Yu, F. Wang, Y. Xu, L. Ma, X. Pi, and D. Yang, Adv. Mater. **28**, 4912 (2016).

[7]L. Ostrovska, A. Broz, A. Fucikova, T. Belinova, H. Sugimoto, T. Kanno, M. Fujii, J. Valenta, and M. H. Kalbacova, RSC Adv. **6**, 63403 (2016).
[8]F. Erogbogbo, K. Yong, I. Roy, G. Xu, P. N. Prasad, and M. T. Swihart, ACS Nano **2**, 873 (2008).
[9]I. Sychugov, J. Valenta, and J. Linnros, Nanotechnology **28**, 72002 (2017).
[10]C. Delerue, G. Allan, C. Reynaud, O. Guillois, G. Ledoux, and F. Huisken, Phys. Rev. B **73**, 235318 (2006).
[11]F. Sangghaleh, B. Bruhn, T. Schmidt, and J. Linnros, Nanotechnology **24**, 225204 (2013).
[12]V. Vinciguerra, G. Franzò, F. Priolo, F. Iacona, and C. Spinella, J. Appl. Phys. **87**, 8165 (2000).
[13]F. Priolo, G. Franzò, D. Pacifici, V. Vinciguerra, F. Iacona, and A. Irrera, J. Appl. Phys. **89**, 264 (2001).
[14]H. E. Roman and L. Pavesi, J. Phys.: Condens. Matter **8**, 5161 (1996).
[15]K. Dunn, J. Derr, T. Johnston, M. Chaker, and F. Rosei, Phys. Rev. B **80**, 35330 (2009).
[16]F. Sangghaleh, I. Sychugov, Z. Yang, J. G. C. Veinot, and J. Linnros, ACS Nano **9**, 7097 (2015).
[17]S. L. Brown, J. B. Miller, R. J. Anthony, U. R. Kortshagen, A. Kryjevski, and E. K. Hobbie, ACS Nano **11**, 1597 (2017).
[18]X. Liu, Y. Zhang, T. Yu, X. Qiao, R. Gresback, X. Pi, and D. Yang, Part. Part. Syst. Charact. **33**, 44 (2016).
[19]U. R. Kortshagen, R. M. Sankaran, R. N. Pereira, S. L. Girshick, J. J. Wu, and E. S. Aydil, Chem. Rev. **116**, 11061 (2016).
[20]J. Valenta and M. Greben, AIP Adv. **5**, 47131 (2015).
[21]S. Miura, T. Nakamura, M. Fujii, M. Inui, and S. Hayashi, Phys. Rev. B **73**, 245333 (2006).
[22]R. J. Walters, J. Kalkman, A. Polman, H. A. Atwater, and M. J. A. de Dood, Phys. Rev. B **73**, 132302 (2006).
[23]J. Kalkman, H. Gersen, L. Kuipers, and A. Polman, Phys. Rev. B **73**, 75317 (2006).
[24]E. M. Purcell, Phys. Rev. **69**, 674 (1946).
[25]T. Nakamura, B. P. Tiwari, and S. Adachi, Opt. Express **20**, 26548 (2012).
[26]G. Zatryb, A. Podhorodecki, X. J. Hao, J. Misiewicz, Y. S. Shen, and M. A. Green, Opt. Express **18**, 22004 (2010).
[27]I. Pelant and J. Valenta, *Luminescence Spectroscopy of Semiconductors* (Oxford University Press, New York, 2012), p. 68.
[28]M. Greben and J. Valenta, Rev. Sci. Instrum. **87**, 126101 (2016).
[29]F. Huisken, G. Ledoux, O. Guillois, and C. Reynaud, Adv. Mater. **14**, 1861 (2002).
[30]D. Amans, O. Guillois, G. Ledoux, D. Porterat, and C. Reynaud, J. Appl. Phys. **91**, 5334 (2002).
[31]C. Meier, A. Gondorf, S. Lüttjohann, A. Lorke, and H. Wiggers, J. Appl. Phys. **101**, 103112 (2007).
[32]N. Tit, Z. H. Yamani, J. Graham, and A. Ayesh, J. Lumin. **130**, 2226 (2010).
[33]J. C. Vial, A. Bsiesy, F. Gaspard, R. Hérino, M. Ligeon, F. Muller, R. Romestain, and R. M. Macfarlane, Phys. Rev. B **45**, 14171 (1992).
[34]M. Greben, A. Fucikova, and J. Valenta, J. Appl. Phys. **117**, 144306 (2015).
[35]I. Sychugov, A. Fucikova, F. Pevere, Z. Yang, J. G. C. Veinot, and J. Linnros, ACS Photonics **1**, 998 (2014).
[36]J. Valenta, R. Juhasz, and J. Linnros, Appl. Phys. Lett. **80**, 1070 (2002).
[37]V. A. Belyakov, V. A. Burdov, R. Lockwood, and A. Meldrum, Adv. Opt. Technol. **2008**, 1 (2008).
[38]K. D. Sattler, *Handbook of Nanophysics: Nanoelectronics and Nanophotonics* (CRC Press, 2011), pp. 25–13.
[39]A. N. Poddubny, J. Opt. **17**, 35102 (2015).
[40]J. Valenta, Nanosci. Methods **3**, 11 (2014).
[41]R. Limpens and T. Gregorkiewicz, J. Appl. Phys. **114**, 74304 (2013).
[42]J. Valenta, M. Greben, S. Gutsch, D. Hiller, and M. Zacharias, Appl. Phys. Lett. **105**, 243107 (2014).

Paper III

PHYSICS, CHEMISTRY AND APPLICATION OF NANOSTRUCTURES, 2017

THE ADVANCED ANALYSIS OF SLOW NON-STRETCHED EXPONENTIAL DECAY KINETICS FROM Si NANOCRYSTALS

M. Greben, J. Valenta

Department of Chemical Physics & Optics, Faculty of Mathematics & Physics
Charles University, Prague, CZ-12116, Czechia
leibnits@gmail.com

P. Khoroshyy

Institute of Organic Chemistry and Biochemistry, Czech Academy of Sciences
Flemingovo namesti 2, 16000 Prague 6, Czechia
khoroshyy@gmail.com

The procedure of reliable extraction of average decay lifetimes was demonstrated with an example of slow non-stretched exponential photoluminescence kinetics from multilayers of Si nanocrystals and three different fitting models, namely: 1) multi-exponential, 2) combination of mono- and stretched exponential as well as 3) lognormal distribution of decay rates. All three decay models gave the same average decay lifetime 68 ± 1 μs.

1. Introduction

The stretched exponential (SE) line shape became classical footprint of silicon nanocrystals (Si NCs) that demonstrate slow non-exponential decay:

$$I(t) = I(0)e^{-(\frac{t}{\tau_0})^{\beta}} + background \qquad (1)$$

where τ_0 is the lifetime parameter and β is the dispersion factor. This decay law is relatively simple and describes quite well the photoluminescence (PL) decays of colloidal Si NCs [1] or porous silicon. Unfortunately, the decay kinetics of Si NCs in a solid matrix (for instance, SiO_2) do not always reveal SE behavior [2]. An exact procedure to analyze such complex decays has not been developed yet.

2. Results and discussion

Recently we have discussed [3] special requirements that restrict the experimental measurements of slow PL kinetics in μs to ms scale namely: low excitation power, low pulse repetition rate, and long excitation pulses. Those conditions ensure that NCs are not overexcited, PL decays are not truncated and a signal to noise (S/N) ratio is high enough. However, the above given points make any experiment of great challenge and in some cases a curve truncation becomes unavoidable.

As an example in Fig. 1 we present PL decay of Si NC multilayers in high quality PE-CVD sample [2]. The SE fit is not ideal (Fig. 1a) and it might be noticed a characteristic S-shape of fit residuals (Fig. 1b). Keeping into account slight truncation of the curve one could expect even more pronounced disagreement of SE fit in case of longer curve. Therefore SE fit cannot be used for the reliable analysis of such decay. Instead, we applied a set of other fitting models and compared the results (Fig. 1c,d).

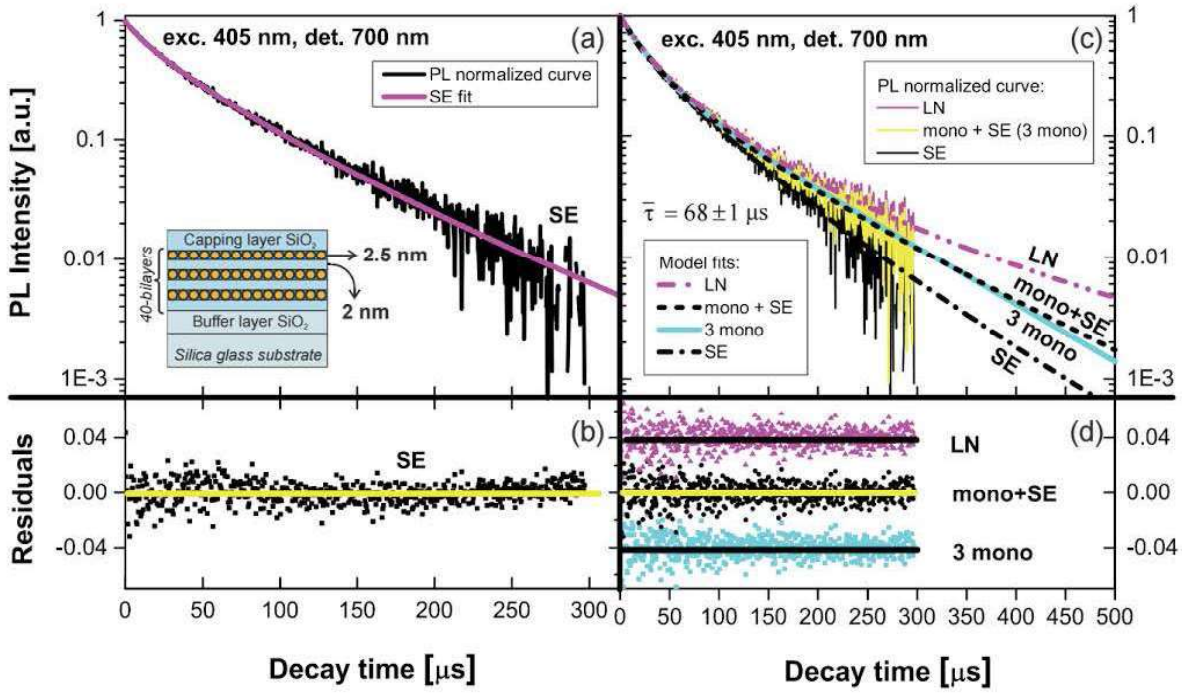

Figure 1. Normalized PL decay curves (a, c) and stretched exponential (SE) fits (a) or fits by different other models (c): combination of three mono-exponentials (3 mono), combination of mono- and stretched-exponentials (mono+SE), log-normal (LN) distribution of rates. (b, d) residuals to corresponding fits.

The most straight-forward approach is to try the multi-exponential (ME) fit ($N = 3$ in our case):

$$I(t) = \sum_{i=1}^{N} A_i e^{-(\frac{t}{\tau_i})} + background \qquad (2)$$

where A_i and τ_i are the amplitude and lifetime parameters, accordingly.

Another approach is based on fitting by combination of mono- and SE (MSE) [4]:

$$I(t) = A_1 e^{-(\frac{t}{\tau_1})} + A_2 e^{-(\frac{t}{\tau_2})^{\beta}} + background \qquad (3)$$

Finally the model proposed by van Driel *et al.* [5] was applied, which imply the lognormal (LN) distribution of decay rates:

$$I(t) = I(0)\int_0^\infty f(k)e^{-(kt)}dk + background \tag{4}$$

where $f(k)$ is LN distribution of the decay rate k. It is given by:

$$f(k) = Ae^{-(\frac{\ln(k/k_m)}{\sinh^{-1}(k_d/2k_m)})^2} \tag{5}$$

where k_m and k_d are the fitting parameters.

The results of fitting as well as fit residuals of experimental PL decay curves by the above mentioned models are presented in Fig. 1c,d. The normalized PL curve is varying in dependence on a chosen model (Fig. 1c) due to the model-dependent fit amplitude $I(0)$ and background:

$$I_{norm}(t) = (I(t) - background)/(I(0) - background) \tag{6}$$

All models fit the curve pretty well though the resulting fits are different. This difference provides an evidence to the fact that a good fit does not necessarily mean that a chosen model is correct and unique. Obviously, if one would apply an inverse Laplace transform to different fitting models quite different lifetime distributions will be obtained. Hence, the detailed analysis of a lifetime distribution is meaningless. Therefore we should focus on extraction of average PL decay lifetimes.

The average lifetimes of SE (Eq. (7)), ME (Eq. (8)), MSE (Eq. (9)) and LN (Eq. (10)) were calculated by the following equations:

$$\bar{\tau}_{SE} = \Gamma(\frac{2}{\beta})/\Gamma(\frac{1}{\beta})\tau_0 \tag{7}$$

$$\bar{\tau}_{ME} = \sum_{i=0}^{3} A_i\tau_i^2 / \sum_{i=0}^{3} A_i\tau_i \tag{8}$$

$$\bar{\tau}_{MSE} = (A_1\tau_1^2 + A_2\frac{\tau_2^2}{\beta}\Gamma(\frac{2}{\beta}))/(A_1\tau_1 + A_2\frac{\tau_2}{\beta}\Gamma(\frac{1}{\beta})) \tag{9}$$

$$\frac{1}{\bar{\tau}_{LN}} = k_m \exp(\frac{3}{4}(\sinh^{-1}(k_d/2k_m))^2) \tag{10}$$

The obtained average PL decay lifetime by ME, MSE and LN methods is $\bar{\tau} = 68 \pm 1$ μs. In contrast, the average decay lifetime obtained by SE model is expectedly different and equals to $\bar{\tau}_{SE} = 58$ μs. The average lifetime of our

Si NCs in SiO_2 is roughly 1.5 times shorter than the average lifetime of Si NCs in colloidal suspensions. This indicates that non-radiative processes are more pronounced in solid samples.

3. Conclusion

The procedure of reliable extraction of average decay lifetimes was demonstrated with an example of slow non-stretched exponential PL kinetics with three different fitting models. Though the lifetime distributions are different for the applied models, the average lifetime is the same for all of them. It demonstrates that the average decay lifetime is model-free and could be reliably determined even in the case of slightly truncated curves. On the other hand, we should note that the results are highly disputable in the case of good fits by a set of models and different average lifetimes until the true decay model is known.

In addition, the shorter is the curve (truncation), the higher is the probability of an successful fit by a model though the subsequently extracted average decay lifetime is not necessarily correct. By applying different fit models one could confirm the correctness of extracted average values.

Acknowledgments

The authors acknowledge S. Gutsch, D. Hiller, and M. Zacharias (IMTEK, Freiburg University, Germany) for providing high quality PE-CVD samples. We would like to thank also to A. Meldrum (University of Alberta, Canada) for the topic discussion.

References

1. F. Sangghaleh *et al.*, *ACS Nano* **9**, 7097 (2015).
2. J. Valenta *et al.*, *Appl. Phys. Lett.* **108**, 023102 (2016).
3. M. Greben, J. Valenta, *Rev. Sci. Instr.* **87**, 126101 (2016).
4. J. Linnros *et al.*, *J. Appl. Phys.* **86**, 6128 (1999).
5. A. F. van Driel *et al.*, *Phys. Rev. B* **75**, 035329 (2007).

Paper IV

REVIEW OF SCIENTIFIC INSTRUMENTS **87**, 126101 (2016)

Note: On the choice of the appropriate excitation-pulse-length for assessment of slow luminescence decays

M. Greben and J. Valenta[a)]
Department of Chemical Physics and Optics, Faculty of Mathematics and Physics, Charles University, Prague, Czechia

(Received 19 August 2016; accepted 21 November 2016; published online 7 December 2016)

The decay-time distribution deduced from luminescence kinetics experiments is, in general, dependent on the excitation pulse length as a direct consequence of different onset dynamics. We demonstrate this effect for the case of square excitation pulses applied to study the luminescence kinetics in Si nanocrystals. The short- and long-pulse limits are defined as 0.1 times the shortest lifetime in the distribution and 3 times the longest time, respectively. Outside these limits the decay-time distribution is independent on the pulse duration. In addition, we describe experimental conditions required to obtain a correct depiction of slow luminescence decay in the μs to ms time range. *Published by AIP Publishing.* [http://dx.doi.org/10.1063/1.4971368]

Time-resolved luminescence (TRL) spectroscopy is a widely applied method to study the kinetics of energy relaxation, transport, etc., in various materials. The characteristic decay time τ_{PL} of these processes can cover extremely a broad time range from fs to s, which cannot be covered by a single experimental apparatus. In this note, we aim to propose and test the optimum experimental parameters to measure relaxation on the slow time scale from μs to ms, which are not commonly known and implemented (the typical error being the application of too short pulses and/or over-excitation).[1] Such long lifetimes are a characteristic of a variety of important materials, e.g., luminescence of semiconductors with indirect transition[2] and their low-dimensional or disordered structures,[3] and rare-earth ion dopants or phosphorescence of organic materials. Often, these slow decays are non-exponential due to the inherent distribution of lifetimes in a studied material and any attempt to uncover this distribution must be based on very careful experiments and calculations.[4] This paper is illustrated by photoluminescence (PL) of multilayers of Si nanocrystals (NCs) in a silica matrix.[5]

There are three basic points to be considered prior setting up an experimental apparatus for the detection of a slow PL decay: signal saturation, truncation, and quality as follows.

(a) *PL saturation*: Long excited state lifetime leads to PL saturation and/or other non-linear effects already at quite low excitation power. In case of a confined PL center (e.g., a nanocrystal), there is a high probability of creating second exciton during the lifetime of the previous one. Consequently, a fast non-radiative decay (e.g., Auger recombination) takes place and removes one or both excitons. As the first approximation, the mean number of excitons per NC can be calculated from $I_{ex}\sigma\tau_{PL}$, where I_{ex} and σ is the excitation photon flux and absorption cross section, respectively. Then the excitation photon flux creating average population 1 is equal to $I_{ex} = 1/(\sigma\tau_{PL})$. Using typical values for SiNCs[6] $\sigma = 1.5 \times 10^{-15}$ cm^2 and $\tau_{PL} = 0.25$ ms, we get $I_{ex} = 2.7 \times 10^{18}$ photon·cm^{-2}·s^{-1}, which gives 1.3 W cm^{-2} for violet photons (405 nm).

(b) *Incomplete decay—truncation*: In order to observe the complete decay down to the background signal level, one has to use a long detection window after the excitation pulse. The decay window must be usually at least 4 or 5 times the average lifetime.[7] Otherwise only a truncated signal is obtained, which compromises the precision of fits (mostly due to uncertainty of the background level (BL)).

(c) *Signal quality—noise*: Precision of the fitting parameters strongly depends on the signal quality, namely, the signal to noise (S/N) ratio. Traditionally, it was required that the signal decay must be followed over three decades or more[8] in order to get a correct decay shape which requires a very high S/N ratio.

The above given points imply the following three requirements for experiments: low excitation power, low pulse repetition rate, and long excitation pulses. All together these requirements make experiments very difficult, especially for materials with a low luminescence quantum yield. Therefore, the optimum experimental conditions must be carefully determined.

One possible realization of a TRL system dedicated to slow decays is the following (this system is applied by the authors to get illustrations for this paper): Excitation is provided by a continuously emitting diode laser (405 nm) whose beam is modulated using an acousto-optic modulator (AOM) with a rf-power supply controlled by a (square) pulse-generator. The speed of switching on and off is determined by the AOM and the diameter of the laser beam; the typical value is about 100 ns (in some cases a good laser modulation can be obtained by simply modulating the laser power supply). The laser is sent on a sample and its emission is coupled by an optical system to a detection branch. The spectral region for detection is selected either by filters or a spectrometer. Output

a)Author to whom correspondence should be addressed. Electronic mail: jan.valenta@mff.cuni.cz

from a photon counting detector (photomultiplier tubes (PMT) or avalanche photodiodes (APD)) is sent to a multi-channel scaler, where the detected counts are sorted by their delay after the reference pulse and counted in time bins, i.e., many counts can be obtained after each excitation pulse.

Experimentally measured decay curves contain a "constant" signal background level that is composed of electronic noise, dark counts, and the other signal that does not originate from PL of a sample under pulsed excitation. BL can be either (i) characterized separately (by performing experiment with blocked excitation) and subtracted from data or (ii) determined as a fitting parameter.[9] The latter approach increases the number of fitting parameters and may compromise precision of some parameters, especially in the case of multi-exponential decays and incomplete decay data.

The effect of pulse length is illustrated in Fig. 1(a) showing PL kinetics of Si NCs[10] excited by square pulses of a variable length. The continuous excitation power density on the sample is kept very low (80 mW/cm^2) in order to avoid saturation effects (starting around 1 W/cm^2). The average lifetime is about 0.28 ms and can be fitted either by double-exponential or stretched-exponential functions. One can see that the PL signal decreases significantly when the pulse becomes shorter. This is due to the slow PL onset after switching on excitation. From simple kinetic equations[6] we see that the characteristic time for both the PL onset and decay is equal (under low excitation).

For a given decay parameter, we can determine optimum experimental conditions for obtaining the highest signal. The following derivation is done for a mono-exponential decay with a characteristic decay time τ_{PL} (the multi-exponential or other forms of decays can be treated in a similar way). During the excitation pulse duration T_1, PL signal increases up to $I_{PL}^{\max} = I_{PL}^{cw}(1 - \exp(-T_1/\tau_{PL}))$. PL decay is then observed for the time T_2, long enough to allow observation of the major part of the decay shape ($\geq 4\tau_{PL}$), see Fig. 2. The integral PL decay signal obtained during the interval T_2 is $I_{PL}^{\max}\tau_{PL}(1 - \exp(-T_2/\tau_{PL}))$. One experimental cycle $(T_1 + T_2)$ can be repeated with a repetition rate of $1/(T_1 + T_2)$. All together, the integral PL decay signal $I_{PL}^{\text{int.dec.}}$ (normalized to $I_{PL}^{cw} = 1$) is given by the following equation:

$$I_{PL}^{\text{int.dec.}} = \frac{(1 - e^{-T_1/\tau_{PL}})(1 - e^{-T_2/\tau_{PL}})\tau_{PL}}{T_1 + T_2}. \quad (1)$$

This relation is plotted in Fig. 2(a) as a function of T_1 for different T_2 equal to 3, 4, 5, or 6 times τ_{PL} ($\tau_{PL} = 0.2$ ms). The optimum signal is obtained for T_1 around twice of τ_{PL}. Fig. 2(b) shows the simulated PL signal for a single-exponential lifetime of $\tau_{PL} = 0.2$ ms and $T_2 = 4\tau_{PL}$. The ideal pulse length is 386 μs. If we use instead a typical nanosecond pulse of 5 ns (e.g., from a diode-pumped solid-state laser), the signal will be 23 000 times lower!

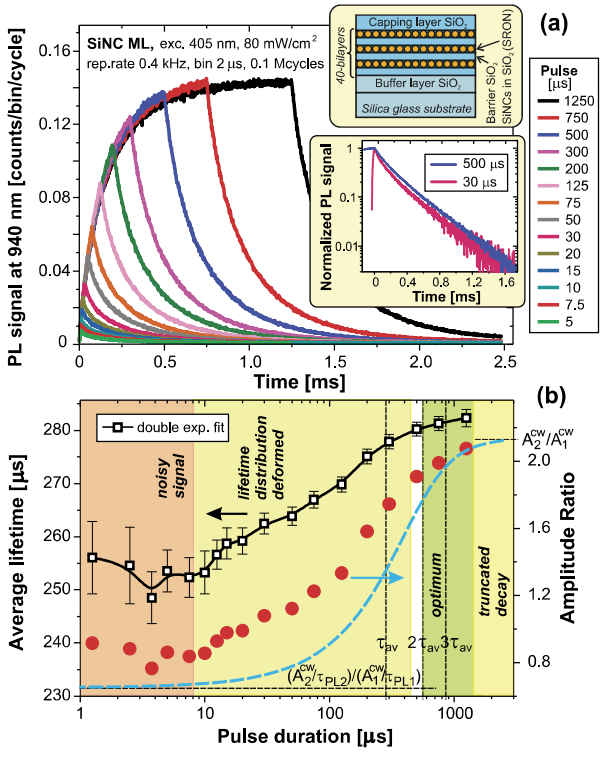

FIG. 1. (a) PL onset and decay curves following the square excitation pulses with a variable duty cycle from 50% to 0.2% (rep. rate of 0.4 kHz) for Si NC multilayers detected at 940 nm (PL peak). The upper inset shows the sample schematics and the lower one shows the normalized and background subtracted PL decays (log intensity scale) for the excitation pulses of 0.5 and 0.03 ms revealing the difference of decay signals. (b) The amplitude-weighted average lifetime (squares) obtained by fitting the PL decay from the upper panel with double-exponential functions. Red circles show the ratio of amplitudes of long and slow decay components (310 and 95 μs lifetimes) and the dashed blue line is a simple model of changing amplitudes' ratio due to different onset speeds.

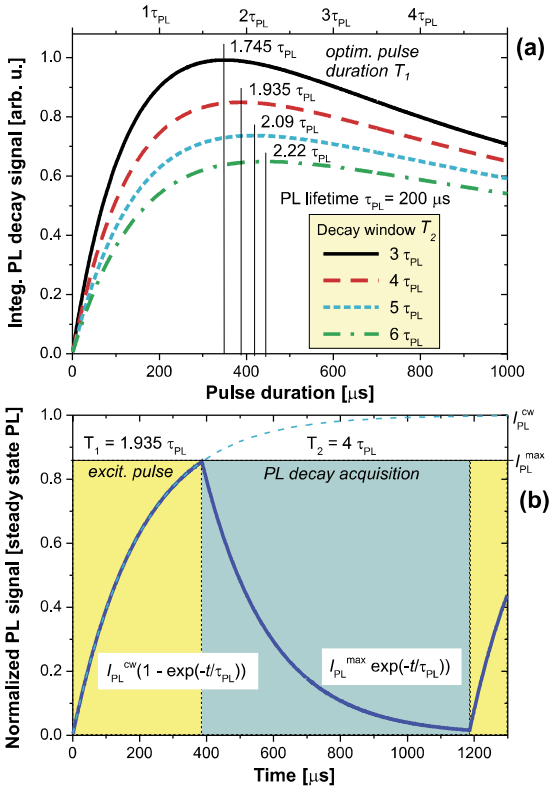

FIG. 2. (a) Simulation of the optimum pulse duration for a given average lifetime τ_{PL} (here 0.2 ms) and the desired observation time window equal to 3, 4, 5, and 6 times τ_{PL} (the curves from up down). (b) The simulated PL kinetics under the optimal conditions derived in the upper panel for $\tau_{PL} = 0.2$ ms and the decay time window $T_2 = 4\tau_{PL}$.

The results of double-exponential fits of data from Fig. 1(a) confirm the optimum condition for the pulse duration of $T_1 \geq 2\tau_{PL}$ (when $T_2 \sim 7\tau_{PL}$) in perfect agreement with Fig. 2(a). Moreover, this experiment reveals significant changes of the intensity average lifetime when decreasing the pulse duration (see inset in Fig. 1(a)). The origin of this change can be understood for the simple case of sample with a "mixture" of non-interacting emission centers with different exponential decay times. Under continuous excitation, each component reaches its continuous amplitude level A_i^{cw} with different speed. For the pulse duration of T_1, the i-th component reaches the amplitude of

$$A_i(T_1) = A_i^{cw}(1 - \exp(-T_1/\tau_{PLi})). \quad (2)$$

The double-exponential fits of data from Fig. 1 were done with fixed lifetimes of 95 μs and 310 μs and only amplitudes of these components were fitted. Red circles in Fig. 1(b) are the obtained amplitude ratios of long/short decay components. They can be compared with the model (blue line) considering the above given pulse-length dependent amplitude with the cw ratio of amplitudes of 0.68/0.32. It approximates experimental results qualitatively well. We have to note that at the short-pulse limit, the amplitude ratio reaches the pulse-independent value of $(A_2^{cw}/\tau_{PL2})/(A_1^{cw}/\tau_{PL1})$.

We can define the long- and short-pulse limit by allowing, e.g., 5% deviation (experimental uncertainty is often of this order or bigger). More specifically, we define the long-pulse limit T_{long} as the length of pulse for which a component with lifetime τ_{PL} reaches 95% of its cw amplitude. Using Eq. (2) we obtain $T_{long} = 2.996\tau_{PL}$.

The short-pulse limit can be defined similarly. Considering the approximation of Eq. (2),

$$A_i(T_1) = A_i^{cw}(T_1/\tau_{PLi} - (T_1/\tau_{PLi})^2/2 + \cdots) \quad (3)$$

and requiring that the second term of the Taylor series is 5% of the first one, we get $T_{short} = 0.1\tau_{PL}$.

One should better avoid intermediate pulses where the results are sensitive to the pulse duration. Using the above definition, the *intermediate range* is $T_1 \in \left(0.1\,\tau_{PL}^{short}; 3\,\tau_{PL}^{long}\right)$, where τ_{PL}^{short} and τ_{PL}^{long} are the shortest and the longest (significant) lifetimes in the distribution, respectively. In some cases, like extremely broad lifetime distribution, it may be very difficult to avoid the effect of intermediate pulses. Also the above derived optimum pulse duration ($T_1 \sim 2\tau_{PL}$) for obtaining the best signal for a single-exponential decay is within the range of intermediate pulses; therefore, we should use longer pulses in case of studying samples with a distribution of lifetimes.

In conclusions, we demonstrated the effect of intermediate-long pulses on the distribution of lifetimes revealed from TRL experiments. Intermediate pulses can be defined as pulses longer than 0.1 times the shortest lifetime in the distribution and shorter than 3 times the longest lifetime. Distributions of lifetimes obtained under the short-pulse limit and the long-pulse limit cannot be directly compared as amplitudes in the former case are weighted by the respective decay rates. This effect is a direct consequence of the fact that the onset dynamics is (at low excitation) equal to the decay dynamics. Our description and model experiments concern the most simple and illustrative case of rectangular pulses and a double-exponential kinetics. Similar effects (with more complex description) will take place for excitation with smoothly changing pulses (Gaussian, etc.) and discrete or continuous distribution of lifetimes.

In addition, we stress that the experimental characterization of slow luminescence decay kinetics in the μs to ms time scale requires special experimental conditions that are dictated by the three main problems of (i) luminescence non-linearity under strong excitation, (ii) truncation of the long decay traces at higher repetition rates, and (iii) low signal to noise ratio due to low emission rate. Therefore the adequate experiments must be done with low excitation power, low pulse repetition rate, and long excitation pulses, which make experiments challenging. We believe that our note should help researchers who deal with slow luminescence decay experiments to correctly set up experiments and extract (from decay curves) undistorted information that could have a great practical significance in the optical characterization of materials.

The authors would like to thank S. Gutsch, D. Hiller, and M. Zacharias (IMTEK, Freiburg University, Germany) for providing high quality PE-CVD samples. This work was supported by bilateral Czech-German DFG-GACR Project No. 16-09745J.

[1]A. Hartel, S. Gutsch, D. Hiller, and M. Zacharias, Phys. Rev. B **85**, 165306 (2012).
[2]I. Pelant and J. Valenta, *Luminescence Spectroscopy of Semiconductors* (Oxford University Press, 2012).
[3]K. Nishio, J. Koga, T. Yamaguchi, and F. Yonezawa, Phys. Rev. B **67**, 195304 (2003).
[4]A. F. van Driel *et al.*, Phys. Rev. B **75**, 035329 (2007).
[5]J. Linnros, N. Lalic, A. Galeckas, and V. Grivickas, J. Appl. Phys. **86**, 6128 (1999).
[6]J. Valenta, M. Greben, Z. Remes, S. Gutsch, D. Hiller, and M. Zacharias, Appl. Phys. Lett. **108**, 023102 (2016).
[7]R. W. K. Leung, S.-C. A. Yeh, and Q. Fang, Biomed. Opt. Express **2**(9), 2517 (2011).
[8]A. K. Jonscher and A. de Polignac, J. Phys. C: Solid State Phys. **17**, 6493 (1984).
[9]D. V. O'Connor and D. Phillips, *Time-Correlated Single Photon Counting* (Academic Press, 1984).
[10]A. M. Hartel, D. Hiller, S. Gutsch, P. Löper, S. Estradé, F. Peiró, B. Garrido, and M. Zacharias, Thin Solid Films **520**, 121 (2011).

Paper V

JOURNAL OF APPLIED PHYSICS **117**, 144306 (2015)

Photoluminescence quantum yield of PbS nanocrystals in colloidal suspensions

M. Greben, A. Fucikova, and J. Valenta
Department of Chemical Physics & Optics, Faculty of Mathematics & Physics, Charles University, Ke Karlovu 3, Prague 2, CZ-121 16 Czech Republic

(Received 12 December 2014; accepted 27 March 2015; published online 13 April 2015)

The absolute photoluminescence (PL) quantum yield (QY) of oleic acid-capped colloidal PbS quantum dots (QDs) in toluene is thoroughly investigated as function of QD size, concentration, excitation photon energy, and conditions of storage. We observed anomalous decrease of QY with decreasing concentration for highly diluted suspensions. The ligand desorption and QD-oxidation are demonstrated to be responsible for this phenomenon. Excess of oleic acid in suspensions makes the QY values concentration-independent over the entire reabsorption-free range. The PL emission is shown to be dominated by surface-related recombinations with some contribution from QD-core transitions. We demonstrate that QD colloidal suspension stability improves with increasing the concentration and size of PbS QDs. © *2015 AIP Publishing LLC*.
[http://dx.doi.org/10.1063/1.4917388]

I. INTRODUCTION

Colloidal semiconductor quantum dots (QDs) are the subject of fundamental and applied research because of their unique optical properties based on the quantum confinement effect.[1] This effect reveals itself when the QD radius R is less than or comparable to that of the Bohr exciton radius a_B in the corresponding bulk material. A quantum confinement regime is called "strong," when $R < a_e, a_h$, where a_e and a_h are the Bohr radii of electron and hole, respectively. As most of II–VI and III–V materials have small Bohr radius of holes,[2] very small QDs are required to achieve strong quantum confinement limit in these semiconductors. On the other hand, semiconductor QDs composed of IV–VI materials and, in particular, the lead chalcogenides PbX (X = S, Se, Te) offer unique access to the regime of extreme quantum confinement, for instance, bulk PbS has small direct band gap (0.41 eV), with $a_e = a_h = 10$ nm and $a_B = 18$ nm. Thus, such large Bohr radius provides strong confinement even for quite large QDs (~10 nm), where the influence of surface effects is less pronounced than for QDs of II–VI or III–V materials with the same level of confinement because of reduced surface-to-volume ratio.

The fundamental theoretical work on electronic structure and optical properties of PbS and PbSe QDs has been presented by Kang *et al.*[3] in 1997 and the procedure of a reliable and flexible colloidal synthesis of PbSe QDs was developed in 2001.[4] During the last decade, lead chalcogenide QDs have been investigated as potential active materials for low-cost and efficient photovoltaic devices. The tunable electronic transitions of PbX QDs from infrared to ultraviolet region are of interest for producing multi-junction solar cells, which could harvest large part of the solar spectrum. Lead chalcogenides QDs have already been successfully used in LEDs,[5,6] lasers,[7] solar cells,[8–10] photodetectors,[11–13] luminescent solar concentrators,[14,15] and biolabeling.[16–19] However, despite the intensive investigation it is still a challenge to synthesize colloidal quantum dots of narrow-size distribution and well-passivated surface. To the best of our knowledge, there are currently two well-developed methods to synthesize PbS QDs. The first route is based on the injection of bis(trimethylsilyl)sulfide (TMS) in octadecene to a hot solution of lead oleate (Hines and Scholes synthesis[20]), which offers monodisperse QDs over a broad size range (2.5–8.8 nm).[21] Recent modifications of the method allow for synthesis of ultrasmall PbS QDs with sizes between 1 and 2 nm.[22–24] The second route includes lead chloride ($PbCl_2$) and elemental sulfur (S) as precursors and oleylamine is used as a solvent (Cademartiri *et al.* synthesis[25]). Recently, Cademartiri method was modified by adding tri-n-octylphosphine (TOP) to solution,[26] which offers available size tunability between 3 and 10 nm.

In spite of the growing number of reports about colloidal suspensions of PbS QDs, detailed knowledge of some important parameters is still missing. One of them is the photoluminescence (PL) quantum yield (QY) which characterizes quality of a luminescent material. Many PL QY set-ups have limited number of available excitation wavelengths (laser lines or lamps with band-pass filters). But this limitation is commonly considered to be acceptable as the Kasha-Vavilov (KV) rule is believed to be fulfilled (The rule states that both the luminescence spectral shape and its QY do not depend on the applied excitation wavelength[27]). However, PL QY of QDs was found to be excitation wavelength dependent due to the size-distribution and other effects.[20] But there are no in-detail studies on the excitation dependence of PL QY for PbS QDs yet. Moreover, it is commonly recommended that luminescent solutions must be strongly diluted to avoid the concentration quenching. However, such dilute suspensions of QDs could suffer from instability of QDs and reveal perturbations of PL QY values. Thus, the investigation of PL QY of PbS QDs depending on the concentration of suspensions and the QD size is of immense practical importance.

The main goal of this work was to study PL QY of conventional oleic acid-capped PbS QDs in toluene for various

concentrations and over a broad excitation spectral range. We uncover and discuss some specific features of the PL QY like the abnormal increase of PL QY with concentration or violation of the KV rule.

II. INSTRUMENTATION AND MATERIALS

The oleic-acid (OA) capped PbS QDs were purchased from MK Nano (mean diameter $d = 2.4$ nm and 3.3 nm) and Strem Chemicals ($d = 3$ nm) and dispersed in toluene (Uvasol, Merck) at different concentrations. The stock suspension nominal concentrations were 60, 50, and 93 μM/l for 2.4, 3, and 3.3 nm QD's sizes, respectively. The size and the spectral position of the first absorption peak of PbS QDs obtained from MK Nano are in agreement with the following equation:[28]

$$E_0 = 0.41 + \frac{1}{0.0252\,d^2 + 0.283\,d}, \quad (1)$$

where d is the QD diameter.

Absorption and emission spectra of the three samples are presented in Fig. 1. The PbS QDs suspensions were sealed into quartz cuvettes of either the standard size of 1×1 cm^2 (sample volume of 3 ml) or smaller 0.5×0.5 cm^2 cuvettes (0.75 ml volume for highly concentrated samples). The absorption spectra were taken using the double-beam spectrophotometer (Specord 250, Analytik Jena) with the pure solvent as a reference sample. We have to note that toluene has some absorption features in the spectral range between 850 and 950 nm that slightly influence the measured PL spectra (see supplementary information,[29] Fig. S1).

For the time-resolved PL spectroscopy (TRS), we have used excitation by the diode pumped solid-state laser (MPL-F-355, Changchun Industries Optoelectronics Tech. Co. Ltd.) emitting at 355 nm (pulse duration ~ 5 ns and repetition rate 5 kHz) and detection with the photon-counting photomultiplier (H11526-20-NF, Hamamatsu) connected to a multichannel scaler (MS-300, Becker & Hickl).

The UV-stability experiment was performed by continuous irradiation with UV light from the 380-nm LED. The absorbed dose during one irradiation step was 9.8×10^{15} photons. This means the average absorption of 0.7 photon per NC for a sample which contains 1.4×10^{16} NCs.

We determined the absolute external PL QY directly by using a set-up based on an integrating sphere (IS) with diameter of 10 cm (SphereOptics GmbH). The measured cuvette was introduced from top through a square port and excited by indirect diffused light (see Fig. 2(b)). Light from IS was coupled to a silica fibre bundle whose output was imaged to an imaging spectrometer (Acton SpectraPro SP2150i, focal length $f = 15$ cm) with a deep-depletion back-illuminated CCD camera (Spec-10:400B, Princeton Instruments). The apparatus response was radiometrically calibrated in the range from 300 to 1100 nm (for details see Ref. 30). PL was excited by various LEDs emitting in the range from UV to NIR region. The PL QY was calculated as the ratio of the number of emitted photons (the difference between the investigated and the reference sample signals in the region of

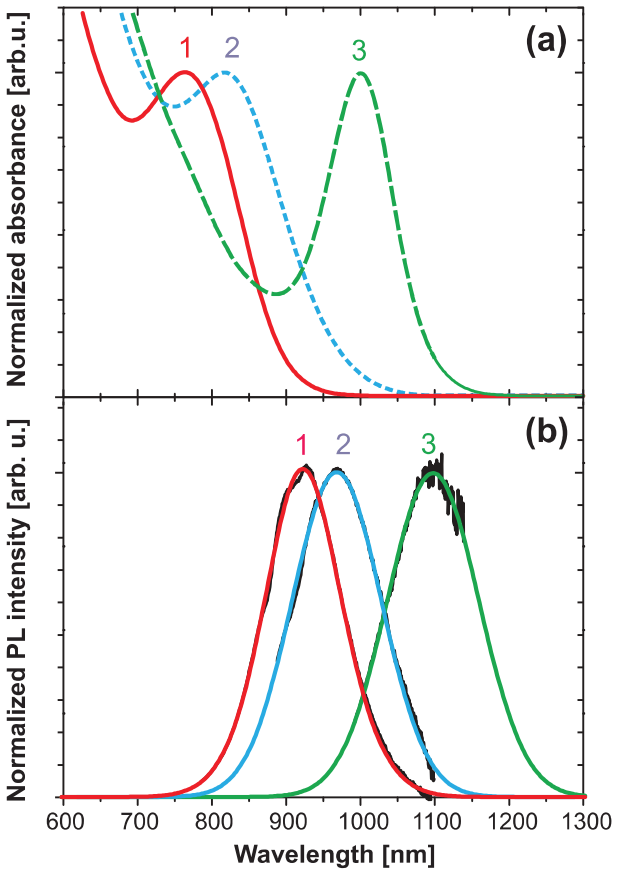

FIG. 1. Absorption (a) and photoluminescence (b) spectra of investigated samples of PbS QDs with the mean diameter of 2.4 nm (1), 3 nm (2), and 3.3 nm (3). The experimental PL spectra (black lines) are fitted by Gaussian bands in order to extend the spectrum above the detection limit at around 1100 nm.

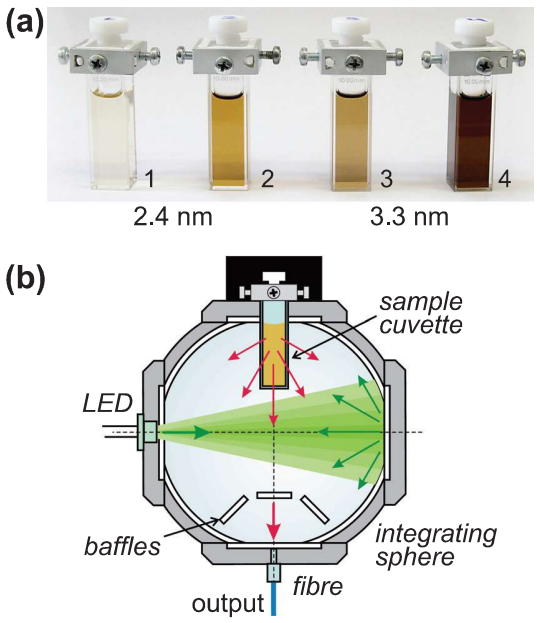

FIG. 2. (a) Suspensions of OA-capped PbS QDs in toluene with the mean diameter of 2.4 nm (1,2) and 3.3 nm (3,4) and concentrations of 1.55 μM/l (1), 7.75 μM/l (2), 3 μM/l (3), and 8 μM/l (4); (b) schematic representation of the integrating sphere set-up with an indirect LED excitation of PbS QDs samples in cuvettes.

photoluminescence) and the number of absorbed photons (integrated decrease of the excitation source signal in the sample compared to the reference)

$$QY = \frac{\sum_{em.band}\left[\frac{I^{em}_{PbS}(E_{em}) - I^{em}_{ref}(E_{em})}{C(E_{em}) \times T_{emF}(E_{em}) \times E_{em}}\right]}{\sum_{ex.band}\left[\frac{I^{ex}_{ref}(E_{ex}) - I^{ex}_{PbS}(E_{ex})}{C(E_{ex}) \times T_{exF}(E_{ex}) \times E_{ex}}\right]}, \quad (2)$$

where I^{em} and I^{ex} are the measured emission and excitation intensities for the PbS QDs solutions and reference pure toluene samples (marked by subscripts "PbS" and "ref"). C is the sensitivity spectrum of the apparatus lamp. The functions T_{exF} and T_{emF} represent transmittance spectra of filters used during acquisition of excitation and emission signal, and E_{ex} and E_{em} are the emission and excitation photon energies, respectively.[31]

III. RESULTS AND DISCUSSION

A. Excitation photon energy dependence of PL QY

PL QY of all three PbS QD samples with various concentrations was determined in a broad excitation spectral range (from about 300 nm up to an excitonic absorption band) using excitation by about 30 different LEDs. The results are presented in Figs. 3 and 4. While the absolute QY values are sample dependent, the general tendency in QY excitation spectra is the same: PL QY for the resonant photon energies (within the excitonic absorption peak) is higher than for excitation to higher energy states. It is commonly expected that PL QY of QDs decreases for larger excitation photon energies because the relaxation of generated hot carriers can take place via various non-radiative pathways related to surface and other trap states.[32] We observe that for all investigated sizes of PbS QDs the non-resonantly excited PL QY is approximately linearly decreasing with increasing photon energy. Only the 3.3 nm dots reveal QY increase in the UV region.

The literature reports on excitation spectra of PL QY in PbS QDs are very rare. We can refer to the paper by Fernee *et al.*,[33] who reported on two linear regimes of QY vs. photon energy dependence for a resonant and non-resonant excitation of 2 nm PbS QDs in hexane with PL QY values close to our results on 2.4 nm PbS QDs.

B. Concentration dependence of PL QY

The concentration dependence of PL QY is extracted in Figs. 3(c) and 4(b). The QY values for big QDs (3 nm and 3.3 nm) are concentration-independent for concentrations up to 5 μM/l (Fig. 3(c)). At higher concentrations, PL QY is reduced due to the well-known effect of reabsorption — emitted light can be reabsorbed by QDs in the region of the spectral overlap between absorption and emission. The reabsorption reveals itself in a distortion of the emission spectrum at its high-energy edge with the red-shift of the emission maximum upon increasing concentration. Moreover, the reabsorption effect is particularly pronounced for integrating sphere setups, where

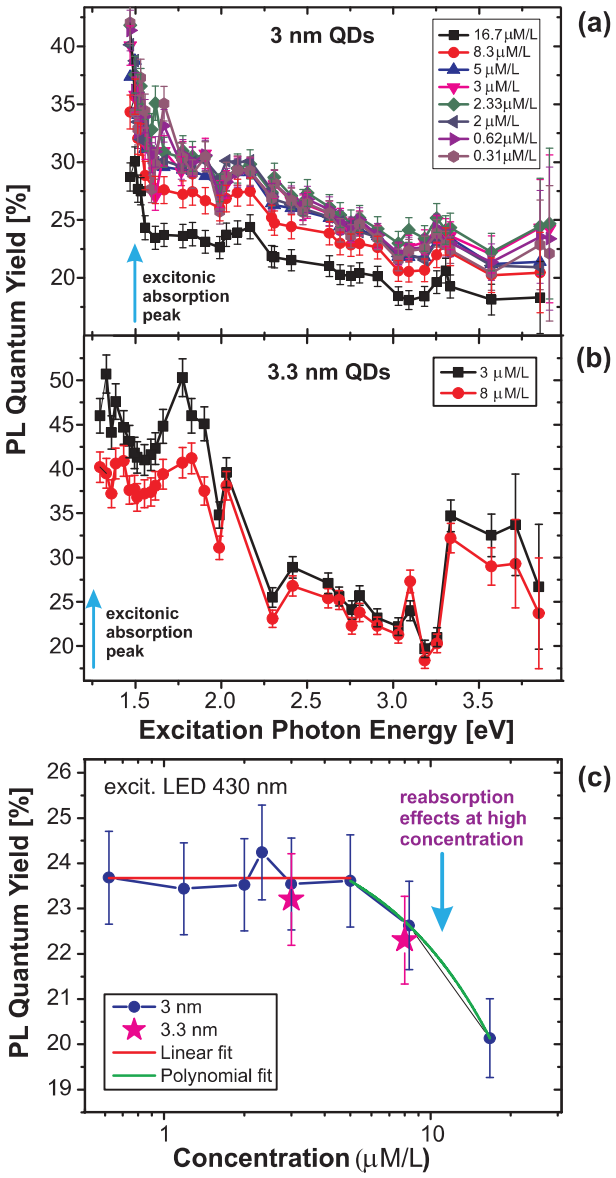

FIG. 3. PL QY dependence on the excitation photon energy ((a) and (b)) and solution concentrations (c) for 3 nm (a) and 3.3 nm (b) PbS QDs in toluene. The blue arrows indicate positions of the excitonic absorption peaks.

the mean light pass through a sample is increased by multiple reflections. To avoid this effect, the measurements should be done for sufficiently diluted suspensions of QDs or a reabsorption correction should be applied. Another motivation for avoiding too high concentrations of QDs is aggregation, which could disturb the correct determination of absorbance in some spectral regions and the contribution of QD aggregates should be considered in this case.[34]

C. Abnormal dependence of PL QY on concentration

In the case of small PbS QDs (2.4 nm), we observe surprising decrease of PL QY with decreasing concentration (B) even for highly diluted samples (<5 μM/l, Fig. 4(b)) with negligible reabsorption. In our opinion, the most probable origin of such behaviour is the surface quality which changes with concentration in case of small QDs. Namely, the ligand

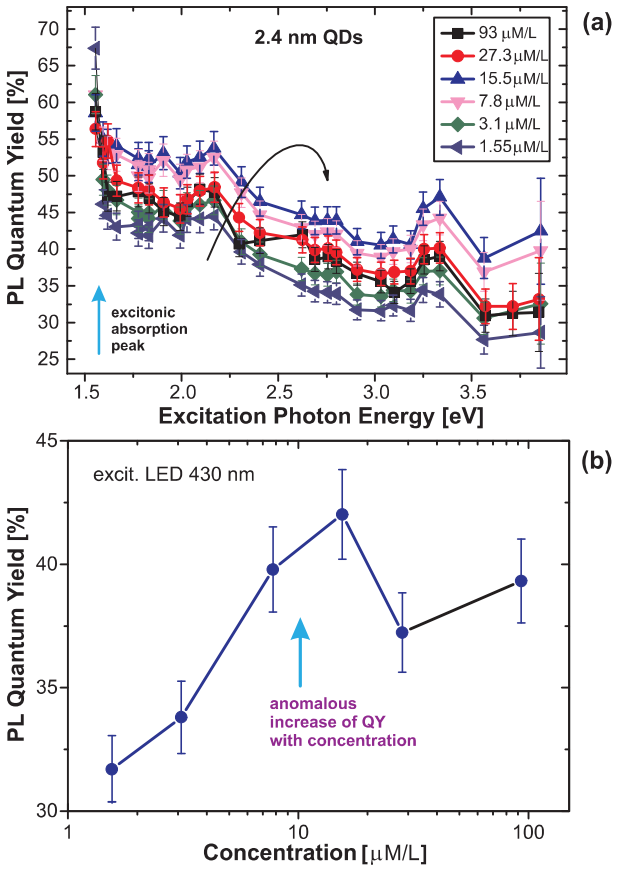

FIG. 4. PL QY dependence on the excitation photon energy (a) and solution concentrations (b) for 2.4 nm PbS QDs in toluene.

desorption and oxidation of QD surfaces can take place and affect the PL QY values.

The abnormal PL QY concentration dependence was previously reported for QDs of CdTe[35] and CdSe/ZnSe/ZnS[36] and was attributed to the ligand adsorption-desorption equilibrium. As the smaller QDs have higher surface-to-volume ratio, the probability of partial ligand desorption at lower QD concentrations is higher for small QDs than for big ones. When QDs become less protected from their environment, the reduction of PL QY is observed. This effect could be, in general, expected for QDs consisting of a semiconductor core and surface-bound ligands that are non-covalently bound to the particle surface.[34] The second argument why smaller QDs could be more sensitive to the concentration of suspension is the size-dependence of oxidation itself. It was reported[37] that larger PbS QDs are more robust against oxidation compared to smaller QDs, which effect was attributed to the trap site oxidation effects. This behaviour is in agreement with our experiment and will be discussed in Sec. III D.

Thus, relatively small PbS QDs can be considered as stable particles only at sufficiently high concentrations.[38] Obviously, for very high QD concentrations the PL-reabsorption effect reduces PL QY values of small PbS QDs as well as for bigger QDs (Figs. 3 and 4). That points out the importance of measuring PL QY for different concentrations to reveal and correct for possible ligand desorption and PL reabsorption effects. However, for larger PbS QDs the ligand desorption effects may be observed only at very low concentration,[35] where QY measurements become difficult. The concentration-selective ligand desorption dynamics has been reported as the main parameter determining the photo-oxidation process of 3.7 nm PbS QDs. The effect was well pronounced for low QD concentrations only (0.06–0.3 μM/l). To support the idea of ligand desorption, we have prepared two set of 3.3 nm PbS QD suspensions with different concentrations. Into one set we added 10 μl of OA in toluene (1:4 OA in toluene, i.e., 2 μl of pure OA, Sigma Aldrich). As expected, a small reduction of QY has been observed for concentrations lower than 0.5 μM/l (see Fig. S2 in supplementary information[29]). On the other hand, for samples with added OA we observed almost no decrease of QY with decreasing concentration, so indicating that the ligand desorption from surfaces of QDs can be the origin of the abnormal QY concentration dependence.

D. Degradation of optical properties

Previous reports[24,26,39] about lead chalcogenide QDs reveal the dependence of QD stability not only on particle size, concentration, ligand, solvent, and conditions of storage (darkness, room light, or UV exposure)[40] but also on other parameters such as nanocrystal surface geometry and shape[23] and synthesis method.[26] While the PbS QDs synthesized by modified Cademartiri method are air-stable over the entire available size range,[26] the QDs produced by Hines method[20] are commonly considered as air-stable only for rather small QD sizes,[23,39] The enhanced stability of QDs synthesized by the Cademartiri method can be due to the $PbCl_x$ passivation layer that prevents QD surface from oxidation.[26,41]

In contrast, our PbS/OA QDs reveal better air-stability for larger QDs. After 13 days of storage, the 2.4 nm QDs demonstrate blue shift of 12 nm for 7.75 μM/l, while for the 3.3 nm QDs it is only 4 nm for 8 μM/l (Fig. 5). The same size-dependent stability was reported also for PbS/OA[37] and CdTe[42] QDs but reports on concentration-dependent stability of PbX (X = S or Se) QDs are very scarce.[40,43]

In Fig. 5(b), we present the concentration dependence of air-stability of 2.4 nm and 3.3 nm PbS QDs stored in darkness. One can see that the stability of suspensions is improving with increasing concentration for both QD sizes. This observation can be understood in the framework of the ligand adsorption-desorption equilibria hypothesis mentioned in Sec. III C: for less concentrated samples, the ligand is less stable and higher fraction of QD surface is oxidized. Moreover, we observe (Fig. 6) more pronounced concentration-dependence of QD stability for small QDs, which have higher ligand desorption probability and so becomes more prone to oxidation. These results are in agreement with paper 43 but in contrast to Ref. 40 related to PbSe QDs.

The process of QD surface oxidation and ligand degradation can be accelerated by illumination with UV light (see Fig. S3 and supplementary information).

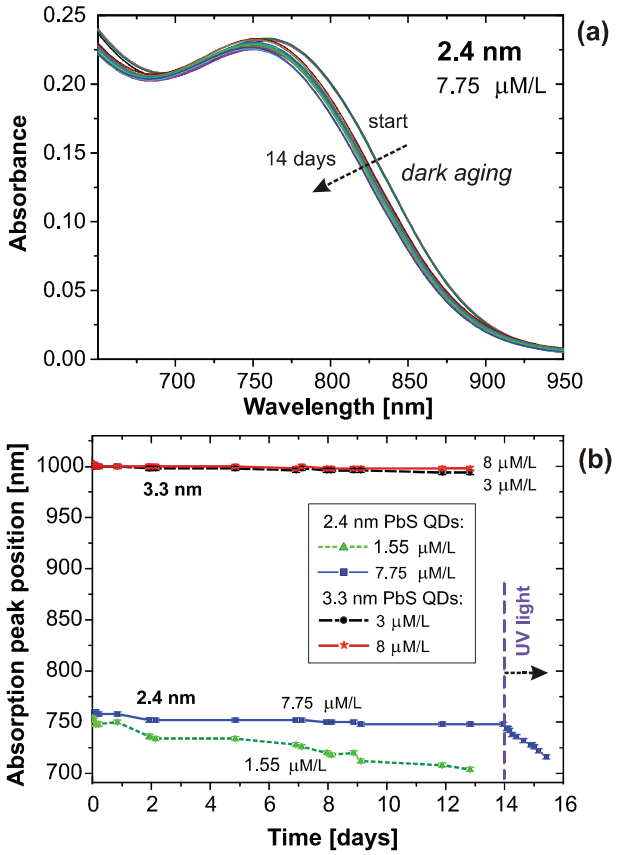

FIG. 5. (a) Optical evolution of the first absorption peak of 2.4 nm PbS QDs stored in darkness for 13 days. (b) The shift of absorption peak for 2.4 nm (▲, ■) and 3.3 nm (●, ★) OA-capped PbS QDs in toluene at different concentrations stored in darkness. The UV light marked region is related to the storage regime under continuous UV light illumination which accelerates degradation of PbS QDs.

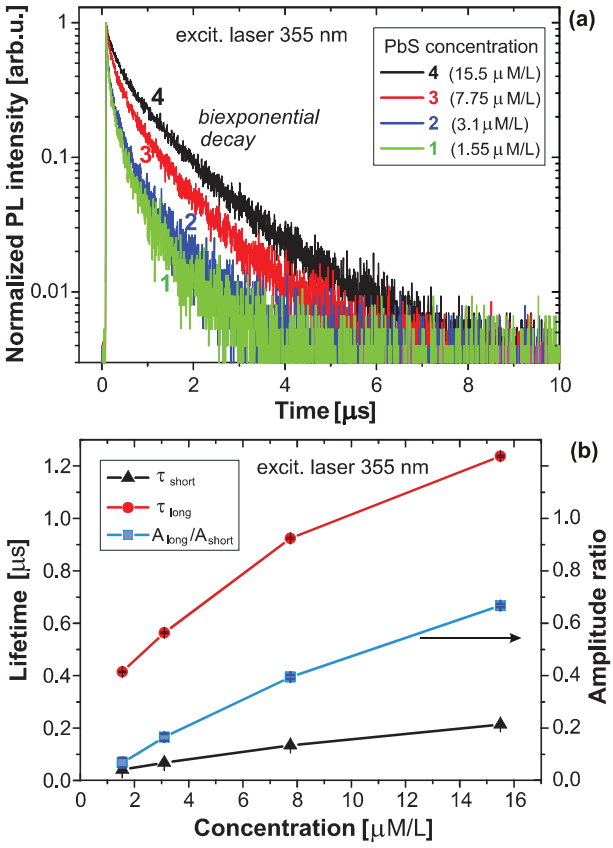

FIG. 6. (a) Time-resolved PL decay of 2.4 nm PbS QD suspensions of different concentrations. (b) The concentration dependence of long and short lifetime components as well as their amplitude ratio.

E. The origin of PL

More information on the origin of PL in PbS QDs can be obtained from time-resolved PL experiments that could reveal a single- or multiple-component decay, depending on charge-transfer and relaxation processes. PL decay kinetics of the 2.4 nm QDs with different concentration are shown in Fig. 6(a). All the kinetics are well fitted by a biexponential decay

$$I_{PL} \sim A_1 \exp(-t/\tau_1) + A_2 \exp(-t/\tau_2), \quad (3)$$

with τ_1 and τ_2 in the range of 40–215 ns and 415–1240 ns, respectively. Even if such form of PL decay is quite typical for colloidal QDs,[44] many papers on PbS QDs report on a single-exponential decay.[21,22,45,46] However, two papers[21,46] present analytical models which predict the biexponential PL decay of PbS QDs. Ushakova *et al.*[21] derived the shorter lifetime value of about 100 ns for 3 nm diameter of PbS QDs in tetrachloromethane including the increase of lifetime by factor 11 due to the dielectric screening. Similar screening factor $\varepsilon \sim 9.5$ for toluene solvent can be calculated by Eq. (4)

$$\varepsilon = \frac{(\varepsilon_1 + 2\,\varepsilon_2)}{(3\,\varepsilon_2)^2}, \quad (4)$$

where $\varepsilon_1 = 17.2$ and $\varepsilon_2 = 2.38$ are dielectric constants for toluene and PbS, respectively. Taking into account that most of theoretical models use bulk material parameters for calculation and the fact that toluene is absorbing light in the emission range of our QDs (see supplementary information[29]), we found good agreement of our fast lifetime components with theoretically predicted ones. We suppose that this fast τ_1 component appears as the radiative recombination of excited carriers in a QD core. To our best knowledge, there is only one paper reporting about fast lifetime component (~100 ns) of PbS QDs in TCE and water.[16]

Long PL lifetimes have been reported previously for lead selenide[47,48] and lead sulfide[16,22,45,46,49] QDs. Such longer lifetime component could be attributed to the recombination of spatially separated carriers in surface-localized states and core states.[33] Because of the small overlap of wavefunctions of these separated carriers, the radiative lifetime becomes much longer.[21] Indeed, there are several papers reporting on the presence of in-gap surface states in PbS QDs.[21,33,46,50] The large inhomogeneous line-width of PL spectra of single PbS QD could indirectly indicate on exciton trapping in surface states or defect sites.[51] Defects can consist of unpassivated sulfur atoms, as it is known[52] that oleic acid bounds only to lead surface atoms. The model of Fernee *et al.*[33] assumes that these surface states act as shallow hole traps in QDs and lie about 370 meV below the bulk semiconductor valence band-edge. However, the exact structure of surface states must be investigated separately.

Fig. 6(b) demonstrates that the amplitude ratio of longer versus shorter lifetime components is decreasing with concentration of suspension (QY). It indicates that the surface-related emission is mainly responsible for the efficient PL of our QDs, which is in contrast to the usual assignment of high QY to an efficient electron-hole recombination in a QD core. However, it was recently demonstrated that radiative surface sites could serve as efficient luminescent centers for strongly quantum confined PbS[33] or CdSe[44] QDs and does not necessary lead to PL quenching. This is consistent with our observation of concentration-dependent surface changes. The enhanced oxidation of more diluted samples results in concomitant surface passivation that partially eliminates luminescent trap centers. Moreover, the surface quality degrades because of newly introduced non-radiative quenching defects that suppress the fraction of surface-related emission.

Both the radiative and non-radiative decay rates are decreasing as the solution becomes more diluted as it can be calculated from our QY and PL decay data using Eq. (5)

$$QY = \frac{\tau_{PL}}{\tau_r}, \quad \frac{1}{\tau_{PL}} = \frac{1}{\tau_r} + \frac{1}{\tau_{nr}}, \tag{5}$$

where τ_r, τ_{nr}, and τ_{PL} are radiative, non-radiative, and PL decay lifetimes, respectively. However, the non-radiative decay rate is changing more. Thus, the higher oxidation rate of QDs in low-concentrated suspensions results in larger number of non-radiative pathways introduced by oxidation products. The radiative part of decay rate is increasing most likely because of stronger contribution by core-state recombination.

F. The comparison of QY values

There are various PL QY values of PbS QDs reported in the literature that were obtained for different QY measurement techniques, excitation photon energies, QD synthesis methods, QD sizes and concentrations, solvents, etc. All of these parameters are more or less important. Therefore, a systematic analysis of literature data, missing so far, is of a big importance. In Fig. 7, we present comparison of QY of PbS QDs capped by oleic acid in toluene or hexane reported in different papers. In the previous paragraphs, we have demonstrated that values of QY depend on several factors (mainly on excitation photon energy and concentration of suspensions) and can vary in a broad range, which makes the comparison of literature data difficult. In spite of this, most of PL QY values in Fig. 7 are quite systematic. The trend of decreasing PL QY with increasing QD size of PbS[26,53] and PbSe[54] QDs observed by us and others is quite evident from Fig. 7.

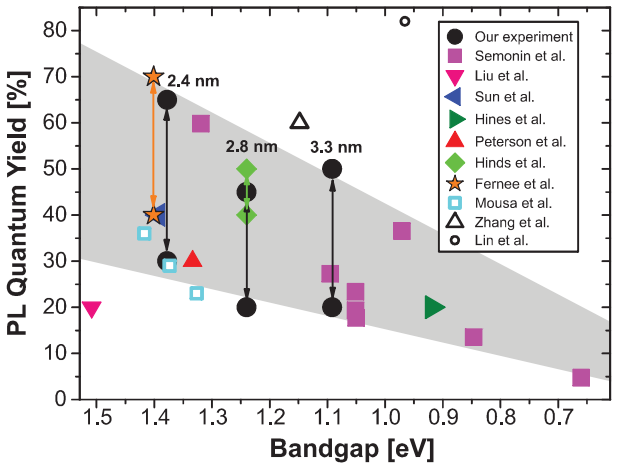

FIG. 7. Relation between PL QY and optical gap (inversely related to the QD size, see Eq. (1)). Our data are represented by black circles and literature data for PbS/OA QDs in toluene or hexane are extracted from the following papers: ■ (Ref. 53), ▼ (Ref. 55), ◀ (Ref. 56), ▶ (Ref. 20), ▲ (Ref. 51), ◆ (Ref. 57), ★ (Ref. 33), □ (Ref. 58), △ (Ref. 43), and ○ (Ref. 59). The arrows define the limits where the PL QY corresponding to a size of QD could vary depending on the excitation photon energy or solution concentration.

IV. CONCLUSIONS

In this work, we have studied absolute PL QY of PbS/OA colloidal QDs in toluene depending on the QD size, concentration, excitation photon energies, and conditions of storage. We have demonstrated that PbS QDs violate the Kasha-Vavilov rule and pointed out that PL QY must be detected over a broad excitation spectral range instead of just one or a few excitation wavelengths. PL QY value for a given sample should be, in principle, independent on concentration in low concentrated suspensions and exhibit a decrease at high concentrations due to reabsorption. Such normal behaviour was observed for PbS QDs with the mean diameter of 3 nm and bigger for solution concentrations more than 0.5 μM/l, while an abnormal decrease with decreasing concentration was observed for lower concentration solutions. The same effect has been observed for smaller 2.4 nm PbS QDs even at much higher concentrations (up to 5 μM/l).

The size- and concentration-dependent surface modifications of QDs caused by ligand desorption and oxidation have been shown to be responsible for the abnormal concentration dependence. Thus, the larger QDs in higher concentrated suspensions proved higher stability in comparison with smaller QDs and less concentrated suspensions. Therefore, the information about the concentration of QD suspension is of crucial importance when QY values are reported. Anyway, we can propose the size-invariant optimum concentration (the least affected by artefacts) of PbS QDs for PL QY characterization to be around 5 μM/l. Moreover, the addition of extra volume of OA molecules to QD solutions reduces the ligand desorption probability from the surface of QD and the QY values become more or less concentration independent in the entire reabsorption-free concentration range. Nevertheless, the storage conditions of such samples are extremely important as the UV light illumination leads to dramatic acceleration of ligand desorption and photo-oxidation processes and exponential decrease of PL QY with time of UV exposure.

The double-exponential form of the PL decay kinetics reveals two distinct relaxation processes. The short lifetime component (up to 0.4 μs) could be attributed to the intrinsic recombination of initially populated electron-hole pairs in a

QD core. The long lifetime component (up to $\sim 1.2\ \mu s$) originates from efficient surface carrier trapping, which appears to be dominant in our PbS QDs.

Our experimental results clearly point to the crucial role of surface states for relaxation processes, PL QY and stability of QDs and could facilitate the optimization of PbS QDs performance for various applications.

ACKNOWLEDGMENTS

This work was supported by the Bonus programme of Charles University. We acknowledge technical assistance by M. Scholz during the PL kinetics experiments.

[1]A. P. Alivisatos, Science **271**, 933 (1996).
[2]A. Lipovskii, E. Kolobkova, V. Petrikov, I. Kang, A. Olkhovets, T. Krauss, M. Thomas, J. Silcox, F. Wise, Q. Shen, and S. Kycia, Appl. Phys. Lett. **71**, 3406 (1997).
[3]I. Kang and F. W. Wise, J. Opt. Soc. Am. B **14**, 1632 (1997).
[4]C. B. Murray, S. Sun, W. Gaschler, H. Doyle, T. A. Betley, and C. R. Kagan, IBM J. Res. Dev. **45**, 47 (2001).
[5]L. Sun, J. J. Choi, D. Stachnik, A. C. Bartnik, B.-R. Hyun, G. G. Malliaras, T. Hanrath, and F. W. Wise, Nat. Nanotechnol. **7**, 369 (2012).
[6]R. S. Sanchez, E. Binetti, J. A. Torre, G. Garcia-Belmonte, M. Striccoli, and I. Mora-Sero, Nanoscale **6**, 8551 (2014).
[7]S. Hoogland, V. Sukhovatkin, I. Howard, S. Cauchi, L. Levina, and E. H. Sargent, Opt. Express **14**, 3273 (2006).
[8]E. H. Sargent, Nat. Photonics **3**, 325 (2009).
[9]J. M. Luther, M. Law, M. C. Beard, Q. Song, M. O. Reese, R. J. Ellingson, and A. J. Nozik, Nano Lett. **49**, 3488 (2008).
[10]G.-H. Kim, B. Walker, H.-B. Kim, J. Y. Kim, E. H. Sargent, and J. Park, Adv. Mater. **26**, 3321 (2014).
[11]S. A. McDonald, G. Konstantatos, S. Zhang, P. W. Cyr, E. J. D. Klem, L. Levina, and E. H. Sargent, Nature Mater. **4**, 138 (2005).
[12]G. Konstantatos and E. H. Sargent, Proc. IEEE **97**, 1666 (2009).
[13]S. H. Im, H. Kim, and S. Il Seok, Nanotechnology **22**, 395502 (2011).
[14]G. V. Shcherbatyuk, R. H. Inman, C. Wang, R. Winston, and S. Ghosh, Appl. Phys. Lett. **96**, 191901 (2010).
[15]U. Aeberhard, R. Vaxenburg, E. Lifshitz, and S. Tomić, Phys. Chem. Chem. Phys. **14**, 16223 (2012).
[16]B.-R. Hyun, H. Chen, D. A. Rey, F. W. Wise, and C. A. Batt, J. Phys. Chem. B **111**, 5726 (2007).
[17]L. Turyanska, F. Moro, A. N. Knott, M. W. Fay, T. D. Bradshaw, and A. Patanè, Part. Part. Syst. Charact. **30**, 945 (2013).
[18]X. Michalet, F. F. Pinaud, L. A. Bentolila, J. M. Tsay, S. Doose, J. J. Li, G. Sundaresan, A. M. Wu, S. S. Gambhir, and S. Weiss, Science **307**, 538 (2005).
[19]R. Gill, M. Zayats, and I. Willner, Angew. Chem. Int. Ed. **47**, 7602 (2008).
[20]M. A. Hines and G. D. Scholes, Adv. Mater. **15**, 1844 (2003).
[21]E. V. Ushakova, A. P. Litvin, P. S. Parfenov, A. V. Fedorov, M. Artemyev, A. V. Prudnikau, I. D. Rukhlenko, and A. V. Baranov, ACS Nano **6**, 8913 (2012).
[22]J. H. Warner, E. Thomsen, A. R. Watt, N. R. Heckenberg, and H. Rubinsztein-Dunlop, Nanotechnology **16**, 175 (2005).
[23]H. Choi, J.-H. Ko, Y.-H. Kim, and S. Jeong, J. Am. Chem. Soc. **135**, 5278 (2013).
[24]N. Reilly, M. Wehrung, R. A. O'Dell, and L. Sun, Mater. Chem. Phys. **147**, 1 (2014).
[25]L. Cademartiri, J. Bertolotti, R. Sapienza, D. S. Wiersma, G. von Freymann, and G. A. Ozin, J. Phys. Chem. B **110**, 671 (2006).
[26]I. Moreels, Y. Justo, B. De Geyter, K. Haustraete, J. C. Martins, and Z. Hens, ACS Nano **5**, 2004 (2011).
[27]J. R. Lacowicz, *Principles of Fluorescence Spectroscopy*, 3rd ed. (Springer, Singapore, 2006), p. 7.
[28]I. Moreels, K. Lambert, D. Smeets, D. De Muynck, T. Nollet, J. C. Martins, F. Vanhaecke, A. Vantomme, C. Delerue, G. Allan, and Z. Hens, ACS Nano **3**, 3023 (2009).
[29]See supplementary material at http://dx.doi.org/10.1063/1.4917388 for the solvent artefacts and the improvement of QY stability by adding oleic acid.
[30]J. Valenta, Nanosci. Methods **3**, 11 (2014).
[31]I. Pelant and J. Valenta, *Luminescence Spectroscopy of Semiconductors* (Oxford University Press, New York, 2012), p. 560.
[32]D. Timmerman, J. Valenta, K. Dohnalová, W. D. A. M. de Boer, and T. Gregorkiewicz, Nat. Nanotechnol. **6**, 710 (2011).
[33]M. J. Fernee, E. Thomsen, P. Jensen, and H. Rubinsztein-Dunlop, Nanotechnology **17**, 956 (2006).
[34]C. Würth, M. Grabolle, J. Pauli, M. Spieles, and U. Resch-Genger, Nat. Protoc. **8**, 1535 (2013).
[35]M. Grabolle, M. Spieles, V. Lesnyak, N. Gaponik, A. Eychmuüller, and U. Resch-Genger, Anal. Chem. **81**, 6285 (2009).
[36]J. Laverdant, W. D. De Marcillac, C. Barthou, V. D. Chinh, C. Schwob, L. Coolen, P. Benalloul, P. T. Nga, and A. Maître, Materials (Basel) **4**, 1182 (2011).
[37]J. J. Peterson and T. D. Krauss, Phys. Chem. Chem. Phys. **8**, 3851 (2006).
[38]H. Dollefeld, K. Hoppe, J. Kolny, K. Schilling, H. Weller, and A. Eychmuller, Phys. Chem. Chem. Phys. **4**, 4747 (2002).
[39]J. Tang, L. Brzozowski, D. A. R. Barkhouse, X. Wang, R. Debnath, R. Wolowiec, E. Palmiano, L. Levina, A. Pattantyus-Abraham, D. Jamakosmanovic, and E. H. Sargent, ACS Nano **4**, 869 (2010).
[40]Q. Dai, Y. Wang, Y. Zhang, X. Li, R. Li, B. Zou, J. Seo, Y. Wang, M. Liu, and W. W. Yu, Langmuir **25**, 12320 (2009).
[41]W. K. Bae, J. Joo, L. A. Padilha, J. Won, D. C. Lee, Q. Lin, W. Koh, H. Luo, V. I. Klimov, and J. M. Pietryga, J. Am. Chem. Soc. **134**, 20160 (2012).
[42]S. K. Poznyak, N. P. Osipovich, A. Shavel, D. V. Talapin, M. Gao, A. Eychmuller, and N. Gaponik, J. Phys. Chem. B **109**, 1094 (2005).
[43]T. Zhang, H. Zhao, D. Riabinina, M. Chaker, and D. Ma, J. Phys. Chem. C **114**, 10153 (2010).
[44]X. Wang, L. Qu, J. Zhang, X. Peng, and M. Xiao, Nano Lett. **3**, 1103 (2003).
[45]S. W. Clark, J. M. Harbold, and F. W. Wise, J. Phys. Chem. C **111**, 7302 (2007).
[46]A. P. Litvin, P. S. Parfenov, E. V. Ushakova, A. V. Fedorov, M. V. Artemyev, A. V. Prudnikau, S. A. Cherevkov, I. D. Rukhlenko, and A. V. Baranov, Proc. SPIE **8564**, 85641Z–1–7.
[47]H. Du, C. Chen, R. Krishnan, T. D. Krauss, J. M. Harbold, F. W. Wise, M. G. Thomas, and J. Silcox, Nano Lett. **2**, 1321 (2002).
[48]B. L. Wehrenberg, C. Wang, and P. Guyot-Sionnest, J. Phys. Chem. B **106**, 10634 (2002).
[49]B.-R. Hyun, A. C. Bartnik, J.-K. Lee, H. Imoto, L. Sun, J. J. Choi, Y. Chujo, T. Hanrath, C. K. Ober, and F. W. Wise, Nano Lett. **10**, 318 (2010).
[50]D. Kim, T. Kuwabara, and M. Nakayama, J. Lumin. **119–120**, 214 (2006).
[51]J. J. Peterson and T. D. Krauss, Nano Lett. **6**, 510 (2006).
[52]A. Lobo, T. Möller, M. Nagel, H. Borchert, S. G. Hickey, and H. Weller, J. Phys. Chem. B **109**, 17422 (2005).
[53]O. E. Semonin, J. C. Johnson, J. M. Luther, A. G. Midgett, A. J. Nozik, and M. C. Beard, J. Phys. Chem. Lett. **1**, 2445 (2010).
[54]J. M. Pietryga, R. D. Schaller, D. Werder, M. H. Stewart, V. I. Klimov, and J. A. Hollingsworth, J. Am. Chem. Soc. **126**, 11752 (2004).
[55]T.-Y. Liu, M. Li, J. Ouyang, M. B. Zaman, R. Wang, X. Wu, C.-S. Yeh, Q. Lin, B. Yang, and K. Yu, J. Phys. Chem. C **113**, 2301 (2009).
[56]L. Sun, J. Fang, J. C. Reed, L. Estevez, A. C. Bartnik, B.-R. Hyun, F. W. Wise, G. G. Malliaras, and E. P. Giannelis, Small **6**, 638 (2010).
[57]S. Hinds, S. Myrskog, L. Levina, G. Koleilat, J. Yang, S. O. Kelley, and E. H. Sargent, J. Am. Chem. Soc. **129**, 7218 (2007).
[58]A. Mousa, *Synthesis and Characterization of PbS Quantum Dots* (Lund University, 2011).
[59]W. Lin, K. Fritz, G. Guerin, G. R. Bardajee, S. Hinds, V. Sukhovatkin, E. H. Sargent, G. D. Scholes, and M. A. Winnik, Langmuir **24**, 8215 (2008).

Paper VI

JOURNAL OF APPLIED PHYSICS **122**, 144303 (2017)

Photoluminescence performance limits of Si nanocrystals in silicon oxynitride matrices

Jan Valenta,[1,a)] Michael Greben,[1] Sebastian Gutsch,[2] Daniel Hiller,[2] and Margit Zacharias[2]
[1]*Department of Chemical Physics and Optics, Faculty of Mathematics and Physics, Charles University, Prague, Czechia*
[2]*Faculty of Engineering, IMTEK, Albert-Ludwigs-University Freiburg, Freiburg, Germany*

(Received 4 August 2017; accepted 28 September 2017; published online 10 October 2017)

The present comprehensive study of photoluminescence (PL) quantum yield (QY) of Si nanocrystals (SiNCs) in Si-rich oxynitride (SRON) superlattices was performed over a broad set of samples. The PL QY is sensitive mostly to the thickness of SRON and barrier oxide layers and to the passivation procedures. Annealing in hydrogen improves the QY proportionally to the NC surface area by passivating the NC/oxide interface defects present at a surface density of about $2.5 \times 10^{12}\,cm^{-2}$. The maximum external QY of nearly 30% is found in well-passivated superlattices with a SiNC size of about 4 nm and a SiO_2 barrier thickness of 2 nm or larger. We reveal the existence of an extended near-infrared tail of the PL spectra, whose weak intensity anti-correlates with the external QY. The relative intensity of this emission increases with temperature as well as for strong excitation above the PL saturation level and may be related to excitation energy transfer to the structural defects near NCs. Finally, we discuss the possible mechanisms which are responsible for limiting the attainable PL QY and which may be the subject of future efforts to further increase the PL QY. *Published by AIP Publishing*. https://doi.org/10.1063/1.4999023

I. INTRODUCTION

Luminescence quantum yield (QY) is a crucial parameter for any material to be used in light-emitting devices (LEDs),[1–3] as wavelength converters for lighting or photovoltaics,[4–6] etc. Silicon nanocrystals (SiNCs) embedded in silica (silicon dioxide - SiO_2) have been shown to provide a relatively high photoluminescence (PL) QY of the order of 10%, which is tunable in the spectral region from orange to near infrared (NIR), i.e., about 650–1100 nm (roughly 1.9–1.1 eV).[7]

Two types of PL QYs must be distinguished: (i) *External* QY (EQY), which is the ratio of numbers of emitted and absorbed photons (photon rates) for the whole investigated sample. (ii) *Internal* QY (IQY), which is defined as the ratio of the radiative decay rate to the total decay rate (sum of radiative and non-radiative rates). (Note: This definition of IQY is different from that used for characterization of LEDs, where it means the overall emission efficiency without outcoupling losses). Outcoupling losses can be neglected in plate-shaped samples on transparent substrates when the PL reabsorption is negligible (i.e., for a large Stokes shift between emission and absorption) like in the case of SiNCs studied here. On the other hand, EQY may become smaller than IQY when an ensemble of nanocrystals contains some "*dark*" nanocrystals (NCs) or defects (which absorb, but do not emit photons due to very fast and efficient non-radiative relaxation). The existence of dark NCs can be directly revealed by combining the luminescence and AFM imaging of single NCs[8] or indirectly estimated by PL QY studies.[9]

In this paper, we provide a comprehensive study of PL EQY of SiNCs in Si-rich oxynitride (SRON) superlattices (SL) separated by silica barriers. The SL configuration enables superior control of SiNC size and uniform deposition over considerable areas. By systematic variation of the most important sample parameters, we found that the maximum EQY of about 27% is achieved in well-passivated superlattices with SiNC size of about 4 nm and the SiO_2 barrier thickness of 2 nm or larger. We also obtain an estimate of IQY by analyzing PL decay kinetics in comparison with organically passivated SiNCs in colloidal suspensions. Using a broadband micro-spectroscopy set-up, we reveal the presence of a weak infrared emission tail (extending well below the bulk-Si band-gap), whose intensity in different samples anti-correlates with the EQY values. This weak emission may be due to the low-probability radiative recombination in defect centers at the interface of SiNCs and silica. Finally, we discuss mechanisms that are responsible for limiting the attainable EQY of SiNCs and which may be the subject of future effort to further increase the emission efficiency.

II. EXPERIMENTAL TECHNIQUES

A. Photoluminescence quantum yield measurement apparatus

PL EQY was studied using a spectroscope with an integrating sphere (IS) designed and built in our laboratory. Both the set-up and the theoretical background of EQY determination were described in our recent paper.[10] The inner surface of the IS (diameter of 10 cm) is covered by the Spectraflex coating. Samples are placed in the IS on one removable port in the position opposite to the excitation port where various light-emitting diodes (LEDs) are mounted to provide the PL

[a)]Author to whom correspondence should be addressed: jan.valenta@mff.cuni.cz

TABLE I. Description of sample parameters.

Label	Layer stack	SiO_X thick. (nm)	SiO_2 thick. (nm)	Stoichiometry x-value	H-annealing
M1-1x	40 bilayers	2	2	0.93	No
M1-1	40 bilayers	2	2	0.93	Yes
M1-2x	40 bilayers	3.5	2	0.93	No
M1-2	40 bilayers	3.5	2	0.93	Yes
M1-3x	40 bilayers	5	2	0.93	No
M1-3	40 bilayers	5	2	0.93	Yes
M1-4	40 bilayers	3.5	2	0.64	Yes
M1-5	40 bilayers	3.5	2	0.85	Yes
M1-6	40 bilayers	3.5	2	1.0	Yes
M2-1x	40 bilayers	1.5	2	1.00[a]	No
M2-1	40 bilayers	1.5	2	1.00[a]	Yes
M2-2x	40 bilayers	2.5	2	1.00[a]	No
M2-2	40 bilayers	2.5	2	1.00[a]	Yes
M2-3x	40 bilayers	3.5	2	1.00[a]	No
M2-3	40 bilayers	3.5	2	1.00[a]	Yes
M2-4x	40 bilayers	4.5	2	1.00[a]	No
M2-4	40 bilayers	4.5	2	1.00[a]	Yes
M3-1	40 bilayers	4.5	1.0	0.93	Yes
M3-2	40 bilayers	4.5	1.6	0.93	Yes
M3-3	40 bilayers	4.5	2.2	0.93	Yes
M3-4	40 bilayers	4.5	2.8	0.93	Yes
S3-1	Single layer	200	…	0.64	Yes
S3-2	Single layer	200	…	0.93	Yes
S3-3	Single layer	200	…	1.05	Yes
S3-4	Single layer	200	…	1.10	Yes
S3-5	Single layer	200	…	1.15	Yes

[a]Oxynitride $SiO_{1.00}N_{0.22}$. (see Ref. 13).

excitation. The power emitted by the respective LEDs is typically less than 1 mW and is not focused on the sample. It means that we work several orders of magnitude below saturating power density, which is about 1 W/cm^2 for Si NCs in the SiO_2 matrix (at this power, the average population is about one exciton per NC and PL saturation is observed for stronger pumping[11]). Alternatively, a laser-driven light source (LDLS, EQ-99X, Energetiq) coupled to the 15-cm monochromator (Acton SpectraPro SP-2150i) was used for the tunable excitation of EQY. The output signal from the IS is collected by a fused-silica fiber bundle placed in the direction perpendicular to the excitation axis, and it is shielded by baffles against the direct visibility of both the LED excitation source and the sample. The end of the fiber bundle (which has a stripe-like shape) is imaged to the input slit of an imaging spectrograph (15-cm focal length), and a liquid-nitrogen-cooled CCD camera is used for detection. The spectral sensitivity of the complete apparatus is calibrated over the broad UV-NIR spectral range (300–1100 nm) using two radiation standards (Newport Oriel): a 45-W tungsten halogen lamp (above 400 nm) and a deuterium lamp (below 400 nm). Special attention is paid to avoid stray-light effects in the spectrometer.

Due to technical reasons, the temperature variation of EQY was determined indirectly by measuring the temperature evolution of PL intensity $I_{PL}(T)$ and absorption cross-section $\sigma(T)$ of a sample placed in a cryostat and excited by a 405-nm laser whose continuous wave emission was modulated with an acousto-optical modulator (the leading and the trailing edge of the "rectangular" excitation pulses is about 0.1 μs, the frequency is 900 Hz and the duty cycle is 40%). Absorption cross-section is calculated from the intensity dependence of the PL onset and decay rates as described in our recent paper.[11]

B. Sample fabrication and characterization

The samples were deposited as alternating layers of silicon-rich silicon oxynitride (SRON; SiO_xN_y) and nitrogen-free stoichiometric silicon dioxide (SiO_2) on fused silica substrates by plasma-enhanced chemical vapor deposition (PECVD). The y value was found to be almost constant at 0.23 in all studied samples. On top and below the SL stack, 10 nm of SiO_2 were deposited as a capping and a buffer layer, respectively. The samples were consequently annealed in a quartz tube furnace at 1150 °C for 1 h in high purity N_2 gas in order to achieve phase separation between Si and SiO_2 (i.e., forming SiNCs). Part of the samples was additionally passivated by annealing in H_2 at 450–500 °C. Further details of sample preparation as well as structural properties of the NC samples are given in our recent papers.[12–14] In this study, we present results obtained on three series of *superlattice* samples and one series of *thick single-layers* (TSL) (i.e., a SRON monolayer without SiO_2 barriers), whose parameters are described in Table I.

Superlattice samples enable control of the mean diameter of SiNCs by varying the thickness of the Si-rich layers. This approach works quite effectively for sizes between 1.5

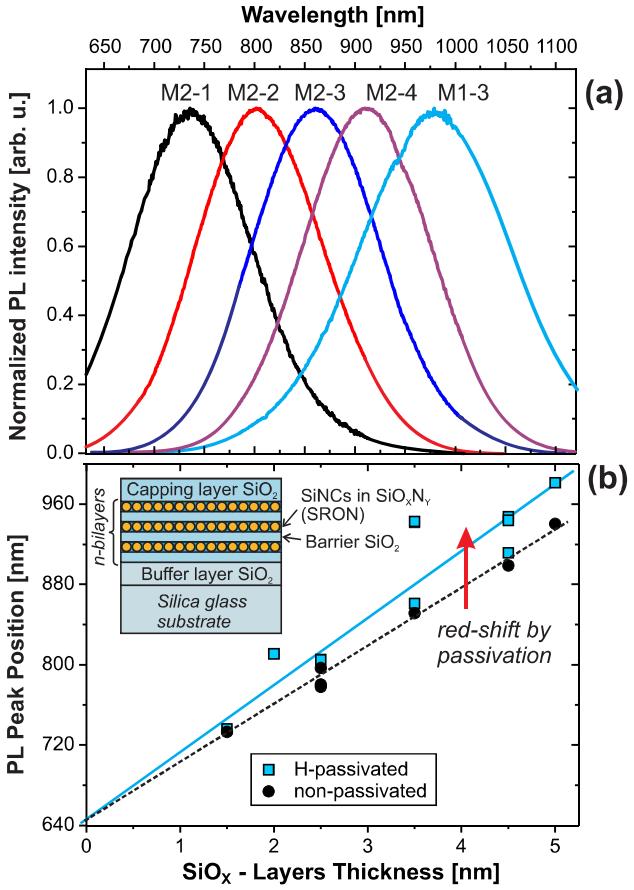

FIG. 1. (a) Normalized PL spectra for several SL samples under excitation by the 405-nm LED. (b) PL peak position as a function of SRON layer thickness. The inset shows schematics of SL sample composition.

and 5 nm.[14] The PL peak can be varied between 700 to 1000 nm [Fig. 1(a)] with approximately linear dependence on the SRON layer thickness [Fig. 1(b)]. Obviously, the stoichiometry value is very important, and the method works best for SiO_x close to silicon monoxide ($x = 1$). The H-passivation increases the PL yield and red-shifts the peak. The shift is due to the fact that bigger NCs contain more defects, which can be healed by passivation and their PL increase, see the results given below.

III. PHOTOLUMINESCENCE QUANTUM YIELD INVESTIGATION

A. Excitation spectra of EQY

Luminescence QY values are usually measured (and reported in the literature) for only one excitation wavelength. It is supposed that, especially for organic fluorescent materials, the so-called *Kasha-Vavilov (KV) rule* is fulfilled. The KV rule says that both the luminescence spectral shape and its QY do not depend on the applied excitation wavelength.[15] However, there may be exceptions to the KV rule. In general, for a semiconductor, one tends to expect decreasing PL QY for excitation addressing higher states above the band gap as more non-radiative paths can be opened for hotter carrier relaxation.

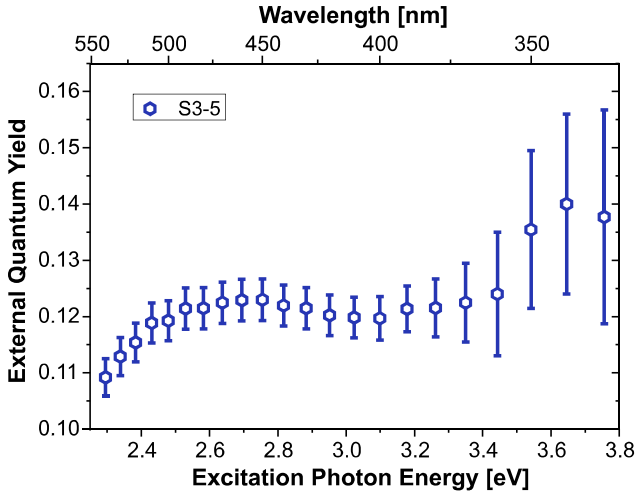

FIG. 2. EQY excitation spectrum of sample S3-5 measured under the tunable excitation by a laser-driven light source (step 10 nm) at room temperature.

For the studied samples, we found only very weak variation of EQY with excitation wavelengths (i.e., the KV rule is well fulfilled). In Fig. 2, we report an example of the EQY excitation spectrum (other samples give very similar results). Over the green-blue-violet spectral region, the EQY values are very uniform around 12%. The commonly observed decrease toward lower photon energies (below 2.4 eV) can be due to absorption into defect states. When approaching the band gap, the intrinsic absorption of SiNCs rapidly drops,[11] and the defect absorption becomes important. The presence of an exponential absorption tail in similar H-passivated samples was proved recently by photothermal deflection spectroscopy (PDS) and associated with non-paramagnetic structural defects like Si-O-Si bridging bonds or distorted Si-Si bonds at the SiNC interface.[16] This defect-related absorption resembles exponential tail states in amorphous Si below the mobility edge.[17]

The increase of EQY at high photon energies above 3.5 eV is within the experimental error. In this ultraviolet spectral region, the sensitivity of the CCD detector drops very fast, which makes the overall sensitivity calibration extremely difficult (also the shift between excitation and emission wavelengths becomes very large—about 500 nm, 2 eV—which compromises the precision of sensitivity ratio in these two regions).[10] Otherwise, such an increase of EQY may be related to carrier multiplication (CM)—i.e., generation of two electron-hole pairs after absorption of a single photon.[18] However, we cannot prove the CM effect even for the samples without an oxide barrier, like S3–5 presented in Fig. 2.

B. H-passivation effects

The improvement of EQY by H-annealing may be related to the passivation of P_b-type defects, dangling bonds, on the Si/SiO_2 interface. In Fig. 3, we plot the EQY ratio of H-passivated and non-passivated samples (logarithmic scale) versus the mean nanocrystal surface area in the respective sample. The experimental points follow a linear dependence.

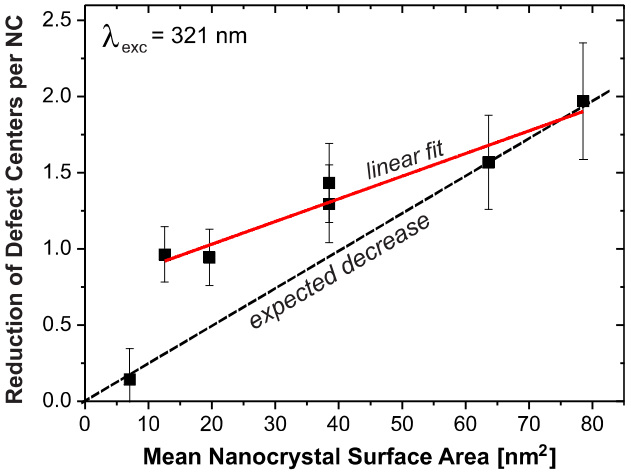

FIG. 3. The logarithm of EQY increase upon H-passivation scales linearly with the nanocrystal-surface area. This fact indicates that H-annealing reduces the surface non-radiative centers, namely the dangling bonds.

In order to describe changes in the number of defects, we recall the following simple model.

As a discrete quantity, the number of NCs having just k defects is given by the Poissonian distribution

$$P(k) = \frac{e^{-\lambda} \cdot \lambda^k}{k!}, \tag{1}$$

where λ is the mean number of defects per NC. Then, the change in the number of defect-free NCs by H-annealing is equal to

$$\frac{P_H(0)}{P(0)} = \frac{e^{-n_{dH}}}{e^{-n_d}} = e^{\Delta n} = \frac{I_{PLH}}{I_{PL}} = \frac{\eta_{EH}}{\eta_E}, \tag{2}$$

where Δn is the average change in the number of defects in a NC and η_E is the PL EQY. (Note that this model neglects possible NC-NC coupling effects and considers only those PL-quenching defects that are healed by hydrogen). The plot of Δn as a function of surface area (Fig. 3) is well linear, but it is not going right to zero. This can indicate that the scaling of defects with size is not straightforward as supposed. For example, more defects can be formed in smaller NCs with a sharper curvature of the surface. In addition, because of the effect of NC-size distribution,[14] the values of surface area for different samples are in fact considerably blurred.

Nevertheless, the slope of the linear plot of data in Fig. 3 (red line) indicates a density of defects of about $2.5 \times 10^{12}\,\mathrm{cm}^{-2}$, which corresponds well with the value previously derived from EPR studies.[19] In agreement with the recent study of defects in similar samples,[16] we can state that proper H-annealing effectively removes most of the P_b-type defects known as efficient non-radiative centers on the Si/SiO_2 interface.[20]

C. The role of barrier thickness in superlattice samples

The third series of samples (M3-1 to M3-4) enables us to investigate the dependence of EQY on the SiO_2 barrier thickness. The results of that study were published recently,[21] therefore, we shall comment on them here only briefly. The EQY increases with barrier thickness (from 1.0 to 2.8 nm) following an exponential dependence with the characteristic distance of 0.4 nm (the barrier thickness for which EQY drops to 1/e of the maximal value). One of the single-layer samples, S3-4, shows the same PL peak position as sample M3-1 (which has narrow barriers of 1 nm), and both these samples reveal the same EQY. Therefore, we can state: The transition from a thick monolayer to the well separated (>2 nm) stack of narrow monolayers increases the EQY by a factor of two (see Fig. 4).

The decrease of EQY with decreasing barrier thickness is accompanied by a small red-shift, which can indicate either the growth of bigger NCs or the increased energy transfer from smaller to bigger NCs. Indeed, the presence of barriers reduces the total Si excess concentration as a function of the oxide barrier thickness.

Previous studies revealed that the interface between the SiNC crystalline core and the SiO_2 matrix has a form of an amorphous shell (with a thickness of 1–2 atomic layers[22]) which contains various structural defects that can trap excitons and/or facilitate transport between neighbor nanocrystals or towards more distant defects in the silica matrix. Decreasing the distance between SiNCs below ~2 nm brings the amorphous shells almost in contact, which increases the number of available traps and the probability of non-radiative losses.

D. Overview of room-temperature EQY of all samples

In order to get a general view on the EQY of all the studied samples, we plot in Fig. 4 the EQY (at room-temperature under excitation by the 405-nm-LED) as a function of PL peak wavelength [i.e., directly proportional to the SiO_x thickness, see Fig. 1(b)]. The observed EQY maximum is around 27%. For the thick monolayer samples, there is a limit of about 12%.

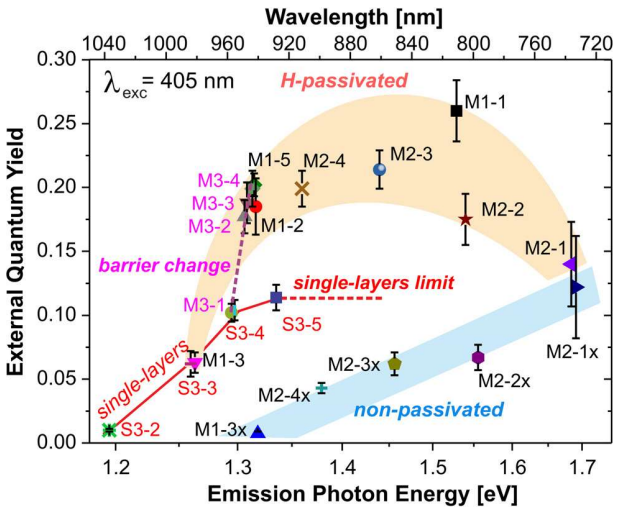

FIG. 4. Overview of EQY values (405 nm excitation) plotted versus PL-peak photon energy. The maximum EQY for superlattice samples is about 27%, while for thick single-layers, it is only ~12%. The samples M3-1 to M3-4 show the increase of EQY with the thickness of barrier layers.

Hence, from this overview, we can extract the main parameters leading to the highest EQY:

(1) The optimum size of NCs is about 3.5–4 nm (which gives a PL peak around 810–850 nm),
(2) the oxide barrier thickness must be at least 2 nm,
(3) the stoichiometry of the deposited SRON layer must be around x ≈ 1, and
(4) the best possible defect passivation by H_2 post-annealing has crucial importance.

At this point, it is useful to compare our findings with the published reports on the EQY of SiNCs. There are quite many such reports. There is no evident system in the reported values of EQY, because QY is sensitive to many parameters like surface passivation, strain in the matrix (thermal treatment), passivation of defects, etc. Interestingly, those reports that present spectral dependence of EQY reveal a peak for some "optimal" SiNC size (e.g., Refs. 23–28) The highest EQY value for oxide embedded SiNCs of ~35% was reported by Limpens *et al.*,[29] while the colloidal samples of organically passivated SiNCs often reach 60% or even more (see e.g., Refs. 30 and 33)

E. Luminescence decay kinetics and IQY

As we mentioned in the Introduction, the IQY η_I is related to the emission decay kinetics and defined as the ratio of the radiative k_r to the total k_{PL} decay rates k_r/k_{PL}, where $k_{PL} = k_r + k_{nr}$. A more precise definition[31] specifies that the rates are related to a vacuum. In a real environment, the radiative rate is modified by the Purcell factor F_p, defined as the ratio of radiative time in a vacuum and in the environment τ_r^{vac}/τ_r^{e}. The Purcell factor can be calculated using the dielectric constant of the medium and the local field factor, which is often a quite complex task.[32] Assuming that the Purcell factors for radiative and total decay times are equal, the IQY relation is simplified as follows:

$$\eta_I(E) = \frac{k_r^{vac}(E)}{k_{PL}^{vac}(E)} = \frac{\tau_{PL}^{vac}(E)}{\tau_r^{vac}(E)} = \frac{F_P \tau_{PL}^{e}(E)}{F_P^{*} \tau_r^{e}(E)} \sim \frac{\tau_{PL}^{e}(E)}{\tau_r^{e}(E)}, \qquad (3)$$

where the index e indicates the lifetime in some environment and E is the emission photon energy ($E = h\nu$) introduced explicitly to stress the spectral dependence of all quantities.

We present the results of spectrally resolved PL decay measurements in Fig. 5 for the sample M3–1 at T = 77 and 294 K. The average decay time τ_{av} is obtained from the double- or three-exponential decay fits.[33]

The main features of the spectral distribution of average decay times are common to all SL and TSL samples studied here. Namely (for the case of room temperature), τ_{av} increases exponentially when going from the high-energy edge to lower energies. This increase becomes gradually attenuated from about 1.5 eV, and τ_{av} reaches maximum around 1.2 eV. Then, τ_{av} decreases toward the bulk Si band-gap (1.12 eV) and approximately reaches a constant value below this gap. This intriguing below-bulk band-gap emission will be discussed later.

In order to get information on IQY, one has to separate radiative and non-radiative contributions to the PL decay and apply Eq. (3). This can be achieved using special samples, where the radiative rate is varied by changing the local density of optical states via the variable distance from a reflecting surface, and assuming that the non-radiative rate is unaffected. To our knowledge, such experiments were reported only by two groups. While the experiments by Walters *et al.*[31] on implanted SiNCs show a QY of up to 60% almost independent of the wavelength, Miura *et al.*[34] reported different IQYs for different sputtered samples reaching up to 100% for well-isolated big NCs emitting at wavelengths above 850 nm. Here, we estimate the IQY via a comparison of decay kinetics of our samples with dodecyl-passivated SiNC suspension in toluene, which reveal an IQY close to unity (see our recent paper for details[33]). This comparison is based on the assumption that the spectral dispersion of radiative decay in SiNCs is "universal," which means that all kinds of SiNCs have the same spectrally selected radiative rate (at least for the standard slow emission in the red/infrared spectral region).

We also have to consider different environments of SiNCs in a SL sample and in toluene suspension. Using the high frequency dielectric constants 12, 2.1, and 2.38 for Si, SiO_2,[32] and toluene,[35] respectively, we obtain the ratio $F_P^{ML}/F_P^{T} \cong 0.78$. However, the effective medium in a SL sample has higher dielectric constant due to the close proximity of SiNCs. Estimating the volume filling factor of Si (using morphology data obtained by Gutsch *et al.*[14]) to be 0.1 and using the approach of Poddubny,[32] we found that the

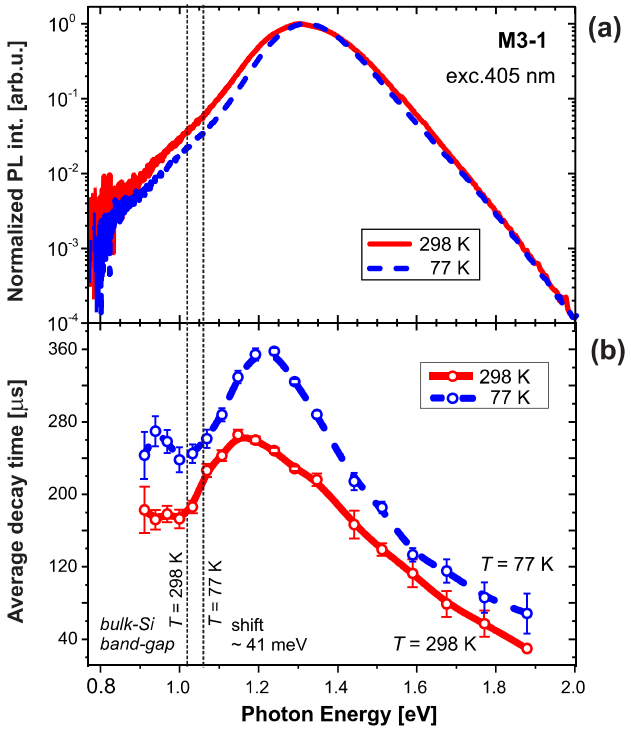

FIG. 5. (a) Normalized PL spectra of sample M3-1 at 77 (blue dashed line) and 294 K (red line) measured over very broad spectral range. (b) Spectrally resolved average decay times at 77 and 294 K. The bulk Si band-gap for these two temperatures is indicated by dashed lines.

dielectric constant increases to about 2.4—it means that both media are effectively the same and have approximately equal values of the Purcell factor.

The PL spectra and the average decay times of M3–1 and the dodecyl-SiNC samples are compared in Fig. 6. The green line in Fig. 6(b) is the theoretical calculation by the envelope function approximation (see Refs. 33 and 36) which approximates well the average decay time of colloidal SiNCs down to about 1.5 eV. By dividing τ_{av} of the SL sample with τ_{av} of the colloidal sample (representing τ_r) and approximating the ratio of Purcell factors to be 1, we get an estimate of the IQY shown in Fig. 6(c). The IQY has values between 40% and 60% with a peak and agrees surprisingly well with the results of Walters *et al.*[31] (gray squares). The apparent peak of IQY around 1.6 eV roughly corresponds to the EQY maximum (see Fig. 4).

F. Estimated temperature dependence of IQY

The temperature variation of IQY can be determined indirectly by measuring the temperature evolution of PL intensity $I_{PL}(T)$ and absorption cross-section $\sigma(T)$ of a sample placed in a cryostat and excited by a modulated 405-nm laser. The absorption cross-section is calculated from the intensity dependence of the PL onset and decay rates.[11] The relative temperature changes of $\eta_I\ (T)$ are derived from the relation for PL intensity

$$I_{PL}(T) = N_b(T)\cdot I_{ex}\cdot\sigma(T)\cdot\eta_I(T)\ \rightarrow\ \eta_I(T) = const\frac{I_{PL}(T)}{N_b(T)\cdot\sigma(T)}, \tag{4}$$

where I_{ex} is the excitation photon flux, which is kept constant, and N_b is the density of luminescing (bright) SiNCs that may change with temperature (e.g., due to the PL intermittency with longer off states[37]). Unfortunately, to our best knowledge, there is no method to determine T-dependence of N_b in SiNC-ensembles like here. Therefore, we shall suppose that this number is constant and then, we can use Eq. (4) for the estimation of temperature changes of QY. In our recent paper,[21] we demonstrated that the ratio $I_{PL}(T)/\sigma(T)$ increases approximately twofold when decreasing the temperature from RT to ~120 K. Then, we converted this relative change to absolute EQY using the room temperature value determined with the integrating sphere setup (implicitly assuming N_b to be T-independent).[21] As the relation between EQY and IQY is simply

$$\eta_E(T) = \frac{N_b}{N_{tot}}\eta_I(T), \tag{5}$$

where N_{tot} is the total number of all absorbing NCs (i.e., the sum of bright and dark ones), which is independent of T. Therefore, if we still suppose N_b as T-independent, relative changes of both EQY and IQY with T are the same. In the case of IQY, we above estimated the room temperature value to be around 50% [Fig. 6(c)]. Then, doubling with a decrease of T brings the IQY value to 100%. However, this value is a very rough estimate as both IQY at RT and all absorption

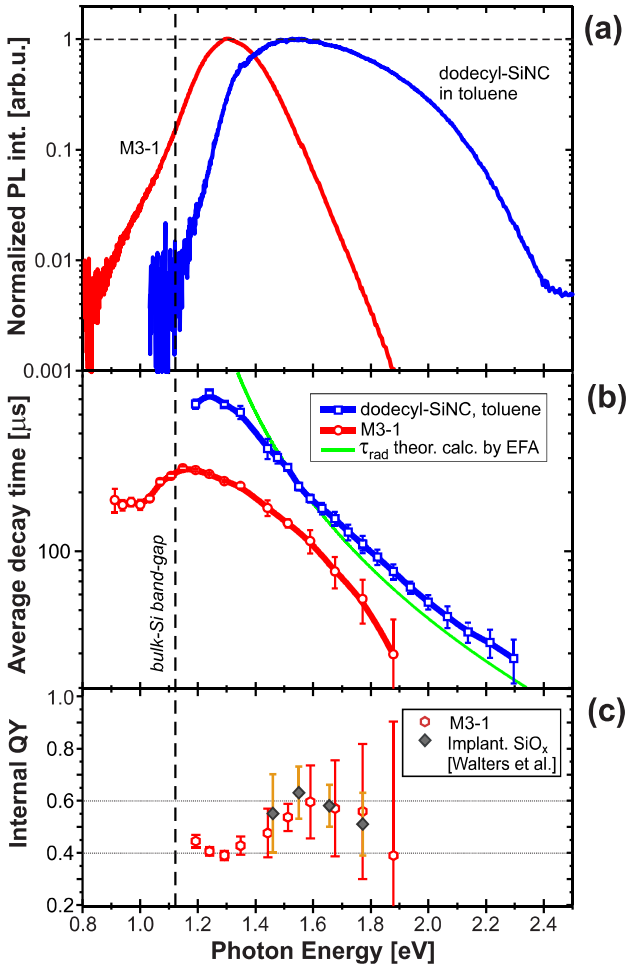

FIG. 6. (a) Normalized room-temperature PL spectra of sample M3-1(red line) and the dodecyl-passivated SiNC suspension in toluene (blue line). (b) Spectrally selected average decay times for the two samples compared with theoretical calculation of the radiative lifetime by the envelop function approximation (EFA) (green line). (c) Estimation of IQY for sample M3-1 obtained as the ratio of red to blue data from panel (b). Data from the work by Walters *et al.*[31] are given by gray rectangles.

cross-section values are subject to large experimental uncertainty, which is typically 20% or even more.[38] Moreover, the assumption of T-independence of N_b may not be valid due to e.g., PL intermittency (blinking) effects, which is usually showing prolonged off-periods at lower T.[39] In order to prove 100% IQY at low-T, the methods of direct measurement of IQY in special samples[31] must be extended by implementation of a cryostat.

G. Extended infrared emission (EIE) tail

Now, we would like to turn our attention to the low-energy side of PL spectra [see Figs. 5(a) and 6(a)], where a long exponential tail is revealed. We propose that this extended infrared emission (EIE) is due to the radiative recombination in defect-related trap states in the interface between SiNCs and the surrounding oxide matrix. Excited carriers (excitons) in a NC-core can escape to this interface by either tunneling or thermally activated transport. Then, trapped in defect states, they recombine mostly non-

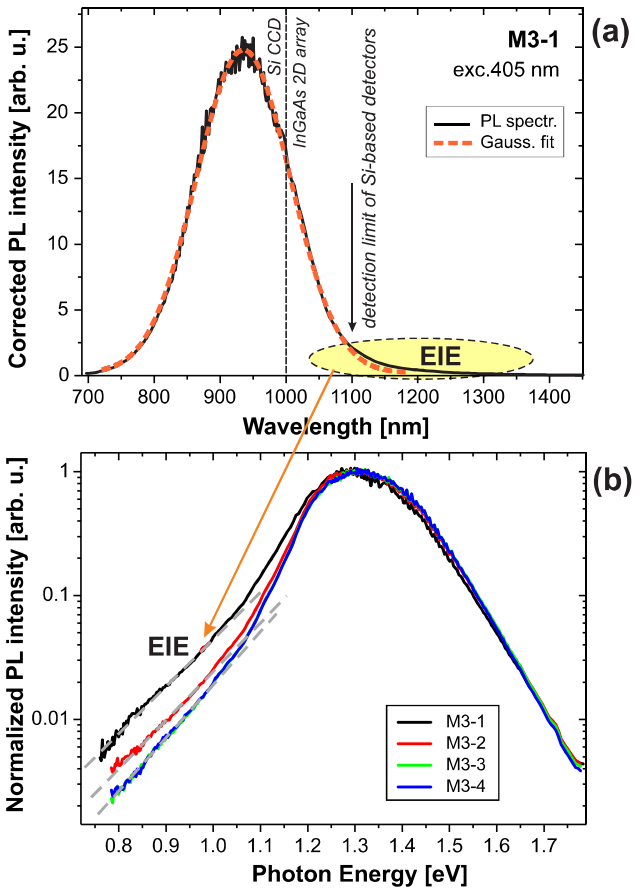

FIG. 7. (a) VIS/NIR combined spectra of sample M3-1. The red-line is a Gaussian fit revealing small (but clear) deviation of PL from the Gaussian shape above 1100 nm, which is the extended IR tail (EIE). (b) The transformed spectrum from the upper panel and several other samples from the same series normalized to the peak value. The EIE side of the band has an exponential shape (gray dashed lines), i.e., giving straight lines in the semi-logarithmic plot.

radiatively, but some of them may have a certain probability of radiative recombination.

The EIE spectral feature can be revealed, thanks to our unique visible (VIS)/near-infrared (NIR) micro-spectroscopy setup with two parallel detection branches covering a very broad spectral range from 350 to 1640 nm. The carefully corrected PL spectra clearly show EIE on the long-wavelength side of the PL band (Fig. 7), which extends far below the band gap of bulk Si of ~1.12 eV (1130 nm) at RT, so it cannot be due to the broad distribution of Si-NC sizes. Note that a correct transformation of such broad spectra (measured with a constant bandwidth in the wavelength using a grating spectrometer) must be done (see Ref. 40) by multiplying the PL spectra measured (and corrected) in the wavelength scale by λ^2/hc, which relatively increases the low-energy side of the spectrum and the inverse x-scale shrinks the extension of the NIR region. Emission intensity within the EIE tail is usually very low, on the level of 1% of peak intensity or weaker. This may be one of the reasons why the EIE emission escaped from the attention of researchers. Another reason is its spectral position in the region, where sensitivity of the commonly used detectors (Si-based CCDs or photomultipliers with the S-1 photocathode) fades out. The EIE can

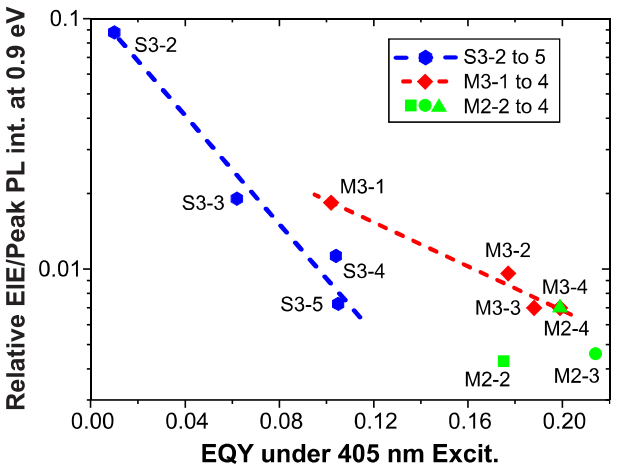

FIG. 8. Relative intensity of PL at 0.9 eV (relative to the PL peak) vs. EQY. There is a rough anti-correlation between EQY and the EIE intensity.

eventually be considered as a background signal and subtracted from PL spectra. In Fig. 7(a), the Gaussian fit (orange dashed line) demonstrates that the peak is an almost perfect Gaussian band (when plotted vs. wavelengths) with only a small discrepancy above 1100 nm—EIE. Similar PL with slow kinetics was observed in hydrogenated amorphous Si (a-Si:H), and attributed to the band tail-to-tail recombination of electrons and holes.[41]

In order to characterize the quantity of the EIE signal, we shall define an appropriate parameter. As a fast and simple characterization, we used the relative value of PL at 0.9 eV (relative to the peak PL intensity) or at an energy of 0.4 eV below the PL peak position (this can compensate the influence of the PL peak shift between different samples).

The plot of EIE characteristics vs. EQY (Fig. 8) reveals a general trend of decreasing EIE with increasing EQY. This anti-correlation of EIE and EQY, however, is not perfectly valid between different series of samples, but holds well within one type of sample (dashed lines in Fig. 8). The increase of EIE in samples with a narrower barrier thickness or non-passivated samples is probably due to energy transfer to the defect states facilitated by defects or decreased barriers.

Finally, we measured the extended spectra of sample M2–4 under increasing excitation pumping (Fig. 9). There is a clear increase of EIE for powers above the PL-saturation threshold, which is relatively small compared to the deviation of PL from the linear dependence. Such a power dependence suggests that the Auger recombination can eject carriers into the interface states. This is also in agreement with the proposed models for PL intermittency (blinking) in single SiNCs.[37]

IV. DISCUSSION

Based on the presented results and the relevant literature, we can summarize the mechanisms reducing the EQY of SiNCs in oxynitride films:

(a) *Strong excitation effects*: The decrease of EQY under strong pumping (above ~1 W/cm^2) is caused by

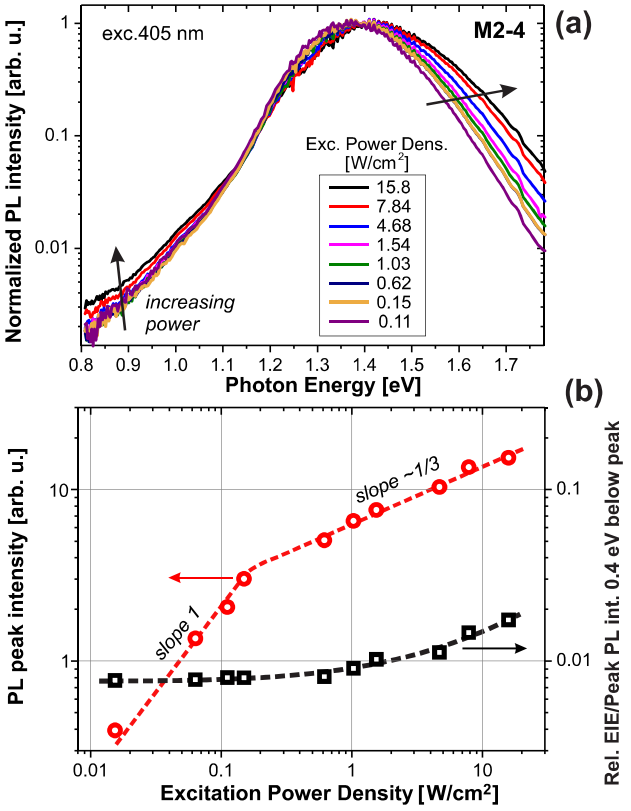

FIG. 9. (a) Normalized PL spectra of sample M2-4 under increasing pumping power (405 nm). In spite of the blue-shift of the PL peak above saturation, the increase of EIE is evident. (b) Excitation power dependence of the PL peak intensity (red dots) and the EIE (black dots; relative PL at an energy of 0.4 eV below the peak). The EIE increases for power exceeding the saturation level.

Auger-like non-radiative transitions—relaxation of two electron-hole pairs (excitons) in one NC proceeds by non-radiative recombination of one pair, which transfers its energy to the remaining pair. In the present study, we avoided such effects by low pumping power ($\ll$1 W/cm^2), except for the experiment shown in Fig. 9.

(b) *Defective (dark) nanocrystals*: The main part of efficiency losses is caused by the presence of dark SiNCs which absorb, but not emit photons due to efficient recombination via a defect center. The number of dark NCs can be efficiently decreased by a proper passivation procedure. We show that H-annealing decreases the number of defects proportionally to the NC-surface area (Fig. 3). A recent work on similar samples has shown that this procedure efficiently removes dangling bonds (P_b-type centers), but other structural defects like distorted Si-Si bonds or Si-O-Si bridging bonds are still present at the SiNC/SiO_2 interface.[16] Also, the presence of nitrogen in the matrix can cause both the healing of defects and the creation of new types of defects.[42] EPR studies have shown that the dominant N-related EPR-active defect is the K^0 center ($\equiv Si^{\cdot}$), which is, however, effectively inactivated by the H-annealing. There may be other EPR-inactive centers, for example, N-interstitial whose energy was calculated to range from mid-gap to the conduction band of Si depending on the local oxidation status.[43] The best of presented samples contains about 50% of dark NCs after annealing. We should note that the population of dark NCs may be "dynamic," i.e. some NCs may switch between dark and bright periods (the so-called intermittency or blinking), mostly due to the charging of NCs by the trapping of charge carriers at the NC interface.[37] The energy transfer to defect centers is revealed by the weak extended infrared emission, whose relative intensity anticorrelates with EQY values.

(c) *Absorption by defects*: The decrease of EQY for excitation at longer wavelengths, closer to the band gap (Fig. 2), is probably due to the direct absorption by defect states. They induce an exponential tail in absorption spectra[16] competing with absorption by NCs that rapidly drops towards the band gap. This defect absorption can also reabsorb PL as their spectral ranges partially overlap.

(d) *Thermal effects*: An indirect estimation of temperature-induced changes in the QY (using the ratio of PL intensity and absorption cross-section) shows the QY peak for T between 100 and 120 K. Increasing T to room temperature causes a decrease to about half value and also decreasing to lower T causes a smaller QY decrease.[21] These changes can be either due to changing population of bright NCs N_b or changes in IQY. Supposing that N_b is T-independent, the decrease of IQY (as well as EQY) toward RT can be explained by thermally activated transfer of excitons from the SiNC-core to the interface trap centers. The decrease of IQY at very low T could also be related to the freezing out of phonons, which are required for the indirect-like transition recombination. For the best of presented samples, the thermal effect is responsible for about 25% of QY losses at RT.

The observed limit of EQY ~27% can probably be improved further by reducing the number of defects inducing the existence of dark NCs as well as thermally activated decrease of IQY. For example, we can avoid the presence of nitrogen in the matrix by adopting strictly N-free technology.[44] Also, the optimization of annealing procedures may reduce the strain and structural defects on the nanocrystal interface that cannot be inactivated by the H-annealing. We are now working on the optimization of the promising N-free technology.[44] But, already the present SiNC SL samples can find applications as, for example, NIR fluorescence standards. Organic dyes emitting in the region around 800–900 nm have QYs of only a couple of percent and poor photostability, i.e., orders of magnitude worse than our SL samples. We have already presented one example of such application for quantitative microscopy calibration in our recent paper.[45]

V. CONCLUSIONS

We performed a comprehensive study of PL quantum yield with a large number of nanocrystalline Si/SiO_2 superlattices. The optimum configuration of the SiNC/SiO_2 SL for achievement of the highest external QY of ~27% is the following: (i) Thickness of the SiO_x layers around 3.5–4 nm

and a stoichiometry value around 1 (PL peak ~800–850 nm), (ii) SiO_2 barrier of 2 nm or thicker, and (iii) careful H_2-passivation. The SL structure doubles EQY compared to the equivalent thick-layer sample without oxide barriers, therefore, we could suppose that better isolation of SiNCs within SiO_x layers should also increase the PL QY further.

As the main EQY-limiting factor, we propose a non-radiative recombination in the defect-centers at the interface between SiNCs and the oxide matrix. Photoexcited carriers may escape from a NC core into defect traps via thermally activated transfer or tunneling. There is a certain probability of radiative recombination of excitons in trap centers that is revealed as the exponential NIR tail in PL spectra (extending far below the band gap of bulk Si). The intensity of extended infrared emission anti-correlates with the value of EQY.

Internal QY at room temperature is estimated via analysis of PL decay kinetics to be around 50%, while the external QY of the best sample is about 27%. We assume that this roughly two-fold reduction of EQY compared to IQY is caused by the presence of dark SiNCs, which form about half of the whole ensemble. The QY limit can be probably further increased by adapting the nitrogen-free fabrication technology, thus avoiding N-related defect centers.

ACKNOWLEDGMENTS

This work was supported by the bilateral Czech-German DFG-GACR Project No. 16-09745J and ZA 191/36-1.

[1]K.-Y. Cheng, R. Anthony, U. R. Kortshagen, and R. J. Holmes, Nano Lett. **11**, 1952 (2011).
[2]F. Maier-Flaig, J. Rinck, M. Stephan, T. Bocksrocker, M. Bruns, C. Kübel, A. K. Powell, G. A. Ozin, and U. Lemmer, Nano Lett. **13**, 475 (2013).
[3]W. Mu, P. Zhang, J. Xu, S. Sun, J. Xu, W. Li, and K. Chen, IEEE J. Sel. Top. Quantum Electron. **20**, 8200106 (2014).
[4]F. Meinardi, S. Ehrenberg, L. Dhamo, F. Carulli, M. Mauri, F. Bruni, R. Simonuti, U. Kortshagen, and S. Brovelli, Nat. Photonics **11**, 177 (2017).
[5]X. Pi, L. Zhang, and D. Yang, J. Phys. Chem. C **116**, 21240 (2012).
[6]*Nanotechnology and Photovoltaic Devices: Light Energy Harvesting with Group IV Nanostructures*, edited by J. Valenta and S. Mirabella (Pan Stanford Publishing, Singapore, 2015).
[7]K. Dohnalová, T. Gregorkiewicz, and K. Kůsová, J. Phys.: Condens. Matter **26**, 173201 (2014).
[8]M. D. Mason, G. M. Credo, K. D. Weston, and S. K. Burrato, Phys. Rev. Lett. **80**, 5405 (1998).
[9]R. Limpens and T. Gregorkiewicz, J. Appl. Phys. **114**, 074304 (2013).
[10]J. Valenta, Nanosci. Methods **3**, 11 (2014).
[11]J. Valenta, M. Greben, Z. Remes, S. Gutsch, D. Hiller, and M. Zacharias, Appl. Phys. Lett. **108**, 023102 (2016).
[12]A. M. Hartel, D. Hiller, S. Gutsch, P. Löper, S. Estradé, F. Peiró, B. Garrido, and M. Zacharias, Thin Solid Films **520**, 121 (2011).
[13]A. Hartel, S. Gutsch, D. Hiller, and M. Zacharias, Phys. Rev. B **85**, 165306 (2012).
[14]S. Gutsch, D. Hiller, J. Laube, M. Zacharias, and C. Kübel, Beilstein J. Nanotechnol. **6**, 964 (2015).
[15]J. R. Lakowicz, *Principles of Fluorescence Spectroscopy*, 3rd ed. (Springer Science + Business Media LLC, 2006).
[16]B. G. Lee, D. Hiller, J.-W. Luo, O. E. Semonin, M. C. Beard, M. Zacharias, and P. Stradins, Adv. Funct. Mater. **22**, 3223 (2012).
[17]R. A. Street, *Hydrogenated Amorphous Silicon* (Cambridge University Press, Cambridge, 1991).
[18]D. Timmerman, J. Valenta, K. Dohnalova, W. D. A. M. de Boer, and T. Gregorkiewicz, Nat. Nanotechnol. **6**, 710 (2011).
[19]M. Jivanescu, D. Hiller, M. Zacharieas, and A. Stesmans, Eur. Phys. Lett. **96**, 27003 (2011).
[20]C. Delerue, G. Allan, and M. Lannoo, Phys. Rev. B **48**, 11024 (1993).
[21]J. Valenta, M. Greben, S. Gutsch, D. Hiller, and M. Zacharias, Appl. Phys. Lett. **105**, 243107 (2014).
[22]S. Hernández, J. López-Vidrier, L. López-Conesa, D. Hiller, S. Gutsch, J. Ibáñez, S. Estradé, F. Peiró, M. Zacharias, and B. Garrido, J. Appl. Phys. **115**, 203504 (2014).
[23]G. Ledoux, J. Gong, F. Huisken, O. Guillois, and C. Reynaud, Appl. Phys. Lett. **80**, 4834 (2002).
[24]A. Sa'ar, J. Nanophotonics **3**, 032501 (2009).
[25]J. B. Miller, A. R. Van Sickle, R. J. Anthony, D. M. Kroll, U. R. Kortshagen, and E. K. Hobbie, ACS Nano **6**, 7389 (2012).
[26]D. Jurbergs, E. Rogojina, L. Malgolini, and U. Kortshagen, Appl. Phys. Lett. **88**, 233116 (2006).
[27]M. L. Mastronardi, F. Maier-Flaig, D. Faulkner, E. J. Henderson, C. Kübel, U. Lemmer, and G. A. Ozin, Nano Lett. **12**, 337 (2012).
[28]X. Liu, Y. Zhang, T. Yu, X. Quiao, R. Gresback, X. Pi, and D. Yang, Part. Part. Syst. Charact. **33**, 44 (2016).
[29]R. Limpens, S. L. Luxembourg, A. W. Weeber, and T. Gregorkiewicz, Sci. Rep. **6**, 19566 (2016).
[30]F. Sangghaleh, I. Sychugov, Z. Yang, J. G. C. Veinot, and J. Linnros, ACS Nano **9**, 7097 (2015).
[31]R. J. Walters, J. Kalkman, A. Polman, H. A. Atwater, and M. J. A. de Dood, Phys. Rev. B **73**, 132302 (2006).
[32]A. Poddubny, J. Opt. **17**, 035102 (2015).
[33]M. Greben, P. Khoroshyy, X. Liu, X. Pi, and J. Valenta, J. Appl. Phys. **122**, 034304 (2017).
[34]S. Miura, T. Nakamura, M. Fujii, M. Inui, and S. Hayashi, Phys. Rev. B **73**, 245333 (2006).
[35]S. O. Morgan and W. A. Yager, Ind. Eng. Chem. **32**, 1519 (1940).
[36]V. A. Belyakov, V. A. Burdov, R. Lockwood, and A. Meldrum, Adv. Opt. Technol. **2008**, 1.
[37]I. Sychugov, J. Valenta, and J. Linnros, Nanotechnology **28**, 072002 (2017).
[38]M. Greben, P. Khoroshyy, S. Gutsch, D. Hiller, M. Zacharias, and J. Valenta, "Absorption cross-section changes with temperature and distance of Si nanocrystals," Beilstein J. Nanotechnol. (to be published).
[39]U. Banin, M. Bruchez, A. P. Alivisatos, T. ha, S. Weiss, and D. S. Chemla, J. Chem. Phys. **110**, 1195 (1999).
[40]I. Pelant and J. Valenta, *Luminescence Spectroscopy of Semiconductors* (Oxford University Press, Oxford, 2012), pp. 58–63.
[41]S. Q. Gu, P. C. Taylor, and J. Ristein, J. Non-Cryst. Solids **137–138**, 591 (1991).
[42]D. Hiller, S. Goetze, F. Munnik, M. Jivanescu, J. M. Gerlach, J. Vogt, E. Pippel, N. Zakharov, A. Stesmans, and M. Zacharias, Phys. Rev. B **82**, 195401 (2010).
[43]E.-C. Lee, Phys. Rev. B **77**, 104108 (2008).
[44]J. Laube, S. Gutsch, D. Hiller, M. Bruns, C. Kübel, C. Weiss, and M. Zacharias, J. Appl. Phys. **116**, 223501 (2014).
[45]J. Valenta and M. Greben, AIP Adv. **5**, 047131 (2015).

Paper VII

APPLIED PHYSICS LETTERS **108**, 023102 (2016)

Determination of absorption cross-section of Si nanocrystals by two independent methods based on either absorption or luminescence

J. Valenta,[1,a)] M. Greben,[1] Z. Remeš,[2] S. Gutsch,[3] D. Hiller,[3] and M. Zacharias[3]
[1]*Department of Chemical Physics and Optics, Faculty of Mathematics and Physics, Charles University, Ke Karlovu 3, 121 16 Prague 2, Czechia*
[2]*Institute of Physics, Academy of Sciences of the Czech Republic, Cukrovarnická 10, Prague 6, Czechia*
[3]*Faculty of Engineering, IMTEK, Albert-Ludwigs-University Freiburg, Georges-Köhler-Allee 103, 79110 Freiburg, Germany*

(Received 25 September 2015; accepted 28 December 2015; published online 11 January 2016)

Absorption cross-section (ACS) of silicon nanocrystals (SiNCs) is determined via two completely independent approaches: (i) Excitation-intensity-dependent photoluminescence (PL) kinetics under modulated (long square pulses) pumping and (ii) absorbance measured by the photothermal deflection spectroscopy combined with morphology information obtained by the high-resolution transmission electron microscopy. This unique comparison reveals consistent ACS values around 10^{-15} cm^2 for violet excitation of SiNCs of about 3–5 nm in diameter and this value is comparable to most of direct band-gap semiconductor nanocrystals; however, it decreases steeply towards longer wavelengths. Moreover, we analyze the PL-modulation technique in detail and propose an improved experimental procedure which enables simpler implementation of this method to determine ACS of various (nano)materials in both solid and liquid states. © *2016 AIP Publishing LLC*.
[http://dx.doi.org/10.1063/1.4939699]

Optical properties of nanostructured materials can significantly differ from the respective bulk materials. Numerous reports showed optical changes like the blue shift of the absorption edge due to the band gap opening and improvement of luminescence efficiency with decreasing size of nanostructures.[1] In case of optically excited nanomaterials (useable as detectors, absorbers in solar cells,[2] or as luminescent labels[3]), a crucial optical property is the ability to efficiently absorb light—most often described by the absorption cross-section (ACS) σ of a nanoobject (nanocrystal (NC), nanowire, etc.). Typical values of σ for direct band gap semiconductor NCs are between[4] 10^{-14} and 10^{-16} cm^2. Very interesting effects can take place for indirect band gap semiconductors, where an increase of absorption probability is expected as a result of strong spatial localization of electron and hole wavefunctions leading to their delocalization in k-space and possible quasi-direct transitions. In spite of this well known prediction, systematical investigation of ACS in the most important semiconductor, i.e., Si, was not reported yet; one of the reasons could be experimental difficulties. In this letter, we describe a modified photoluminescence (PL) modulation technique for the determination of ACS in SiNCs. Direct comparison of ACS values from PL with completely independent absorption method enables to demonstrate advantages and disadvantages of both techniques. Knowledge of effective ACS in ensembles of NCs is crucial for design of nanostructured absorbers for solar cells, detectors, and other applications.

The investigated samples were deposited by the plasma-enhanced chemical vapor deposition (PE-CVD) as alternating layers of silicon-rich silicon oxynitride (SRON) SiO_xN_y and stoichiometric silicon dioxide SiO_2 (2 or 2.2 nm thick) on fused silica substrates. On top and below the 40-bilayer stack, 10-nm layers of SiO_2 were deposited as the buffer and capping layers, respectively. The samples were consequently annealed in a quartz tube furnace at 1150 °C for 1 h in high purity N_2 in order to form SiNCs and then passivated by annealing in H_2 at 500 °C. The main parameters of the investigated samples are given in Table I. Further details of the sample preparation are given in our recent paper.[5] The shape and size distribution of Si NCs were studied by preparing special monolayer (ML)-SRON samples directly on transmission electron microscopy (TEM) grids that were consequently studied by the high-resolution energy-filtered TEM (EF-TEM).[6] For samples W3 to W6, we found[6] the Si NCs areal density between 3.8 and 2.4×10^{-12} cm^{-2} (see Table I), but the narrower SRON layers give no clear EF-TEM images of SiNCs most probably due to imperfect phase separation or low EF-TEM contrast. Therefore, the density of NCs for samples W1 and W2 was estimated by extrapolation.

Absorbance of the studied samples was obtained by the *photothermal deflection spectroscopy* (PDS)[7] which detects heating waves produced by dissipation of modulated incident light. It is able to detect absorbance down to 10^{-5}. PL experiments were performed under excitation by a 405-nm diode laser whose beam was modulated using a quartz acousto-optic cell. The resulting square-shaped pulses have the duty cycle of 40%, the repetition rate of 900 Hz, and the edge switching time of about 100 ns. The laser is coupled to a home made micro-spectroscopy set-up with an inverted microscope in the epifluorescence configuration. There are two detection branches for visible (VIS) and near-infrared (NIR) spectral regions, each one composed of an imaging spectrometer (Acton SpectraPro SP-2358i and SP-2558i, respectively) and a photomultiplier (PMT) for time-resolved

[a)]Author to whom correspondence should be addressed. Electronic mail: jan.valenta@mff.cuni.cz.

TABLE I. Description of the sample parameters.

Label	SiO_xN_y thick. (nm)	SiO_2 thick. (nm)	Stoichiometry x-value	Single layer NC areal density (10^{12} cm^{-2})	PL QY (exc. 405 nm)
W1	1.5	2.0	1.0	Estim. 5 ± 0.5	0.14 ± 0.03
W2	2.5	2.0	1.0	Estim. 4.4 ± 0.4	0.18 ± 0.02
W3	3.5	2.0	1.0	3.8 ± 0.3	0.21 ± 0.02
W4	4.5	2.0	1.0	3.4 ± 0.3	0.20 ± 0.02
W5	4.5	1.6	0.93	2.43 ± 0.05	0.18 ± 0.01
W6	4.5	2.2	0.93	2.43 ± 0.05	0.19 ± 0.02

PL detection (Hamamatsu H11526-20-NF and H10330A-45, respectively, for VIS and NIR). Pulses from PMTs are detected by two multichannel counting cards (Becker-Hickl, MSA-300). The significant advantage of the imaging micro-PL set-up for the PL-modulation ACS method is the good control of the excitation spot size and the signal collection area which enable quite precise determination of excitation photon flux. More details on the set-up can be found in our recent paper.[8]

The first approach to determine ACS is based on measuring the pumping intensity dependence of the time-resolved PL response to the square-modulated excitation. The PL from an ensemble of NCs can be well described by a set of three differential equations, when only three possible states of a NC are considered: ground state, single and double excited state (i.e., one or two electron-hole pairs (excitons) in a NC) with the corresponding occupations N_0, N_1, and N_2

$$\frac{dN_0}{dt} = -N_0 I_{ex}\sigma + \frac{N_1}{\tau_{PL}}, \tag{1}$$

$$\frac{dN_1}{dt} = N_0 I_{ex}\sigma - N_1 I_{ex}\sigma - \frac{N_1}{\tau_{PL}} + \frac{N_2}{\tau_A}, \tag{2}$$

$$\frac{dN_2}{dt} = N_1 I_{ex}\sigma - \frac{N_2}{\tau_A}. \tag{3}$$

Here, I_{ex} is excitation intensity expressed in photon flux (photons per second per cm^2), and τ_{PL} and τ_A are luminescence and Auger lifetime, respectively. The total number of luminescing NCs is $N_T = N_0 + N_1 + N_2$. Any higher excited state is not considered supposing that the Auger quenching of doubly excited population is very fast and efficient (τ_A is reported to be in the ns-range or shorter[9]). A similar description presented by Kovalev *et al.*[10] considered erroneously the radiative lifetime τ_r instead of the correct τ_{PL} which contains both radiative and non-radiative lifetimes ($1/\tau_{PL} = 1/\tau_r + 1/\tau_{nr}$). The use of the same σ for absorption from both the ground state and the single-excited state may be substantiated by the high density of states in SiNCs.[11]

The steady state (i.e., all $dN/dt = 0$) PL intensity at moderate excitation ($N_T \approx N_0$) should, obviously, be a linear function of excitation power. From Eq. (2), we obtain $N_1 = N_T I_{ex}\sigma\tau_{PL}$ and then PL intensity reads as

$$I_{PL} = \frac{N_1}{\tau_r} = N_T I_{ex}\sigma\,\frac{\tau_{PL}}{\tau_r} = N_T I_{ex}\sigma\eta, \tag{4}$$

where $\eta = \tau_{PL}/\tau_r$ is the PL quantum yield (QY).[12] So, the slope of the $I_{PL}(I_{ex})$ linear dependence is $N_T\sigma\eta$ and σ can be determined if the PL QY and density of NCs are known. However, one has also to know the scale of the intensity axis, i.e., the absolute spectral calibration—relation between the detected signal (e.g., in counts per second) and the number of emitted photons. Such an absolute calibration of a spectrometer set-up is complicated, therefore some authors exploited PL intensity saturation instead.[10] Under strong excitation, the assumption that $N_T \approx N_0$ is no more valid. Considering fast Auger quenching, N_2 is negligible and the PL power saturation curve is described by

$$I_{PL} = \frac{N_1}{\tau_r} = \frac{N_T I_{ex}\sigma\eta}{1 + I_{ex}\sigma\tau_{PL}}. \tag{5}$$

The deviation from linear dependence is described by the denominator, namely, the factor $\sigma\tau_{PL}$. When the PL decay time τ_{PL} is determined from a separate experiment, σ can be obtained by fitting of the PL power saturation. In Fig. 2(a), we present an example of the saturation fit, which works well for the beginning of saturation but deviates significantly for stronger pumping. The non-complete saturation of PL of SiNCs under cw excitation seems to be a general effect that we studied in detail and will be published separately. Anyway, PL saturation in our multilayer samples cannot be satisfactorily fitted by Eq. (5) and attempts to do so (see Fig. 2(a)) give quite low values of σ (similar as obtained by Garcia *et al.*[13] using the same method). Therefore, we turned to the PL modulation technique.

The PL onset after switching on a constant excitation is described by Eq. (2), which has the following solution:

$$I_{PL}(t) = \frac{N_1(t)}{\tau_r} = N_T I_{ex}\sigma\eta\left\{1 - \exp\left[-t\left(\frac{1}{\tau_{PL}} + I_{ex}\sigma\right)\right]\right\} = I_{PL}^{cw}\left(1 - e^{-t/\tau_{ON}}\right). \tag{6}$$

This means that the PL intensity exponentially approaches the equilibrium value with characteristic time τ_{ON} which is a function of excitation photon flow

$$\frac{1}{\tau_{ON}} = \frac{1}{\tau_{PL}} + I_{ex}\sigma. \tag{7}$$

Consequently, the ACS can be directly obtained as the slope of pumping power dependence of the ON-OFF differential rate ($1/\tau_{ON} - 1/\tau_{PL}$) which should be a linear function of excitation power. Such approach was exploited in various studies, but its application limits were not described yet. Most importantly, Eq. (7) is valid only within the limited range of excitation power close to the PL saturation; for low I_{ex}, the values of τ_{ON} and τ_{PL} must be equal and for high pumping

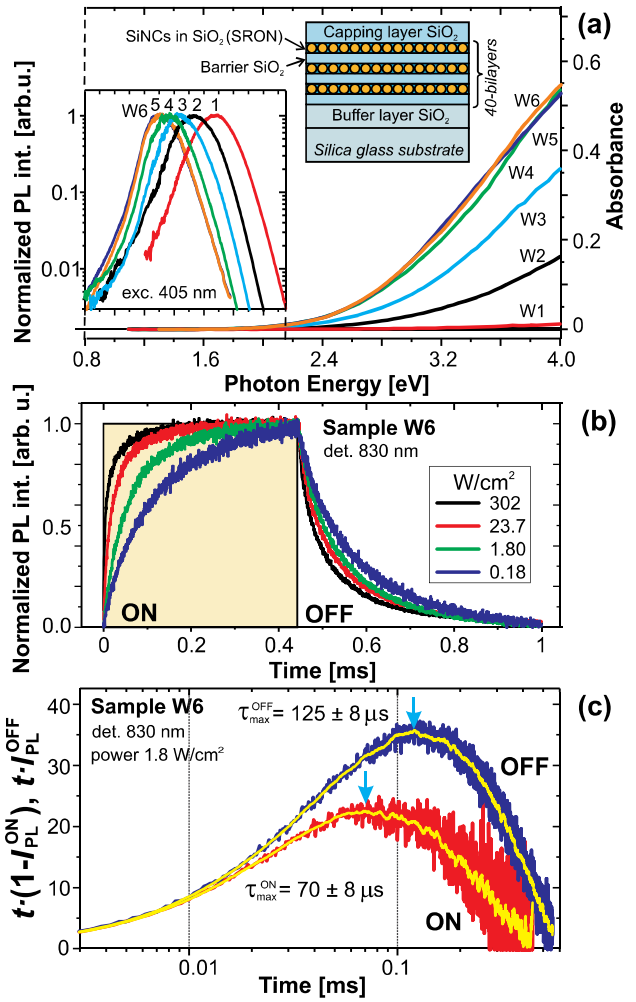

FIG. 1. (a) Absorbance (right) and PL (left) spectra of the investigated samples. The inset illustrates the multilayer sample structure. (b) Time-resolved PL signal excited by the square pulses with power density ranging from 0.18 to 302 W/cm^2. (c) Normalized PL onset and decay signals multiplied by time which represents density of decay rates (yellow lines are smoothed curves obtained by the adjacent-point averaging). The peak positions reveal the dominant time constants.

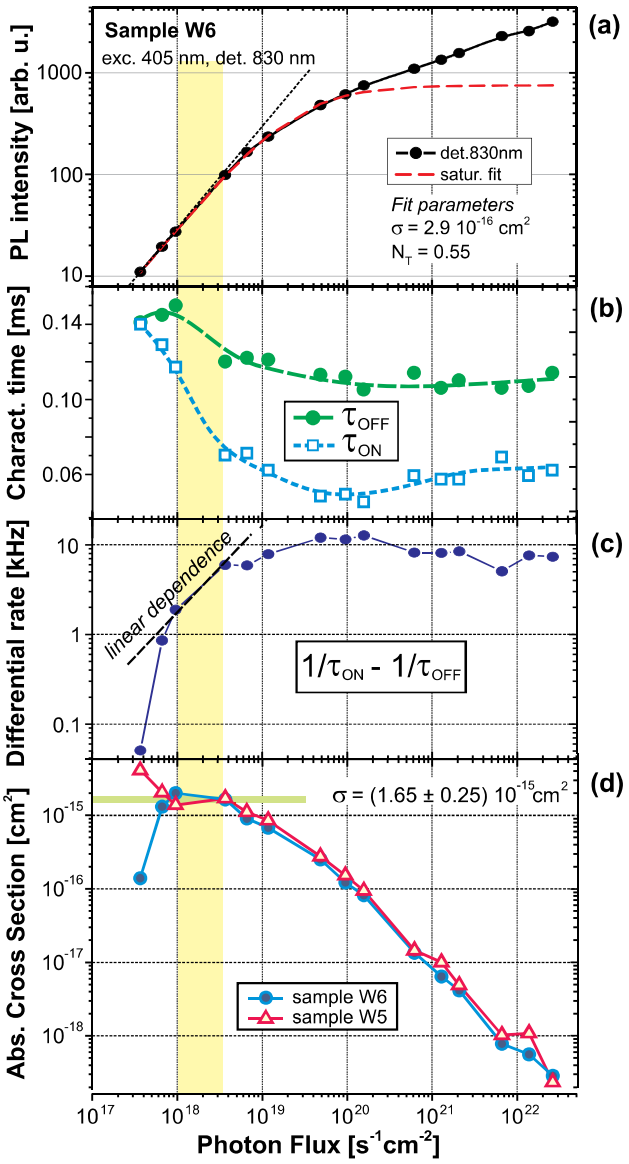

FIG. 2. (a) PL intensity under cw excitation as function of excitation photon flux. The dashed line is the fit using the PL saturation model described by Eq. (5), which deviates significantly from experimental points for strong excitation and gives too low ACS value (about 6 times). (b) The extracted ON and OFF characteristic times and (c) the resulting differential rates. (d) Final ACS obtained from PL-modulation in the samples W5 and W6.

Eq. (6) is no more valid as η becomes power dependent and the population N_2 is non-negligible.

Time-resolved PL traces were measured for various wavelengths (with step of 40 nm) and excitation power varied by five orders of magnitude around the PL saturation level (which is usually ~1 W/cm^2). Fig. 1(b) presents several PL time-traces for the sample W6 detected at 830 nm and normalized to the same peak intensity. For each trace, the peak and background PL signal is retrieved; the trace is normalized and then the major task is to find the representative characteristic times for the PL onset and decay. The problem, however, is that none part of the PL time evolution can be described by a single exponential function. It is well known that the PL decay in SiNCs is most often following the stretch exponential function[14] $I_{PL} = I_0 \exp[-(t/\tau)^{\beta}]$, but sometimes a more complicated function is needed. We tested several approaches for finding the dominant characteristic time and finally adopted the approach described by Higashi and Kastner[15] and recently applied to SiNCs by Hartel *et al.*[16] The method is based on the fact that the function $t \cdot I_{PL}(t)$ (PL decay signal multiplied by the delay time) is revealing a distribution of delay times. Then, the peak of this function can be taken as the dominant decay time of the distribution. More precise treatment must be done using the Laplace transformation but the method of Higashi and Kastner is precise enough and its big advantage is an easy algorithmization. In this paper, we determine τ of both onset and decay as maxima of the smoothed normalized functions $t \cdot (1 - I_{PL}{}^{ON})$ and $t \cdot I_{PL}{}^{OFF}$, see Fig. 1(c) for an example.

The power dependence of PL amplitude and characteristic times τ_{ON}, τ_{OFF} for PL at 830 nm from sample W6 are plotted in Figs. 2(a) and 2(b), respectively. As expected, both times are roughly equal at low excitation and then τ_{ON} decreases faster than τ_{OFF} when approaching PL saturation. In consequence, the resulting differential rate $1/\tau_{ON} - 1/\tau_{OFF}$

(Fig. 2(c)) is noisy at low excitation, almost constant for strong excitation above the saturation level, while the intermediate region of linear power dependence is surprisingly narrow at the toe of PL deviation from a linear dependence. This is the region where the above described model is valid and the ACS can be determined (Fig. 2(d)).

The spectral dependence of ACS was investigated for samples W1 to W4 over a broad range of emission wavelengths. Fig. 3(a) shows that ACS is increasing with the emission wavelength approaching the bulk Si band gap. Similar ACS spectra were obtained by Kovalev *et al.*[10] for porous Si and by Priolo *et al.*[22] for CVD grown SiNCs in oxide. By definition, ACS is related only to the absorption wavelength and should not depend on emission wavelength. The apparent emission-wavelength dependence is an effect of inhomogeneous broadening caused by significant size distribution of SiNCs within each sample. If we consider that ACS is a product of density of states and the transition oscillator strength only, where the former is increasing and the latter decreasing[17] with increasing NC size, then the effect of density of states seems to be stronger inducing ACS growth with SiNC size.[13] One can expect that for independent and well separated NCs, both ACS values and PL emission peak positions depend only on the NC size. But in various NC ensembles, the environment of NCs (matrix with other NCs) is changing which leads to modification of ACS. Indeed, we observe this effect (Fig. 3) especially for SiNC multilayers with SRON thickness below 3 nm (samples W1 and W2).

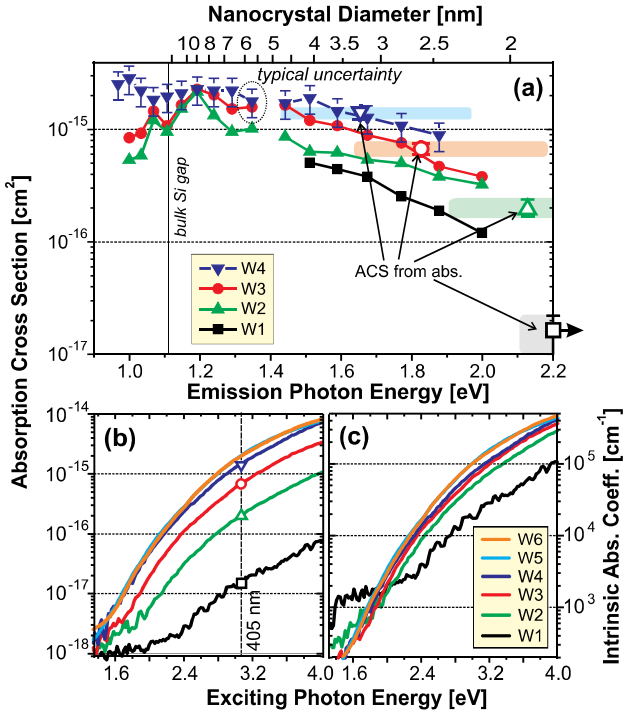

FIG. 3. (a) ACS determined via PL-modulation plotted as function of emission photon energy for samples W1 to W4. Estimated uncertainty (about 28%) is shown only for the sample W4). The upper scale is the NC diameter calculated according to Luo *et al.* Open symbols show ACS values obtained via absorption at 405 nm and plotted here at position of the mean NC size with indicated halfwidth of the size distribution (light rectangles). (b) ACS spectra calculated from absorbance and morphology data. (c) ACS spectra normalized to the mean NC volume.

Based on the presented analysis, we propose the following key points for implementation of the PL-modulation method to reveal ACS: (i) Determine the shape of PL power-saturation (for each studied wavelength) and find the appropriate power range for the time-resolved PL experiments; (ii) measure both onset and decay times of PL for excitation power varied within the defined range; (iii) calculate the differential rate and then ACS as a function of excitation power, and (iv) take the final ACS value from the region of constant power dependence or, if hardly observed, from the region around the PL-saturation onset.

Now we are going to compare the PL modulation results with the independent determination of ACS from absorbance A (logarithm of the ratio of incident to transmitted light power corrected for reflection and scattering losses, here we use the natural logarithm labeled A_e)[18] and the knowledge of NC density using this definition (applicable to optically thin samples)

$$A_e = \alpha\, d = \varepsilon\, c_M\, d = \sigma\, c_V\, d = \sigma\, c_A, \tag{8}$$

where α and ε are absorption and extinction coefficient, respectively. c_M, c_V, and c_A are the molar concentration, volume concentration, and area density, respectively, of absorbing NCs as seen by the incident wave.[19] The ACS spectra obtained from the absorbance and the morphology data (Table I) using Eq. (8) are plotted in Fig. 3(b). ACS values are monotonously increasing with absorbed photon energy and decreasing with the mean size of NCs. The latter effect can be due to decreasing volume of absorbing SiNCs; therefore, we present ACS divided by the NC volume (this quantity is called *intrinsic absorption coefficient* μ_i)[19] in Fig. 3(c). Indeed, for SiNCs with diameter bigger than about 3 nm, all μ_i spectra are almost equal. However, for smaller NCs, μ_i values are reduced in accord with the PL-based method (Fig. 3(a)).

In Fig. 3(a), we compare results of the PL-modulation technique with ACS values obtained by absorption at 405 nm (i.e., the excitation laser wavelength). The PL emission wavelength is converted into NC diameter using calculation by Luo, Stradins, and Zunger.[20] Then, absorption-derived ACS values are plotted (open symbols) at the position of the size-distribution peak and the color rectangles indicate the half-peak width of the distribution. For samples W3 and W4, the real size distributions (published in Ref. 6) are taken and perfect agreement of ACS from both methods is obtained, while for W1 and W2 we have to use estimated values and rough agreement of ACS values is observed.

This unique comparison of the two independent methods reveals the important role of a NC-size distribution. One significant advantage of the PL method is its size-selectivity achieved by limiting the detection range (we used a bandwidth of 5 nm, which correspond to 5–18 meV band in the investigated spectral range). On the other hand, the absorption technique is simpler and straightforward but probes the whole ensemble of size-distributed NCs and relies on the knowledge of a NC density and size-distribution.

In principle, the two methods may reveal different values of ACS as one approach is related to extinction and the other to PL-excitation. For example, a strong PL QY

size-dependence or efficient energy transfer (from small to big NCs) can cause deviation of ACS determined by the two methods. Indeed, in our SRON ML samples, we observe a peak of PL QY for Si NCs with diameter of about 4 nm and considerable decrease toward smaller or bigger NCs (similar to the report by Ledoux *et al.*[21]) which may cause slightly higher ACS values derived from PL in samples W1 and W2. Possible exciton migration effects[22] may be neglected here as our previous studies[23] show that at low electric field the migration is limited to the trapping of carriers in neighboring defects. Such loss of excitons in the non-radiative centers is intrinsically included in the differential equations (Eqs. (1)–(3)) as the non-radiative term of the effective lifetime τ_{PL}.

In conclusions, we have studied and analyzed the method of ACS measurement via the power-dependent PL-kinetics in SiNCs. The limits of its application and the key points for its implementation are defined. The direct comparison of ACS values obtained by the PL technique and the independent absorption method give consistent results around 10^{-15} cm^2 for SiNCs with mean diameters between 3 and 5 nm. For smaller NCs, the ACS value decreases but still giving roughly comparable values by the two methods. The described methods and derived conclusions have general validity for nanocrystalline ensembles independently of their material composition (group IV, II–VI, and III–V semiconductors).

This work was financially supported by the EU-project NASCEnT (FP7-245977). The Prague group acknowledges support within the framework of the Czech-Japan collaborative Project LH14246 (MSMT CR).

[1]D. V. Talapin, J. S. Lee, M. V. Kovalenko, and E. V. Shevchenko, Chem. Rev. **110**, 389 (2010).
[2]*Nanotechnology and Photovoltaic Devices*, edited by J. Valenta and S. Mirabella (Pan Stanford Publishing, Singapore, 2015).
[3]E. Petryayeva, W. R. Algar, and I. R. Medintz, Appl. Spectrosc. **67**, 215 (2013).
[4]P. Yu, M. C. Beard, R. J. Ellingson, S. Ferrere, C. Curtis, J. Drexler, F. Luiszer, and A. J. Nozik, J. Phys. Chem. B **109**, 7084 (2005).
[5]A. M. Hartel, D. Hiller, S. Gutsch, P. Löper, S. Estradé, F. Peiró, B. Garrido, and M. Zacharias, Thin Solid Films **520**, 121 (2011).
[6]S. Gutsch, D. Hiller, J. Laube, M. Zacharias, and C. Kübel, Beilstein J. Nanotechnol. **6**, 964 (2015).
[7]Z. Remeš, R. Vasudevan, K. Jarolimek, A. H. M. Smets, and M. Zeman, Solid State Phenom. **213**, 19 (2014).
[8]J. Valenta and M. Greben, AIP Adv. **5**, 047131 (2015).
[9]M. T. Trinh, R. Limpens, and T. Gregorkiewicz, J. Phys. Chem. C **117**, 5963 (2013).
[10]D. Kovalev, J. Diener, H. Heckler, G. Polisski, N. Künzner, and F. Koch, Phys. Rev. B **61**, 4485 (2000).
[11]P. Hapala, K. Kusova, I. Pelant, and I. Jelinek, Phys. Rev. B **87**, 195420 (2013).
[12]I. Pelant and J. Valenta, *Luminescence Spectroscopy of Semiconductors* (Oxford University Press, 2012).
[13]C. Garcia, B. Garrido, P. Pellegrino, R. Ferre, J. A. Moreno, J. R. Morante, L. Pavesi, and M. Cazzanelli, Appl. Phys. Lett. **82**, 1595 (2003).
[14]J. Linnros, N. Lalic, A. Galeckas, and V. Grivickas, J. Appl. Phys. **86**, 6128 (1999).
[15]G. S. Higashi and M. A. Kastner, Philos. Mag. B **47**, 83 (1983).
[16]A. M. Hartel, S. Gutsch, D. Hiller, and M. Zacharias, Phys. Rev. B **87**, 035428 (2013).
[17]C. Meier, A. Gondorf, S. Lüttjohann, A. Lorke, and H. Wiggers, J. Appl. Phys. **101**, 103112 (2007).
[18]See http://goldbook.iupac.org/A00028.html for IUPAC Gold Book.
[19]Z. Hens and I. Moreels, J. Mater. Chem. **22**, 10406 (2012).
[20]J.-W. Luo, P. Stradins, and A. Zunger, Energy Environ. Sci. **4**, 2546 (2011).
[21]G. Ledoux, J. Gong, F. Huisken, O. Guillois, and C. Reynaud, Appl. Phys. Lett. **80**, 4834 (2002).
[22]F. Priolo, G. Franzo, D. Pacifici, V. Vinciguerra, F. Iacona, and A. Irrera, J. Appl. Phys. **89**, 264 (2001).
[23]S. Gutsch, J. Laube, A. M. Hartel, D. Hiller, N. Zakharov, P. Werner, and M. Zacharias, J. Appl. Phys. **113**, 133703 (2013).

Paper VIII

AIP ADVANCES **5**, 047131 (2015)

Radiometric calibration of optical microscopy and microspectroscopy apparata over a broad spectral range using a special thin-film luminescence standard

J. Valenta[a] and M. Greben
Faculty of Mathematics and Physics, Department of Chemical Physics & Optics, Charles University, Ke Karlovu 3, 121 16 Prague 2, Czechia

(Received 31 December 2014; accepted 10 April 2015; published online 20 April 2015)

Application capabilities of optical microscopes and microspectroscopes can be considerably enhanced by a proper calibration of their spectral sensitivity. We propose and demonstrate a method of relative and absolute calibration of a microspectroscope over an extraordinary broad spectral range covered by two (parallel) detection branches in visible and near-infrared spectral regions. The key point of the absolute calibration of a relative spectral sensitivity is application of the standard sample formed by a thin layer of Si nanocrystals with stable and efficient photoluminescence. The spectral PL quantum yield and the PL spatial distribution of the standard sample must be characterized by separate experiments. The absolutely calibrated microspectroscope enables to characterize spectral photon emittance of a studied object or even its luminescence quantum yield (QY) if additional knowledge about spatial distribution of emission and about excitance is available. Capabilities of the calibrated microspectroscope are demonstrated by measuring external QY of electroluminescence from a standard poly-Si solar-cell and of photoluminescence of Er-doped Si nanocrystals. [http://dx.doi.org/10.1063/1.4918970]

I. INTRODUCTION

Appropriate correction for the spectral response of an experimental apparatus is necessary for any luminescence experiment involving a wide spectral range.[1] The main purpose of such calibration is a correction of spectral-shape distortions and it is most often a *relative calibration* done in "arbitrary units." The *absolute calibration* is only required for special radiometric setups and experiments.[2,3]

Recently, availability of highly-sensitive low-noise CCD cameras and well-corrected spectrographs enabled fast development of various imaging spectroscopes for remote spectroscopy, microspectroscopy etc. The full potential of such devices can be exploited only upon thorough geometrical (imaging) and radiometrical calibration.[4]

Here we describe a straightforward procedure of the absolute calibration of a microscope and/or a microspectroscope over a broad spectral range covering large part of visible (VIS) and near-infrared (NIR) regions. Such a broad range is covered by combining two parallel detection branches – each one consisting of a spectrograph and a 2D-detector array (camera). A key point of our method is exploitation of a luminescing standard sample formed by a thin layer of Si nanocrystals. Finally, two application examples are presented: Electroluminescence (EL) spectroscopy of a silicon solar cell and photoluminescence (PL) quantum yield (QY) measurement of Er-doped Si nanocrystals.

[a]Author to whom correspondence should be addressed. Electronic mail: jan.valenta@mff.cuni.cz

II. EXPERIMENTAL SET-UP

Micro-scopy and -spectroscopy experiments are performed using a specially designed setup (Fig. 1(a)) based on an inverted microscope (Olympus IX-71) with the NIR-optimized objective lens (LMPlan IR 50×/0.55, working distance of 6 mm, focal length f = 3.6 mm). A wide-field excitation is performed in the epifluorescence configuration by a 405-nm diode laser beam whose focal plane is shifted from the sample plane – the circular excited area has diameter of about 94 μm (using the above mentioned objective lens). Laser excitation power in the sample plane is measured by a power meter (Coherent Field Master GS).

Emitted signal is divided by a short-pass dichroic beam-splitter at 1000 nm (Fig. 1(b)). Light with shorter wavelengths (the limits of ~500 - 1000 nm are imposed by the applied dichroic filter) is coupled to a 30-cm imaging spectrograph[5] with a back-thinned LN-cooled CCD camera, while longer wavelengths (> 1000 nm) are detected by a 50-cm imaging spectrograph with an InGaAs camera (the pixel size of both cameras is 20 × 20 μm). In case when the parallel detection in the two spectral regions is not required, the VIS detection branch can be used without the short-pass 1 μm filter, which enlarges the detectable range of this branch to about 350-1100 nm. Magnification factor of both imaging spectrometers is close to 1, therefore the size of an input slit and its image on a camera are equal.

Both the VIS and NIR images (or spectra) of the same sample spot can be acquired simultaneously. Images are obtained using spectrograph gratings turned to zero-order or using a mirror

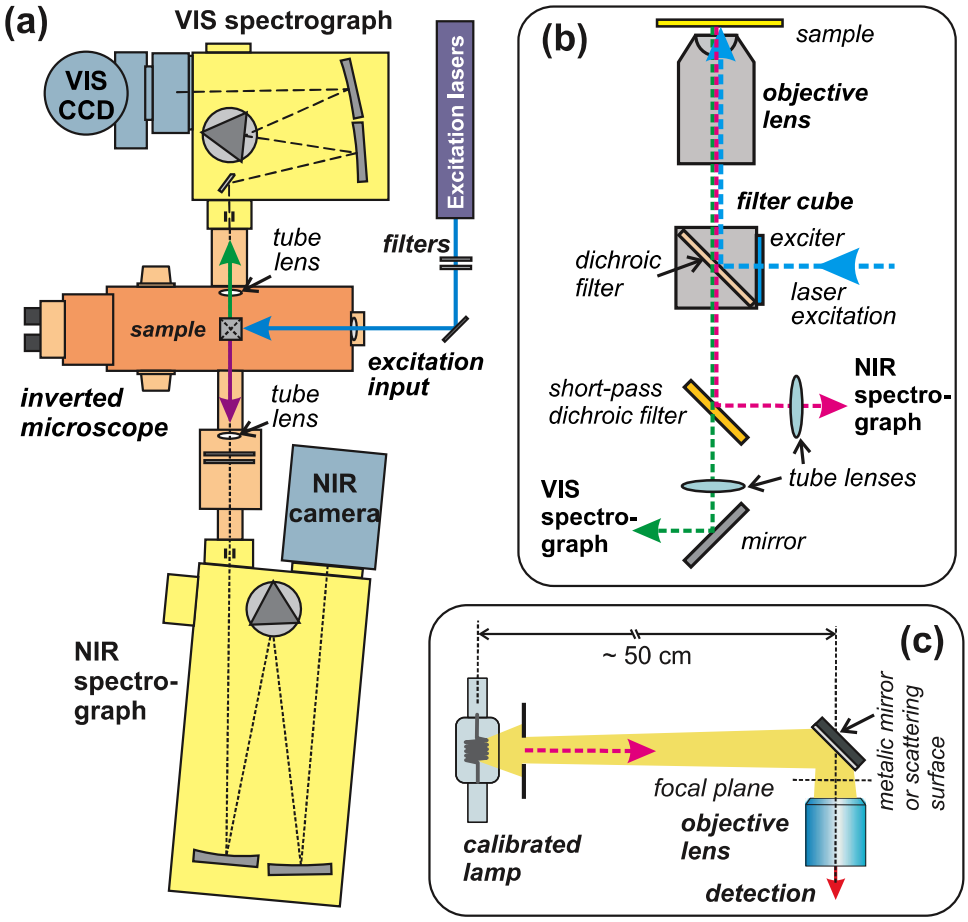

FIG. 1. (a) Top-view scheme of the microspectroscopy set-up based on an inverted optical microscope with two parallel detection branches – visible (VIS) and near-infrared (NIR). Each detection branch consists of an imaging spectrograph and a 2D-detector array (camera). (b) Optical paths in the central part of the microspectroscope (vertical cross-section). (c) Schematical configuration of the sensitivity calibration measurement using a radiance standard (calibrated lamp).

instead of a grating. Imaging magnification (linear) M is measured with a microscale slide giving values of 49× and 58× for VIS and NIR detector, respectively (this is due to different tube lenses with focal length of 18 and 20 cm, respectively). The area for spectral detection is selected by introducing a slit at the input image plane of a spectrometer and detected with a grating turned to a desired central wavelength position.[6] The spatial resolution of this wide-field apparatus is given by the diffraction limit to about $1.1 \times \lambda$, where λ is wavelength of light using for an imaging. The characterization of the apparatus spectral response is described in paragraph III.

Luminescence properties of a standard sample (see paragraph IV.) are characterized by separate devices. Absolute external quantum yield of photoluminescence is determined via a set-up based on an integrating sphere (IS) with diameter of 10 cm (SphereOptics GmbH). A sample is placed inside IS on one removable port in the position opposite to the excitation port where a light-emitting diode (LED) of desirable wavelength is mounted to provide PL excitation. Output signal is collected by a fused-silica fiber bundle whose output is coupled to an imaging spectrometer (Acton SpectraPro SP2150i) with a deep-depletion back-illuminated CCD camera (Spec-10:400B, Princeton Instruments) and a liquid-nitrogen-cooled CCD camera is used for detection. Spectral sensitivity of the complete apparatus is calibrated over a broad spectral range (300-1700 nm) using two radiation standards (Newport Oriel): a 45-W tungsten halogen lamp (above 400 nm) and a deuterium lamp (below 400 nm). The PL QY is calculated as the ratio of the number of emitted photons (the difference between the investigated and the reference sample (i.e. a bare substrate) signals in the region of photoluminescence) and the number of absorbed photons (integrated decrease of the excitation source signal in the sample compared to the reference). More details on the PL QY set-up and the theoretical basis are given in our recent paper.[7]

Spatial distribution of PL is determined via a goniometer set-up. A sample, excited by a diode laser (473 nm) in direction perpendicular to the plane of a luminescing layer, is placed in a center of a rotating stage on which a quartz fiber bundle is mounted and rotated around a sample. The collected PL signal (spatial resolution of about 1°) is detected by the same spectroscope as for PL QY measurements described above. In this way a horizontal cross-section of the spatial distribution of PL is obtained.[8]

III. CALIBRATION OF THE RELATIVE SPECTRAL RESPONSE USING A STANDARD TUNGSTEN LAMP

A calibrated tungsten halogen filament lamp with low power of 45 W (Oriel model No. 63358) is appropriate for microspectroscope calibrations. This lamp is placed at the distance of 50 cm from the objective lens (see Fig. 1(c)) and reflected by a reflectance standard (made from the Spectraflex® material by LabSphere) or a protected aluminium mirror (Thorlabs). The *calibrated spectral irradiance of the standard* ($\Xi_S(\lambda)$ in $W{\cdot}m^{-2}{\cdot}nm^{-1}$) is given for the distance of 50 cm but the reflection $R(\lambda)$ and coupling efficiency K modify the input flux actually entering the microscope (K represents a numerical constant - unknown for this moment - equal to the ratio between nominal irradiance and the irradiance actually entering the apparatus).

First, we perform a *relative sensitivity calibration* of the two spectroscope branches taking $(K{\cdot}\Xi_S{\cdot}R{\cdot}a)/(h\nu)$ [photon$\cdot s^{-1}\cdot nm^{-1}$] as an *input spectral photon irradiance* Φ_{in}, where a is the area from which signal is collected and $h\nu$ is photon energy. The spectral sensitivity of an apparatus $C(\lambda)$ (Eq. (1)) is determined as the ratio of the *spectral signal rate* ${S_\lambda}^A$ (the lower index λ discriminates spectral signal given in [counts$\cdot s^{-1}\cdot nm^{-1}$] from the signal rate S^A in [counts$\cdot s^{-1}$]) collected from the image area A and the *input spectral photon irradiance* from the sample area $a\,{\Phi_{in}}^a$. The sample area a and its image A are related by the imaging magnification M, $a = A/M^2$. We recommend expressing signal in "natural" area units of a 2D detector array (camera), it means *pixels*. Then *signal rate per pixel* S^P is given as $S^A{\cdot}/A^p$, where A^p is the area of a one pixel (here $20 \times 20\,\mu m^2$). For illustration we provide Fig. 2, where the (spectrally integrated) signal S^p is averaged over 3×2 pixels (white rectangles in Fig. 2). In the *spectral mode*, the signal is integrated in vertical direction (3 pixels) and must be divided by a spectral step Δ_λ in order to correctly represented ${S_\lambda}^p$ in units of [count$\cdot s^{-1}\cdot nm^{-1}$ per pixel]. The minimal spectral step Δ_λ is determined by the dispersion of

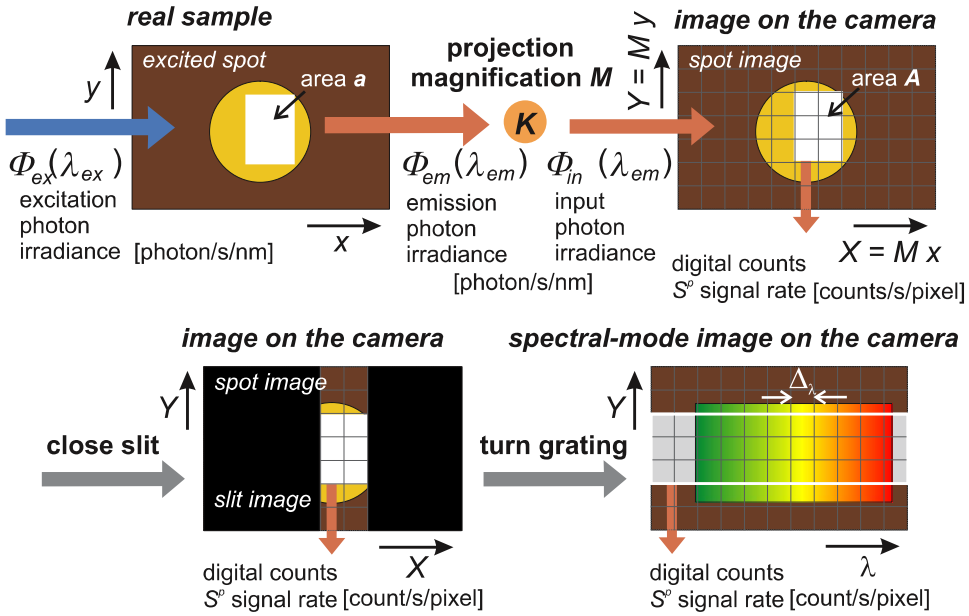

FIG. 2. Relations between the sample, its image and the spectral image and between the input photon irradiance and the detected signal rate.

a spectrometer grating per one detector pixel and the effective spectral step can be increased by binning (integrating) of several pixels along the wavelength axis.

Finally, we obtain the *spectral sensitivity* of the apparatus C_{VIS} and C_{NIR} as

$$C_{VIS/NIR}(\lambda) = \frac{S^A_\lambda\,[count/s/nm]}{\Phi^a_{in}\,[photon/s/nm]} = \frac{S^p(\lambda)\cdot A/(A^p\cdot\Delta_\lambda)}{K\cdot\Xi_S(\lambda)\cdot R(\lambda)\cdot a/h\nu} = \frac{h\nu\cdot S^p(\lambda)\cdot M^2}{K\cdot\Xi_S(\lambda)\cdot R(\lambda)\cdot A^p\cdot\Delta_\lambda}\,[\text{count/photon}], \tag{1}$$

where all quantities are acquired by the calibration experiment, except the constant K. Therefore, we can only determine *relative* (not absolute) *spectral sensitivity* $C_{VIS}{}^{rel} = K\cdot C_{VIS}$ and $C_{NIR}{}^{rel} = K\cdot C_{NIR}$. Later we shall determine K and obtain an absolute sensitivity.

The presented calibration is done with the following parameters: Reflection on a protected aluminium mirror, integration time 0.5 s, slit-width 0.1 and 0.2 mm, number of averaged pixels 50 (H=5/V=10) and 1000 (H=10/V=100), respectively for VIS and NIR detection.[9] The obtained spectral sensitivity curves are shown in Fig. 3. The NIR sensitivity is quite flat while the VIS sensitivity increases toward short wavelengths where it is limited by the short-úass limit of the inverted dichroic beam-splitter.

IV. STANDARD SAMPLE AND ITS USE FOR ABSOLUTE CALIBRATION

Probably the most straightforward way to obtain an *absolute calibration* of the above derived *relative spectral sensitivity* is to measure an appropriate *standard sample* with well *characterized photoluminescence quantum yield* (PL QY) and its *spatial emission distribution*.

A potential standard sample has to fulfill several important requirements:

- Having the form of a thin layer (both physically and optically) in order to avoid problems with distribution of PL intensity in out-of-focus planes and reducing reabsorption and waveguiding effects.
- High PL QY value independent on excitation power (at least within certain range of excitation power).
- Broad PL spectrum located within a convenient wavelength range.

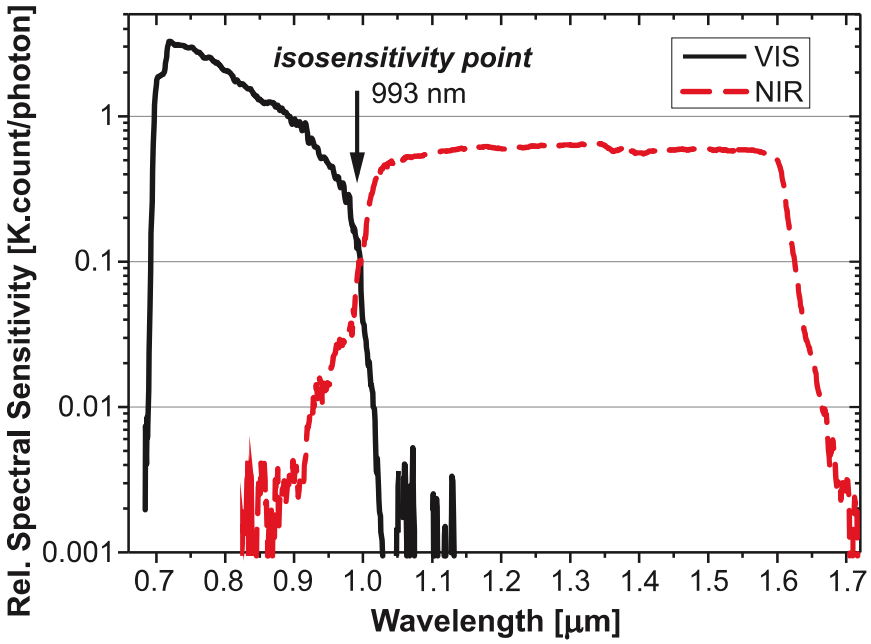

FIG. 3. Relative spectral sensitivity of the two parallel detection branches obtained using the 45 W tungsten lamp and reflection on an Al mirror.

- Spatial uniformity of PL properties (QY, excitation efficiency etc.).
- Perfect temporal- and photo-stability.
- Large Stokes shift between excitation and emission wavelength in order to reduce reabsorption.
- Excitation range matching some of the excitation bands available in the experimental apparatus.

We found that samples formed by a thin ***layer of Si nanocrystals*** (SiNCs) ***embedded in SiO_2*** fulfill most of the requirements for a standard sample. For this demonstration we have chosen a set of four samples formed by a luminescing layer deposited by the plasma-enhanced chemical-vapor deposition (PE-CVD) technique on a quartz substrate (25 × 25 mm) as a 200-nm thick monolayer of SiO_X (with the stoichiometry parameter x = 0.93, 1.05, 1.1, and 1.15) and subsequently annealed in N_2 at 1150 °C for 1 h and in H_2 at 500 °C for 1 h.[10] Normalized PL spectra of these samples are shown in Fig. 4(a) – the PL peak is conveniently placed between 930 and 1040 nm with FWHM of about 0.15 - 0.2 eV and the PL quantum yield is between 11 and 1 %. For the following tests we used sample Q3 (x = 1.05) with the PL peak around 1000 nm.

We have to note that thin luminescent layers have been already applied for microscopy calibration, e.g. Zwier et al.[11] described use of polymer layers with fluorescent dyes for luminescence microscopy image calibrations or recently Antonini et al.[12] described preparation of very thin fluorescent layers for characterization of axial resolution of sectioning microscopes.[13] However, there are probably no reports on the absolute microspectroscopy calibration using thin luminescing layers.

Characterization of the standard sample Q3 gives the following values of key parameters for excitation wavelength of 405 nm (3.0605 eV): Absorbance A = 0.334 and PL QY η = 7 %.[14] From the integral PL QY we can obtain spectral distribution of PL QY (Fig. 4(b)) via scaling of the measured PL spectrum. Such PL QY distribution represents probability that after absorption of one photon a PL photon is emitted at certain wavelength interval (1 nm wide). The integral of this spectrum must be equal to the measured total PL QY of 7 %.

For the absolute sensitivity calculation we must consider also the *angular distribution of PL emission* from the standard sample. It is expected that the emission pattern from a thin layer at an interface of two different media (here a silica glass and air) could deviate from the isotropic emission.[15] Therefore, the actual spatial distribution of PL must be characterized, for example by

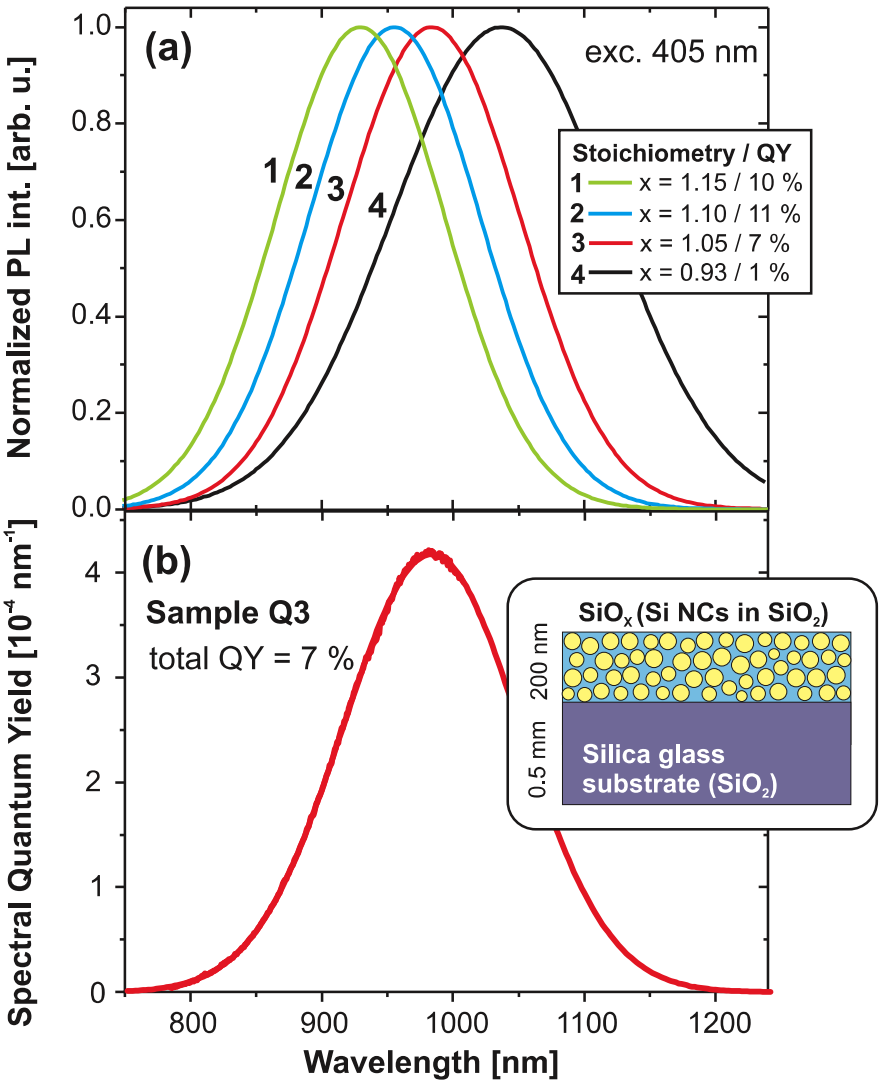

FIG. 4. (a) Normalized PL spectra of the SiNC samples. (b) The spectral quantum yield distribution for the sample Q3 determined in the integrating sphere set-up. The inset illustrates the standard sample structure.

measuring the angular distribution of PL with a goniometer set-up (see inset in Fig. 5). As the PL spectral shape is almost constant, we can plot either the integrated PL intensity or peak intensity (Fig. 5(a)) angle distribution (zero angle is the direction to the laser, the sample is perpendicular to this direction and the deposited SiO_X layer is facing the beam). It is clear (Fig. 5(a)), that more PL emission comes through the substrate (i.e. the medium with higher refraction index) as expected, but four local maxima observed at about 70°, 110°, 250°, and 290° are not well understood yet. The asymmetry of the left and right side of the PL angular distribution is probably due to imperfect symmetry of the goniometer set-up. The non-detectable part of the distribution (around 0° where the detecting fibre obscures the incoming laser beam) is replaced by the constant value of 0.5.

The collection efficiency for an objective lens with numerical aperture NA c_e is calculated as a spherical integral from 0° to arcsin(NA) divided by the total integrated emission. In Fig. 5(b) the experimental result is compared with the theoretical collection efficiency for an isotropic emitter. Due to a non-isotropic angular PL distribution of the standard sample, the objective lens with NA = 0.55 (applied in this work) has collection efficiency only c_e = 6 % (in contrast to 16.5 % for the Lambertian cosine emitter).

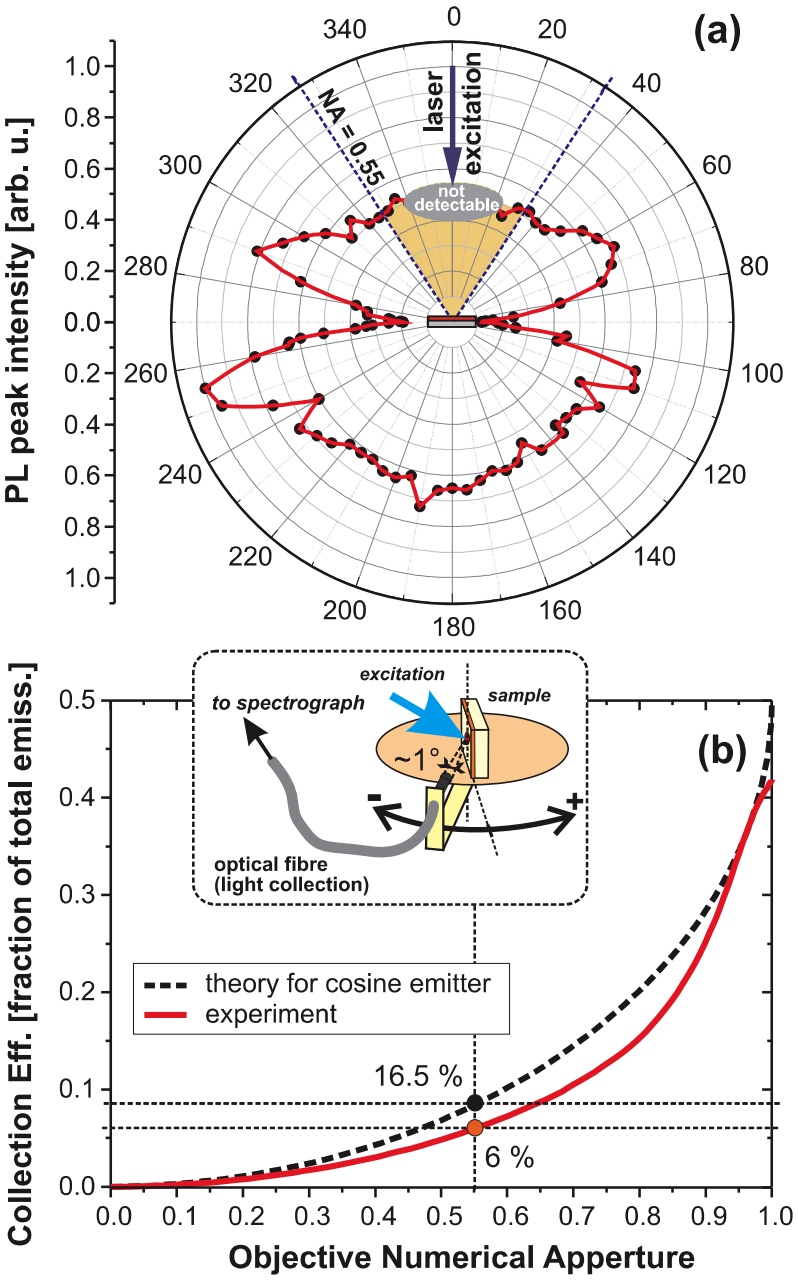

FIG. 5. (a) Angular distribution of PL peak emission from the sample Q3 excited perpendicularly by the 473-nm laser beam. SiNC layer is facing the beam. (b) Collection efficiency as function of numerical aperture. The dashed curve is a theoretical calculation for the cosine emitter and the solid curve is obtained by integrating the measured PL angular distribution (panel (a)).

The micro-PL spectra (VIS and NIR) of the standard sample were measured for different excitation intensities, in order to recognize a linear part of the PL excitation power dependence (Fig. 6(a)). PL saturation – deviation from the linear dependence of PL intensity on excitation power – starts already at power density of about 0.03 W·cm^{-2} (the typical value for SiNCs is 1 W·cm^{-2}).[16] Then, any point from the linear part of the PL power dependence (Fig. 6(a)) can be chosen. Let us take the point corresponding to the excitation power of 15.4 mW·cm^{-2}, i.e. 3.14 × 10^{8} photon·s^{-1}·μm^{-2} (incoming laser beam is attenuated by a filter with optical density OD = 3).

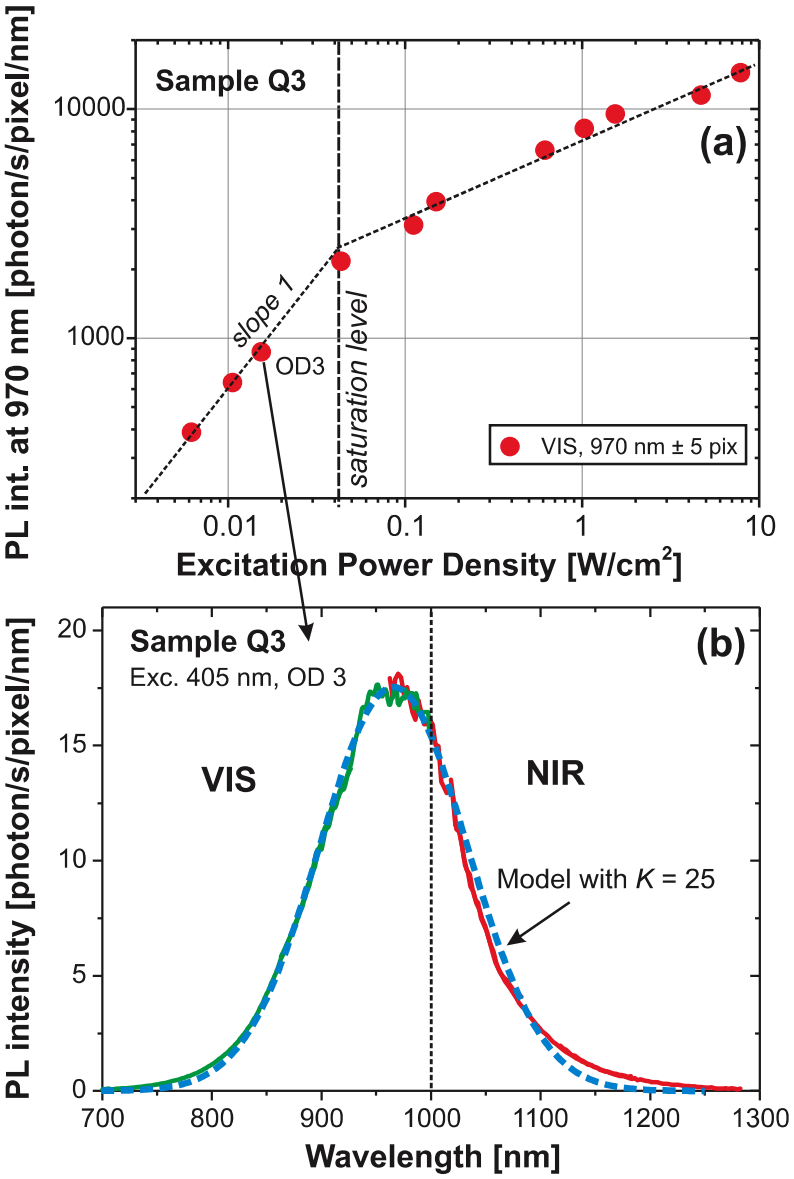

FIG. 6. (a) Excitation power dependence of PL signal from the standard sample at 970 nm. Only the excitation range below saturation, where PL is a linear function of excitation power density, is suitable for calibration purposes. (b) The spectral photon rate from the standard sample measured under 15 mW·cm^{-2} excitation (solid lines) compared with the spectrum (dashed line) calculated from the separately characterized properties of the standard sample. Close matching of the two spectra is possible by setting $K = 25$.

The absolute sensitivity calibration, i.e. determination of the constant K, is based on the following equation derived from Eq. (1)

$$C_{VIS/NIR} = \frac{C^{rel}_{VIS/NIR}}{K} = \frac{S^A_\lambda}{\Phi^a_{in}} = \frac{S^p/\Delta_\lambda}{I_{ex}\cdot\eta\cdot c_e\cdot A^p/M^2}, \tag{2}$$

where an *expected incoming photon irradiance* Φ_{in} from the standard sample is calculated from the excitation photon flux I_{ex} multiplied by absorbance A, PL QY η, coupling efficiency c_e, and the projected size of one pixel ($a = A^p/M^2 = 0.167$ μm^2). This gives the expected signal rate of 7.36×10^4 photon·s^{-1} per pixel. The value of K is then obtained by dividing this number by the measured PL signal with relative correction (i.e. divided by the relative spectral sensitivity).

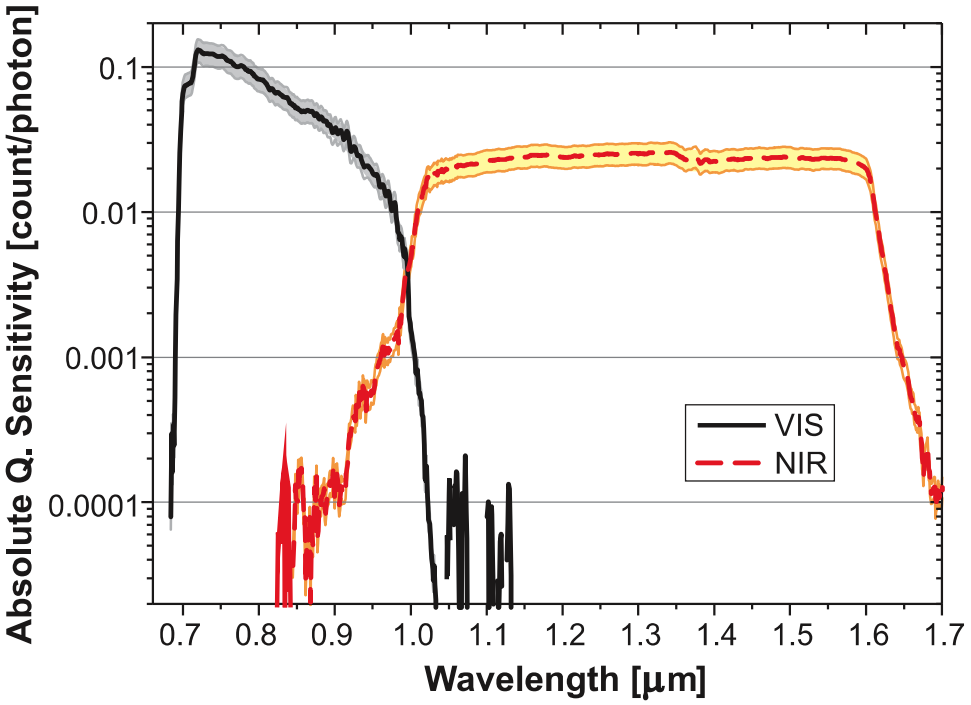

FIG. 7. Spectral sensitivity of the two spectroscope branches set to absolute scale by dividing data from Fig. 4 by K = 25. The shaded area corresponds to the estimated uncertainty of the absolute sensitivity.

This calculation is illustrated in Fig. 6(b), where the spectral distribution of the expected signal is calculated (dashed line) and fitted to the relatively-corrected experimental spectra (solid line) by adjusting the value of K to 25.

Finally, we divide the *relative spectral sensitivity* (Fig. 3) by $K = 25$ and obtain the desired ***absolute spectral sensitivity*** (Fig. 7). In order to estimate *uncertainty* of the derived absolute sensitivity values we take Eq. (2) and consider uncertainties only for variables in the denominator, so neglecting fluctuations of the measured spectral signal (i.e. the shot noise). The estimated relative uncertainties of photon flux I_{ex}, absorbance A, PL QY η, coupling efficiency c_e and the projected size of a pixel a, are 4 %, 2 %, 8 %, 10 %, and 1%, respectively. Applying the rules for propagation of errors in multivariable functions[17] we get the total relative uncertainty of 14 %. This is in fact a scaling error of the sensitivity (uncertainty of the parameter K) valid for the spectral region where the standard sample was measured. However, the broad sensitivity spectrum can be also "deformed" along its spectral axis and consequently the sensitivity uncertainty can increase with increasing spectral distance from the calibrated region. Let us estimate this effect as 1 % increase of relative uncertainty at spectral distance of 100 nm and plot the overall relative uncertainty in Fig. 7.

V. APPLICATION EXAMPLES

The absolute spectral sensitivity calibration, which relates the detected signal to the number of photons emitted from a sample, can be applied to derive external quantum yield of luminescing materials on the microscopy scale. We start from the following basic equation[1] for the photoluminescence intensity I_{PL} from an optically thin layer ($\alpha d << 1$)

$$I_{PL}(\lambda_{em}) = N \cdot I_{ex}(\lambda_{ex}) \cdot \sigma(\lambda_{ex}) \cdot \eta(\lambda_{ex}, \lambda_{em}), \tag{3}$$

where N is the areal density of absorbing centers, I_{ex} is excitation photon flux, σ is absorption cross section ($N \cdot \sigma = A$ is absorbance), and η is PL quantum yield, where λ_{ex} and λ_{em} are wavelengths of excitation and emission, respectively. The first three quantities on the right side of Eq. (3) give

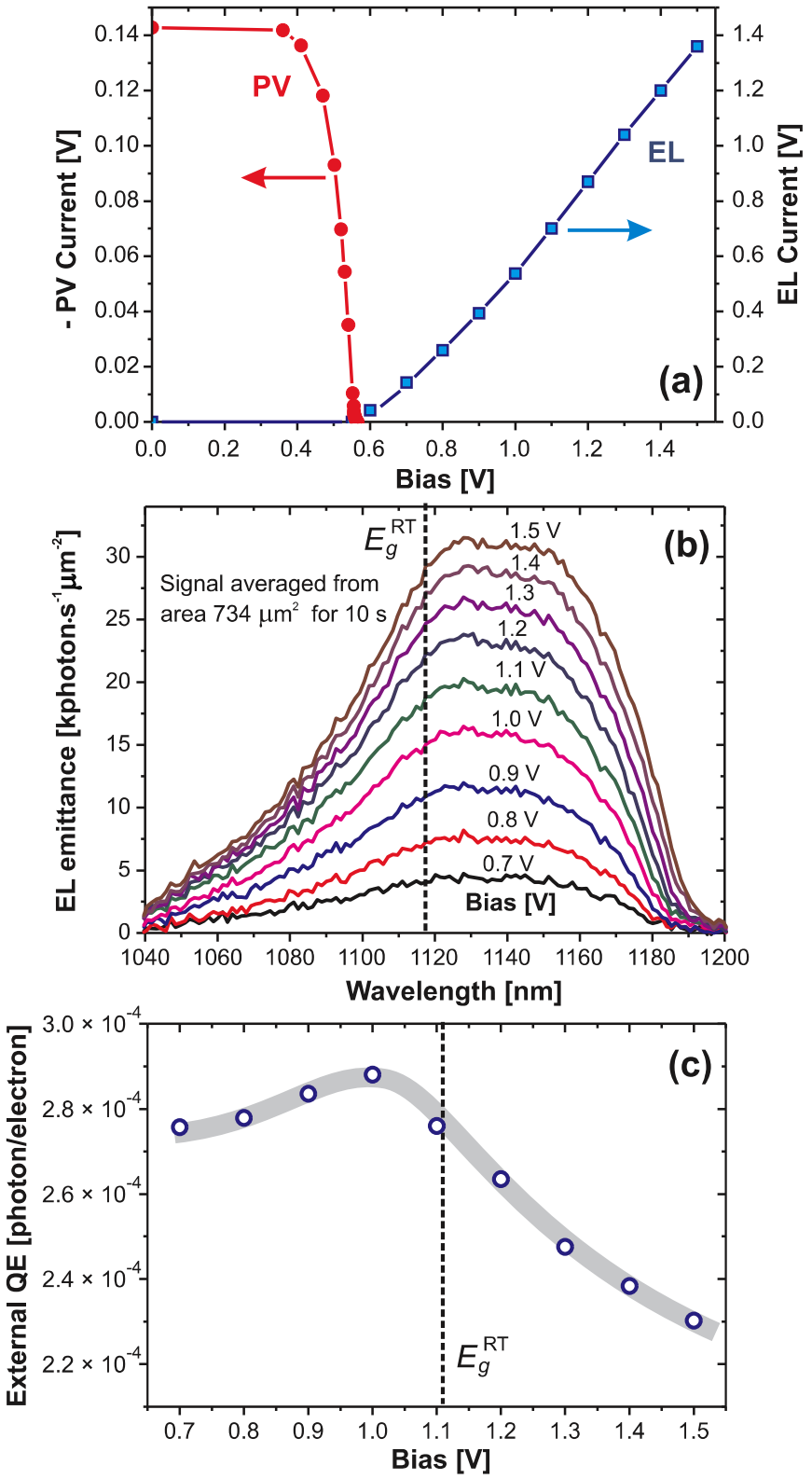

FIG. 8. (a) J-V characteristics of the poly-Si solar-cell under 1 Sun illumination (dots on the left side) and in darkness under externally applied bias during EL measurement (squares on the right side). (b) EL spectra under increasing bias converted to EL emittance using the absolute spectral sensitivity of the apparatus and assumption of the cosine angular distribution of EL emission in the upper hemisphere. (c) External quantum yield of EL emission as function of applied bias.

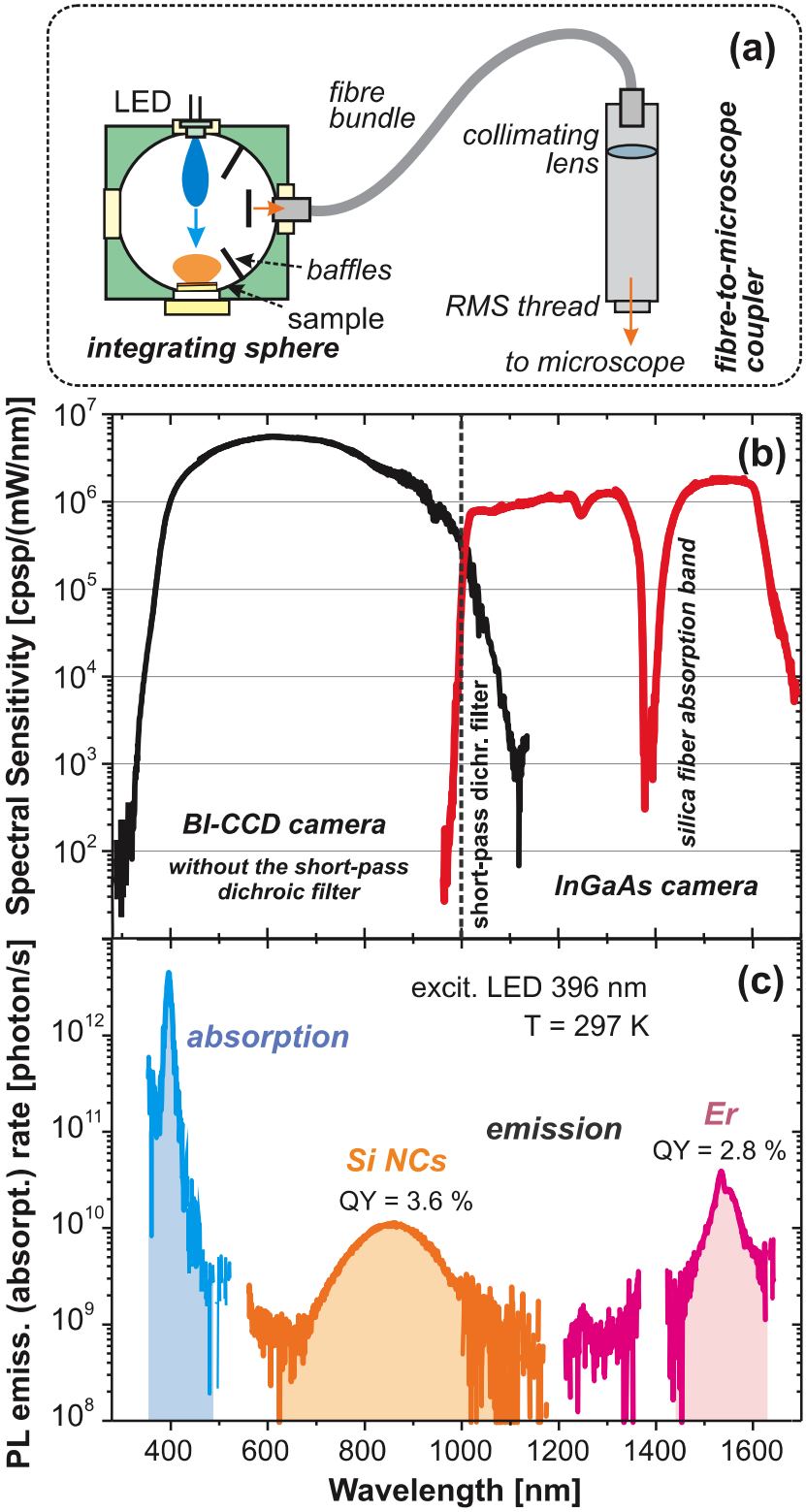

FIG. 9. (a) Schematical illustration of the integrating sphere set-up connected to the microspectroscope via a fiber bundle and an optical coupler (mounted on the objective thread). (b) Spectral sensitivity of the complete apparatus obtained as signal (in counts per second and per pixel - cpsp) divided by incoming spectral irradiance ($mW \cdot nm^{-1}$) entering the IS. The VIS detection is done without the short-pass dichroic filter. (c) PL emission and absorption rate of the SiNC:Er sample used for calculation of PL QY (QY value is indicated above each PL band).

absorption rate. While the incoming photon flux I_{ex} can be measured, N and σ must be determined or estimated separately. Also, for application of the absolute calibration to conversion of detected signal to I_{PL} one has to know or assume spatial distribution of emitted photons (directly related to the signal collection efficiency by an imaging lens).

One of the interesting applications of the above described set-up is characterization of solar-cells (SC) by their PL and EL (in case of silicon SCs their emission is situated between 1000 and 1200 nm, just matching the well calibrated spectral region). Advantage of EL external QY measurement is that number of emitted photons is related to current passing through a device which is easily measured. Therefore, only knowledge (or assumption) of EL spatial distribution is required for derivation of EL QY from detected micro-luminescence signal. EL characteristics are directly related to performance properties of a solar cell device[18] and can be effectively used for fast testing of SCs,[19] e.g. for determining minority carrier diffusion length.[20]

Here, we demonstrate the EL QY characterization of a small polycrystalline Si solar cell (SC) (Conrad Electronic SE, item No. 191254) with active area of 10×30 mm. The power efficiency under 1 Sun illumination (Solar simulator Newport Oriel Sol3A) of the tested SC is found to be about 5 % (J-V characteristics of this SC under 1 Sun illumination is shown in Fig. 8(a)). For EL characterization we mount SC in the above described microspectroscope and detect EL signal emitted from an area of 21 pixels (2.45 μm^2) under various DC bias (see Fig. 8). The measured EL intensity is converted to photon emittance using assumption of the cosine angular dependence of EL emission in the upper hemisphere.[21,22] Then the external EL QY (Fig. 8(c)) is obtained as ratio of emitted photons and number of passing elementary charges. The peak EQE value is around $(2.9 \pm 0.4) \cdot 10^{-4}$ which correspond well to literature data.[23]

Another example demonstrates usefulness of a relative sensitivity calibration over extremely broad spectral range for determination of external PL QY of Er-doped SiNCs. The tested sample is a thin layer of SiNCs in SiO_2 matrix deposited on a fused silica substrate by the radio-frequency magnetron co-sputtering of Si, SiO_2 and Er_2O_3, for details see Refs. 24 and 25. In order to make PL QY measurement independent on spatial distribution of PL emission the sample is placed in an integrating sphere (Fig. 9(a)). Excitation is done by the unfocused 396-nm LED and PL signal is collected by a silica fiber bundle whose output is coupled to the above described microspectroscope. A new relative spectral sensitivity (Fig. 9(b)) is measured for the whole apparatus including IS, the fiber bundle and the coupler (by illuminating the IS input port with the calibrated 45-W tungsten halogen filament lamp). The VIS detection branch is used without the inverted dichroic filter in order to enlarge detectable range down to ~350 nm. The NIR sensitivity dip around 1400 nm is due to absorption in the silica fiber bundle.

PL QY yield is derived from measurement of the SiNC:Er sample and a reference sample (bare substrate) by a procedure described in our recent paper.[7] Fig. 9(c) shows difference (absolute value) between signals from the tested sample and the reference sample converted to photon rate. QY of each PL emission band is then obtained as ratio of its integrated area (giving number of emitted photons) and the absorption band integrated area (number of absorbed photons). We get PL QY of (3.6 ± 0.3) % and (2.8 ± 0.2)% for the PL emission by SiNCs (around 850 nm) and by Er-dopants (around 1540 nm), respectively. The relative uncertainty is estimated (by the procedure described in Ref. 7,) to be ~8% which is much less than for the EL QY experiment (described above) as the IS-based experiment does not rely on the absolute but just the relative calibration. The extraordinary broad spectral range of this PL QY determination technique could be advantageous for studies of many materials, e.g. up-converting or down-converting luminescent materials.[26]

VI. CONCLUSIONS

We have proposed and tested a method of absolute calibration of a microspectroscope over an extraordinary broad spectral range covered by two (parallel) detection branches. The absolute calibration of a relative spectral sensitivity is performed using the standard sample formed by a thin layer of Si nanocrystals with stable photoluminescence around 1000 nm – the area where both detection branches overlap. The spectral PL quantum yield and the PL spatial distribution of

the standard sample were characterized by separate experiments. The relative uncertainty of the absolute calibration is estimated to be around 14 % but it can be reduced down to ~5 %.

This absolute calibration opens new applications of the optical microspectroscopy in quantitative characterization of various materials. For example, it enables us to calculate spectral photon emittance from a selected area of an investigated sample (even on the level of a single emitting nano-object like single molecule or quantum dot) entering the detection system (an objective lens). The total emittance could be estimated when the spatial distribution of PL of the studied sample (or object) is known – estimated or measured. Moreover, we can get also the emission QY if the absorbance (absorption cross section) is known. In the paper we demonstrate capabilities of this set-up by measuring external QY of electroluminescence from a standard poly-Si solar-cell and external QY of photoluminescence of Er-doped Si nanocrystals, where the broad VIS/NIR spectral range is necessary. We expect that the described method should find applications especially in the field of solar-cell materials or biomedical studies (detection of singlet oxygen emission at 1270 nm etc.).

The key component of our approach – the standard sample formed by a thin layer of luminescing Si nanocrystals in silica matrix - can be substituted by similar layers of efficiently luminescing materials (e.g. commercially available PbS quantum dots dispersed in PMMA and deposited by a spin coating an a glass substrate). In future, standard samples could be commercially supplied (including all necessary characterization data). The set-ups used in our calibration procedure may look quite complex but in fact all characterization of a standard sample can be performed using the same microspectroscopy set-up (providing the relative sensitivity was first measured with a radiation standard). Both the integrating sphere (for QY measurements, Fig. 9(a)) and the goniometer (for PL spatial distribution, Fig. 5(b)) can be assembled from standard optomechanical components and connected to a microscope via a fiber light-guide and a coupler (Fig. 9(a), also made from standard components).

ACKNOWLEDGEMENT

This work was performed within the framework of the Czech-Japan collaborative project Kontakt II 7E11021 (MSMT CR) and partially supported by the Bonus programme of Charles University. Authors are indebted to Prof. Zacharias' group at IMTEK, Freiburg, Germany for fabricating high-quality Si nanocrystalline layers used as calibration standards and also to group of Prof. Gregorkiewicz, University of Amsterdam, the Netherlands for providing Er-doped SiNC sample fabricated by D. Timmerman in the laboratory of Prof. Fujii, Kobe University, Japan.

[1] I. Pelant and J. Valenta, *Luminescence Spectroscopy of Semiconductors* (Oxford University Press, 2012).
[2] W. R. McCluney, *Introduction to Radiometry and Photometry* (Artech House Inc., Boston London, 1994).
[3] W.D. Niles and F.S. Cohen, Rev. Sci. Instr. **66**, 3527 (1995).
[4] J. Thigpen, F. A. Merchant, and S.K. Shah, J. Microscopy **239**, 200 (2010).
[5] Note, we recommend to avoid application of small spectrographs – having focal length shorter than about 25 cm – as they suffer from increasing stray light intensity which significantly affects results of sensitivity calibration obtained by measuring broad-band light sources. The stray-light-effects are strong in spectral regions where sensitivity drops down).
[6] J. Valenta, R. Juhasz, and J. Linnros, J. Luminescence **98**, 15 (2002).
[7] J. Valenta, Nanosci. Methods **3**, 11 (2014).
[8] I. Pelant, T. Ostatnický, J. Valenta, K. Luterová, E. Skopalová, T. Mates, and R.G. Elliman, Appl. Phys. B **83**, 87 (2006).
[9] Note, the number of pixels over which signal was averaged is different from the 3x2 pixels in the schematical illustration on Fig. 2. In fact, the result of the described procedure should be independent on the number of averaged pixels; unless the signal distribution changes significantly within the averaged area (such situation must be avoided not only during calibration but also during all subsequent measurements). It means that one can adapt number of averaged pixels and a slit width (within certain limits) in order to improve signal-to-noise ratio.
[10] A. M. Hartel, D. Hiller, S. Gutsch, P. Löper, S. Estradé, F. Peiró, B. Garrido, and M. Zacharias, Thin Solid Films **520**, 121 (2011).
[11] J.M. Zwier, G.J. van Rooij, J.W. Hofstraat, and G.J. Brakenhoff, J. Microscopy **216**, 15 (2004).
[12] A. Antonini, C. Liberale, and T. Fellin, Opt. Express **22**, 14293 (2014).
[13] G.J. Brakenhoff, G.W.H. Wurpel, K. Jalink, L. Oomen, L. Brocks, and J.M. Zwier, J. Microscopy **219**, 122 (2005).
[14] J. Valenta, M. Greben, S. Gutsch, D. Hiller, and M. Zacharias, Appl. Phys. Lett. **105**, 243107 (2014).
[15] H.E. Hellen and D. Axelrod, J. Opt. Soc. Am **4**, 337 (1987).
[16] J. Valenta, A. Fucikova, F. Vácha, F. Adamec, J. Humpolíčková, M. Hof, I. Pelant, K. Kůsová, K. Dohnalová, and J. Linnros, Adv. Functional Materials **18**, 2666 (2008).

[17] I.G. Hughes and T.P.A. Hase, *Measurements And Their Uncertainties: A Practical Guide to Modern Error Analysis* (Oxford University Press, Oxford, 2010).
[18] U. Rau, Phys. Rev. B **76**, 085303 (2007).
[19] T. Fuyuki and A. Kitiyanan, Appl. Phys. A **96**, 189 (2009).
[20] P. Würfel, T. Trupke, T. Puzzer, E. Schäffer, W. Warta, and S.W. Glunz, J. Appl. Phys. **101**, 123110 (2007).
[21] This assumption may be quite rough, but the purpose of this experiment is just to demonstrate application potential of the calibrated VIS/NIR microspectroscope for SC testing via EL yield determination. If necessary, the angular distribution of EL from a SC can be characterized using the goniometer set-up as shown in Fig. 5 (but without the excitation laser).
[22] T. Trupke, E. Dayb, and P. Würfel, Sol. En. Mater. & Sol. Cells **53**, 103 (1996).
[23] T. Kirchartz, A. Helbig, W. Reetz, M. Reuter, J. H. Werner, and U. Rau, Prog. Photovolt: Res. Appl. **17**, 394 (2009).
[24] M. Fujii, M. Yoshida, Y. Kanzawa, S. Hayashi, and K. Yamamoto, Appl. Phys. Lett. **71**, 1198 (1997).
[25] I. Izzedin, D. Timmerman, T. Gregorkiewicz, A.S. Moskalenko, A.A. Prokofiev, I.N. Yassievich, and M. Fujii, Phys. Rev. B **78**, 035327 (2008).
[26] J. Zhao, D. Jin, E.P. Schartner, Y. Lu, Y. Liu, A.V. Zvyagin, L. Zhang, J. M. Dawes, P. Xi, J.A. Piper, E.M. Goldys, and T.M. Monro, Nature Nanotech. **8**, 729 (2013).

Paper IX

APPLIED PHYSICS LETTERS **105**, 243107 (2014)

Effects of inter-nanocrystal distance on luminescence quantum yield in ensembles of Si nanocrystals

J. Valenta,[1,a)] M. Greben,[1] S. Gutsch,[2] D. Hiller,[2] and M. Zacharias[2]
[1]*Faculty of Mathematics and Physics, Department of Chemical Physics & Optics, Charles University, Ke Karlovu 3, 121 16 Prague 2, Czechia*
[2]*Faculty of Engineering, IMTEK, Albert-Ludwigs-University Freiburg, Georges-Köhler-Allee 103, 79110 Freiburg, Germany*

(Received 6 November 2014; accepted 4 December 2014; published online 17 December 2014)

The absolute photoluminescence (PL) quantum yield (QY) of multilayers of Silicon nanocrystals (SiNCs) separated by SiO_2 barriers were thoroughly studied as function of the barrier thickness, excitation wavelength, and temperature. By mastering the plasma-enhanced chemical vapor deposition growth, we produce a series of samples with the same size-distribution of SiNCs but variable interlayer barrier distance. These samples enable us to clearly demonstrate that the increase of barrier thickness from ~1 to larger than 2 nm induces doubling of the PL QY value, which corresponds to the change of number of close neighbors in the hcp structure. The temperature dependence of PL QY suggests that the PL QY changes are due to a thermally activated transport of excitation into non-radiative centers in dark NCs or in the matrix. We estimate that dark NCs represent about 68% of the ensemble of NCs. The PL QY excitation spectra show no significant changes upon changing the barrier thickness and no clear carrier multiplication effects. The dominant effect is the gradual decrease of the PL QY with increasing excitation photon energy. © *2014 AIP Publishing LLC*. [http://dx.doi.org/10.1063/1.4904472]

Silicon nanocrystals (SiNCs) embedded in silicon dioxide (SiO_2) exhibited high photoluminescence (PL) quantum yield (QY) of the order of 10%, which is size tunable in the spectral region from orange to near infrared, i.e., about 650–1100 nm.[1] In case of colloidal suspensions of Si nanocrystals (NCs) passivated by different organic molecules (i.e., well separated NCs), the reported external PL QY can exceed 50%.[2,3] Such high QY can be potentially exploited to provide photon conversion, e.g., in lighting and photovoltaic devices.[4]

In this paper, we present a study of inter-nanocrystal distance effects on PL QY of SiNC/SiO_2 nanocrystalline multilayers. Our multilayer deposition technique provides unique opportunity to vary the vertical separation of nanocrystal layers while keeping the SiNC size distribution unaffected. We show that the PL QY increases about two-times when increasing the SiO_2 barrier from ~1 nm (or smaller) to thicknesses larger than 2 nm. The PL QY limiting mechanism is apparently related to the thermally activated carrier transport from a nanocrystal to silica defects or defective (dark) nanocrystals. Any effects of carrier multiplication (CM), like the so called space-separated quantum cutting (SSQC) which must be very sensitive to inter-nanocrystal distance,[5] have been found to be negligible in our superlattice samples.

The samples were deposited as alternating layers of silicon-rich silicon oxynitride (SRON; SiO_xN_y) and stoichiometric SiO_2 on fused silica substrates by the plasma-enhanced chemical vapor deposition (PECVD). On top and below the superlattice stack, 10 nm of SiO_2 were deposited as a buffer and capping layer, respectively, (see Fig. 1(a)). The samples were consequently annealed in a quartz tube furnace at 1150 °C for 1 h in high purity N_2 in order to achieve phase separation between Si and SiO_2, i.e., forming SiNCs and passivated by annealing in H_2 at 500 °C. In this study, we present results obtained on one series of *multilayer* (ML) samples and one series of *single-layers* (SLs) (i.e., a thick SRON monolayer without barriers), whose parameters are described in the Table I. The SRON stoichiometry parameter y was almost constant $y = 0.23 \pm 0.02$ in all samples and the x value is specified in Table I. Further details of the sample preparation as well as structural properties of the NC samples are given in our recent paper.[6]

The crucial point of the present study is that we can prepare (by adjusting the stoichiometry parameter x) a thick single-layer sample (S4), which has almost the same shape of PL spectrum as the ML samples (see Fig. 1(b)). This means that the size distribution of SiNCs in the sample S4 and M samples are very similar and the only different parameter is the absence or presence of a SiO_2 barrier with variable thickness.

PL QY was studied using a spectroscope with an integrating sphere (IS) designed and built in our laboratory. Both the set-up and the theoretical basis of the PL QY determination were described in our recent paper.[7] The IS has diameter of 10 cm and the internal coating by the Spectraflex® material. Samples are placed inside IS on one removable port in the position opposite to the excitation port where various light-emitting diodes (LEDs) are mounted to provide the PL excitation. Quite broad excitation range of 280–620 nm can be investigated using a set of more than 40 LEDs with various emission wavelengths. The LED output power is typically less than 1 mW, and it is not focused on the sample. Hence, we work several orders of magnitude below the saturating power density, which is about 1 W/cm^2 at room

[a)]Author to whom correspondence should be addressed. Electronic mail: jan.valenta@mff.cuni.cz

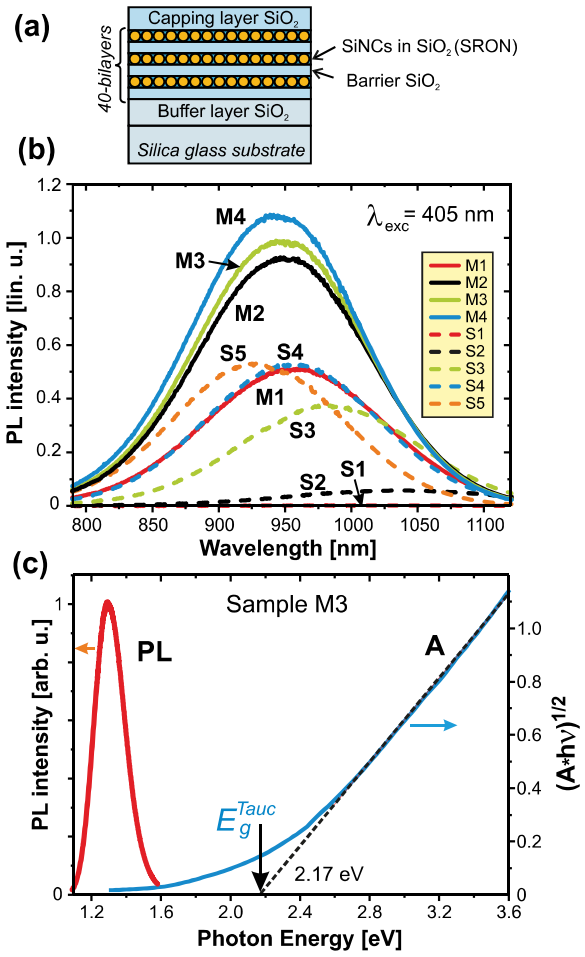

FIG. 1. (a) Schematics of a multilayer sample composition.[23] (b) PL spectra of all ML and SL samples under excitation by the 405-nm LED. (c) PL peak of the sample M3 transformed into the photon energy scale along with its absorbance. The optical gap is estimated from the Tauc plot of absorbance to be around 2.17 eV.

temperature for Si NCs in SiO_2 matrix.[8] The output signal from the IS is collected by a fused-silica fiber bundle and a liquid-nitrogen-cooled CCD camera is used for detection. The spectral sensitivity of the complete apparatus is calibrated over a broad spectral range (300–1100 nm) using two radiation standards (Newport Oriel): a 45 W tungsten halogen lamp (above 400 nm) and a deuterium lamp (below 400 nm). Special attention is paid to avoid stray light effects in the spectrometer.[7]

TABLE I. Description of the sample parameters.

Label	Layer stack	SiO_xN_y thick (nm)	SiO_2 thick (nm)	Stoichiometry x-value
M1	40 bilayers	4.5	1.0	0.93
M2	40 bilayers	4.5	1.6	0.93
M3	40 bilayers	4.5	2.2	0.93
M4	40 bilayers	4.5	2.8	0.93
S1	Single layer	200	…	0.64
S2	Single layer	200	…	0.93
S3	Single layer	200	…	1.05
S4	Single layer	200	…	1.10
S5	Single layer	200	…	1.15

PL QY is determined as a ratio of emitted and absorbed photon rate for the whole investigated sample—it means that we are characterizing the *external quantum yield* (EQY). In case that an ensemble of Si NCs contains some "*dark*" NCs (which absorb but do not emit photons due to the presence of a very fast and efficient non-radiative center), EQY will deviate from the *internal QY* (IQY), which concerns only *bright* NCs (see, e.g., Ref. 9). IQY can be measured in special samples from variation of PL decay rates under different local density of optical states (variable near-field distance from a reflecting surface), which enable to decouple radiative and non-radiative rates. Such experiments were reported only by two groups; while the experiment by Walters *et al.*[10] on implanted SiNCs show QY up to 60% almost independent on wavelength, Miura *et al.*[11] reports different IQY for different sputtered samples reaching up to 100% for well isolated big NCs emitting at wavelengths above 850 nm.

The temperature variation of PL QY was determined indirectly by measuring temperature evolution of PL intensity $I_{PL}(T)$ and absorption cross section (ACS) $\sigma(T)$ of a sample placed in a cryostat and excited by a 405-nm laser whose continuous wave emission was modulated with an acousto-optical modulator (the leading and the trailing edge of the "rectangular" excitation pulses is about 0.1 μs, frequency 900 Hz and the duty cycle is 40%). ACS is calculated from the intensity dependence of the PL onset and decay rate as described, e.g., by Kovalev *et al.*[12] The relative temperature changes of PL QY $\eta(T)$ are then calculated from the following relation:

$$I_{PL}(T) = N I_{ex}\, \sigma(T)\, \eta(T), \tag{1}$$

where N is the density of absorbing SiNCs, which is unknown but supposed to be independent of T, and I_{ex} is the excitation photon flux which is kept constant. The relative change of PL QY with temperature $\eta(T) \sim I_{PL}(T)/\sigma(T)$ is converted to absolute PL QY using the room temperature QY value determined with the integrating sphere setup.

The room temperature PL QY for samples M1 to M4 with increasing thickness of SiO_2 barriers is compared with the appropriate single-layer sample S4 in Fig. 2 for two

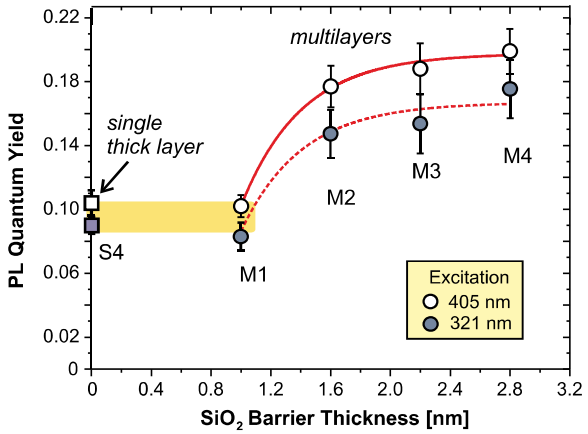

FIG. 2. PL QY (excited at 405 nm and 321 nm) as function of the barrier thickness for ML samples and the S4 sample (the extreme left points). The lines are fitted exponential decays with decreasing barrier thickness.

excitation wavelengths (321 and 405 nm). PL QY clearly grows with increasing barrier thickness. The experimental points can be fitted well by an exponential function with the characteristic distance of 0.4 nm (the barrier thickness for which PL QY drops to 1/e of the maximal value). Interestingly enough, the single-layer sample S4 has almost the same value of PL QY (~10%) as the multilayer sample M3, which has narrow barriers of 1 nm. Therefore, we can state that: (i) The transition from a thick SiNC layer (containing random distributed NCs) to the well separated (>2 nm) stack of confined layers increases the PL QY to approximately double value and (ii) the barrier of 1 nm or thinner becomes ineffective and the PL QY of ML structures is equal to those of the equivalent SL sample.

In the Fig. 1(b) one can see that the decrease of barrier thickness (from the sample M4 to M1) is accompanied by a small red-shift. Such effect can be due to the easier quenching of excitons by neighbor NCs in case of small NCs (there is energy gain when exciton transfers to a bigger NC). At the same time, the presence of barriers alters the distribution of Si excess concentration in multilayer-structures via the diffusion of Si atoms from SRON layers into silica barriers. The diffusion-related loss of Si from the SRON layers must be compensated by a certain increase of the Si excess concentration ($x = 0.93$) in ML samples compared to the SL sample S4 ($x = 1.10$) with equivalent size distribution. Interestingly, for the thermal budget employed, the calculated Si diffusion length in SiO_2 turned out to be about 2 nm. Consequently, the SiO_2 barrier thickness larger than 2 nm reduces the coupling between SiNC layers as the silica barrier contains less excess Si atoms and the barrier height is bigger. However, the nature of the transport (e.g., exciton migration or carrier tunneling) cannot be revealed from data in Fig. 2 due to the NC-size distribution and the barrier control limited to one dimension. Finally, we note that the doubling of PL QY by introducing barriers in the ML structure can be related to the change of number of neighbouring NCs: Supposing that an ensemble of Si NCs can be idealized as the hexagonally close packed (hcp) structure, then a NC has 6 close neighbors in its layer and 3 neighbors in both upper and lower layer. It means that the transition from a thick layer to a monolayer decreases the number of close neighbors to half.

Determination of the PL QY temperature dependence (presented in Fig. 3 for samples M4 and S4) reveals that both ML and SL samples have approximately the same PL QY for T below ~100 K. The PL QY peak of about 32% is around $T = 120$ K from which the PL QY slowly decreases toward lower T. The decrease of PL QY with T increasing above 120 K is more important for the S4 sample and gives hints to the origin of the observed room temperature difference in PL QY. This observation suggests that the QY reducing mechanism is thermally activated, for example, carrier diffusion or dispersive motion of excitons.[8,13] Let us suppose that the peak PL QY of 32%, common for SL and ML samples, corresponds to the situation where no carrier transfer out of a NC is allowed, then the observed EQY is limited by non-radiative losses of excitation in dark NCs and the fraction of bright NCs can be estimated by dividing EQY and IQY. If we suppose that the IQY was 100%,[11] then the fraction of bright NCs is 0.32. Even if this is a very rough estimation, it is in surprisingly perfect agreement with data published recently by Limpens and Gregorkiewicz[9] who reported 68.5% dark SiNCs in passivated $SiNC/SiO_2$ samples, when taking IQY data from Miura *et al.*[11] as we do. The question of whether the dark NCs are permanently off due to presence of a quenching center (structural defect) or some NCs can switch between bright and dark state is very interesting but cannot be answered using the present PL QY experiments.

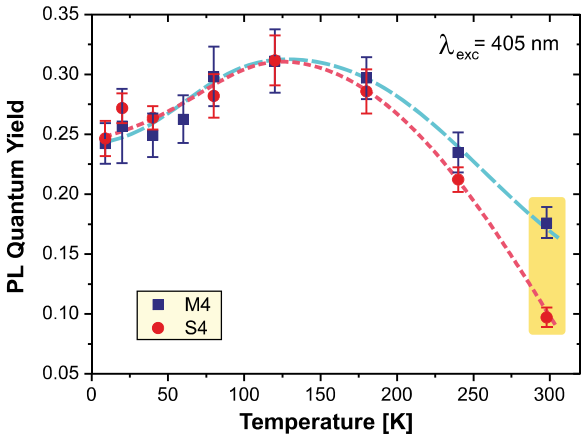

FIG. 3. The temperature changes of PL QY for samples M4 and S4 determined from temperature variation of PL intensity and absorption cross section using the calibration by the PL QY value obtained at room temperature in the integrating sphere setup (highlighted rectangle). The dashed lines are just guides for the eye.

Luminescence QY values are usually measured (and reported in literature) for only one excitation wavelength as it is generally supposed that the so called *Kasha-Vavilov* (KV) *rule* is fulfilled. The KV rule (formulated originally for organic chromophores) says that both the luminescence spectral shape and its QY do not depend on the applied excitation wavelength.[14] However, there may be exceptions from the KV rule. In general, for a semiconductor, one tends to expect a decreasing PL QY for excitation addressing higher states above the band gap as more non-radiative paths can be opened for relaxation of hotter carriers. It was also theoretically proposed and experimentally observed that absorption of one high-energy photon can produce two (or more) low energy photons which is called quantum cutting (so giving a IQY above 1 but the energy efficiency below or equal to 1).[15] In organic materials, an analogous process called singlet fission generates two triplet states from one singlet excited state.[16] For bulk semiconductors a high-energy excitation can create multiple excited electrons by impact ionization and the equivalent effect in nanocrystals is called carrier multiplication. However, multiple excitation of a single SiNC is believed to induce fast and efficient quenching by Auger recombination. Despite of this fact, some experiments suggested that high photon energy excitation can improve luminescence yield in closely packed SiNCs and a model of the SSQC was proposed.[5,17]

In order to reveal the possible variation of PL QY with excitation photon energy we measured the PL QY

excitation spectrum using an excitation by a set of LEDs. In Fig. 4, we compare the PL QY excitation spectrum for one ML sample (M3, however, other samples give very similar results) and the single-layer samples S4 and S2 (which has low QY of about 1%). The PL QY of sample M3 varies between 11% and 22% with three characteristic features superposed on the background QY value (light blue line in Fig. 4) slowly decreasing toward higher excitation photon energy:

(a) The rapidly decreasing QY below 2.2 eV is proposed to be due to preferred absorption into defect states. Such absorbing states located close to the optical gap can be sometimes observed with the photo-thermal deflection spectroscopy.[18] Similar decrease of QY at the long-wavelength edge was observed in porous Si.[13,19]

(b) The PL QY peak around 3.3 eV seems to correspond to the direct $\Gamma'_{25} \rightarrow \Gamma_{15}$ absorption, which is about 3.5 eV in bulk Si but shrinks due to the quantum confinement in SiNCs.[20] The mechanism of boosting the radiative recombination probability by such resonant absorption is not clear but a similar QY peak can be found in some literature data on SiNCs (e.g., Refs. 13 and 21) and we observed similar effects also for other materials like PbS nanocrystals (Σ-point transitions) in liquid suspension.

(c) Finally, the increase of QY for excitation with high energy photons (above 3.9 eV) could be related to the onset of CM—generation of two electron-hole pairs after absorption of a single photon.[17] Unfortunately, the experimental uncertainty of QY values for energies above 4 eV is very large - due to the low UV-sensitivity of the CCD[1]—and the observed QY increase is practically within the error bars. The optical band gap of the studied Si NC sample is estimated from the absorption Tauc plot ($(A^*h\nu)^{1/2}$ vs. $h\nu$) where the linear part of the curve is extrapolated and its intersection with the abscissa is found at about 2 eV. Please note that this is a very rough estimate as the "linear" part of the curve is not clearly defined and there is also a possible influence of the NC size distribution, see Fig. 1(c). Then the QY increase at high energy side occurs above the double of the Tauc gap energy. Alternative explanation of the high energy peak is that it is a part of a peak with maximum around 4.4 eV, which is close to the E_2 critical point resonance in Si and was also observed in some PL excitation spectra.[22]

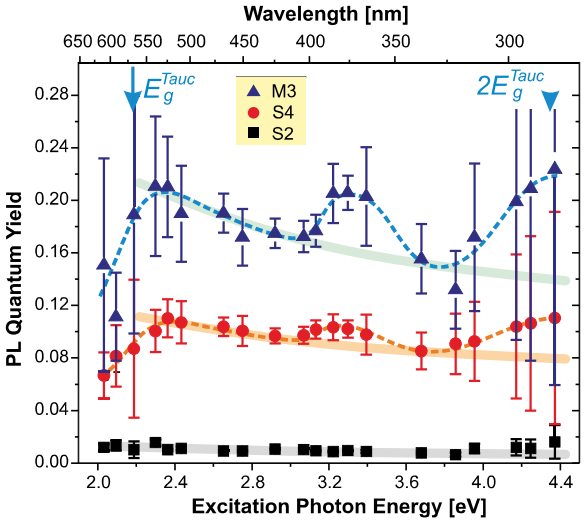

FIG. 4. PL QY excitation spectra for the samples M3, S4, and S2 (points with error bars). The dashed lines are just guides for the eye and the broad semi-transparent lines highlight the general slow decrease of QY with increasing photon energy. The arrows indicate energy 2.2 eV corresponding to the optical gap and its double value of about 4.4 eV derived from the absorption edge (Fig. 1(b)).

Finally, we have to point out, that the above mentioned spectral features in PL QY excitation spectra are not sensitive to the changes of the barrier thickness which excludes any important role of the SSQC processes.

In conclusions, using a special set of SiNC/SiO_2 multilayers, we demonstrated an increase of the luminescence QY at room temperature from ~10% to ~19% for an interlayer barrier thickness of 2 nm or larger. A barrier of 1 nm or narrower is shown to be ineffective and such multilayer samples behave like a thick single-layer of SiNCs. The temperature evolution reveals a merging of the PL QY values of ML and SL samples for temperatures below ~120 K. This fact indicates that the room temperature differences of PL QY are due to the thermally activated transport of excitation into non-radiative centers in dark NCs or in the matrix. We can estimate that dark NCs represent about 68% of the ensemble. The PL QY excitation spectra show no significant changes upon changing the barrier thickness and no clear carrier multiplication effects, like SSQC.

This work was financially supported by the EU-project NASCEnT (FP7-245977). The Prague group acknowledges co-financing by the MSMT through the 7E11021 Project and support from the Charles University Bonus Programme.

[1]K. Dohnalová, T. Gregorkiewicz, and K. Kůsová, J. Phys.: Condens. Matter **26**, 173201 (2014).
[2]J. B. Miller, A. R. Van Sickle, R. J. Anthony, D. M. Kroll, U. R. Kortshagen, and E. K. Hobbie, ACS Nano **6**, 7389 (2012).
[3]D. Jurgbergs, E. Rogojina, L. Mangolini, and U. Kortshagen, Appl. Phys. Lett. **88**, 233116 (2006).
[4]Z. Yuan, G. Pucker, A. Marconi, F. Sgrignuoli, A. Anopchenko, Y. Jestin, L. Ferrario, P. Bellutti, and L. Pavesi, Sol. Energy Mater. Sol. Cells **95**, 1224 (2011).
[5]D. Timmerman, I. Izeddin, P. Stallinga, I. N. Yassievich, and T. Gregorkiewicz, Nat. Photonics **2**, 105 (2008).
[6]A. M. Hartel, D. Hiller, S. Gutsch, P. Löper, S. Estradé, F. Peiró, B. Garrido, and M. Zacharias, Thin Solid Films **520**, 121 (2011).
[7]J. Valenta, Nanosci. Methods **3**, 11 (2014).
[8]A. Hartel, S. Gutsch, D. Hiller, and M. Zacharias, Phys. Rev. B **87**, 035428 (2013).
[9]R. Limpens and T. Gregorkiewicz, J. Appl. Phys. **114**, 074304 (2013).
[10]R. J. Walters, J. Kalkman, A. Polman, H. A. Atwater, and M. J. A. de Dood, Phys. Rev. B **73**, 132302 (2006).
[11]S. Miura, T. Nakamura, M. Fujii, M. Inui, and S. Hayashi, Phys. Rev. B **73**, 245333 (2006).
[12]D. Kovalev, J. Diener, H. Heckler, G. Polisski, N. Künzner, and F. Koch, Phys. Rev. B **61**, 4485 (2000).
[13]L. Pavesi, J. Appl. Phys. **80**, 216 (1996).
[14]J. R. Lakowicz, *Principles of Fluorescence Spectroscopy*, 3rd ed. (Springer Science + Business Media LLC, 2006).
[15]C. Ronda, J. Lumin. **100**, 301 (2002).

[16]M. B. Smith and J. Michl, Chem. Rev. **110**, 6891 (2010).
[17]D. Timmerman, J. Valenta, K. Dohnalová, W. D. A. M. de Boer, and T. Gregorkiewicz, Nat. Nanotechnol. **6**, 710 (2011).
[18]B. G. Lee, D. Hiller, J. W. Luo, O. E. Semonin, M. C. Beard, M. Zacharias, and P. Stradins, Adv. Funct. Mater. **22**, 3223 (2012).
[19]M. Rosenbauer, S. Finkbeiner, E. Bustarett, J. Weber, and M. Stutzmann, Phys. Rev. B **51**, 10539 (1995).
[20]K. Kůsová, P. Hapala, J. Valenta, P. Jelínek, O. Cibulka, L. Ondič, and I. Pelant, Adv. Mater. Interfaces **1**, 1300042 (2014).
[21]V. Svrcek, K. Dohnalová, D. Mariotti, M. T. Trinh, R. Limpens, S. Mitra, T. Gregorkiewicz, K. Matsubara, and N. Kondo, Adv. Funct. Mater. **23**, 6051 (2013).
[22]M. Stutzmann, M. S. Brandt, M. Rosenbauer, J. Weber, and H. D. Fuchs, Phys. Rev. B **47**, 4806 (1993).
[23]S. Gutsch, Ph.D. dissertation, Albert-Ludwigs-University Freiburg, 2013.

Paper X

Non-exponential decay kinetics: Correct assessment and description illustrated by slow luminescence of Si nanostructures

Mikel Greben[1], Petro Khoroshyy[2], Ilya Sychugov[3] and Jan Valenta[1]
[1] *Department of Chemical Physics and Optics, Faculty of Mathematics and Physics, Charles University, Ke Karlovu 3, 121 16 Prague 2, Czechia*
e-mail address: leibnits@gmail.com
[2] *Institute of Organic Chemistry and Biochemistry, Czech Academy of Sciences, Flemingovo namesti 2, 160 00 Prague 6, Czechia*
[2] *KTH – Royal Institute of Technology, Department of Applied Physics, 16440 Kista-Stockholm, Sweden*

The treatment of time-resolved (TR) photoluminescence (PL) decay kinetics is analysed in details and illustrated by experiments on semiconductor quantum dots (QDs), namely silicon nanocrystals (Si NCs). We consider the mono-, stretch- and multi-exponential as well as lognormal and some complex decay models for continuous and discrete distribution of rates (lifetimes). Conditions under which the mono-exponential decay can be observed are outlined. A particular attention is devoted to the thorough analysis of non-exponential decay kinetics. We explicitly show that a lognormal distribution of emitter sizes may results in lognormal distribution of decay rates. On the other hand, the distribution of rates cannot be, strictly speaking, Levy stable distribution (that results in the stretched-exponential decay). Therefore, the stretched exponential model is recommended only for assessment of a distribution average and estimation of degree of dispersion. We introduce theoretical background and derive expressions to calculate the average decay lifetimes for some common decays with practical examples of their applications. The difference between the average decay (intensity average) lifetime and the average lifetime constant (amplitude-average lifetime) is explicitly explained. Experimental aspects are discussed with special attention devoted to the major problems of the accurate TR PL data treatment, including background uncertainty, pulse duration, system response function etc. Finally, a thorough literature survey of TR PL in Si NCs is given. The methods and definitions outlined in this systematic review are applicable to various other material systems with slow decay like rare-earth and transition metal doped materials, amorphous semiconductors, type-II heterostructures, forbidden transitions in molecular systems, singlet oxygen phosphorescence, etc.

Keywords: photoluminescence decay, lifetime distribution, average lifetime, silicon nanocrystals

1. INTRODUCTION

Time-resolved (TR) photoluminescence (PL) spectroscopy is one of the key non-invasive methods to study kinetics of energy relaxation and transport in various systems. When applied to semiconductor quantum dots (QDs) it could help us to distinguish between direct transitions in the core of a QD and phonon-assisted or trap-related relaxations. The proper and careful treatment of decay kinetics of photo-excited population of emitters could also provide information on the quality of the QD surface passivation, the uniformity of sizes and shapes, distribution of decay rates (lifetimes) and energy transfer (interaction) between QDs. A particular interest is that TR PL studies reveal not only characteristic depopulation exciton dynamics in QDs, but also

the information on the surrounding NC environment[1,2] (see the scheme in Fig. 1).

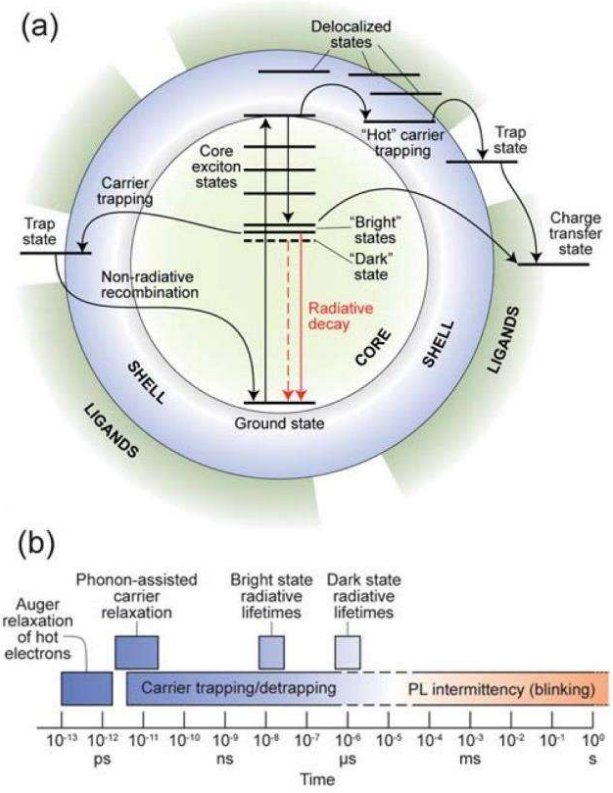

FIG. 1. (a) Schematic illustration of various relaxation processes in photoexcited core/shell QDs. The population of bright and dark exciton states is influenced by carrier (de)trapping, charge transfer to ligand orbitals and non-radiative processes. (b) Timescales of the photo-induces relaxation processes observed in CdSe QDs. Reproduced with permission from Jones *et al*., J. Mat. Chem. **20**, 3533 (2010). Copyright © The Royal Society of Chemistry, 2010.

Surprisingly, in spite of great importance of the technique, there are very few reports[3,4,5] that describe the procedure of data treatment from PL decays. To date, the profound analysis that explains different relaxation processes in an ensemble of emitters is still missing. The deviation from trivial mono-exponential decay is not an exception but rather a rule in most ensembles of QDs. In analogy with emission/absorption spectroscopy, where broad recorded peaks often result from convolution of several different processes, the unique physical information about individual contributions is lost in ensemble transients. However, as Gaussian fittings are commonly used to evaluate peak positions and linewidths (average and dispersion) in spectroscopy, a proper mathematical treatment of non-exponential decays can provide similar information on contributing rate distributions, allowing legitimate comparison between seemingly disparate curves. Therefore, the understanding how to treat non-trivial decay kinetics with distribution of rate (lifetime) constants is of great practical importance. Though there is a tremendous number of papers reporting stretched exponential (SE) decay kinetics, it is still a matter of debates on what to consider as true SE (Kohlrausch) function[4] as different variations of this function can be found in literature.[6,7] In our opinion, the importance of proper average lifetime calculations and their applicability limits are often overlooked.

Here we present the theory of average decay lifetime calculations as well as its common usage in practice. Throughout this review we shall use experimental examples mostly from studies of Si nanostructures. But the described procedures are applicable to large variety of materials exhibiting non-exponential kinetics like rare earth ions, phosphorescence of organic molecules, nuclear spin relaxations, etc.

2. DECAY MODELS

2.1 Mono-exponential decays

In this section we will consider the theory and experimental observations of the most common cases of mono-exponential decays of emitters.

2.1.1. Homogeneous ensemble of non-interacting emitters

Let us consider the case when the entire ensemble of emitters is fully homogeneous and thus both radiative k_r and total k (i.e. the sum of radiative and non-radiative) decay rates are the same for each emitter. The experimentally measured intensity $I(t)$ (i.e. the number of photons emitted

per unit time) is proportional[8] to the population of excited emitters $n(t)$ per excitation cycle and the radiative rate k_r:

$$I(t) = k_r U n(t) \quad (1)$$

where U stands for the number of excitation cycles.

The first order concentration kinetics expresses the probability density of a recombination of an excited state residue at time t and is proportional to the population of excited centers:

$$P = -\frac{dn(t)}{dt} = kn(t) \rightarrow \frac{n(t)}{n(0)} = e^{-kt} \quad (2)$$

After substituting Eq. (2) into Eq. (1) we obtain mono-exponential intensity decay:

$$I(t) = Un(0)k_r e^{-kt} = I(0)e^{-kt} \quad (3)$$

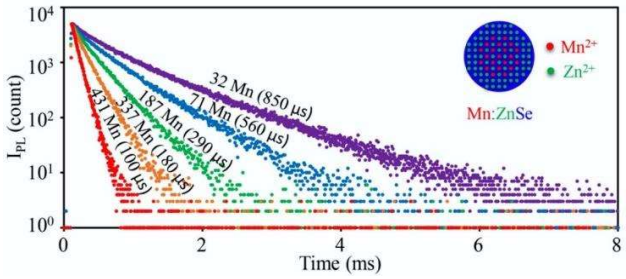

FIG. 2. Nearly mono-exponential PL decay curves of Mn:ZnSe d-dots with different amounts of Mn^{2+} ions. Reproduced with permission from Pu *et al.*, ACS Cent. Sci. **2**, 32 (2016). Copyright © American Chemical Society, 2015.

In fact, the necessary and sufficient condition for a decay to be mono-exponential is *ensemble homogeneity for both radiative and total decay rates*. This condition necessarily means also the homogeneity of non-radiative rates, which is in reality hardly possible as inhomogeneously distributed defect states or energy transfer channels between emitters are likely to take place. Therefore, once we register mono-exponential decay we could state that nearly all emitting centers recombine only radiatively, it means with 100% internal quantum efficiency (IQE). A manifestation of this principle has been reported for, e.g. ensembles of colloidal QDs (see Fig. 2), where both low size-dispersion and high IQE can be achieved by controlling synthesis parameters[9].

In most practical systems, however, post-synthesis purification by physical size-separation or mathematical deconvolution is necessary to reveal uniform fractions. Indeed, mono-exponential decays of colloidal silicon nanocrystals (Si NCs) with perfect passivation by organic ligands were extracted from experimentally measured decay kinetics by deconvoluting the effect of homogeneous broadening[10]. Later, Greben *et al.*[11] reported on size-selected mono-exponential decays of dodecene-passivated Si NCs emitting near 1.5 eV.

2.1.2. Isolated individual emitters

Suppose we have a single emitter which has (at low excitation in the absence of external fluctuations) M radiative and L total decay channels. The average number of excitons in the emitter is the number $0 < \rho \leq 1$ per excitation cycle with low power (below saturation). Keeping into account the number of repetitions (excitation cycles) U, the total number of excitons during the experiment is $p = U\rho$. Then individual probability densities defined by Eq. (1) through every channel represents a system of L differential equations:

$$P_1 = \frac{dp_1(t)}{dt} = -k^1 p(t)$$
$$\ldots \quad (4)$$
$$P_L = \frac{dp_L(t)}{dt} = -k^L p(t)$$

where $dp_i(t)/dt$ represents the population decrease through a particular channel.

Following Eq. (1)–(3) we calculate the total probability density of an exciton recombination at time t and eventually get the kinetic equation for the population $p(t)$ of excited states (excitons) in the emitter that looks the same as in Eq. (2):

$$P_\Sigma = \sum_0^L P_i = \sum_0^L \frac{dp_i(t)}{dt} = -p(t)\sum_0^L k^i$$
$$\Downarrow \qquad (5)$$
$$\frac{dp(t)}{dt} = -kp(t)$$

where the total recombination rate is given by $k = \sum_0^L k^i$. Important to note that here $p(t)$ means the total number of excitons during all excitation cycles in the emitter unlike in Eq. (2) where $n(t)$ stands for the population of excited emitters per excitation cycle.

In its turn, the PL intensity decay could be calculated by combining Eq. (2), (3) and (5):

$$I(t) = p(t)\sum_0^M k_r^j = k_r p(t) = I(0)e^{-kt} \qquad (6)$$

where the radiative rate is found as $k_r = \sum_0^M k_r^j$ by analogy with total decay rate.

Therefore, generally the PL decay of a single emitter is mono-exponential[12] if all decay channels are accessible for the recombination of excited carriers at any time and the decay rate is simply the sum over all partial ones (see Fig. 3). The experimental confirmation of this phenomena is well presented in literature.[13]

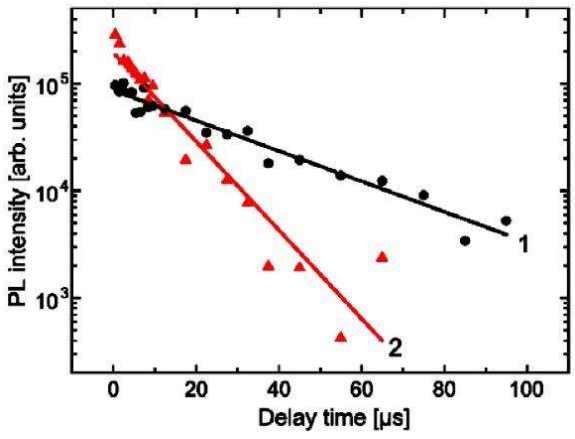

FIG. 3. PL decays and mono-exponential fits for two different Si NCs. Reproduced with permission from Sangghaleh *et al.*, Nanotechnology **24**, 225204 (2013). Copyright © IOP Publishing Ltd. 2013.

A notable exception is the "delayed luminescence",[14,15] where carriers can get trapped in the matrix resulting in multi-exponential (ME) decays even for a single nanocrystal. There is only one decay channel *per se* in such systems, but trapping/detrapping process leads to measurable distribution of radiative lifetimes. Power-law kinetics of trapping/de-trapping process may also lead to power-law decays,[14,15] which represent a particular case and not covered in this review.

2.2 Ensemble of emitters – multiexponential decays

Unlike colloidal QDs, Si NCs in SiO_2 matrix always have a distribution of non-radiative rates that is caused by different NC shapes, interface chemical bonds and defects (e.g. dangling bonds) strain and tension, traps in oxide matrix, etc.

As shown above, we can assign constant radiative k_r^i and total k^i rates to every *i*-th single emitter. The first-order population kinetics for each emitter in an ensemble of T emitters with uniform size (emitting at the same energy) at low excitation is given by

$$\frac{dn_1(t)}{dt} = -k^1 n_1(t)$$
$$\ldots \qquad (7)$$
$$\frac{dn_T(t)}{dt} = -k^T n_T(t)$$

where $n(t)$ stands the population of excited emitters per excitation cycle as in Sec. 2.1.1.

Then we obtain the most general form of time dependence of the total population of excited states $n(t)$ in an ensemble:

$$\frac{dn(t)}{dt} = -\sum_0^T k^i n_i(t) = -k(t)n(t) \qquad (8)$$

The difference with the previous case [see Eq. (5)] is that here the decay channels are considered as parallel and independent, while in Eq. (5) a simultaneous access to them of an exciton is postulated, resulting in a time-

independent total rate k. In its turn the proportionality between PL intensity and concentration of excited carriers during U excitation cycles is presented as the following expression:

$$I(t) = U\sum_{i=0}^{T} k_r^i n_i(0) e^{-k^i t} = \sum_{i=0}^{T} A_i e^{-k^i t} \qquad (9)$$

We considered the most general case of an ensemble of emitters where both $k_r(t)$ and $k(t)$ depend on time as a result of contributing fraction re-distribution with time and PL decay shape is not mono-exponential anymore. This leads to the conclusion that the distribution of rates in an ensemble of emitters results in time variation of the ensemble decay rate. It is often implied that the radiative rate k_r is practically the same for all emitting centers that emit at the same wavelength, i.e. $k_r = \text{const}$ in Eq. (9) and the dispersion of decay rates is solely caused by non-radiative rates. For further discussion see Sec. 5.1.

2.3 Decay rate distributions

2.3.1. General overview

In the above mentioned Eq. (9) T stands for the number of QDs within the excited volume in an ensemble that is usually a very large number. Therefore, instead of considering each QD individually it is more convenient to work with the entire ensemble that generally has either discrete or continuous distribution of rates $H(k)$. For the latter case, in Eq. (9) partial discrete components A_i under the sum should be replaced by continuous distribution function of rate constants $H(k)$ (more precisely, it is probability density function – PDF):

$$I(t,k) = H(k) e^{-kt} \qquad (10)$$

Once we know the distribution $H(k)$, we can restore PL decay $I(t)$ thorough the Laplace transform of $H(k)$:

$$I(t) = \int_0^\infty H(k) e^{-kt} dk \qquad (11)$$

This is the most general representation of PL intensity of any PL deexcitation model. If $H(k)$ stands for PDF of decay rate distribution, then the correct normalization must be done $I(0) = 1$. A great number of QDs in an ensemble does not imply that such a number of exponents should be used to provide good quality fit of $I(t)$. For instance, if an ensemble of QDs have a limited number of well separated decay rates k^i, $H(k)$ has a discrete form of a sum of N delta functions:

$$H(k) = \sum_{i=0}^{N} a_i \delta(k - k_i) \qquad (12)$$

where, N means the number of partial components k^i.

The PL signal with PDF given by Eq. (12) is obtained by employing Eq. (11) and is represented by a reduced number of sums N ($N < T$) in contrast to Eq. (9):

$$I(t) = \sum_{i=0}^{N} a_i e^{-k^i t} \qquad (13)$$

To solve an inverse problem, i.e. to recover the distribution $H(k)$ from experimentally measured signal $I(t)$ is hardly possible because, mathematically speaking, it's ill-conditioned problem[16] and, physically speaking, the unique information is lost in convolution. It is shown schematically in Fig. 4, where a real distribution of individual decay lifetimes results in a measured decay, deviating from a mono-exponential. The decay can be fitted, e.g., by a stretched-exponential function (see Sec. 2.3.3) with only two independent parameters (τ, β). This situation is similar to color coordinates (x, y) used to describe any emission spectra with relation to human eye sensitivity on a color space diagram (3rd coordinate z is redundant because of normalization $x + y + z = 1$). A complex spectrum is simplified by only two numbers and the inverse problem of restoring the spectrum from (x, y) has naturally multiple solutions. Unlike colour

coordinates, however, which are typically obtained from the measured emission spectrum, in case of decay measurements (τ, β) are often the only available experimental parameters. In this case the initial information on $H(k)$ can hardly be unambiguously restored, similar to the impossible backward reconstruction of a spectrum from x and y colour coordinates. In addition, small (experimental) imperfections (noise, truncation etc.) of $I(t)$ data could lead to large errors in extracted $H(k)$.

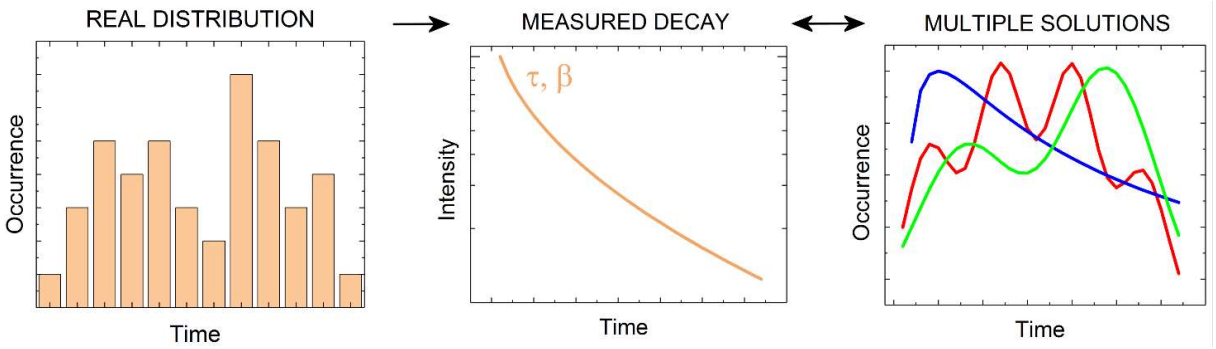

FIG. 4. A schematic representation of a distribution of mono-exponential decays convolutes to a measured decay, which can be fitted with a stretched-exponential function with parameters τ and β. There are multiple distributions, which can yield a decay with such parameters, making it difficult to restore the original distribution from the decay curve.

Anyway, one can attempt to recover $H(k)$ from a decay signal $I(t)$ ainly by three approaches:[16]

1) Data analysis by procedures that attempt to estimate $H(k)$ without an assumption of the rate distribution. The most straight forward and possibly most powerful approach is to take $H(k)$ in the form of Eq. (12) and attempt to make a fit of $I(t)$ with a combination of mono-exponents given by Eq. (13). Almost any decay kinetics irrespectively of how complex it is could be fitted with this model. However, one must be very careful when increasing the number of fitting exponents above three. We cannot consider such fits as an evidence of the presence of three or more luminescence processes until we really know that they take place and are widely separated in decay rates. Therefore, multiple rate values obtained from such an analysis have usually no physical relevance as generally a three-exponential model can adequately describe nearly any data with a continuous distribution of rates. If we desire to restore the shape of continuous distribution of rates $H(k)$, the use of maximum entropy method (MEM)[17] or other numerical techniques[18,19] could be helpful. In the MEM formalism the general idea is that the found distribution $H(k)$ must maximize the entropy:

$$Entropy = -\int_0^\infty H(k)\ln H(k)dk \qquad (14)$$

However, in those above mentioned procedures the obtained $H(k)$ values suffers from the problem of extreme sensitivity to data quality because of the ill-conditioned nature of the above mentioned inverse problem.

2) Data analysis where $H(k)$ is determined by theoretical model from a photoexcitation dynamics scheme, where additional intrinsic parameters of the system are known.[16] Then model parameters could be adjusted by iterative fitting of PL decays. This approach is the most physically relevant, but on the other hand it seems to be the most time consuming and complicated, requiring substantial *a priori* knowledge.

3) The task becomes easier if it is possible to

approximate $H(k)$ by an analytical function that describes the distribution of rates. For example, lognormal (LN) distribution of decay rates was used to fit PL kinetics of Si NCs, where structural characterization reveals LN nanoparticle size distribution, as described below.

2.3.2. Lognormal distribution of decay rates

The LN distribution of rates is the distribution of $k > 0$ whose logarithm x ($k = e^x$) is normally distributed:[20]

$$g(x) \sim \frac{1}{\sqrt{2\pi}\sigma} \exp\left(-\frac{(x - x_0)^2}{2\sigma^2} \right) \qquad (15)$$

with mean value x_0 and variance σ^2.

The distribution of rate k follows the LN distribution:

$$H(k) \sim \frac{1}{k\sqrt{2\pi}\sigma} \exp\left(-\frac{(\ln k - \mu)^2}{2\sigma^2} \right) \qquad (16)$$

It can be shown[4] that

$$\mu = \ln k_{mf}\,;\ \sigma = \frac{1}{\sqrt{2}} \sinh^{-1} \Delta k / 2k_{mf} \qquad (17)$$

where k_{mf} is the most frequent decay rate and Δk is related to the width of the distribution.

The LN distribution, like the normal distribution, is a two-parameter distribution where the parameters μ, σ^2, however, are not identical with the mean value $\langle k \rangle$ and the variance $\mathrm{Var}(k)$, but the former is given by:[20,21]

$$\begin{aligned} \langle k \rangle &= \int_0^\infty kH(k)dk = \\ &= \frac{1}{\sqrt{2\pi}\sigma} \int_0^\infty \exp\left(-\frac{(\ln k - \mu)^2}{2\sigma^2} \right) dk = \\ &= \exp\left(\mu + \frac{\sigma^2}{2} \right) = \\ &= k_{mf} \exp\left(\frac{1}{4} (\sinh^{-1} \Delta k / 2k_{mf})^2 \right) \end{aligned} \qquad (18)$$

The strict proof of Eq. (18) is quite complex and is brilliantly illustrated by Norstad.[21] The PL intensity can be restored by combining Eq. (11) and Eq. (16).

Physically, such distribution may arise from, e.g. LN distribution of particle sizes in the ensemble, which is indeed commonly observed in practice.[22] Starting from a LN size-distribution:

$$\frac{dN}{dL} \sim \frac{1}{L} \cdot \exp\left(-\frac{\ln(L / L_0)^2}{2\sigma^2} \right) \qquad (19)$$

where L stands for the size of a particle and using a general expression for quantum confinement energy $E_c = A/L^x$ one can express energy distribution of particles as

$$\frac{dN}{dE_c} \sim \frac{1}{E_c} \cdot \exp\left(-\frac{\left(\frac{1}{x} \ln E_c + \ln L_0 - \frac{1}{x} \ln A \right)^2}{2\sigma^2} \right) \qquad (20)$$

From that using a semi-empirical dependence[10] of the recombination rate on confinement energy $k = k_0 + \chi E_c^p$, the distribution of rates becomes another LN distribution:

$$\frac{dN}{dk} \sim \frac{1}{k - k_0} \cdot \exp\left(-\left(\begin{array}{l} \frac{1}{px} \ln(k - k_0) + \\ + \ln L_0 - \frac{1}{x} \ln A - \\ - \frac{1}{px} \ln \chi \end{array} \right)^2 \Big/ 2\sigma^2 \right) \qquad (21)$$

Therefore, the practical use of LN unlike the Levy stable distribution of rates (see Sec. 2.3.3) for decay curve fitting is substantiated for ensembles with LN size distribution of particles. Recently, Nguyen *et al.*[23] applied the LN distribution of rates for analysis of changes of SiNC kinetics in detection of nitroaromatics (see Fig. 5).

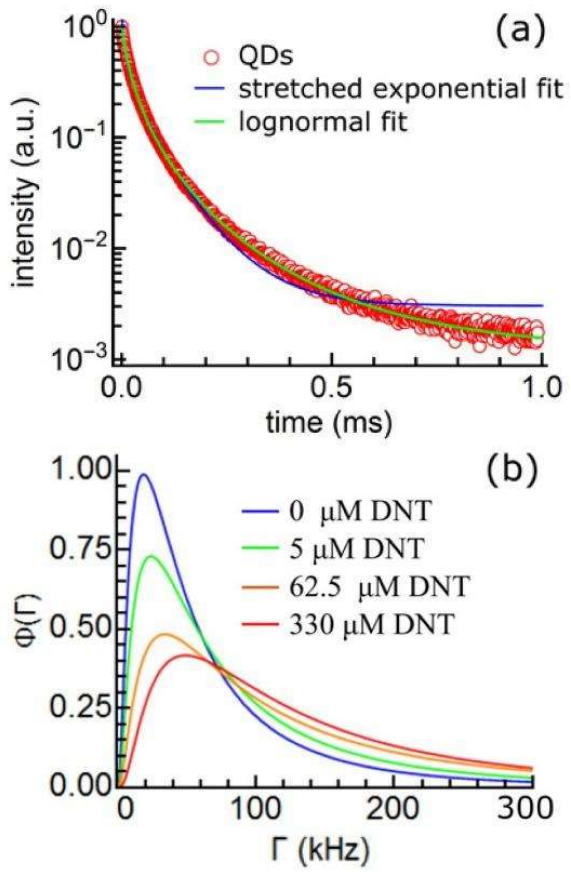

FIG. 5. (a) Comparison of SE and LN fits (blue and green lines, respectively) of PL decay in Si NCs functionalized by monomer dodecyl. (b) LN lifetime distributions obtained for Si NC samples under different concentration of dinitrotoluene (DNT). Reproduced with permission from Nguyen *et al.*, Nanotechnology **27**, 105501 (2016). Copyright © IOP Publishing Ltd. 2013.

2.3.3. Kohlrausch (William-Watts) decay law

Let us consider the case when population relaxation kinetics expressed with Eq. (2) deviates from classical mono-exponential via a perturbation parameter β ($0<\beta\le 1$):

$$\frac{n(t)}{n(0)}=e^{-k_0 t} \rightarrow \frac{n(t)}{n(0)}=e^{-(k_0 t)^{\beta}} \qquad (22)$$

The stretch factor β expresses the degree of kinetics deviation from the mono-exponential law and in its limit $\beta=1$ we obtain Eq. (2) (this parameter is often called dispersion factor, as it shows the dispersion degree in a distribution). The SE function was proposed in the middle of 19th century by Rudolf Kohlausch[24] and is often named after him. It was also used in the analysis of dielectric relaxation by Williams and Watts,[25] and therefore sometimes referred to as Kohlausch-Williams-Watt kinetics. The alternative name "slower-than-exponential" is, in fact, misleading because the most characteristic property of the function is the existence of two regimes[3]: the faster-than-exponential behavior within the time range $0<t<1/k_0$, and the slower-than-exponential regime for times $1/k_0<t<\infty$ [see Fig. 6(a)].

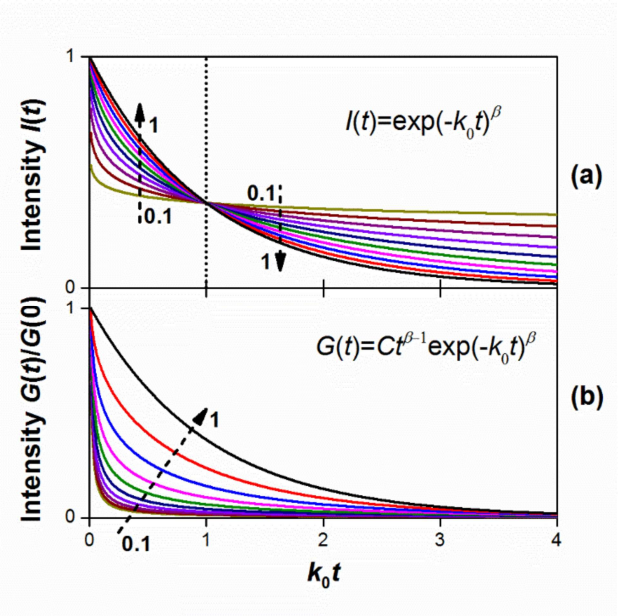

FIG. 6. The stretched exponential function (a) given by Eq. (23) and its derivative (b) given by Eq. (24) for a set of values of β parameter [0.1, 0.2, …, 0.9, 1].

In general case we cannot derive the intensity relation from Eq. (22) because the radiative rate can be a function of time. In assumption of $k_r=\text{const}$ (e.g., monodispersed particles, where non-exponential decay arises from the distribution of non-radiative rates) we derive the intensity of SE decay from Eq. (22):

$$I(t)=Uk_r n(t)=Uk_r n(0)e^{-(k_0 t)^{\beta}}=I(0)e^{-(k_0 t)^{\beta}} \qquad (23)$$

This formula [see Fig. 6(a)] is often used in

describing SE distributions in a variety of fields[26,27] and it is the most widely used one for fitting of decay kinetics of Si NCs.[11,28] Similar to Gaussian fits in spectroscopy it allows quick evaluation of the degree of decay rate dispersion through the value of parameter β. Strictly speaking, β cannot be considered as a measure of neither the statistical width nor the full width at half maximum (FWHM) of the rate distribution.[29] Thus, the FWHM is increasing (decreasing) as β decreases above (below) 0.65. Alternatively, β can be related to the *logarithmic* FWHM of rate distribution. As for an ensemble of Si NCs β is usually above 0.65, it can be accepted that the ensemble approaches monodisperse rate as β is getting closer to 1.

The excited carriers could recombine either radiatively or non-radiatively and the total intensity decay is a sum of these two parts [calculated from Eq. (1), (8) and (22)]:

$$\begin{aligned} G(t) &= k(t)Un(t) = I(t) + k_{nr}(t)Un(t) = \\ &= -U\frac{dn(t)}{dt} = Un(0)\beta k_0{}^{\beta} t^{\beta-1} e^{-(k_0 t)^{\beta}} = \\ &= Ct^{\beta-1} e^{-(k_0 t)^{\beta}} \end{aligned} \qquad (24)$$

Then the experimentally assessed PL signal could be expressed [equivalent to Eq. (23)]:

$$I(t) = Ct^{\beta-1} e^{-(k_0 t)^{\beta}} - k_{nr}(t)Un(t) \qquad (25)$$

Surprisingly in many reports PL decay kinetics is modelled with total intensity decay function [see Fig. 6(b)] presented by Eq. (24) and is called as SE function. We note that, while the Eq. (24) could be axiomatically postulated to describe $I(t)$, it does not represent a SE decay kinetics but rather the first derivative of SE dependence and corresponds to PDF of a random variable from the Weibull distribution.[20] The true Kohlrausch model is presented by Eq. (22) or Eq. (23) and is related to Levy stable distribution.[30] The fact that we had to assume monodisperse ensemble decay rate does not exclude that Eq. (23) could be valid even in the case of distribution of radiative rates. However, in that case Eq. (23) is not derived from Eq. (22) and should be postulated by introducing the perturbation factor β directly to the exponential intensity decay given by Eq. (3). In any case one should consider using a SE function as a way to quantify rate dispersion and average, and the use of Eq. (23) is encouraged here just for better comparison with bulk of the literature that will be explained below.

To illustrate the futility of treating these distributions as strictly correct mathematically,[31] consider the Laplace transform [see Eq. (11)] of a SE distribution ($0 < \beta < 1$):

$$e^{-(k_0 t)^{\beta}} = \int_0^{\infty} e^{-uk_0 t} H_{\beta}(u)\mathrm{du} \qquad (26)$$

where $u = k_s/k_0 = \tau_0/\tau_s$ is the dimensionless recombination rate of a single emitter with decay rate k_s, and $H_{\beta}(u)$ is their PDF, i.e. the normalized fraction of nanocrystals dn with recombination rates in the interval (u; u+du):

$$H_{\beta}(u) = \frac{\mathrm{d}}{\mathrm{du}}\mathrm{n}(u), \int_0^{\infty} H_{\beta}(u)\mathrm{du} = 1 \qquad (27)$$

It was recently shown that for a given k_0 and β a unique solution exists and the PDF of rate distributions $H_{\beta}(u)$ (so called Levy stable distributions) can be conveniently expressed through special functions,[30] which can be relatively easily implemented using commercial mathematical software packages. In other words, by strictly assigning SE function to a measured decay curve one necessarily implies a particular distribution of individual rates in the ensemble. Such approach is plain wrong, since the rate distribution is governed by underlying physical properties in the studied system and, in fact, many physical distributions can form a similar to measured non-monoexponential decay curve (see Fig. 4).

Furthermore, particular properties of the Levy distribution, namely its slowly decaying tail, lead to diverging distributions of relevant PDFs in time domain, which has clearly no physical meaning. Indeed, for the dimensionless lifetime

of a single emitter $\xi = 1/u = \tau_s/\tau_0$ one can introduce the PDF in analogy with Eq. (27):

$$f_\beta(\xi) = \frac{\mathrm{d}}{\mathrm{d}\xi}\mathrm{n}(\xi),\ \int_0^\infty f_\beta(\xi)\mathrm{d}\xi = 1 \qquad (28)$$

Since the probability in a differential area must be invariant under change of variables these two are related in the following way:

$$f_\beta(\xi) = \left|\frac{\mathrm{du}}{\mathrm{d}\xi}\right| H_\beta(u) = u^2 \cdot H_\beta(u) \qquad (29)$$

The solutions $H_\beta(u)$ in the limit of $u \to \infty$ were shown to possess "heavy-tailed" asymptotic:[29,30]

$$H_\beta(u) \to B_\beta / u^{(1+\beta)} \qquad (30)$$

where for $u \to \infty$ and $0 < \beta < 1$, $B_\beta \approx \sin(\pi\beta)/\pi$. For $f_\beta(\xi)$ this is equivalent to the asymptotic:

$$f_\beta(\xi) \to B_\beta / \xi^{1-\beta} \qquad (31)$$

which is a diverging function for $\xi \to 0$ and hence cannot satisfy the normalization condition given by Eq. (28).

Let us consider a practical example. We have measured lifetimes of 38 individual Si NCs with single exponential decays.[13] Obtained recombination rate and lifetime distributions are shown in Fig. 7, left and right. Then we summed all individual decay curves and obtained a SE function, corresponding to the ensemble decay of these NCs (Fig. 7, inset). The fitting of this SE yielded values of $\beta = 0.8$ and $\tau_0 = 10\,\mu\mathrm{s}$. Then we constructed function $H_{0.8}(u)$ from [30] and calculated $f_{0.8}(\xi)$ by Eq. (31). These functions are shown as solid lines in Fig. 7, left and right. One can see that while the function $\mathrm{g}_{0.8}(u)$ nicely envelopes experimental distribution, the function $f_{0.8}(\xi)$ shows clear deviation for short lifetimes and eventually diverges for $\xi \to 0$. For comparison we also show fit to the recombination rate distribution based on the LN function $G(u) \sim \exp\left(-(\ln u - \mu)^2/2\sigma^2\right)/u$ (dotted lines). This function has a much faster decaying asymptotic for $u \to \infty$ (Fig. 7, left) resulting in a proper converging function $g(\xi)$ when expressed via lifetimes (Fig. 7, right).

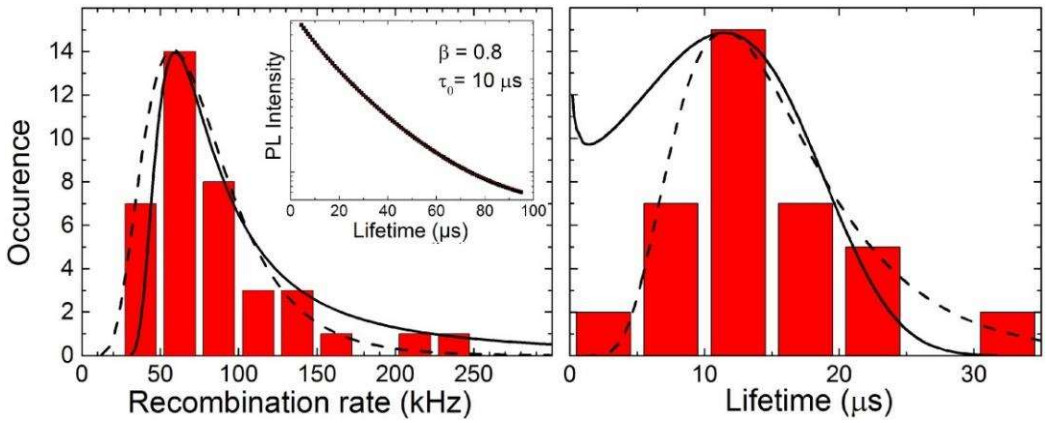

FIG. 7. Histograms of the measured recombination rate (left) and lifetime (right) for 38 single Si NCs. Inset is a sum of all individual decays, fitted with a SE function with β and τ_0 shown. Solid lines are the functions $H_{0.8}(uk_0)$ from [30] and $f_{0.8}(u\tau_0)$ from Eq. (29). Dotted lines are the lognormal distributions $G(uk_0)$ and $g(\xi k_0)$. Original individual decay data are from [13].

Mathematically speaking, the property described above is closely related to well-known characteristics of Levy distribution, namely diverging moments, including the first one (i.e., the average), of its PDF $H_\beta(u)$. These singularities are usually dealt with by introducing an *arbitrary* truncation to the distribution "fat" tail. Then the value of the moments obviously becomes a function of the chosen cutoff position, as was explicitly shown in [29]. In contrast, the first moment of PDF $f_\beta(\xi)$ is finite for $0<\beta\le 1$ that will be revealed in Sec. 3.1 and Sec. 3.2.2.

So we have shown that a decay curve cannot be, strictly speaking, a stretched-exponential. Nevertheless, this function, as its normal distribution counterpart in spectroscopy, can be very useful in assessing distribution average and dispersion, where appropriate numerical methods are discussed below.

2.4 The comparison of different decay models

The high-quality fit over several decades with a chosen decay model does not exclude other possible decay models[11] and thus, the real kinetic model cannot be unambiguously obtained from a decay curve fit (see Fig. 4). Moreover, once a decay model provides an adequate quality fit, a ME fit by Eq. (8) with 2, 3 or more components is also possible. Then the question arises which one of possible fit models to choose. If a decay is non-exponential, it is always worth to try fitting with more than one exponential. We have to stop adding exponential components, when the next added exponent does not change the residuals or the targeting result (average decay lifetime, for instance). The number of fitting components could give us an idea on how much the fitted curve is non-exponential. In multi-mode case ($N\ge 3$) this method indicates on strong non-exponential nature of the curve while it often suffers from the above mentioned (see Sec. 2.3.1) problems of physical relevance and the correlation of fitting parameters. On the other side, the possibility to fit a curve by only two components ($N=2$) does not necessarily mean that those components have any physical significance as it was illustrated in papers.[10,11] It is possible to compare two decay models by analysing the goodness-of-fit and selecting the model that provides the best fit residuals as well as reduced chi-squared values χ^2_R (see [32]). Moreover, the precision of results strongly depends on the number of fitting parameters and the model with lower number of adjustable parameters is highly preferable. Thus, in terms of average lifetime extraction, for instance, both SE and LN decay models (four free parameters) are preferable over already 2 ME model (five fitting parameters). Ideally, to reduce the number of free parameters, a sample with narrower size dispersion (then less exponents is needed to fit) or additional *a priori* knowledge of the whole studied system is desirable.

It is often important to evaluate the average and dispersion of a rate-distribution in order to quantitatively monitor changes in the studied system in response to external effects, such as temperature, chemical environment, excitation power, etc. Though ME model with many components ($N\ge 3$) can be very helpful for average lifetime extraction if none of other models is valid, the information on how broad is the distribution of lifetimes is missing. In contrast, the LN model directly retrieve the PDF $H(k)$ [see Eq. (16)] as well as the width of rate distribution Δk [see Eq. (17)], but needs additional justification to be applied. In comparison, the task of SE $H(k)$ recovery is void of physical meaning. At the same time it is relatively easy to extract the dispersion parameter β that normally anti-correlates with the distribution width of lifetimes (rates). The last is related to the homogeneity of an ensemble. In regards to Si NCs it could indicate both the dispersion of defect states as well as the interaction between NCs (it is of extreme difficulty to distinguish between these two effects).

3. AVERAGE DECAY RATE (LIFETIME)

3.1 General overview

One of the most important information that one could extract from TR PL decay is the average value of decay parameters. Up to now, we were operating mostly with the concept of rates. However, in TR PL spectroscopy the lifetime concept is widely used as the PL decay is measured over time scale. While using decay rates is very convenient to describe PL kinetics, we find reasonable to express lifetimes in terms of average decay parameters. Hereafter we will switch to consideration of lifetimes.

The Laplace transform of $I(t)$ could be expressed by considering the distribution of lifetime constants with PDF $f(\tau)$ ($\int_0^\infty f(\tau)d\tau = 1$) following similar logic as Eq. (11):

$$I(t) = I(0)\int_0^\infty f(\tau)\,\mathrm{e}^{-\frac{t}{\tau}}\,d\tau \qquad (32)$$

Unlike in Sec. 2.3, where the intensity was implied to normalized, here $I(t)$ is intentionally taken as non-normalized to underline that the normalization of the decay curve is not necessarily for the average lifetime calculation.

Then we could define the *average lifetime constant* over the distribution of $f(\tau)$ as a first moment of PDF $f(\tau)$:

$$\begin{aligned}\langle\tau\rangle &= \int_0^\infty \tau f(\tau)d\tau = \int_0^\infty f(\tau)(\int_0^\infty e^{-\frac{t}{\tau}}dt)d\tau = \\ &= \int_0^\infty\int_0^\infty f(\tau)e^{-\frac{t}{\tau}}d\tau dt = \int_0^\infty \frac{I(t)}{I(0)}dt\end{aligned} \qquad (33)$$

As we did before in Eq. (12), after assuming the distribution of time constants $f(\tau)$ as the sum of delta functions:

$$f(\tau) = \sum_{i=0}^{N} A_i\delta(\tau-\tau_i) \qquad (34)$$

we come to simple combination of mono-exponentials in Eq. (32):

$$I(t) = \sum_{i=0}^{N} A_i e^{-(\frac{t}{\tau_i})} \qquad (35)$$

Finally, the average lifetime constant corresponding to the condition in Eq. (34) could be calculated by substituting Eq. (35) into Eq. (33):

$$\langle\tau\rangle = \int_0^\infty \frac{I(t)}{I(0)}dt = \frac{\sum_{i=0}^{N} A_i\tau_i}{\sum_{i=0}^{N} A_i} = \sum_{i=0}^{N} a_i\tau_i \qquad (36)$$

where a_i are normalized amplitudes.

Equation (33) corresponds to continuous and Eq. (35) to discrete distribution of lifetime constants. As $f(\tau)$ and a_i represent amplitudes of lifetime components, in photochemistry and photobiology literature the above mentioned lifetime $\langle\tau\rangle$ is often called amplitude-weighted[17] or *amplitude averaged*[33,34] lifetime. In some papers[3] it is named "average lifetime constant" that reveals physical meaning of $\langle\tau\rangle$: the mean lifetime value in the distribution of lifetime constants $f(\tau)$. There is a number of occasions (primarily in biochemistry) when the average lifetime constant $\langle\tau\rangle$ could be useful. For instance, to diagnose and calculate efficiency of donor-acceptor energy transfer[17] or protein denaturation.[33] However, $\langle\tau\rangle$ does not represent average decay lifetime in which we are essentially interested in when analysing TR PL decay of an ensemble of QDs. To calculate the average decay lifetime we have to use the statistical formula[8] that presents the mean value (expected value or mathematical expectation) of a random variable:

$$\bar{\tau} = \frac{\int_0^\infty tI(t)dt}{\int_0^\infty I(t)dt} \qquad (37)$$

In biochemical literature this decay lifetime is often called as *intensity average lifetime*.[33,34] The

physical meaning of $\bar{\tau}$ is the average time during which the emitters (PL centers) remain in the excited state after the end of an excitation pulse. There are numerous incorrect applications of these values in literature and that is why understanding the difference between $\langle\tau\rangle$ and $\bar{\tau}$ is of great importance to provide correct TR PL analysis.

3.2 Examples of average lifetime calculations

In this section we would like to introduce the calculations of average decay lifetimes $\bar{\tau}$ for some common cases of PL decays that could be essentially useful for TR PL analysis of Si NCs. Ultimately, the average decay lifetime can be extracted from high-quality decay data using Eq. (37) in the absence of any decay model at all. However, a decay curve must have high signal-to-noise ratio as well as to be long enough with known background.[35] Otherwise, a decay fit must be tested for an average lifetime extraction. Consequently, all selected models that provide high-quality fit of a decay curve should give roughly the same values of $\bar{\tau}$.[11,36]

3.2.1. Combination of mono-exponential kinetics

In the most general case the intensity kinetics could be fitted as a sum of mono exponents as presented in Eq. (35), and the average decay lifetime could be quantified as:

$$\bar{\tau}_{ME} = \frac{\int_0^\infty t\sum_{i=0}^{N} A_i e^{-(\frac{t}{\tau_i})}\,dt}{\int_0^\infty \sum_{i=0}^{N} A_i e^{-(\frac{t}{\tau_i})}\,dt} = \frac{\sum_{i=0}^{N} A_i \int_0^\infty te^{-(\frac{t}{\tau_i})}\,dt}{\sum_{i=0}^{N} A_i \int_0^\infty e^{-(\frac{t}{\tau_i})}\,dt} = \frac{\sum_{i=0}^{N} A_i\tau_i^2}{\sum_{i=0}^{N} A_i\tau_i} \tag{38}$$

Beside the problem of physical relevance of ME fits with $N \geq 3$ described in Sec. 2.3.1, there is well-known mathematical problem with resolution of ME decays.[17] In fact, fitting parameters A_i and τ_i could be correlated that means they compensate each other to give the same $I(t)$ curve. To extract precise values of fitting parameters more complex methods like, for instance, global analysis with multi-wavelength measurements[37] should be employed.

As an example, below introduced exponents in Eq. (39) and Eq. (40) result in the same decay curve with the difference much lower than the noise level of a detector:[38]

$$I_1(t) = e^{-\frac{t}{200\mu s}} + e^{-\frac{t}{350\mu s}} + e^{-\frac{t}{600\mu s}} \tag{39}$$

$$I_2(t) = e^{-\frac{t}{226\mu s}} + e^{-\frac{t}{546\mu s}} \tag{40}$$

However, one of the most outstanding properties of average decay lifetime is its independence on the correlation of fit parameters. For the above mentioned example we get:

$$\bar{\tau_1} = \bar{\tau_2} = (453 \pm 1)\ \mu s \tag{41}$$

3.2.2. Stretched exponential kinetics

For SE decay kinetics in the form of Eq. (23), the average lifetime could be numerically calculated by Eq. (37):

$$\bar{\tau}_{SE} = \frac{\int_0^\infty te^{-(\frac{t}{\tau_0})^\beta}\,dt}{\int_0^\infty e^{-(\frac{t}{\tau_0})^\beta}\,dt} = \frac{\langle\tau^2\rangle}{\langle\tau^1\rangle} = \frac{\frac{\tau_0^2}{\beta}\Gamma(\frac{2}{\beta})}{\frac{\tau_0}{\beta}\Gamma(\frac{1}{\beta})} = \frac{\Gamma(\frac{2}{\beta})}{\Gamma(\frac{1}{\beta})}\tau_0 \tag{42}$$

where Γ corresponds to gamma-function.

In case of $\beta = 1$ we deal with mono-exponential kinetics with characteristic lifetime τ_0. After this time the SE function drops to the $1/e$ of the initial amplitude:

$$I(t) = I(0)e^{-(\frac{t}{\tau_0})^\beta} \Downarrow I(\tau_0) = \frac{I(0)}{e} \approx 0.37I(0) \tag{43}$$

In many papers dealing with non-exponential

decays authors use the "1/e decay time" as a representative value instead of average lifetime. In other words, the characteristic time for which the initial PL intensity at the end of an excitation pulse $I(t=0)$ drops to the $I(0)/e$. We must note that this lifetime value cannot be considered as even an approximation of average decay lifetime. For example, for SE decay this characteristic lifetime represents τ_0. The relative difference between $\bar{\tau}_{SE}$ and τ_0 as a function of β is plotted in Fig. 8 (blue curve). Clearly $\bar{\tau}_{SE}$ is always longer than τ_0 and in extreme case of mono-exponential decay $\bar{\tau}_{SE}=\tau_0$. For too low $\beta<0.3$ the average lifetime $\bar{\tau}_{SE}$ is infinitely long in comparison with τ_0. One may note that for already beta $\beta=0.7$ the relative difference $\Delta\tau=(\bar{\tau}_{SE}-\tau_0)/\bar{\tau}_{SE}$ is reaching 50%. This indicates that τ_0 is very poor approximation of $\bar{\tau}_{SE}$. Though for decay curves with similar and high beta values τ_0 can still be used as a characteristic lifetime – all lifetimes will be equally shifted by $\Delta\tau$ from $\bar{\tau}_{SE}$. The situation changes, though, when curves with different beta need to be compared.

If one need just a fast estimation of $\bar{\tau}_{SE}$, the procedure described by Higashi and Kastner[39] and recently applied[40,41] to SiNCs can be used. The idea is to find the time position of a maximum value of the function that is a product of variable time and time-dependent intensity:

$$\frac{d}{dt}(tI(t))=0 \;\rightarrow\; \tau_{\max}=\left(\frac{1}{\beta}\right)^{1/\beta}\tau_0 \qquad (44)$$

In case of $\beta=1$ we retrieve the mono-exponential lifetime $\tau_{\max}=\tau_0$. For SE function it follows from Eq. (23) and Eq. (44) that $\tau_{\max}$ is the time at which intensity $I(\tau_{\max})$ is decreased $e^{1/\beta}$ times:

$$I(t)=I(0)e^{-\left(\frac{t}{\tau_0}\right)^{\beta}} \;\rightarrow\; I(\tau_{\max})=\frac{I(0)}{e^{1/\beta}} \qquad (45)$$

where again β defines the deviation from the mono-exponential behaviour (see Sec. 2.3.3).

The interconnection between the average decay lifetime $\bar{\tau}_{SE}$ and approximated lifetime $\tau_{\max}$ could be easily derived from Eq. (42) and Eq. (44):

$$\bar{\tau}_{SE}=\frac{\Gamma\left(\frac{2}{\beta}\right)}{\Gamma\left(\frac{1}{\beta}\right)}\frac{\tau_{\max}}{\left(\frac{1}{\beta}\right)^{1/\beta}} \qquad (46)$$

The relative difference between $\tau_{\max}$ and $\bar{\tau}_{SE}$ is depicted in Fig. 8 (red curve). For high values of β above 0.8 the difference $\Delta\tau$ will not exceed 10%. Moreover, if all curves are fitted with the same value of beta, $\tau_{\max}$ will be just shifted by factor $\Delta\tau$ and qualitatively the lifetime analysis will be the same as by working with $\bar{\tau}_{SE}$.

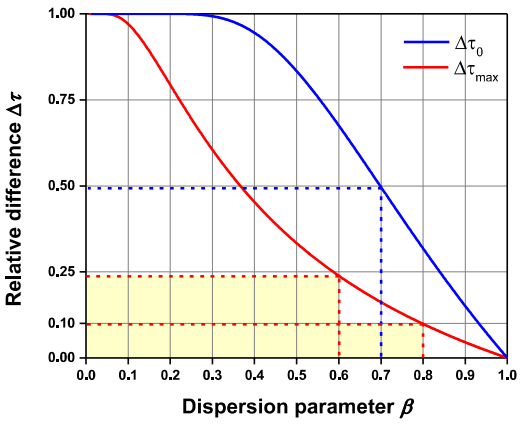

FIG. 8. The relative differences $\Delta\tau=(\bar{\tau}_{SE}-\tau)/\bar{\tau}_{SE}$ between SE lifetime $\bar{\tau}_{SE}$ [calculated from Eq. (42)] and characteristic lifetime $\tau=\tau_0$ (blue line) or approximated lifetime $\tau=\tau_{\max}$ (red line) as functions of dispersion parameter β.

From Fig. 8 one can see that strongly dispersed systems with a low β value are difficult to treat statistically and, hence, to establish clear

causality relations under external stimuli. Characteristic parameters become very much fitting-dependent and changes in already broad, non-symmetric distributions are difficult to trace adequately. A better experiment needs to be designed to probe various processes selectively in such complicated systems.

So, in the general case of different dispersions we recommend using $\tau_{\max}$ or $\bar{\tau}_{SE}$ values, where the main advantage of the former is that it is free of fit and is relatively easy applied.[40,41]

3.2.3. Complex kinetics

The SE decay law often describes Si NCs quite well. However, sometimes there appears a fast or slow decay component[2,41] that obscures the fits made by the SE function. This can be an indication of undesired over-excitation effect, i.e. the situation when the average population of excitons per QD exceeds one (for Si NCs this takes place for excitation power around $1\ \mathrm{W/cm^2}$ in case of blue/violet excitation light). Though even at low excitation powers one might expect such a scenario.[36,] To elucidate the decay perturbation caused by the fast component, a combination of one mono- and one SE decays can be employed and it usually gives quite nice fits:

$$I(t) = A_1 e^{-(\frac{t}{\tau_1})} + A_2 e^{-(\frac{t}{\tau_2})^{\beta}} \tag{47}$$

The average decay lifetime for the PL intensity modelling given by Eq. (47) can be derived from Eq. (37):

$$\bar{\tau} = \frac{A_1\tau_1^2 + A_2\frac{\tau_2^2}{\beta}\Gamma(\frac{2}{\beta})}{A_1\tau_1 + A_2\frac{\tau_2}{\beta}\Gamma(\frac{1}{\beta})} \tag{48}$$

And somitimes even fast component is not mono-exponential, but resembles SE shape.[42] In that case the PL signal is a combination of two SE functions:

$$I(t) = A_1 e^{-(\frac{t}{\tau_1})^{\beta_1}} + A_2 e^{-(\frac{t}{\tau_2})^{\beta_2}} \tag{49}$$

Again employing Eq. (37) one might derive the average decay lifetime for this case:

$$\bar{\tau} = \frac{A_1\frac{\tau_1^2}{\beta_1}\Gamma(\frac{2}{\beta_1}) + A_2\frac{\tau_2^2}{\beta_2}\Gamma(\frac{2}{\beta_2})}{A_1\frac{\tau_1}{\beta_1}\Gamma(\frac{1}{\beta_1}) + A_2\frac{\tau_2}{\beta_2}\Gamma(\frac{1}{\beta_2})} \tag{50}$$

Both forms [Eq. (47) and Eq. (49)] were used in practice for modelling the PL decay signal of Si NCs (see Sec. 3.3.1 and Sec. 5.3 for details). Equation (48) and Eq. (50) presented here can be practically useful for precise analytical calculations of average decay lifetimes. In practice, however, fast and slow components often represent totally different physical processes and there might be an interest to treat their averages separately.

3.3 Practical usage of the average lifetime knowledge

Beside the fact that the average lifetime value gives us the information on the speed of depopulation of excited carriers in an ensemble of PL emitters, it also finds use in various practical applications where some of them are presented below.

3.3.1. Calculation of absorption cross-section

The determination of absorption cross-section (ACS) σ by PL modulation technique that was described in details recently[40,43] is based on utilization of the equation on linear excitation power regime:

$$I_{PL}(t) = \frac{N_T I_{ex}\sigma/\tau_r}{1/\tau_{PL}(I_{ex}) + I_{ex}\sigma} \times \\ \times(1 - e^{-(\frac{1}{1/\tau_{PL}(I_{ex})} + I_{ex}\sigma)t}) = I_{PL}^{cw}(1 - e^{-(t/\tau_{ON}(I_{ex}))}) \tag{51}$$

where N_T is the density of absorbing emitters, I_{ex} is the excitation photon flux; τ_r, $\tau_{ON}(I_{ex})$ and $\tau_{PL}(I_{ex})$ are radiative as well as average PL rise and decay lifetimes, respectively.

From Eq. (51) it follows that ACS can be

directly determined as:

$$\sigma = \frac{1}{I_{ex}}\left(\frac{1}{\tau_{ON}(I_{ex})} - \frac{1}{\tau_{PL}(I_{ex})}\right) \qquad (52)$$

Therefore, the knowledge of average PL rise and PL lifetimes is helpful for calculation of ACS. Moreover, at low excitation powers $I_{ex} \to 0$ the values of $\tau_{ON}(I_{ex})$ and $\tau_{PL}(I_{ex})$ are close to each other [see Eq. (52)] that could serve as an indicator that we do not overexcite our sample (see Fig. 9).

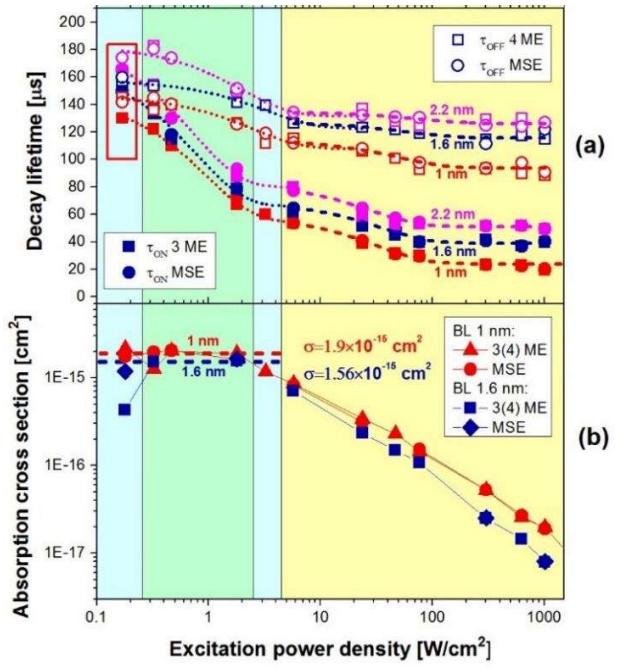

FIG. 9. (a) The onset (filled symbols) and PL (opened symbols) characteristic lifetimes extracted by fitting with either combination of 4 ME (squares) given by Eq. (38) or mono- and stretched (SE) exponentials (circles) given by Eq. (48) and their corresponding exponential fits (dotted and dashed lines). b) Final ACS obtained by Eq. (52) for different samples. Reproduced with permission from Greben *et al*., *Beilstein Journal of Nanotechnology* in print (2017). Copyright © Greben et al.; licensee Beilstein-Institut.

3.3.2. Calculation of internal quantum efficiency

By definition the IQE[11] is given by:

$$\eta_I(\hbar\omega_{em}) = \frac{\tau_{PL}^{vac}(\hbar\omega_{em})}{\tau_r^{vac}(\hbar\omega_{em})} \qquad (53)$$

where $\hbar\omega_{em}$ is photon emission energy, $\tau_r^{vac}(\hbar\omega_{em})$ and $\tau_{PL}^{vac}(\hbar\omega_{em})$ are radiative and total average PL decay lifetimes in vacuum, respectively.

The radiative and non-radiative lifetimes can be decoupled thanks to a variation of Purcell factor[11] F_P by proximity of a reflecting interface in specially prepared samples (see Fig. 10). In such samples the radiative decay lifetime τ_r is varied by changing the local density of optical states (LDOS) while the non-radiative lifetime τ_{nr} is assumed to be unaffected:[44,45]

$$1/\tau_{PL}(\hbar\omega_{em}, d) = \frac{F_P(\hbar\omega_{em}, d)}{\tau_r^{vac}(\hbar\omega_{em}, d)} + 1/\tau_{nr}(\hbar\omega_{em}, d) \qquad (54)$$

where d is the variable distance from Si NC layer to a reflecting surface.

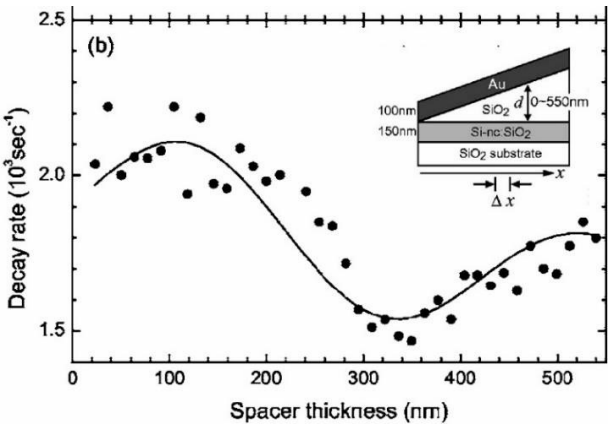

FIG. 10. The variation of PL decay rate ($k = 1/\tau_{PL}$) in dependence on SiO_2 spacer thickness. Insert: schematic representation of the sample structure. Reproduced with permission from Miura *et al*., Phys. Rev. B **73**, 245333 (2006). Copyright © The American Physical Society, 2006.

Therefore, the knowledge of average lifetime τ_{PL} can be also employed for IQE calculation.

4. EXPERIMENTAL ASSESSMENT OF SLOW PL DECAYS

Experimental determination of slow PL kinetics requires special experimental conditions, which is not commonly known and implemented. From one point of view we have to care about quality of acquired TR PL data to ensure subsequent precise mathematical treatment – this is determined mainly by the high signal-to-noise ratio and dynamic range as well as avoided truncation of decay. From the second point of view, we have to consider that some experimental conditions can influence the detected shape of the TR PL decay. These are mainly: the length of excitation pulse and the excitation power density (should be below saturation levels for any of the decay components). Moreover, important signal distortions can be induced by the detection system with limited linearity of response (see Sec. 4.3),[46] low dynamic range, signal-dependent background, etc.[47]

For some slowly decaying systems (like Si NCs) the above given points imply the following requirements for experimental set ups: low excitation power, low pulse repetition rate and long excitation pulses.[35] A pulse truncation could lead to a large ambiguity in background determination (see Sec. 4.2) and, consequently, PL decay lifetime In addition, one has to mind a dependence of lifetime distribution on excitation power (e.g. due to fast non-radiative processes, for example the Auger recombination) and pulse length (see Sec. 4.4). Thus, an optimum experimental conditions must be chosen to fulfil above mentioned requirements, which is often a challenging task.

4.1 Experimental set-up

Recently, TR PL experiments became easily accessible using relatively inexpensive pulsed diode lasers (emitting ns or even sub-ns pulses at > MHz repetition rates) or diode-pumped solid-state lasers (DPSSL) (ns pulses at kHz repetition rate) and photomultipliers (PMT) or avalanche photodiodes (APD) as detectors and suitable electronics for acquiring time-correlated signal counts. But these TR PL systems are not suitable for measurement of slow PL decays, as the short pulses produce PL inefficiently (and distort the rate distribution, see below) and often the repetition rate cannot be reduced down to required kHz or less.

Also the application of wide-spread time-correlated single-photon-counting (TC-SPC) systems is excluded because they detect only the first signal count after each pulse (moreover, the signal must be reduced so that only about 1/10 of pulses gives a count). Even if the repetition rate was reducible to kHz range (which is often not the case) the experiment duration would be extremely long in order to get enough signal counts.

The possible realization of a TR PL set-up dedicated for slow PL decays is the following:

(a) Excitation pulses: Long pulses are conveniently produced by a continuously emitting (cw) diode laser whose beam is modulated using either an acousto-optic modulator (AOM) or a direct modulation by the laser power-supply (PS). The speed of switching on and off is typically 100 ns for AOM (depends on the AOM type and the diameter of the laser beam) while it can be as short as ~1 ns (for the PS-modulation, where the shape of pulse must be thoroughly checked as some unwanted oscillations may appear especially at the leading edge). Mechanical shutters and choppers were also used in past but they produce trapezoidal pulses and limit the studied kinetics to about 0.05 ms and longer – such instruments are sometimes called phosphoroscopes.[48]

(b) Detection system: The laser pulses are send to a sample (possibly focused by a lens or objective and controllably attenuated) and PL is coupled by an optical system to a detection branch. The spectral region for detection is selected either by filters or a spectrometer. The most often applied detectors are PMTs or APDs working in the photon counting mode. The output pulses are treated by electronic devices (can have form of a computer card) called *multi-channel*

scalers where the detected counts are sorted by their delay after the reference pulse and counted in time bins, i.e. many counts can be obtained after each excitation pulse in contrast to TC-SPC (for details see e.g. [49]). Alternatively, the simple direct-detection system can be set-up by connecting an output of a PMT (not in the counting mode) to a digital oscilloscope. The sensitivity is basically lower and attention must be paid to the transient response (related to the input impedance of the oscilloscope). This is applied in many papers to record PL kinetics of Si NCs. In case of detection of slow PL from single NCs the microscopic images within certain delayed time-windows are detected by a CCD with a gated image amplifier (iCCD) (see Fig. 11).

Other possible TR PL techniques, e.g. phase-shift method, box-car integrators or streak-cameras are not used for studies of slow non-exponential decay kinetics.[8]

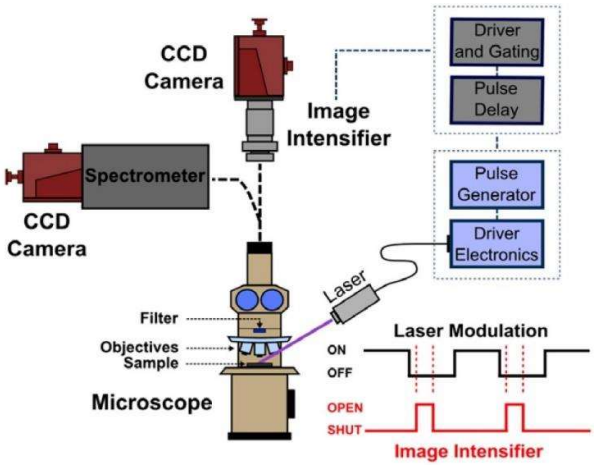

FIG. 11. A schematic image of the micro-spectroscopy set-up with time-resolved detection applied to detect PL kinetics of single Si NCs. The excitation diode laser (405 nm) is modulated via its power supply and PL images are detected by a LN-cooled CCD with a gated image-intensifier. Reproduced from Sangghaleh *et al.*, Nanotechnology **24**, 225204 (2013) with permission.

4.2 The background (offset) subtraction

We did not consider background level in the above-given theoretical introduction implying it to be zero. However, experimentally measured decay curves contain a "constant" signal background that is composed of electronic noise, dark counts, parasitic luminescence and other signals that do not originate from luminescence of a sample under pulsed excitation. If possible, long laser OFF periods should be used to unambiguously determine the background level from the experiment.

There are two[50] basic techniques for the background subtraction: (a) subtract a fixed value or (b) add it as a fitting parameter:

a) The background level could be measured over the entire time window by running experiment with an excitation shutter closed (or using sample-free substrate) for exactly the same number of excitation cycles as are used with the opened shutter (sample measurements). Then the measured background level of the set-up could be used for correction of all measured decay data. This method requires absence of any background connect to the excitation (e.g. stray light in a spectrometer) and perfect detector stability. This is an issue especially for detectors (photomultipliers, avalanche photodiodes) without active temperature control. The background level can be possibly revealed from the signal preceding an excitation pulse (proving that the experimental system triggering and timing allows such mode). This however requires a complete decay of PL, i.e. long enough interval between consecutive pulses (for truncated decay, PL never reach the real background, even shortly before the coming excitation pulse).

b) We can add the background level as an offset parameter when fitting experiment by any expression of $I(t)$ (see Sec. 2.3). The advantage of this approach is that there is no need to care about noise level measurement during the experiment (and save experimental time). For complete (the interval between two excitation pulses should be more than four or five times of the average decay lifetime[51]) and low-noise decay curves the offset parameter in the least-squares fitting procedure could be recovered with high accuracy. The disadvantage is an increase in

number of fitting parameters by one. The intensity simulated in the form of ME decay [Eq. (13) or Eq. (35)] could be particularly sensitive to inclusion of a variable background-level parameter as, firstly, it has more fitting parameters in comparison to LN or SE fit, and, secondly, one of exponentials can become very long in order to compensate the background instead of the offset parameter. Even though it usually indicates overfitting, we practically noticed that, for instance, the SE fit is usually more resistant to background uncertainty compared to ME or LN fitting.

TR PL decay analyses from Si NCs is especially challenging at longer wavelengths (NIR region) where PL lifetimes become very long (several hundreds of μs) and PL is week. In addition, silicon-based photodetector sensitivity drops at those wavelengths. The non-linear response of the detector introduces additional dispersion in the decay curves taken in a broad spectral range. Then the detection time window must approach or exceed 1 ms.

We have to note that the background level is not always constant but may contain a signal-dependent component, which is mostly due to the after-pulsing. This peculiar effect is produced by most of detectors except the so called hybride detectors (electrons from a semiconductor photocathode are accelerated and bombard an APD[52]). After-pulsing occurs on the time scale of a few microseconds,[47] therefore it may not be important for slower decays.

4.3 Detection system response

In general, the temporal and even spectral response of the whole detection system affects the measured TR PL signal. In case when the duration of excitation pulses is comparable to some lifetimes in the rate-distribution, the experimental decay curve must be deconvoluted using the knowledge of the temporal response of the system (sometimes called the *prompt* signal). The prompt signal can be obtained by measuring of PL from sample with decay faster than the system response; alternatively, reflection or scattering of excitation light can be detected.

In decay measurements of the broad emission spectrum the instrument spectral sensitivity may also play a role. For example, a silicon-based photodetector, such as an APD, typically has a falling sensitivity curve towards ~ 1.1 μm (silicon bandgap). Therefore low-energy contributions to the measured full decay will be underrepresented. The general Eq. (11) should be then slightly modified to reflect this fact:

$$I(t) = \int_0^\infty H(k)\phi(k)e^{-kt}dk \qquad (55)$$

where $\varphi(k)$ is a system response curve expressed through decay rates, which can be derived from the known $\varphi(E)$ and a semi-empirical relation between rates and energy, such as the one used above (see Sec. 2.3.2): $k = k_0 + \chi E_c^p$. So the inverse Laplace transform in this case, if ever successful, would yield not the original rate distribution, but rather its convolution with a system response curve.

At the same time for spectrally-resolved decays non-flat system response can be largely ignored, since the detection spectral window is usually very narrow (only a few nanometers), in which the instrument sensitivity can be considered essentially uniform.

4.4 The choice of the excitation pulse length

It is well known that the excitation pulse duration affects the intensity of registered PL signal. But the possibility that it can affect also the observed distribution of lifetimes (and consequently the average lifetime) is counter-intuitive and was mostly ignored. This effect is a consequence of the PL-onset kinetics [see Eq. (54)]. For excitation power well below the saturation level the onset kinetics is close to the PL decay kinetics. (This holds for independent relaxation processes – e.g. in ensembles of non-interacting NCs). Therefore, the longer component needs longer pulse to reach the constant level (cw amplitude) I_{PL}^{cw}. Let us take a ME decay where

τ_{PL}^{short} and τ_{PL}^{long} are the shortest and the longest of *i*-component. Then for pulses with duration between $0.1\tau_{PL}^{short}$ and $3\tau_{PL}^{long}$ (so called intermediate pulses) the relative amplitude of the decay components (and so the average lifetime) will be a function of the pulse length [see Fig. 12(b)].

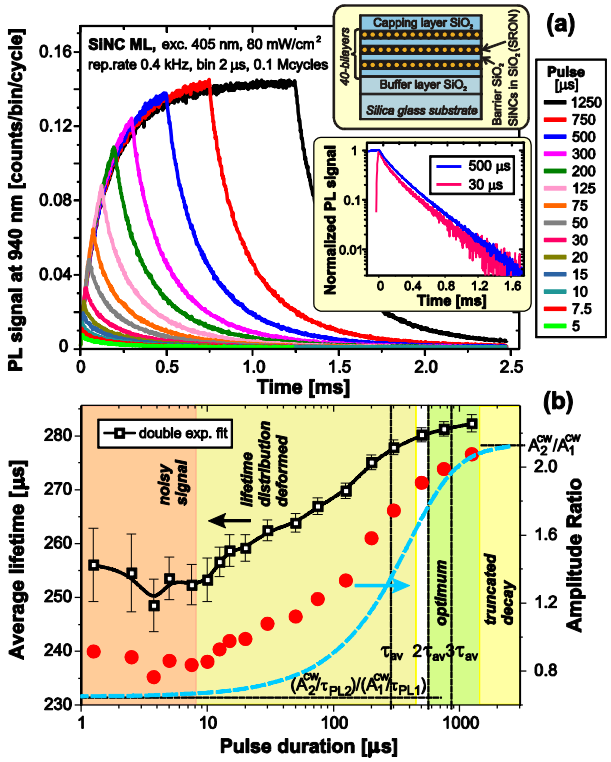

FIG. 12. (a) PL onset and decay curves following the square excitation pulses with variable duty cycle from 50% to 0.2% (rep. rate of 0.4 kHz) for Si NCs (detected at the PL peak 940 nm). The upper inset shows the multilayer sample schematics and the lower one shows normalized and background subtracted PL decays (log intensity scale) for excitation pulses of 0.5 and 0.03 ms revealing the difference of decay signals. (b) The average lifetime (squares) obtained by fitting the PL decay from the upper panel with double-exponential functions. Red circles show ratio of amplitudes of long and slow decay components (310 and 95 µs) and the dashed blue line is a simple model of changing amplitudes ratio due to different onset speeds. Reproduced with permission from Greben *et al*., Rev. Sci. Instrum. **87**, 126101 (2016). Copyright © AIP Publishing LLC, 2016.

For both longer and shorter pulses (the long- and short-pulse limits) the amplitudes are pulse independent and have the values of I_{PL}^{cw} and $I_{PL}^{cw}/\tau_{PL}^{i}$ for the long- and short-limit, respectively.[35] It means that the rate-distributions obtained using short and long pulses cannot be directly compared!

The pulse-length effect on the decay kinetics can have also a real physical origin, as was mentioned in literature,[53] but always without considering the onset effect described above.

The last note is related to the unwanted effect of long excitation pulses, namely deposition of more energy in the excitation spot which causes increase of temperature. In poorly thermally conducting samples (like Si NCs in silica) even weak pumping power (well below saturation threshold) induces heating. This can be observed in Fig. 12(a) as slight overshoot of PL signal amplitude produced at certain time by shorter pulses compared to longer pulses.

5. SLOW PL DECAY IN SI NANOSTRUCTURES

It is now generally accepted[11] that radiative recombination of localized excitons in Si NCs is following quantum confinement (QC) model (see Sec. 5.1). A close similarity of optical properties of all form of nc-Si, i.e. Si NCs (colloidal or matrix embedded) and porous Si (PSi),[2] suggests that the carrier relaxation mechanisms in these systems are similar despite large differences in surrounding environment, when core-related emission is observed.

The presence of various relaxation processes on very different time-scales (from fs to ms) was demonstrated already with PSi (see Fig. 13).[54] Very often, the fast and slow decaying emission is separated spectrally and called as F-band and S-band[55] (see Fig. 14). The F-band with ns-decay lie in the UV-blue-green spectral region (its peak shifts with excitation wavelength) while the S-band is size-tunable within the yellow-red-NIR spectral region. The origin of the F-band is controversial – it is related either to defects or "direct-like" transitions in very small Si NCs (below 2 nm)[56] or in surface-engineered (strained) Si NCs.[57] Here only the slow microsecond S-band will be considered.

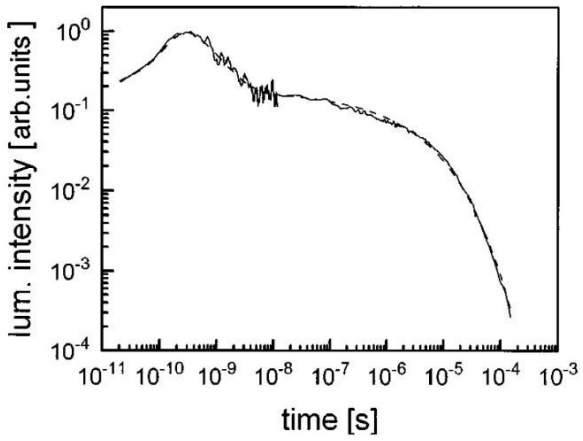

FIG. 13. Extremely broad scale dynamics of Psi from 20 ps to 0.2 ms obtained using two different setups. Reproduced with permission from Malý *et al*., Phys. Rev. B **54**, 7929 (1996). Copyright © The American Physical Society, 1996.

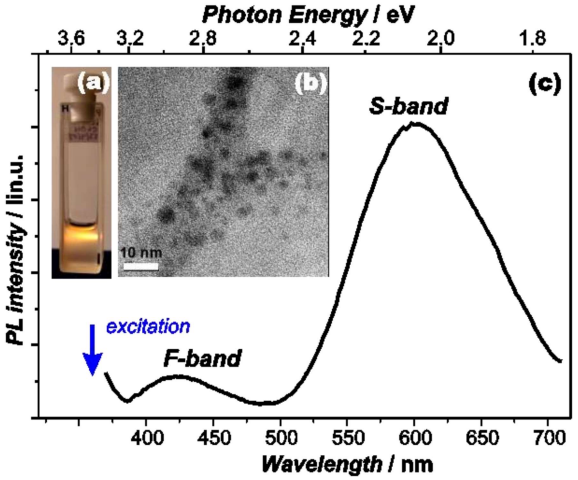

FIG. 14. Characterization of the PSi suspension in ethanol. (a) The photograph of the UV-laser excited cuvette with suspension demonstrating yellow appearance of PL. (b) The HR-TEM image of one PSi grain. (c) The PL spectrum of a typical ''yellow'' PSi colloidal suspension (nonfiltered) under UV excitation (a Xe lamp monochromatized at 360 nm) Reproduced with permission from Valenta *et al*., Adv. Funct. Mater. **18**, 2666 (2008). Copyright © Wiley-VCH Verlag, 2008.

5.1 Stretched-exponential decay

In the earlier works[58,59] TR studies reported a non-exponential PL relaxation kinetics of PSi. For the first time a successful fitting of PSi decays by SE function was applied[59] in analogy with decay fits of ZnS:Mn thin films.[60] Later numerous papers experimentally confirmed an applicability of the SE model on all forms of nc-Si. Since this type of relaxation is often encountered in disordered systems such as a-Si:H and chalcogenide glasses, the same recombination mechanism was associated with nc-Si. A key role of disorder in the form of large distribution of inter-NC distances, NC sizes and the structure of NC surfaces was suggested to explain the observed decay law. More specifically, a dispersive diffusion of the photoexcited carriers among different spatial sites: (i) from localized to extended states (varying carrier localization as a consequence of multiple trapping-detrapping mechanism)[58,61] or (ii) hopping among localized states (migration of excitons between inter-connected NCs).[2,62,63] The latter idea was adopted by various authors until a number of papers with alternative explanation appeared. Thus, Chen *et al.*[7] proposed a numerical model being able to describe SE decay even in an ordered crystal. There was utilized the idea that the SE relaxation might result from each of NC rather than from the whole ensemble. In recent experimental work of Sangghaleh *et al.*[13] it was shown that a decay of single Si NC is rather mono-exponential at room temperature.

Mihalcescu *et al.*[1] challenged the hopping hypothesis providing the evidence that the luminescent centers in PSi must be considered as independent. Their conclusion was based on negligible contribution of a "feeding term" from hopping carriers in PL dynamics. Later, Guillois *et al.*[64] reported on SE kinetics of even completely isolated Si NCs in deposited NC-films and proposed that SE decay must be associated with Si NC as its actual internal characteristic. Recently[11] decay curves of certain sizes of non-interacting colloidal Si NCs were shown to be non-exponential though dispersion factor β was much larger than for Si NCs in solid matrix. All above mentioned results suggest that the physical phenomenon of possible NC interaction alone could hardly explain the experimentally observed SE kinetics. Up to now a number of explanations were proposed yet the fundamental issue of the

physical mechanism responsible for the SE decay is still unresolved. This is because of both theoretical complexities related to the simulation of atomic NCs and the experimental difficulty related to the intrinsic polydispersity of large NC ensembles. In spite of the recent tremendous progress in single-dot spectroscopy, it is not trivial how the attributes of single-particles can be combined and scaled for the large populations of NCs.[65] Besides all, although the SE function described phenomenologically experimental decay curves quite well, it has little physical significance (as discussed before in Sec. 2.3.3).

Here we summarize possible origins of SE decay function besides the energy transfer between Si NCs:

1) Distribution of decay rates (radiative and/or non-radiative) for NCs of a certain size;

As it was shown above, the SE function with $\beta < 1$ can be related *a priori* to some distribution of decay rates $H(k)$. The hypothesis of independent luminescent centers with different crystalline shapes and fluctuation of surface structure and stoichiometry, tensions, etc. resulting in a distribution of recombination rates was proposed in earlier papers.[61,64,66,67] Recently, Sangghaleh *et al.*[13] (see Fig. 3) measured PL decays of single Si NCs and showed that SE decays can be explained by large variation of individual decay lifetimes from dot to dot even for the same emission wavelength. That utilizes the idea that a SE curve might be a convolution of a distribution of mono-exponentials with different τ_0 values. In some papers[61] a dispersion of decay rates was approximated by a distribution of non-radiative rates that must be largely depend on the crystallite environment. In its turn the radiative rate was shown theoretically to be sensitive to the geometry (shape) of NCs.[12,68] This idea of distribution of NC shapes that results in scattering of radiative rates at a given energy was utilized by Guillois *et al.*[64] and Delerue *et al.*[12] as an intrinsic effect to explain SE decays of Si NCs. Linnros *et al.*[2] observed single exponential behaviour at the decay ends and argued that the distribution of radiative rates alone cannot explain this effect. Only recently a strong argument on negligible dispersion of radiative rates was obtained experimentally by Sangghaleh *et al.*[10] The size-selected decays (emission from monodisperse NCs) were deconvoluted from spectrally-selected ones (emission at a single wavelength) of colloidal Si NCs and were proved to be mono-exponential that eliminates any dispersion of recombination rates for structurally homogeneous NCs.

2) The effect of intensity intermittence or "blinking" in single NC;

It was demonstrated that most of single fluorophores (quantum emitters) of different types ranging from single dye molecules to semiconductor NCs exhibit a fluorescence intermittency (blinking).[65,69] Thus, single NCs are observed to switch between discrete luminescence intensity levels resulting in altering series of bright (on) and dark (off) periods. Recently Dunn *et al.*[65] developed a model that links the interaction of relaxing carriers with the blinking mechanism. This model provides suitable fits of experimental PL decay curves and allows the deconvolution of intrinsic recombination rates and extrinsic blinking effects which can possible explain SE nature of kinetics of Si NCs.

3) The effect of homogeneous linewidth (HL) broadening;

Here it is important to distinguish spectrally resolved and size-selected decays. Spectrally resolved decay is simply a decay that is measured at a certain wavelength. A size-selected decay is TR characteristics related to NCs of a certain size separated from a polydisperse ensemble of NCs. When the PL HL of single emitter in an ensemble is narrow, the concepts of spectrally resolved and size-selected decays are essentially the same. Unfortunately, at room temperature individual Si NCs yield broad HL of ~100–200 meV.[70] Recently, Sangghaleh *et al.*[10] reported that SE decay behavior of colloidal Si NCs can be the result of a convolution of mono-exponentials with different τ_0 values. However, unlike to the first point in the list where different τ_0 was related to a dispersion of decay rates in size-selected decay,

here it is related to different size-selected rates in spectrally resolved decay. A numerical method was suggested to resolve intrinsic size-selected recombination decays which were shown being mono-exponential. It is important to note that this effect alone is not sufficient to explain SE decays of Si NCs in solid matrix. Comparing Si NCs in solid matrix with colloidal ones: a) the dispersion factor is much lower (larger inhomogeneity) while b) the effect of HL is less pronounced (narrower HL).[70] Moreover, at reduced temperatures Si NCs reveal[71] a significant line-narrowing reaching a few meV at 35 K that eliminates the described effect though kinetics are still SE.[72,73,74]

In literature both the decay lifetime τ (SE characteristic lifetime τ_0) and dispersion factor β are analysed in dependence on variety of parameters. Thus, τ, β as functions of the Si concentration for Si-rich SiO_2 annealed films were presented.[62,75] While the lifetime was proven decreasing, the dispersion parameter in different papers was shown to decrease[62] or increase[75] with increasing of Si concentration. Linnros *et al.*[2] showed that both τ, β are decreasing functions of implantation Si dose (i.e. the concentration of excess Si in SiO_2 linked to size and density of Si NCs formed by annealing) and the effect of implantation temperature is weak. A slight decrease of τ, β for higher excitation intensities I_{ex} was reported by Pavesi[72] and this trend of $\tau(I_{ex})$ was confirmed recently.[40,43]

The variation of τ, β with sample temperature was presented in a number of papers. Thus, $\beta(T)$ was shown to be constant for high temperatures, and then it is a decreasing function of temperature with sample cooling.[72,73,74,76] In contrast, $\beta(T)$ is presented as a modulated function with maxima and minima in other papers.[54,77,78,79] For above room temperatures $\beta(T)$ is expected to decrease with sample heating.[1] A detailed study of $\tau(T)$ was presented by Hartel *et al.*[41] The lifetime $\tau(T)$ was shown to be an increasing function of decreasing sample temperature exhibiting a kink in the region $70\ \mathrm{K} < T < 150\ \mathrm{K}$ delimiting the regions with dominating radiative and non-radiative decays (see Fig. 15).

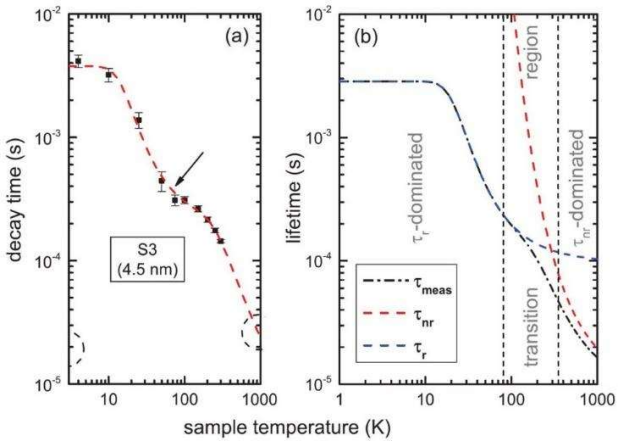

FIG. 15. (a) Thermal evolution of decay times for SiNC multilayer structure. Experimental points (black squares) are fitted by the model formulated by Hartel *et al.* The arrow indicates the kink. (b) Theoretical calculation of radiative (blue dashed line) and nonradiative (red dashed line) lifetimes compared with experimental dependence. Reproduced with permission from Hartel *et al.*, Phys. Rev. B **87**, 035428 (2013). Copyright © The American Physical Society, 2013.

Finally, an energy dependence of these key parameters was also investigated. Pavesi[72,63] reported that τ, β are independent on excitation photon energy while the dependence on emission energy was presented in a large number of papers. With increasing photon energy $\beta(\hbar\omega_{em})$ was shown to decrease above 1.4 eV (see [10,72,54,80,81]) or above 1.7 eV (see [82,83]). It can be at least partially understood taking into account that for shorter lifetimes (larger energy) the variation in contributed lifetimes from spectrally neighboring NCs is larger in relative terms, resulting in a stronger dispersion (decreased β). On the other side, a decrease of $\beta(\hbar\omega_{em})$ for lower photon energies below 1.4 eV (see [11,65] and Fig. 16) or 1.7 eV (see [2,82]) was observed. In contrast, in some papers[1,72,63,65,73,84] β is reported to be almost independent on emission energy $\hbar\omega_{em}$. The variation of lifetimes $\tau(\hbar\omega_{em})$ or decay rates $k(\hbar\omega_{em})$ was confirmed in many reports to follow the quantum confinement (QC) model[11] that reveal exponential dependence:

$$\tau(\hbar\omega_{em}) = Ae^{-\frac{\hbar\omega_{em}}{\Delta E}};\ k(\hbar\omega_{em}) = Ae^{\frac{\hbar\omega_{em}}{\Delta E}} \quad (56)$$

where A is a constant, ΔE is a characteristic energy depending on temperature.

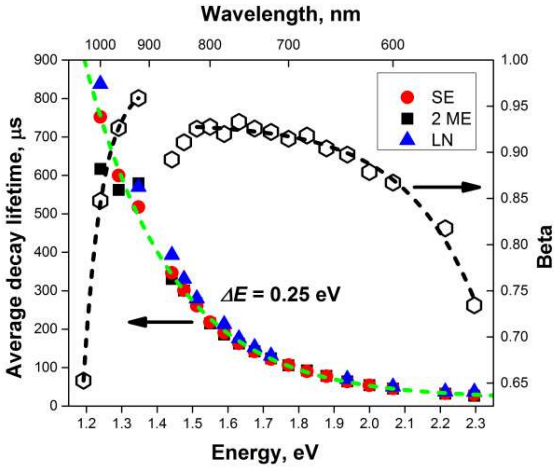

FIG. 16. PL average lifetimes of dodecyl-passivated colloidal Si NCs obtained by fitting with different decay models as well as dispersion factor β of SE fits in dependence on emission photon energy. The dashed green line is an exponential fit of SE average lifetimes while dashed black lines correspond to exponential fits of dispersion factors β. Reproduced with permission from Greben *et al*., J. Appl. Phys. **122**, 34304 (2017). Copyright © AIP Publishing 2017.

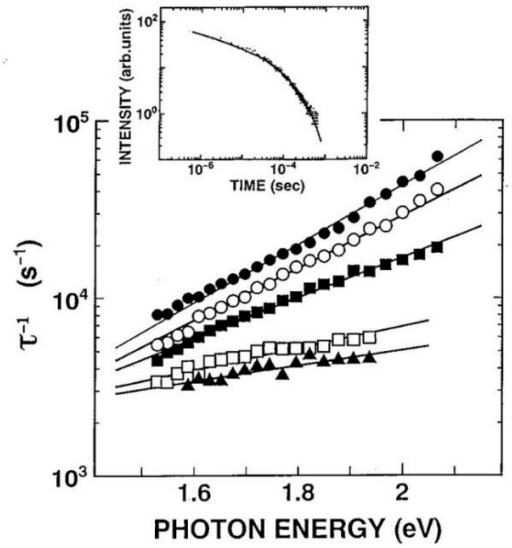

FIG. 17. The effective PL decay rate as function of emission photon energy at temperatures of 280, 220, 150, 80, and 30 K. The exponential slope increases with increasing T. The inset shows PL decay curve at 80 K and 1.65 eV in the log-log plot fitted by SE. Reproduced with permission from Kanemitsu, Phys. Rev. B **53**, 13515 (1996). Copyright © The American Physical Society, 1996.

Thus, exponential dependence [see Eq. (56)] of both $\tau(\hbar\omega_{em})$ and $k(\hbar\omega_{em})$ was confirmed in papers.[67,79,85] Delerue *et al.*[12] theoretically calculated $\Delta E = 0.31$ eV (see [12]) for $k(\hbar\omega_{em})$ based on QC model that was confirmed experimentally.[72,86] The lifetime $\tau(\hbar\omega_{em})$ was proven[11,87,88] to follow the Eq. (56) where $\Delta E = 0.25$ eV (see Fig. 16). Earlier, Kanemitsu demonstrated that ΔE is changing with temperature, see Fig. 17.

5.2 Lognormal rate distribution decay

It is well known that size distribution of QDs[89] is often well described by a LN function. Similar to this, a decay rate probability distribution can be assumed in the form of Eq. (16) and then the intensity decay should be described by Eq. (11). This type of decays is usually modelled when SE function fails (see Fig. 5 and Sec. 2.4) to fit decay curves. In application to PL decays of QDs the theory of LN distribution of rates was well described by van Driel, Nikolaev *et al.*[4,90] There is very limited number of papers where the distribution of decay rates of Si NCs is assumed by LN function. Thus, Zatrub *et al.*[22] analysed strongly non-exponential TR PL spectra of boron-doped and undoped SRO/SiO_2 multilayers and successfully modelled decay kinetics assuming LN distribution of decay rates. The distribution of decay rates of boron-doped samples expectedly occurred broader as boron-doping introduces more defect states to the matrix with Si NCs. Later LN decay model was applied by Nakamura *et al.*[91] in their study of decay rates of Si NCs near thin semicontinuous gold film. There was made a comparison of fits by reduced chi-squared values χ_R^2 with SE decay model and the LN model achieved better fit. Recently, Nguyen *et al.*[23] applied LN model to describe decays of organically-capped Si NCs with different surface functionalization where the SE model failed. Our recent studies demonstrate that LN model can describe well both PL decays of Si NC multilayers in high quality PE-CVD samples[36] (see Fig. 18) as well as kinetics of dodecyl-passivated colloidal Si NCs (see Fig. 16 and [11]).

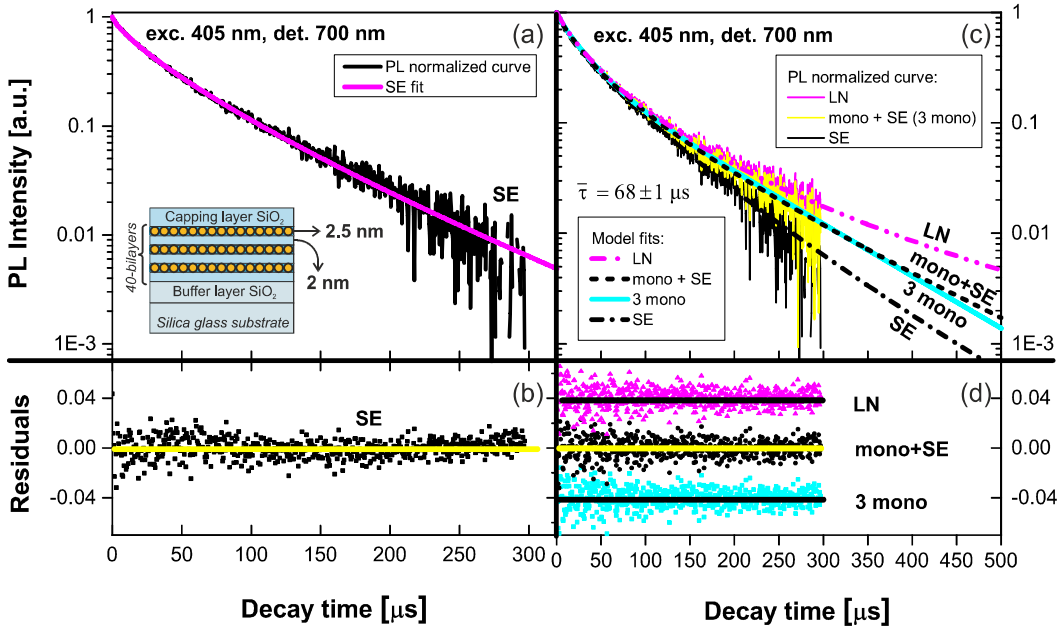

FIG. 18. PL decay normalized curve (a, c) of Si NCs/SiO_2 superlattice and its SE fit (a) or fits by different other models (c): combination of 3 mono-exponentials (3 mono), combination of mono and stretched exponentials (mono + SE), lognormal (LN) distribution of rates. (b,d) residuals to corresponding fits. The pink and cyan points were displaced vertically by ± 0.04 to not overlap. Reproduced with permission from Greben *et al*., in *Physics, Chem. Appl. Nanostructures* (2017), pp. 110–113. Copyright © World Scientific Publishing Co. Pte. Ltd. 2017.

5.3 Complex decays

Sometimes neither LN nor SE decay models can describe PL kinetics, yielding unsatisfactory fits to the measured decays. In such a complex case besides ME fitting a combination of mono- and SE [see Eq. (47)] or 2 SE [see Eq. (49)] can be helpful. Thus, Linnros *et al.*[2] modelled decay kinetics of SiO_2/Si implanted samples containing Si NCs by Eq. (47). The tail of decays revealed mono-exponential behavior that was assigned to a fraction of well-separated homogeneously emitting Si NCs with identical decay rates (see Fig. 19). In contrast, SE term was concluded to come from a partially interconnected system of NCs where excitons may migrate and be trapped in larger NCs. Pitanti *et al.*[92] studied spontaneous emission rate enhancement of Si NCs embedded in a whispering gallery mode (WGM) resonator. For excitons that were considered as uncoupled to any cavity mode (measurements in spectral dips between neighboring WGM resonances)

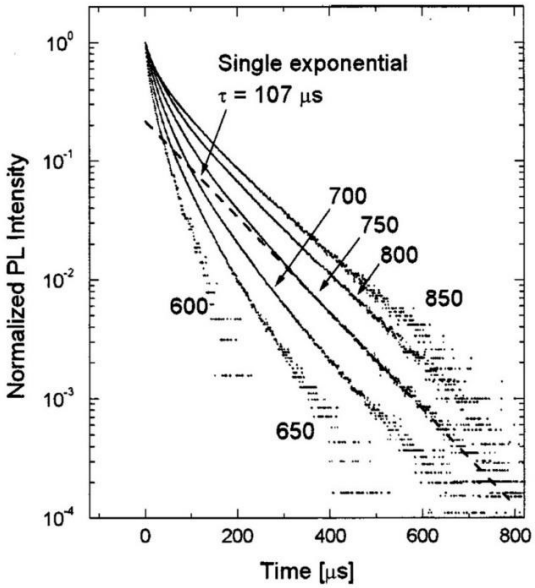

FIG. 19. Normalized PL decays of SiNC in Si-implanted silica (dose 10^{17} cm^{-2}, annealing at 1100 °C for 2 hours). The detection wavelengths from 600 to 850 nm are indicated (excitation with ns-pulses at 532 nm) and the dashed lines shows the 107 μs single exponential decay. Reproduced with permission from Linnros *et al*., J. Appl. Phys. **86**, 6128 (1999). Copyright © AIP Publishing 1999.

the decays were fitted well with SE function [see Eq. (23)]. PL decays at cavity peak wavelengths were considered as a convolution of coupled and uncoupled photons to the cavity mode and was modelled with Eq. (47), where SE lifetime corresponds to mode-coupled emitters. At the same time mono-exponential lifetimes represented the average lifetime of extracted data for dips.

Recently we employed the model given by Eq. (47) for the decay analysis of PECVD-synthesized Si NCs embedded in SiO_2. While SE model fails to fit the decays, a combination of mono- and SE serves perfectly for the average lifetime extraction (see Fig. 18). [36] This knowledge was utilized in ACS extraction[43] of Si NCs (see Sec. 3.3.1). It is worth to note that the Eq. (47) was also utilized to describe TR ultrafast carrier dynamics in as-grown nc-Si films[93] as well as in other materials, i.e., for instance, lead halide perovskites.[94]

Hartel *et al.*[41] studied temperature-dependent properties of Si NCs in PECVD samples. PL transients revealed a pronounced fast decay component that made SE fitting unrealistic. The average decay lifetime was extracted approximately according to technique of Higashi and Kastner[39] that is described above in Sec. 3.2.2. We employed[40] this approach in calculation of ACS of Si NCs in similar multilayer samples. Recently Brown *et al.*[42] studied PL relaxation in monodisperse colloidal Si NCs where fast and slow relaxation modes were revealed. The sum of 2 SE [see Eq. (49)] was utilized to fit decay curves.

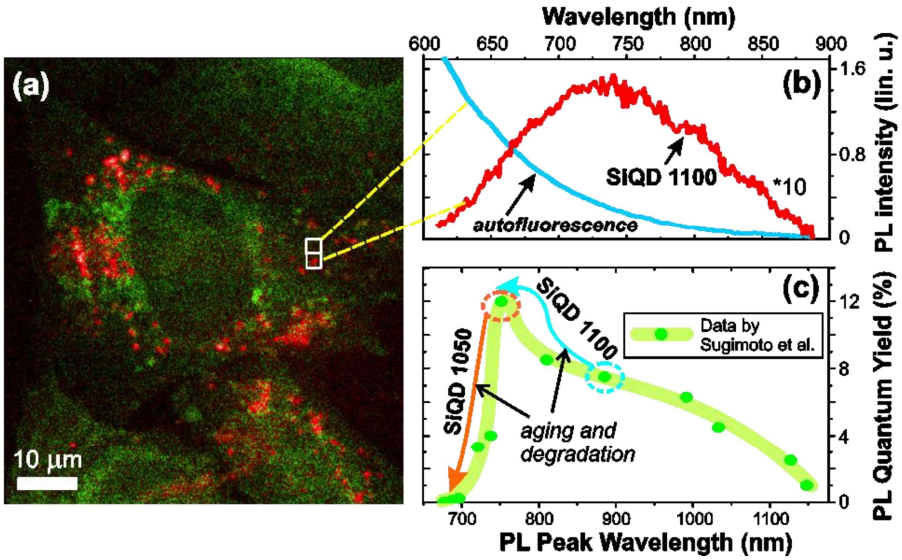

FIG. 20. Wide-field fluorescence microscopy and spectroscopy of B,P-codoped Si NCs cultivated with SAOS-2 cells: (a) combined fluorescence image with the green layer showing the full signal (dominated by cell autofluorescence) and the orange layer showing signal above 785 nm (dominated by Si NC PL). The vertical stripe shows area of the spectrometer slit introduced for spectral measurements. (b) Luminescence spectrum of cell autofluorescence (blue) and emission of Si NC cluster (red line) from area indicated by a rectangle in the panel (a). The autofluorescence signal estimated from area around the Si NC cluster was subtracted. (c) Observed shift of PL peak and quantum yield of Si NCs – the slow changes due to aging of Si NC suspensions in methanol are accelerated in water based media during bio-studies. Reproduced from Ostrovska *et al.*, RSC Adv. **6**, 63403 (2016) with permission from The Royal Society of Chemistry. Copyright © The Royal Society of Chemistry 2016.

We should note that rather diverse results found in literature and presented here in Sec. 5 can be the result of both physical difference of differently prepared materials and the non-

optimal experimental conditions. Evidently, many authors did not pay enough attention to the effects of pulse length (short, intermediate or long regime), excitation power (below or above saturation threshold), truncation of the decay curve, signal-to-noise quality, etc. For example, the appearance of a fast decay component is often linked to excitation by too short and/or too intense pulses.

5.4 Applications of slow PL decay in nc-Si

We have already mentioned in Sec. 3.3 that studies of variation in PL kinetics under different pumping intensity or in changing environment enable to reveal important parameters like ACS and IQY. Besides that, the slowly decaying PL signal of Si NCs may be exploited in bio-imaging as it has not only the convenient spectral position (red and near-infrared where is the transparency window of tissues) but also enable efficient temporal filtering.[95,96] Luminescence of conventional fluorescent labels as well as the inherent emission of cells (so called autofluorescence) has fast nanosecond decay, so it can be separated from the PL of Si NCs using a gated detection [see e.g. recent work by Ostrovska *et al*.[97] (Fig. 20) or [98]]. Moreover nc-Si materials proved to be nontoxic and biodegradable.[99,100]

6. CONCLUSIONS

We have presented the detailed theoretical and experimental study of slow TR PL decay kinetics from ensembles of excited emitters, in particular Si NCs. The most common cases of mono-exponential PL decays are analysed including homogeneous ensemble of non-interacting emitters and isolated individual emitters. The treatment of mono- and ME, SE, LN as well as some complex cases of PL decay models is presented using PDF in the form of both continuous and discrete distribution of rates (lifetimes). We explicitly show that a LN distribution of emitter sizes may results in LN distribution of decay rates. We illustrate the futility of treating decays that can be fitted with SE function by restoring its distribution of decay rates (PDF) and demonstrate that this PDF is diverging in time domain that is void of physical meaning. Therefore, we encourage authors to treat decays with SE model only for the assessment of distribution average and estimation of degree of dispersion. We explicitly show the difference between average decay (intensity average) lifetime $\bar{\tau}$ and the average lifetime constant $\langle\tau\rangle$ (amplitude-average lifetime). The understanding of the fundamental difference between $\bar{\tau}$ and $\langle\tau\rangle$ is of great practical importance to its proper use in diverse conditions and there is accumulating number of publications where these terms are misused. We derive mathematical expressions to calculate the average decay lifetimes and its approximation for some common $I(t)$ decays of Si NCs. Some examples of the most important uses of the average lifetime concept are presented. The experimental assessment of PL kinetics is discussed including the background subtraction and optimal excitation conditions. Finally, a throughout literature review of PL decay kinetics of Si NCs covering different fitting models is presented. We believe that our report could help researchers who deal with TR PL experiments in nanocrystals and other physical systems with dispersed kinetics to correctly extract quantitative information from decay curves that could have great practical significance in characterization of materials.

ACKNOWLEDGEMENTS

The authors would like to thank Prof. J. Collins and our colleagues: F. Pevere, F. Sangghaleh, J. Linnros, I. Pelant, J. Hala, R. Dedic and J. Alster, for fruitful discussions. Two of authors (MG and JV) acknowledge support by the bilateral Czech-German DFG-GACR project 16-09745J and the Visegrad4 + Japan Joint Research Project on Advanced Materials (MEYS CR project No. 8F15001 cofinanced by the International Visegrad Fund).

REFERENCIES

[1] I. Mihalcescu, J.C. Vial, and R. Romestain, Phys. Rev. Lett. **80**, 3392 (1998).

[2] J. Linnros, N. Lalic, A. Galeckas, and V. Grivickas, J. Appl. Phys. **86**, 6128 (1999).

[3] M.N. Berberan-Santos, E.N. Bodunov, and B. Valeur, Chem. Phys. **315**, 171 (2005).

[4] A.F. Van Driel, I.S. Nikolaev, P. Vergeer, P. Lodahl, D. Vanmaekelbergh, and W.L. Vos, Phys. Rev. B - Condens. Matter Mater. Phys. **75**, 1 (2007).

[5] N. Boens and M. Van der Auweraer, Photochem. Photobiol. Sci. **13**, 422 (2014).

[6] G. Zatryb, A. Podhorodecki, J. Misiewicz, J. Cardin, and F. Gourbilleau, Nanoscale Res. Lett. **6**, 106 (2011).

[7] R. Chen, J. Lumin. **102**–**103**, 510 (2003).

[8] I. Pelant and J. Valenta, *Luminescence Spectroscopy of Semiconductors* (Oxford University Press, New York, 2012).

[9] C. Pu, J. Ma, H. Qin, M. Yan, T. Fu, Y. Niu, X. Yang, Y. Huang, F. Zhao, and X. Peng, ACS Cent. Sci. **2**, 32 (2016).

[10] F. Sangghaleh, I. Sychugov, Z. Yang, J.G.C. Veinot, and J. Linnros, ACS Nano **9**, 7097 (2015).

[11] M. Greben, P. Khoroshyy, X. Liu, X. Pi, and J. Valenta, J. Appl. Phys. **122**, 34304 (2017).

[12] C. Delerue, G. Allan, C. Reynaud, O. Guillois, G. Ledoux, and F. Huisken, Phys. Rev. B **73**, 235318 (2006).

[13] F. Sangghaleh, B. Bruhn, T. Schmidt, and J. Linnros, Nanotechnology **24**, 225204 (2013).

[14] F.T. Rabouw, M. Kamp, R.J.A. Van Dijk-Moes, D.R. Gamelin, A.F. Koenderink, A. Meijerink, and D. Vanmaekelbergh, Nano Lett. **15**, 7718 (2015).

[15] A. Marchioro, P.J. Whitham, K.E. Knowles, T.B. Kilburn, P.J. Reid, and D.R. Gamelin, J. Phys. Chem. C **120**, 27040 (2016).

[16] M. Jones and G.D. Scholes, J. Mater. Chem. **20**, 3533 (2010).

[17] J.R. Lakowicz, *Principles of Fluorescence Spectroscopy* (Springer US, Boston, MA, 2006).

[18] A. Siemiarczuk, B.D. Wagner, and W.R. Ware, J. Phys. Chem. **94**, 1661 (1990).

[19] A.M. Kapitonov, A.P. Stupak, S. V. Gaponenko, E.P. Petrov, A.L. Rogach, and A. Eychmüller, J. Phys. Chem. B **103**, 10109 (1999).

[20] G. Bohm and G. Zech, *Introduction to Statistics and Data Analysis for Physicists* (Verlag Deutsches Elektronen-Synchrotron, 2010).

[21] J. Norstad, *The Normal and Lognormal Distributions* (2011).

[22] G. Zatryb, A. Podhorodecki, X.J. Hao, J. Misiewicz, Y.S. Shen, and M.A. Green, Opt. Express **18**, 22004 (2010).

[23] A. Nguyen, C.M. Gonzalez, R. Sinelnikov, W. Newman, S. Sun, R. Lockwood, J.G.C. Veinot, and A. Meldrum, Nanotechnology **27**, 105501 (2016).

[24] R. Kohlrausch, Ann. Der Phys. Und Chemie **91**, 179 (1854).

[25] G. Williams and D.C. Watts, Trans. Faraday Soc. **66**, 80 (1970).

[26] R.A. Street, Adv. Phys. **25**, 397 (1976).

[27] J. Laherrère and D. Sornette, Eur. Phys. J. B **2**, 525 (1998).

[28] L. Vivien and L. Pavesi, *Handbook of Silicon Photonics* (CRC Press, 2013).

[29] D.C. Johnston, Phys. Rev. B - Condens. Matter Mater. Phys. **74**, 1 (2006).

[30] K.A. Penson and K. Górska, Phys. Rev. Lett. **105**, 210604 (2010).

[31] G. Dattoli, K. Górska, A. Horzela, and K.A. Penson, Phys. Lett. Sect. A Gen. At. Solid State Phys. **378**, 2201 (2014).

[32] J. Wolberg, *Data Analysis Using the Method of Least Squares* (2006).

[33] A. Sillen and Y. Engelborghs, Photochem. Photobiol. **67**, 475 (1998).

[34] S.G. Lopez, L. Crovetto, J.M. Alvarez-Pez, E.M. Talavera, and E. San Román, Photochem. Photobiol. Sci. **13**, 1311 (2014).

[35] M. Greben and J. Valenta, Rev. Sci. Instrum. **87**, 126101 (2016).

[36] M. Greben, J. Valenta, and P. Khoroshyy, in *Physics, Chem. Appl. Nanostructures* (2017), pp. 110–113.

[37] J.R. Knutson, J.M. Beechem, and L. Brand, Chem. Phys. Lett. **102**, 501 (1983).

[38] A. Grinvald and I.Z. Steinberg, Anal. Biochem. **59**, 583 (1974).

[39] G.S. Higashi and M.A. Kastner, Philos. Mag. Part B **47**, 83 (1982).

[40] J. Valenta, M. Greben, Z. Remeš, S. Gutsch, D. Hiller, and M. Zacharias, Appl. Phys. Lett. **108**, 23102 (2016).

[41] A.M. Hartel, S. Gutsch, D. Hiller, and M. Zacharias, Phys. Rev. B **87**, 35428 (2013).

[42] S.L. Brown, J.B. Miller, R.J. Anthony, U.R. Kortshagen, A. Kryjevski, and E.K. Hobbie, ACS Nano **11**, 1597 (2017).

[43] M. Greben, P. Khoroshyy, S. Gutsch, D. Hiller, M. Zacharias, and J. Valenta, Beilstein J. Nanotechnol. (n.d.).

[44] R.J. Walters, J. Kalkman, A. Polman, H.A. Atwater, and M.J.A. de Dood, Phys. Rev. B **73**, 132302 (2006).

[45] S. Miura, T. Nakamura, M. Fujii, M. Inui, and S. Hayashi, Phys. Rev. B **73**, 245333 (2006).

[46] G.H. Rieke, *Detection of Light From the Ultraviolet to the Submillimeter* (Cambridge University Press, 2003).

[47]*The Bh TCSPC Handbook* (Becker&Hickl, Berlin, 2010).

[48] J. Valenta, I. Pelant, V. Kohlova, V. Bradnova, M. Trchova, J. Klimovic, and J. Hala, J. Phys. Condens. Matter **7**, 433 (1995).

[49] J. Valenta and M. Greben, AIP Adv. **5**, 47131 (2015).

[50] D.V. O'Connor and D. Phillips, *Time-Correlated Single Photon Counting* (Academic Press, inc., London, 1984).

[51] R.W.K. Leung, S.-C.A. Yeh, and Q. Fang, Biomed. Opt. Express **2**, 2517 (2011).

[52] W. Becker, B. Su, O. Holub, and K. Weisshart, Microsc. Res. Tech. **74**, n/a (2010).

[53] S.J. Parus, Z.Y. Shi, and R. Kopelman, J. Lumin. **45**, 43 (1990).

[54] M. Kořínek, M. Kozák, F. Trojánek, D. Hiller, A.M. Hartel, S. Gutsch, M. Zacharias, and P. Malý, in *Proc. SPIE*, edited by S. Cabrini, G. Lérondel, A.M. Schwartzberg, and T. Mokari (2013), p. 88070V.

[55] J. Valenta, A. Fucikova, F. Vácha, F. Adamec, J. Humpolíčková, M. Hof, I. Pelant, K. Kůsová, K. Dohnalová, and J. Linnros, Adv. Funct. Mater. **18**, 2666 (2008).

[56] J. Valenta, A. Fucikova, I. Pelant, K. Kusová, K. Dohnalová, A. Aleknavičius, O. Cibulka, A. Fojtík, and G. Kada, New J. Phys. **10**, (2008).

[57] K. Kůsová, P. Hapala, J. Valenta, P. Jelínek, O. Cibulka, L. Ondič, and I. Pelant, Adv. Mater. Interfaces **1**, 1300042 (2014).

[58] J.C. Vial, A. Bsiesy, F. Gaspard, R. Hérino, M. Ligeon, F. Muller, R. Romestain, and R.M. Macfarlane, Phys. Rev. B **45**, 14171 (1992).

[59] X. Chen, B. Henderson, and K.P. O'Donnell, Appl. Phys. Lett. **60**, 2672 (1992).

[60] P. Benalloul, J. Benoit, R. Mach, G.O. Müller, and G.U. Reinsperger, J. Cryst. Growth **101**, 989 (1990).

[61] I. Mihalcescu, J.C. Vial, and R. Romestain, J. Appl. Phys. **80**, 2404 (1996).

[62] F. Priolo, G. Franzò, D. Pacifici, V. Vinciguerra, F. Iacona, and A. Irrera, J. Appl. Phys. **89**, 264 (2001).

[63] L. Pavesi and M. Ceschini, Phys. Rev. B **48**, 17625 (1993).

[64] O. Guillois, N. Herlin-Boime, C. Reynaud, G. Ledoux, and F. Huisken, J. Appl. Phys. **95**, 3677 (2004).

[65] K. Dunn, J. Derr, T. Johnston, M. Chaker, and F. Rosei, Phys. Rev. B **80**, 35330 (2009).

[66] E. Bustarret, I. Mihalcescu, M. Ligeon, R. Romestain, J.C. Vial, and F. Madéore, J. Lumin. **57**, 105 (1993).

[67] Y. Kanemitsu, Phys. Rev. B **53**, 13515 (1996).

[68] I. Sychugov, F. Sangghaleh, B. Bruhn, F. Pevere, J.-W. Luo, A. Zunger, and J. Linnros, Nano Lett. **16**, 7937 (2016).

[69] B. Bruhn, J. Valenta, F. Sangghaleh, and J. Linnros, Nano Lett. **11**, 5574 (2011).

[70] I. Sychugov, A. Fucikova, F. Pevere, Z. Yang, J.G.C. Veinot, and J. Linnros, ACS Photonics **1**, 998 (2014).

[71] I. Sychugov, R. Juhasz, J. Valenta, and J. Linnros, Phys. Rev. Lett. **94**, 4 (2005).

[72] L. Pavesi, J. Appl. Phys. **80**, 216 (1996).

[73] M. Dovrat, Y. Goshen, J. Jedrzejewski, I. Balberg, and A. Sa'ar, Phys. Rev. B - Condens. Matter Mater. Phys. **69**, 1 (2004).

[74] W. Yu, H. Feng, J. Wang, W. Dai, X. Yu, J. Zhang, W. Lai, and G. Fu, Phys. B Condens. Matter **434**, 177 (2014).

[75] S. Kim, D.H. Shin, D.Y. Shin, C.O. Kim, J.H. Park, S.B. Yang, S.H. Choi, S.J. Yoo, and J.G. Kim, J. Nanomater. **2012**, (2012).

[76] A. Kobitski, K. Zhuravlev, H. Wagner, and D. Zahn, Phys. Rev. B **63**, 1 (2001).

[77] S. Gardelis, A.G. Nassiopoulou, N. Vouroutzis, and N. Frangis, J. Appl. Phys. **105**, (2009).

[78] J. Heitmann, F. Müller, L. Yi, M. Zacharias, D. Kovalev, and F. Eichhorn, Phys. Rev. B - Condens. Matter Mater. Phys. **69**, 1 (2004).

[79] N. Ookubo and S. Sawada, Phys. Rev. B **51**, 17526 (1995).

[80] M. Kořínek, M. Kozák, F. Trojánek, D. Hiller, A. Hartel, S. Gutsch, M. Zacharias, and P. Malý, Phys. E Low-Dimensional Syst. Nanostructures **56**, 177 (2014).

[81] G.B. De los Reyes, Ultrafast Photoluminescence Spectroscopy of Silicon Nanocrystals, University of Alberta, 2015.

[82] X. Liu, Y. Zhang, T. Yu, X. Qiao, R. Gresback, X. Pi, and D. Yang, Part. Part. Syst. Charact. **33**, 44 (2016).

[83] N. Ookubo, J. Appl. Phys. **74**, 6375 (1993).

[84] J. Linnros, A. Galeckas, N. Lalic, and V. Grivickas, Thin Solid Films **297**, 167 (1997).

[85] L.J. Borrero-Gonzalez, L.A.O. Nunes, M.R.B. Andreeta, J. Wojcik, P. Mascher, Y.A. Pusep, D. Comedi, and F.E.G. Guimarães, J. Appl. Phys. **108**, 13105 (2010).

[86] J. Derr, K. Dunn, D. Riabinina, F. Martin, M. Chaker, and F. Rosei, Phys. E Low-Dimensional Syst. Nanostructures **41**, 668 (2009).

[87] D. Amans, O. Guillois, G. Ledoux, D. Porterat, and C. Reynaud, J. Appl. Phys. **91**, 5334 (2002).

[88] F. Huisken, G. Ledoux, O. Guillois, and C. Reynaud, Adv. Mater. **14**, 1861 (2002).

[89] V.A. Belyakov, V.A. Burdov, R. Lockwood, and A. Meldrum, Adv. Opt. Technol. **2008**, 1 (2008).

[90] I.S. Nikolaev, P. Lodahl, A.F. van Driel, A.F. Koenderink, and W.L. Vos, Phys. Rev. B **75**, 115302 (2007).

[91] T. Nakamura, B.P. Tiwari, and S. Adachi, Opt. Express **20**, 26548 (2012).

[92] A. Pitanti, M. Ghulinyan, D. Navarro-Urrios, G. Pucker, and L. Pavesi, Phys. Rev. Lett. **104**, 1 (2010).

[93] E. Lioudakis and A. Othonos, Phys. Status Solidi – Rapid Res. Lett. **2**, 19 (2008).

[94] J.A. Guse, A. Mahboubi Soufiani, L. Jiang, J. Kim, Y.-B. Cheng, T.W. Schmidt, A. Ho-Baillie, and D.R. McCamey, Phys. Chem. Chem. Phys. **18**, 12043 (2016).

[95] F. Erogbogbo, K.-T. Yong, I. Roy, R. Hu, W.-C. Law, W. Zhao, H. Ding, F. Wu, R. Kumar, M.T. Swihart, and P.N. Prasad, ACS Nano **5**, 413 (2011).

[96] Y. Zhai, M. Dasog, R.B. Snitynsky, T.K. Purkait, M. Aghajamali, A.H. Hahn, C.B. Sturdy, T.L. Lowary, and J.G.C. Veinot, J. Mater. Chem. B **2**, 8427 (2014).

[97] L. Ostrovska, A. Broz, A. Fucikova, T. Belinova, H. Sugimoto, T. Kanno, M. Fujii, J. Valenta, and M.H. Kalbacova, RSC Adv. **6**, 63403 (2016).

[98] J. Joo, X. Liu, V.R. Kotamraju, E. Ruoslahti, Y. Nam, and M.J. Sailor, ACS Nano **9**, 6233 (2015).

[99] N.H. Alsharif, C.E.M. Berger, S.S. Varanasi, Y. Chao, B.R. Horrocks, and H.K. Datta, Small **5**, 221 (2008).

[100] A. Fucikova, J. Valenta, I. Pelant, M.H. Kalbacova, A. Broz, B. Rezek, A. Kromka, and Z. Bakaeva, RSC Adv. **4**, 10334 (2014).